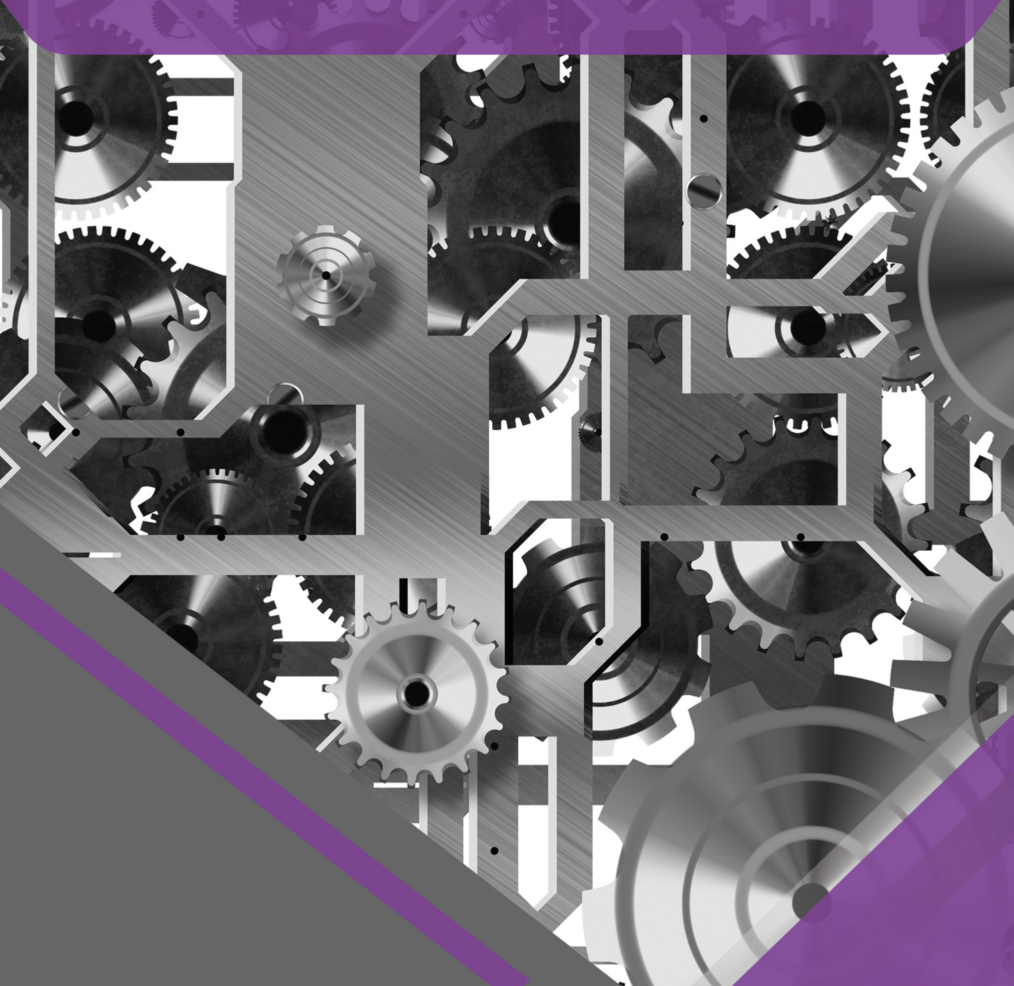

New Horizons in Engineering

2019

Editor

Mahmut TURHAN
(MEDEL MÜHENDİSLİK VE ELEKTRONİK SAN.TİC.A.Ş.)

GECE AKADEMİ

New Horizons in Engineering

GECE AKADEMİ

İmtiyaz Sahibi / Publisher • Gece Kitaplığı
Genel Yayın Yönetmeni / Editor in Chief • Doç. Dr. Atilla ATİK
Editör / Editor • Mahmut Turhan (Medel Mühendislik ve Elektronik San.Tic.A.Ş.)
Kapak & İç Tasarım / Cover & Interior Design • Didem S. KORKUT
Sosyal Medya / Social Media • Arzu Betül ÇUHACIOĞLU

Birinci Basım / First Edition • ©EKİM 2019

ISBN • 978-605-7749-98-7

Gece Kitaplığı / Gece Publishing
ABD Adres/ USA Address: 387 Park Avenue South, 5th Floor,
New York, 10016, USA
Telefon / Phone: +1 347 355 10 70
Türkiye Adres / Turkey Address: Kızılay Mah. Fevzi Çakmak 1. Sokak
Ümit Apt. No: 22/A Çankaya / Ankara / TR
Telefon / Phone: +90 312 384 80 40
+90 555 888 24 26
web: www.gecekitapligi.com
e-mail: geceakademi@gmail.com

GECE AKADEMİ

Baskı & Cilt / Printing & Volume
Sertifika / Certificate No:29377

New Horizons in Engineering

GECE AKADEMİ

CONTENTS

A COMPARISON OF ORB , LBP AND PCA ALGORITHMS FOR A REAL-TIME FACIAL RECOGNITION SYSTEM

Abdullah Mohammed NOORİ

Murat SELEK

CHAPTER 1

A COMPARISON OF ORB , LBP AND PCA ALGORITHMS FOR A REAL-TIME FACIAL RECOGNITION SYSTEM

Abdullah Mohammed NOORİ, Murat SELEK

INTRODUCTION

Facial recognition and identification are challenging research problem that spanning various disciplines. That's because the technology has many practical applications that require accurate and secure techniques such as bankcard identification, security monitoring, and surveillance. The first technique of classifying faces proposed by [1] which collecting the faces as curves to find their norm and classifying them using the deviations of the norm. The fast development of the field is due to many factors; active algorithms development by researchers, availability of large databases and the method of evaluating the performance of the systems. Face recognition progress has many steps, it starts with detection of the face in the images that sometimes with cluttered scenes, followed by normalization of the face to account for illumination changes. The key applications of the technology can be summarized as two parts: law enforcement application and commercial application. Face recognition used primarily in law enforcement application such as mug shot image search and video surveillance. The commercial application of the face recognition ranges from use the face in the ATM for bank cards security and passports for matching with available databases [2-4]. In this paper, we introduce a comparison of three facial recognition techniques that applied to a real-time application of door lock. The first algorithm is Oriented FAST and Rotated BRIEF(ORB) [5] which is a key points extractor and descriptor algorithm used FAST (Features from accelerated segment test) [6] corner detector and BRIEF (Binary Robust Independent

Elementary Features) descriptor. The ORB is introduced as a free alternative of SIFT and SURF algorithms [7,8] because these algorithms are patented. The other algorithm used is Principal component analysis which is a dimensionality reduction algorithm used in facial recognition and called eigenfaces [9]. The third algorithm used is Local binary patterns (LBP) which is a visual descriptor used in facial recognition and a type of Texture Spectrum model proposed in 1990 [10]. The software is implemented using Python programming language and using the Lattepanda computer-on-module we develop the door-lock system to work in a real-time environment. The three algorithms tested on dataset that we collected from the students with a total of 3600 faces with many poses, illumination, distances, with and without glasses. The k-nearest neighbor classifier is used and trained on 2520 faces for each algorithm features and tested on 1080 images. The ORB approach achieved the higher accuracy with 86.29% accuracy followed by LBP 85.92% and PCA 82.87%.

Materials and Methods:

1. Materials:

We built a system that powered by Lattepanda Computer-on-module mounted to an LCD screen and Logitech webcam 720p. the system is used to control the door lock by using the on-board Arduino Leonardo and relay circuit. The figure 1 shows the assembled system in a 3D printed plastic case.

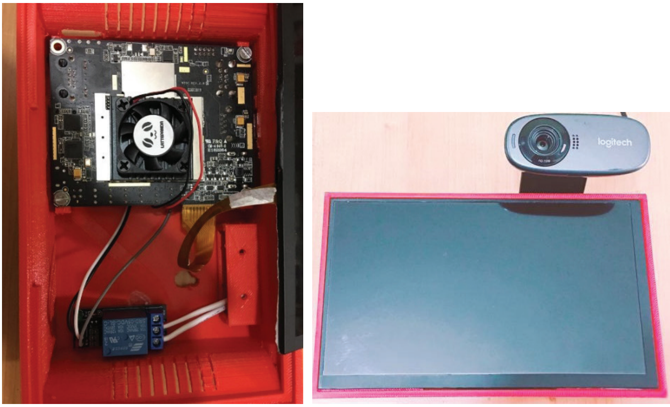

Figure 1. *The Proposed system.*

2. ORB (Oriented FAST and Rotated BRIEF):

ORB is an computer vision algorithm developed by Ethan Rublee[5] in 2011, it's basically a fusion of two algorithms; FAST(Features from accelerated segment test) and BRIEF(Binary Robust Independent Elementary Features) with some modifications to enhance the performance. ORB perform FAST as the first step to detect and find the keypoints then apply Harris corner measure to find top N points among them, but the problem that is FAST doesn't compute the orientation so the author of the ORB make some modifications by computing the intensity centroid of the patch with located cornet the center of it. So the orientation is calculated by measuring the direction from this corner point to the centroid. They called this modified FAST algorithm as oFAST. Also ORB algorithm uses BRIEF descriptor that perform poorly with the rotation, so the author proposed the rBRIEF which is a rotation-invariant BREIF. The rBRIEF steer the keypoints that detected by oFAST according the orientation of these keypoints. Figure 2 shows the ORB features matching.

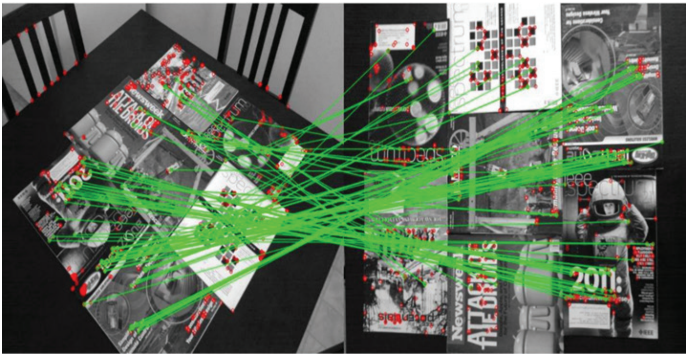

Figure 2. *ORB features matching.*

3. Principal Component Analysis (PCA)

PCA is a dimensionality reduction algorithm usually called Eigenfaces when used in the face recognition field proposed by M. Kirby[9]. Eigenfaces is an appearance-based method used in facial recognition applications. The Eigenfaces calculate the variations in a set of face images in order to encode and compare images of subjects faces in a holistic manner. The eigenface is the principal component of the distribution of faces. It' also the eigenvector of the covariance matrix of the faces images set. Figure 3 shows the example of eigenfaces.

Figure 3. *Example of Eigenfaces.*

4. Local Binary patterns (LBP)

LBP is a texture operator that encode the pixels of the image by thresholding the neighborhood of each pixel and consider the results as a binary number. It's proposed by Ahonen [10]. Because of its simplicity it used in many computer vision applications including the face recognition field. In the facial recognition the LBP approach works in few steps; first the face image is divided into local regions, for each region the LBP descriptor is extracted. Then these descriptors will be merged together to build the face features. Then the histogram will be calculated from these features. The histogram is containing information on the pixel-level about the face texture. Figure 4 shows the LBP process.

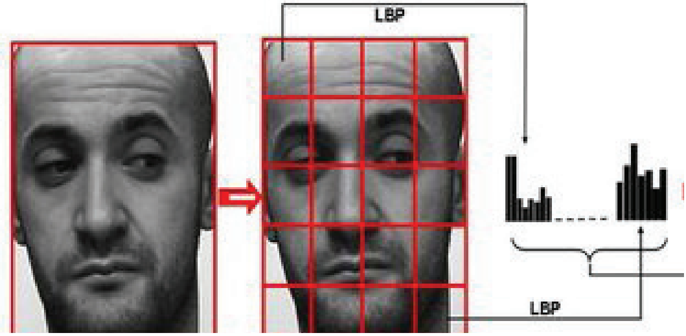

Figure 4. *LBP process in facial recognition.*

5. Dataset

We collect a dataset of faces from 30 subjects, the dataset has many variations in illumination, pose, distance, with and without glasses. The total images in the dataset is 3600. Figure 5 shows the samples from the dataset.

Figure 5. *Samples from the Dataset.*

Results

In this study, we tested the proposed three algorithms for facial recognition. The dataset used contain face images of 30 subjects the total images is 3600. The dataset contains many poses, illumination levels, distance with and without glasses. Each subject in the dataset have a total of 120 image. For each image we apply the three algorithms in order to extract the face unique features and we trained KNN classifier with these features. The total training images for each subject are 84 and the other 36 for testing the performance of the classification.

We used HAAR cascade classifier to remove the background from images and extract the face only.

Table 1. *ORB+KNN results (with glasses)*

ID No.	Az Işık																				Orta Işık																				Çok Işık																			
	50cm					100cm					150cm					200cm					50cm					100cm					150cm					200cm					50cm					100cm					150cm					200cm				
	1	2	3	4	5	1	2	3	4	5	1	2	3	4	5	1	2	3	4	5	1	2	3	4	5	1	2	3	4	5	1	2	3	4	5	1	2	3	4	5	1	2	3	4	5	1	2	3	4	5	1	2	3	4	5	1	2	3	4	5
1																																							X																					
2																				X																																								
3																																						X																						
4											X																	X																												X				
5																																								X																				X
6																												X			X																											X		
7																																																												
8																X																																						X				X		
9																																																												
10																																																								X				X
11													X																																											X	X	X		
12																																																				X								X
13																				X																														X					X		X			X
14																																								X																X				
15																																														X														X
16																																							X																					
17																																							X											X							X			
18					X			X																	X																				X		X													
19																																																												
20																							X																				X										X							
21														X			X																							X																		X		
22																																							X															X						X
23									X																				X							X		X																						
24																X				X																				X																				
25																		X		X																				X																		X		
26																																							X	X																	X		X	
27																																																												
28																																															X													
29																																																												
30																																																												

Table 2. *ORB+KNN results (without glasses)*

ID No.	Az Işık																				Orta Işık																				Çok Işık																			
	50cm					100cm					150cm					200cm					50cm					100cm					150cm					200cm					50cm					100cm					150cm					200cm				
	1	2	3	4	5	1	2	3	4	5	1	2	3	4	5	1	2	3	4	5	1	2	3	4	5	1	2	3	4	5	1	2	3	4	5	1	2	3	4	5	1	2	3	4	5	1	2	3	4	5	1	2	3	4	5	1	2	3	4	5
1															X				X						X										X																						X				
2		X								X												X				X																																						
3																																																												
4																																																												
5												X																																													X			
6														X				X																																										X
7														X					X																X																									
8																																							X																				X	
9																																						X																					
10				X										X					X																			X					X					X										X	
11																X			X										X																			X							X			X		
12																		X	X																				X	X											X						X	X	X	
13																																											X														X		
14																				X																			X																				
15																X			X									X										X																					
16																																									X					X		X											X			
17										X																																																	
18						X																											X																							X			X	
19	X																				X																			X																		
20																																																	X									X		
21																																																												
22																																																												
23																																				X													X											X
24														X				X																										X					X												
25																				X																								X														X		
26																																																			X					X	X			
27																																																												
28																																																								X			
29																																												X															
30								X																				X																				X								X				

In these tables the false classified images are indicated by “X”.

Table 3. *LBP+KNN Results (With glasses)*

ID No.	Az Işık																				Orta Işık																				Çok Işık																			
	50cm					100cm					150cm					200cm					50cm					100cm					150cm					200cm					50cm					100cm					150cm					200cm				
	1	2	3	4	5	1	2	3	4	5	1	2	3	4	5	1	2	3	4	5	1	2	3	4	5	1	2	3	4	5	1	2	3	4	5	1	2	3	4	5	1	2	3	4	5	1	2	3	4	5	1	2	3	4	5	1	2	3	4	5
1				X																																								X	X																	
2																								X																																			
3																																																												
4																																																												
5																																																												
6		X																					X																						X															
7																																																												
8																																																												
9		X																																																										
10																																																												
11																																																												
12																																																				X									
13			X	X																X				X																																					X
14			X		X																				X																			X															
15											X				X					X		X																		X		X													X					X
16										X					X					X	X										X																									X				
17						X																			X																X																		
18				X	X																			X	X																				X														
19																																																												
20		X		X																X			X																				X										X					
21		X			X																		X																		X		X															X		
22										X					X					X				X																X								X					X							
23											X														X						X															X														
24						X										X																										X																			
25		X																			X	X																																					
26																																																												
27																																																												
28																																																												
29				X																			X																																			
30																																																												

Table 4. *LBP+KNN Results (Without glasses)*

ID No.	Az Işık																				Orta Işık																				Çok Işık																			
	50cm					100cm					150cm					200cm					50cm					100cm					150cm					200cm					50cm					100cm					150cm					200cm				
	1	2	3	4	5	1	2	3	4	5	1	2	3	4	5	1	2	3	4	5	1	2	3	4	5	1	2	3	4	5	1	2	3	4	5	1	2	3	4	5	1	2	3	4	5	1	2	3	4	5	1	2	3	4	5	1	2	3	4	5
1																								X																					X																
2		X		X																																									X																
3					X																																																							
4		X		X																																						X			X															
5																																																												
6		X																																	X															X						X					
7																																																												
8																																			X																									
9		X												X					X	X																				X																			
10												X											X	X							X										X		X																
11																								X																				X																
12	X	X							X			X											X		X							X					X								X				X	X					X					X
13															X																											X	X																
14				X				X															X					X																															
15																					X				X																			X															
16				X																																				X																				
17					X																																							X															
18																																											X																
19																																																											
20																																								X																				
21		X	X		X				X					X					X																				X								X		X			X		X					X	
22																							X	X																			X								X								
23																																												X															
24																								X	X																			X															
25																									X																		X																
26																																																											
27																																																											
28																																																											
29																									X																			X															
30																																																											

Table 5 *PCA+KNN Results (with glasses)*

ID No.	Az Işık																				Orta Işık																				Çok Işık																			
	50cm					100cm					150cm					200cm					50cm					100cm					150cm					200cm					50cm					100cm					150cm					200cm				
	1	2	3	4	5	1	2	3	4	5	1	2	3	4	5	1	2	3	4	5	1	2	3	4	5	1	2	3	4	5	1	2	3	4	5	1	2	3	4	5	1	2	3	4	5	1	2	3	4	5	1	2	3	4	5	1	2	3	4	5
1																																												X											X						
2																																																											
3																																																	X											
4		X															X										X					X	X														X										X			
5																																																									X			
6																							X					X																														X		
7																																																											
8									X										X																																								
9																																													X					X										
10																																																											
11																																																											
12																																																											
13					X															X										X					X															X					X					X
14																																																											
15																																																							X					
16										X			X		X					X										X								X	X				X												X					
17																										X															X										X									
18																									X																				X					X										
19																																																											
20				X					X																				X										X				X	X										X	X						
21																		X																														X										X		
22									X					X	X				X											X									X															X					X	
23																																																											
24																																																											
25		X								X		X								X		X		X			X							X			X			X							X										X			X
26																																																							X					
27																																																											
28																																																											
29				X											X									X						X										X																			X	
30																																																											

Table 6. *PCA+KNN Results (without glasses)*

ID No.	Az Işık																				Orta Işık																				Çok Işık																			
	50cm					100cm					150cm					200cm					50cm					100cm					150cm					200cm					50cm					100cm					150cm					200cm				
	1	2	3	4	5	1	2	3	4	5	1	2	3	4	5	1	2	3	4	5	1	2	3	4	5	1	2	3	4	5	1	2	3	4	5	1	2	3	4	5	1	2	3	4	5	1	2	3	4	5	1	2	3	4	5	1	2	3	4	5
1	X					X					X					X			X					X		X								X		X								X					X					X		X				
2										X									X						X																				X					X					X					X
3																																																												
4				X						X				X	X					X									X	X					X				X						X				X						X				X	
5																																																												
6					X																														X					X										X					X					X
7																						X																									X													
8																																																												
9																					X																				X																			
10				X			X		X			X		X					X			X		X															X			X										X								
11																																																												
12		X										X													X		X			X		X			X		X			X					X					X					X		X			X
13																																																								X			
14								X				X										X					X																										X					X	
15																																																											
16				X							X			X															X							X					X					X					X						X			
17																																																												
18																																																												
19																																																												
20																																																												
21														X					X																				X										X					X					X	
22																			X					X																				X					X										
23										X					X																				X										X					X										
24														X										X										X																									
25																								X										X										X															
26																																																												
27																																																												
28																																																												
29																																																												
30																																																												

When 3 different algorithms are applied on the data set containing different features, the test results provide information about the performance of the algorithms. To better understand these, these data are expressed numerically in the following Tables. When we examine these tables, it becomes more evident how the performance of the algorithms is affected by 4 different features in the data set.

Table 7. *Number of incorrect images according to face detail.*

Feature	ORB	LBP	PCA
With glasses	66	71	80
Without glasses	82	81	105
Total	148	152	185

Table 8. *Accuracy according to face detail (%)*

Feature	ORB	LBP	PCA
With glasses	87,77	86,85	85,18
Without glasses	84,81	85	80,55
Total (%)	86,29	85,92	82,87

The values given in the tables clearly show how the ORB, LBP and PCA algorithms are affected by situations such as face detail, light level, distance and viewing position in the data set.

In Table 7 and Table 8, the test results of the algorithms are given on the data sets consisting of glasses with and without glasses, which are expressed as face details.

Table 9, Table 10 and Table 11 show the test results of 3 different algorithms depending on the change in the light level of the environment.

Table 9. *Incorrect number of images according to light level*

feature	Light level	ORB	LBP	PCA
With glasses	Low	14	29	23
	Medium	20	22	25
	High	32	20	32
Without glasses	Low	27	25	32
	Medium	17	23	34
	High	38	33	39

Table 10 *Accuracy of algorithms according to Light Level (%)*

Feature	Light Level	ORB	LBP	PCA
With glasses	Low	92,22	83,88	87,22
	Medium	88,88	87,77	86,11
	High	82,22	88,88	82,22
Without glasses	Low	85	86,11	82,22
	Medium	90,55	87,22	81,11
	High	78,88	81,66	78,33

Table 11 *Total accuracy of algorithms according to Light Level (%)*

Light Level	ORB	LBP	PCA
Low	88,61	85	84,72
Medium	89,72	87,5	83,61
High	80,55	85,27	80,27

Table 12, Table 13 and Table 14 show the results of 3 different algorithms depending on distance.

Table 12. *Incorrect number of images according to distance*

Feature	Distance	ORB	LBP	PCA
With glasses	50cm	5	45	17
	100cm	10	6	21
	150cm	9	10	19
	200cm	42	10	23
Without glasses	50cm	12	52	27
	100cm	17	9	24
	150cm	9	14	29
	200cm	44	6	25

Table 13. *Accuracy of algorithms according to distance (%)*

Feature	Distance	ORB	LBP	PCA
With glasses	50cm	96,29	66,66	87,4
	100cm	92,59	95,55	84,44
	150cm	93,33	92,59	85,92
	200cm	68,88	92,59	82,96
Without glasses	50cm	91,11	61,48	80
	100cm	87,40	93,33	82,22
	150cm	93,33	89,62	78,51
	200cm	67,4	95,55	81,48

Table 14. *Total accuracy percentages of algorithms according to distance (%)*

Distance	ORB	LBP	PCA
50cm	93,7	64,07	83,7
100cm	90	94,44	83,33
150cm	93,33	91,11	82,22
200cm	68,14	94,07	82,22

Table 15, Table 16 and Table 17 show the test results of 3 different algorithms according to 5 different view poses.

Table 15. *Incorrect number of images according to the pose*

Feature	Pose	ORB	LBP	PCA
		10	5	26
	Front	8	11	3
With glasses	Up	15	10	14
	Down	11	18	13
	Left	22	27	23
	Right	17	6	14
	Front	10	17	15
Without glasses	Up	20	7	4
	Down	30	26	40
	Left	8	26	32

Table 16. *Accuracy of algorithms according to the pose (%)*

Feature	Pose	ORB	LBP	PCA
	Front	90,74	95,37	75,92
	Up	92,59	89,81	97,22
With glasses	Down	86,11	90,74	87,03
	Left	89,81	83,33	87,96
	Right	79,62	75	78,7
	Front	84,25	94,44	87,03
	Up	90,74	84,25	86,11
Without glasses	Down	81,48	93,51	96,29
	Left	72,22	75,92	62,96
	Right	92,59	75,92	70,37

Table 17. *Total accuracy of algorithms according to the pose (%)*

Pose	ORB	LBP	PCA
Front	87,5	94,90	81,48
Up	91,66	87,03	91,66
Down	83,79	92,12	91,66
Left	81,01	79,62	75,46
Right	86,11	75,46	74,53

Conclusion

In this paper, the facial recognition performance of 3 different algorithms consisting of ORB, PCA and LBP were examined. These three algorithms were tested on data sets collected from 30 subjects with different conditions such as light, Distance, Feature, and exposure. These approaches were used in real time and were implemented using an embedded system of Lattepanda in a door lock based facial recognition for students in the laboratory.

As a result of the tests, it is seen that the ORB algorithm fails more at high light level and at long distance. In addition, the increase in facial detail increases the success rate of the algorithm. PCA method is not affected by distance and light changes. However, it is excluded from the application of the system due to its high computing power requirements. The LBP approach has been good for the accuracy of computational power and works perfect in real time without any delay. However, the success rate at close range decreases considerably and is found to be relatively more successful at medium light level. When we look at the camera in terms of exposure differences, it is seen that the success rate of the algorithms decreases in the side images which usually cover one half of the face. Considering that our system will operate in a closed environment at low or medium light levels and close range, it is predicted that ORB based face recognition system will be more successful on the embedded system. For this reason, the practical system which will perform as a door lock has been implemented by using ORB based face recognition algorithm.

REFERENCES

[1] Francis Galton, "Personal identification and description," In Nature, pp. 173-177, June 21, 1888.

[2] Peter, K. John, et al. "Improving ATM security via face recognition." 2011 3rd International Conference on Electronics Computer Technology. Vol. 6. IEEE, 2011.

[3] Karovaliya, Mohsin, et al. "Enhanced security for ATM machine with OTP and Facial recognition features." Procedia Computer Science 45 (2015): 390-396.

[4] Burton, A. Mike, et al. "Face recognition in poor-quality video: Evidence from security surveillance." Psychological Science 10.3 (1999): 243-248.

[5] Rublee, Ethan, et al. "ORB: An efficient alternative to SIFT or SURF." ICCV. Vol. 11. No. 1. 2011.

[6] Viswanathan, Deepak Geetha. "Features from accelerated segment test (fast)." (2009): 1-5.

[7] Lowe, David G. "Distinctive image features from scale-invariant keypoints." International journal of computer vision 60.2 (2004): 91-110.

[8] Bay, Herbert, Tinne Tuytelaars, and Luc Van Gool. "Surf: Speeded up robust features." European conference on computer vision. Springer, Berlin, Heidelberg, 2006.

[9] Turk, Matthew, and Alex Pentland. "Eigenfaces for recognition." Journal of cognitive neuroscience 3.1 (1991): 71-86.

[10] Ahonen, Timo, Abdenour Hadid, and Matti Pietikainen. "Face description with local binary patterns: Application to face recognition." IEEE Transactions on Pattern Analysis & Machine Intelligence 12 (2006): 2037-2041.

INVESTIGATION OF HIGH STRENGTH CONCRETE PRODUCTION FROM PUMICE SAND IN RIGID PAVEMENT CONSTRUCTION

Abdulrezzak BAKİS[1]

CHAPTER 2

1 Bitlis Eren University, Faculty of Engineering and Architecture, Department of Civil Engineering, Bitlis

INVESTIGATION OF HIGH STRENGTH CONCRETE PRODUCTION FROM PUMICE SAND IN RIGID PAVEMENT CONSTRUCTION

Abdulrezzak BAKİS[1]

INTRODUCTION

The first applications on concrete pavement were done at the end of the 19^{th} century (Arslan, 2007). Today, in the 20-year project period, the roads with 8.2 tone standard axle load number more than 60×10^6 have the obligation of being made of rigid pavement (Tunc, 2007). The purpose in the plan of rigid pavement is to find out the pavement thicknesses and the properties of the material used in concrete road (Bayrak, 2007). In this study, pumice sands (0.15-1 mm) were used as concrete pavement aggregate. Pumice formations created as a result of volcanic eruptions have a spongy structure and are found in different regions of the world where there are volcanic activities (Gunduz, 1998). The pumice has innumerable independent pores ranging from macro scale to micro scale due to the abrupt abandonment of the gases in the environment during the formation and sudden cooling (Anon, 2001). Today, pumice is used in many fields such as construction, chemistry and cosmetics (Akin, 2013).

Pumice resources detected worldwide are approximately 18 billion m^3 (Dincer et al, 2015). According to the studies made on concrete, it has been intended to get different strength concretes through materials including cement (Aitcin, 2000; Tasdemir et al, 2004; Bakis, 2015; Turkmenoglu et al., 2015). Pumice concrete (PC) can be included in the high strength concrete class.

1 Bitlis Eren University, Faculty of Engineering and Architecture, Department of Civil Engineering, Bitlis

The mixture ratios of pumice concrete are similar to the mixture ratios of reactive powder concrete (RPC). Reactive powder concretes can give 2-4 times more mechanical strength than high strength concretes (Dallaire and Aitcin, 1998). In this study, pumice sand was used as aggregate. By using very fine aggregate in the mixture, the micro voids in the structure are reduced, and the bending and compressive strength of the concrete are increased (Dallaire et al, 1998). In this study, pumice aggregate diameter was 0.15-1.00 mm in PC production. In PC production, super plasticizer additive is added to the mixture to increase the workability of the mixture and to obtain high strength to the concrete. In the study, pumice concretes were produced in two types as fibrous PC and non-fibrous PC. The difference between fibrous PC and non-fibrous PC is that steel fibers are added to the fibrous PC mixture. Altoubat et al. (2006) stated that the addition of steel fibers to non-reinforced concrete will increase the bending capacity of the concrete. Steel fiber is added to the concrete to improve mechanical properties such as the bending strength of the concrete (Civici, 2006; Bakis, 2015). Zheng et al. (2013) stated that the bending and compressive strength of concrete can be increased in concrete production of 2% steel fiber content of concrete by volume. In PC production, one of the most important factors affecting the bending and compressive strength of concrete is the type of curing applied to concrete.

In the study, different types of curing such as 20°C water curing, autoclave curing and combined curing were applied to PC. Combined curing can be defined as application of different types of curing one after another. Topcu and Karakurt (2005) applied 90°C water curing for 7 days and later 250°C steam curing for 7 days to concrete. Talebinejad et al. (2004) applied curing at different days and periods at 20°C and 90°C. Yazici (2007) applied 3 different curing methods as water curing, autoclave curing and steam curing.

Yazici et al (2013) stated that autoclave curing considerably affected the mechanical property of concrete.

The usability of pumice concrete for concrete pavement was researched in this study. No study on pumice concrete (PC) pavement in rigid pavement has been encountered yet. For concrete pavement, 3 different concrete types as reference sample (C30/37 normal strength concrete), fibrous PC and non-fibrous PC were chosen. In the study, 20^{o}C water curing was applied to reference concrete for 7 and 28 days. However, 3 different types of curing as 20^{o}C water curing, autoclave curing and combined curing were applied to fibrous PC and non-fibrous PC at different periods. After curing, all samples were applied compressive and bending test. As a result of data obtained from the study, it was seen that PC compensates limit values required in conditions of contract in concrete road pavement production.

Materials and Method

Materials

CEM I 42.5 R type cement was used in types of concrete mixtures.

Table 1. *Chemical properties of the cement*

Component	Percentage, %
SiO_2	18.70
Fe_2O_3	3.26
Al_2O_3	5.35
CaO	63.69
MgO	1.53
K_2O	0.75
SO_3	2.69
Cl	0.02
Na_2O	0.44
Ignition loss	3.57

Chemical properties of the cement are seen in Table 1 (Cimsa, 2018).

Table 2. *Mechanical and physical properties of the cement*

Properties	Value
Specific surface, cm^2/g	3770
Specific gravity, g/cm^3	3.19
Final set, minute	213
Initial set, minute	167
Compressive strength 28-day, MPa	56.49

Mechanical and physical properties of the cement are given in Table 2 (Cimsa, 2018).

The properties of the super plasticizer used in PC are seen in Table 3 (Iksa, 2018).

Table 3. *The properties of the super plasticizer*

Properties	Value
Density	1.1 kg/Liter
Form	Liquid
Chloride quantity	(TS EN 480–10) < 0.1%
pH	4.00–5.50

Physical properties of pumice are seen in Table 4 (Tokyap, 2018).

Table 4. *Physical properties of pumice*

Properties	Value
Specific gravity, g/cm^3	2.07
Hardness, Mohs	5.43
Porosity, %	43
Water absorption, %	29

Low Specific gravity of pumice indicates that pumice has a porous structure.

a. Pumice coarse aggregate **b.** Pumice sand

Figure 1. *Pumice coarse aggregate and pumice sand*

Pumice coarse aggregate and pumice sand used in the production PC are seen in Figure 1.

Table 5. *Chemical properties of pumice*

Component	Percentage, %
SiO_2	71
Fe_2O_3	2.6
Al_2O_3	13
MgO	0.7
CaO	0.8
K_2O+Na_2O	9.11
SO_3	0.61
Ignition loss	2.18

Chemical properties of pumice are seen in Table 5 (Efe, 2011).

Chemical and physical properties of silica fume are seen in Table 6 (Iksa, 2018).

Table 6. *Chemical and physical properties of silica fume*

Properties	Percentage, %
SiO_2, %	95.83
Fe_2O_3, %	0.37
Al_2O_3, %	0.76
MgO (%)	1.29
CaO, %	0.53
SO_3, %	0.63
Ignition loss, %	0.59
Specific surface, cm^2/g	200000
Specific gravity, g/cm^3	2.19

Hooked-end steel fibers used in the production of PC are seen in Figure 2.

Figure 2. *Hooked-end steel fibers*

Hooked-end steel fibers used in PC were selected with a length of 30 mm and a diameter of 0.55 mm.

Table 7. *Mechanical and physical values of fiber*

Fiber	Length (mm)	Diameter (mm)	Specific gravity (g/cm^3)	Tensile strength (MPa)	Length (mm)	Slenderness ratio
Steel	30	0.55	7.85	1100	30	55

Mechanical and physical values of steel fibers are seen in Table 7 (Aral, 2006). Crushed stone limestone aggregate was used in the mixture of C30/37 normal strength concrete (reference concrete). Water from the city of Bitlis was used as mixture water in concrete.

Method

For compressive test, concrete mold size was 150×150×150 mm. For bending test, concrete mold size was 100×100×400 mm. After 24 hours, the hardened concrete was taken out of the molds. The hardened concrete was taken to 20°C water curing for 7 and 28 days. After curing, compressive and bending tests were carried out on C30/37 reference concrete samples. The values–in kg-of amounts included in a mixture of 1 m^3 in the production of C30/37 concrete (reference concrete) are seen in Table 8.

Table 8. *The amount of materials in reference concrete*

Material	**Quantity, kg/m^3**
Portland cement	420
0-4 mm (crushed limestone)	815
4-8 mm (crushed limestone)	405
8-16 mm (crushed limestone)	573
Water	187
Total	2400

Mooney's model was considered for the PC in the study. RPC is an ultra-high strength concrete (Ipek, 2009). The amount of the other materials was proportioned in terms of weight by the amount of the cement used in RPCs. The other materials were sliced into the percentage of the ratio by weight according to the amount of the cement, and then the mixture was done.

There is no standard for the mixture formula of RPC. In the study, different mixture formulas were used in proportion to the granular materials forming the mixture in a manner to form a tight structure (Ipek, 2009; Bakis, 2015). These formulas were obtained from Mooney's suspension viscosity model (Ipek, 2009; Larrard and Sedran, 1994; Bakis, 2015). RPC mixture design in 1 unit according to Mooney's suspension viscosity model is seen in Table 9 (Richard and Cheyrezy, 1995).

Table 9. *Mixture ratios of RPC*

Material	Fibrous	Non-Fibrous
Portland cement	1	1
Silica fume	0.25	0.25
Quarts sand (150–600 µm)	1.1	1.1
Steel wire (L=12 mm)	0.175	-
Super plasticizer	0.016	0.016
Water	0.17	0.15

In Table 9, in consideration with the mixture ratios given in one unit, the formula between the total mixture weight and the cement amount is formulated as the following to provide convenience in the calculations (Richard and Cheyrezy, 1995; Bakis, 2015):

Non-fibrous PC mixture weight in 1 m^3 = 2.516 × 1 m^3 amount of cement in 1 m^3 (1)

If 1 m^3 non-fibrous PC mixture weight was 2400 kg, the amount of cement to be used in this mixture would be nearly 954 kg as a result of the 2400/2.516 ratio from Formula 1. After the amount of cement is found as 954 kg, the amount of other materials to be used in the mixture is determined by the following mixture ratios (Richard and Cheyrezy, 1995; Bakis, 2015). In Table 9, in consideration with the mixture ratios given in one unit, the mixture is done in the generation of non-fibrous PC by preparing the silica fume at 25% of the amount of cement, the pumice sand content at 110% of the amount of cement, the super plasticizer at 1.6% of the amount of cement and the mixing water at 15% of the amount of cement (Richard and Cheyrezy, 1995; Bakis, 2015). For non-fibrous PC samples, the water/binder ratio was 0.12, and the silica fume/cement ratio was 0.25.

Non-fibrous PC mixture ratios are seen in Table 10.

Table 10. *Non-fibrous PC mixture ratios*

Material	Quantity, kg/m^3
Portland cement	954
Silica fume	238
Pumice sand (0.15-1 mm)	1050
Super plasticizer	15
Water	143
Total	2400

In Table 9, in consideration with the mixture ratios given in one unit, the formula between the total mixture weight and the cement amount is formulated as the following to provide convenience in the calculations (Richard and Cheyrezy, 1995; Bakis, 2015):

Fibrous PC mixture weight in 1 m^3 = 2.711× amount of cement in 1 m^3 (2)

If 1 m^3 fibrous PC mixture weight was 2400 kg, the amount of cement to be used in this mixture would be nearly 885 kg as a result of the 2400/2.711 ratio from Formula 2. After the amount of cement is found as 885 kg, the amount of other materials to be used in the mixture is determined by the following mixture ratios (Richard and Cheyrezy, 1995; Bakis, 2015).

In Table 9, in consideration with the mixture ratios given in one unit, the mixture is done in the generation of fibrous PC by preparing the silica fume at 25% of the amount of cement, the pumice sand content at 110% of the amount of cement, the super plasticizer at 1.6% of the amount of cement, the steel fibers at 17.5% of the amount of cement and the mixing water at 17% of the amount of cement (Richard and Cheyrezy, 1995; Bakis, 2015). For fibrous PC samples, the water/binder ratio was 0.13, and the silica fume/cement ratio was 0.25. Fibrous PC mixture ratios are seen in Table 11.

Table 11. *Fibrous PC mixture ratios*

Material	Quantity, kg/m^3
Portland Cement	885
Silica Fume	221
Pumice Sand (0.15-1 mm)	975
Super Plasticizer	14
Hooked-and Steel Fibers	155
(D= 0.55 mm) (L= 22 mm)	
Water	150
Total	2400

PC samples taken from molds were applied different kinds of curing. Pumice concrete (PC) type 1 water curing samples were taken to water curing at 20^{o}C at different periods. For concrete production, the autoclave curing time should be at least 2 hours (Sahinoglu, 2010). Uygunoglu and Unal (2007) reported in their autoclave curing studies that the optimum autoclave curing time was 8 hours. For this reason, pumice concrete (PC) type 2 autoclave curing samples were applied autoclave curing for 4, 8 and 12 hours in this study. For combined curing, no standard is found in literature studies. Bakis (2015) stated that the curing manner providing the highest compressive strength was the combined curing applied as 20°C water curing for 7 days, 90°C water bath curing for 2 days and 180°C drying oven curing for 2 days (Hattatoglu and Bakis, 2017).

Based on this study, pumice concrete (PC) Type 3 combined curing the samples were applied water curing at 20°C for 7 days, water bath curing at 90°C for 2 days and lastly drying oven curing at 180°C for 2 days. TS EN 12390-5: 2010 standard was applied in the bending test. TS EN 12390-3: 2010 standard was applied in the compressive test.

The ratios regarding concrete pavement in rigid pavements are obtained based on one or more of the following measures in the specifications: 0.40-0.45 as maximum water/binder ratio; 28 MPa as minimum compressive strength, 4.5 MPa as minimum bending strength; 270-335 kg/m^3 as minimum cement amount (Tunc, 2007).

Results and Discussion

Reference concrete (C30/37 concrete) compressive test results are seen in Table 12.

Table 12. *Reference concrete (C30/37) compressive test results*

Concrete type	Water curing (20°C)	Compressive strength (MPa)
C30/37 reference concrete	7-day	34.80
C30/37 reference concrete	28-day	40.25

Fibrous PC and non-fibrous PC compressive test results are seen in Table 13.

Table 13. *Fibrous PC and non-fibrous PC compressive test results*

Water curing (20°C)	Compressive strength (MPa)	
	Non-fibrous PC	Fibrous PC
8-hour	16.55	19.87
1-day	22.13	27.23
2-day	30.75	39.46
3-day	33.25	45.87
7-day	45.12	62.96
28-day	52.27	73.61

Table 13 shows that leaving non-fibrous PC in 20°C standard water curing for 3 days came closer to the 7-day compressive strength of C30/37 reference concrete in equal curing conditions. In addition, it was seen that, by leaving non-fibrous PC in 20°C standard water curing for 7 days, it exceeded the 28-day compressive strength of C30/37 reference concrete. Table 13 shows that, by leaving fibrous PC in 20°C standard water curing for 2 days, it exceeded the 7-day compression strength of C30/37 reference concrete sample in equal curing conditions, whereas by leaving fibrous PC in 20°C standard water curing for 3 days, it was seen that it exceeded the 28-day compressive strength of C30/37 reference concrete. Table 13 shows that, as the period of 20°C standard water curing increases, compressive strength of fibrous PC increases. When the values in Table 13 are taken into consideration, it can be said that fibrous PC and non-fibrous PC road pavements can be opened to traffic earlier than C30/37 reference concrete pavement. Compressive test results after autoclave curing of fibrous PC and non-fibrous PC are seen in Table 14.

Table 14. *Compressive test results after autoclave curing of fibrous PC and non-fibrous PC*

Autoclave curing	Compressive strength (MPa)	
(1.3 MPa-180°C)	Non-fibrous PC	Fibrous PC
4-hour	68.51	79.48
8-hour	98.85	117.69
12-hour	49.94	65.27

As seen in Table 14 and Figure 3, compressive strength of fibrous PC and non-fibrous PC increases until the 8th hour of autoclave curing, whereas it decreases after 8 hours. It was seen Table 14 and Figure 3 that fibrous PC and non-fibrous PC reach a specific compressive strength in autoclave curing in 4 hours, reach their maximum level in 8 hours and their strength decreases in 12 hours. Compressive test results after autoclave curing of fibrous PC and non-fibrous PC are seen in Figure 3.

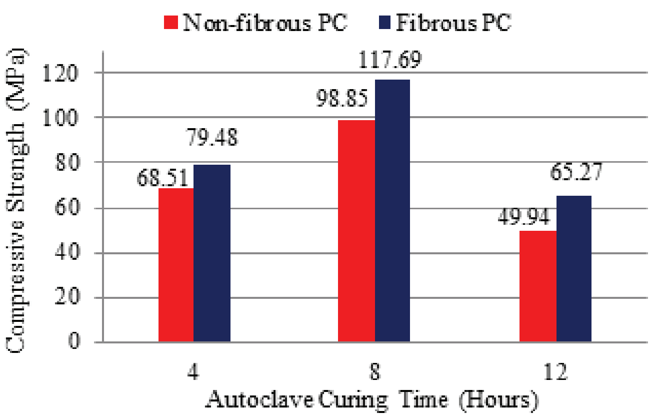

Figure 3. *Compressive test results after autoclave curing of fibrous and non-fibrous PC*

Maximum bending and compressive strength after different curing of reference concrete (C30/37), fibrous PC and non-fibrous PC are seen in Table 15.

Table 15. *Maximum compressive and bending strength*

Concrete type	Curing type	Maximum compressive strength (MPa)	Maximum bending strength (MPa)
Reference concrete	Water curing	40.25	4.97
Non-fibrous PC	Water curing	52.27	6.19
	Autoclave curing	98.85	11.75
	Combined curing	84.92	10.17
Fibrous PC	Water curing	73.61	8.73
	Autoclave curing	117.69	13.91
	Combined curing	105.93	12.63

As shown in Table 15, the maximum bending and compressive strength of fibrous PC and non-fibrous PC were obtained after autoclave curing.

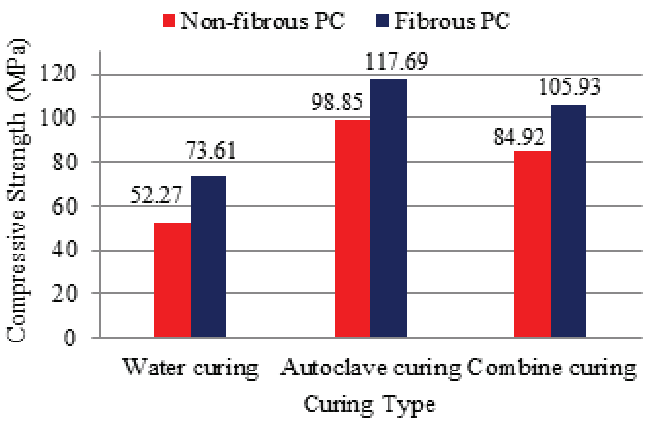

Figure 4. *Compressive strength of fibrous PC and non-fibrous PC*

Figure 4 shows the maximum compressive strength after different curing of fibrous PC and non-fibrous PC.

The maximum compressive strength of fibrous PC and non-fibrous PC were obtained after autoclave curing, as shown in Figure 4. Figure shows the bending strength after different curing of fibrous PC and non-fibrous PC.

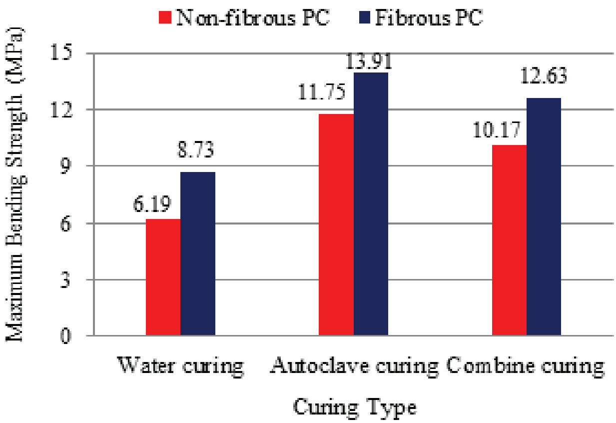

Figure 5. *Bending strength of fibrous PC and non-fibrous PC*

The maximum bending strength of fibrous PC and non-fibrous PC were obtained after autoclave curing, as seen in Figure 5.

Conclusion

C30/37 reference concrete sample was applied standard water curing for 7 and 28 days, whereas fibrous PC and non-fibrous PC were applied 3 different types of curing as 20°C standard water curing, autoclave curing and combined curing at different periods, and the results below were obtained from the studies done:

The water/binder ratio of non-fibrous PC formed in the study was selected as 0.12 in average. The water/binder ratio of fibrous PC was selected as 0.13 in average. In the specification limits in proportion to concrete of rigid pavement, the maximum water/binder ratio is required to be between 0.40-0.45. Therefore, fibrous PC and non-fibrous PC may be constructed as concrete of rigid pavement.

According to Figures 4 and 5, bending and compressive strength of fibrous PC and non-fibrous PC samples are higher than those of C30/37 concrete. After autoclave curing, the maximum compressive strength of non-fibrous PC was found as 98.85 MPa, and the maximum bending strength was found as 11.75 MPa. After autoclave curing, the maximum bending strength of fibrous PC was found as 13.91 MPa, and the maximum compressive strength was found as 117.69 MPa. In the specification limits, the minimum bending strength is required to be 4.5 MPa, and the minimum compressive strength is required to be 28 MPa in proportion to the rigid road pavement concrete. For these reasons, fibrous PC and non-fibrous PC may be used as rigid road pavement.

Acknowledgement

We would like to thank the Rector of Bitlis Eren University who provided all his support in our studies, the Rector of Afyon Kocatepe University, and the Van lake Building Quality Control Laboratory Construction Industry Trade Limited Company.

REFERENCES

Aitcin PC. 2000. Cements of Yesterday and Today Concrete of Tomorrow. Cement and Concrete Research, 30, 1349-1359.

Akin G, Akin M. 2013. Pomzanin Ozellikleri, Kullanim Alanlari ve Uretiminde Yasanan Sorunlar. II. Uluslararasi Ahlat - Avrasya Bilim, Kultur ve Sanat Sempozyumu.

Altoubat SA, Roesler JR, Lange DA, Rieder KA. 2006. Simplified Method for Concrete Pavement Design with Discrete Structural Fibers. Construction and Building Materials.

Anon. 2001. Endustriyel Hammaddeler Alt Komisyonu Yapi Malzemeleri, S: 3-23, DPT Madencilik Ozel Ihtisas Komisyonu Raporu Endustriyel Hammaddeler Alt Komisyonu Yapi Malzemeleri Calisma Grubu Raporu. Cilt III, Ankara.

Aral M. 2006. Karma lif iceren cimento esasli kompozitlerin mekanik davranisi, bir optimum tasarim. Yuksek Lisans Tezi, ITU, Fen Bilimleri Enstitusu, Istanbul.

Arslan M. 2007. Beton Yol Kaplamalarinda Alternatif Beton ve Yapim Yontemi Arastirmalari. Gazi Universitesi Bilimsel Arastirma Projesi, Ankara.

Bakis A. 2015. Rijit Yol Ustyapi Insasinda Reaktif Pudra Betonun (RPB) Kullanilabilirliginin Arastirilmasi. Doktora Tezi, Ataturk Universitesi, Fen Bilimleri Enstitusu, Erzurum.

Bayrak OÜ. 2007. Rijit Ustyapi Tasarimina Yeni Bir Yaklasim. Doktora Tezi, Ataturk Universitesi, Fen Bilimleri Enstitusu, Erzurum.

Cimsa Cimento Sanayi ve Ticaret A.S. http://www.cimsa.com.tr (15.01.2018).

Civici F. 2006. Çelik Lif Donatili Betonun Egilme Toklugu. Pamukkale Universitesi, Muhendislik Bilimleri Dergisi, 12 (2), 183-188.

Dallaire E, Aitcin PC. 1998. Reactive Powder Concrete in Use. ASCE Journal of Civil Engineering, 68 (1), 4-48.

Dallaire E, Aitcin PC, Lachemi M. 1998. High-Performance Powder. Civil Engineering, ABI/INFORM Global, 68, 48-51.

Dincer I, Orhan A, Coban S. 2015. Pomza Arastirma ve Uygulama Merkezi Fizibilite Raporu, Nevşehir.

Efe T. 2011. Edremit Travertenleri ve Van Golu Kuzeyinde Yuzeylenen Pomzalarin Cimento Sektorunde Kullanilabilirliginin Arastirilmasi. Yuksek Lisans Tezi, Yuzuncu Yil Universitesi, Fen Bilimleri Enstitusu, Van.

Gunduz L. 1998. Pomza Teknolojisi, Cilt 1, 285 s, Isparta.

Hattatoglu F, Bakis A. 2017. Usability of ignimbrite powder in reactive powder concrete road pavement. Road Materials and Pavement Design, 18(6), 1448-1459.

Iksa Insaat Katkilari San. Tic. Ltd. Sti. http://www.iksa.com.tr (17.01.2018).

Ipek M. 2009. Reaktif Pudra Betonlarin Mekanik Davranisina Katilasma Suresince Uygulanan Sikistirma Basincinin Etkileri. Doktora Tezi, Sakarya Universitesi, Fen Bilimleri Enstitusu, Sakarya.

Larrard F, Sedran T. 1994. Optimization of Ultra-High-Performance Concrete by the Use of a Packing Model. Cement and Concrete Research, 24 (6), 997–1009.

Richard P, Cheyrezy M. 1995. Composition of Reactive Powder Concretes. Cement and Concrete Research, 25, 1501-1511.

Sahinoglu SA. 2010. Reaktif pudra betonlar. Yuksek Lisans Tezi, Karadeniz Teknik Universitesi, Fen Bilimleri Enstitusu, Trabzon.

Talebinejad I, Bassam SA, Iranmanesh A, Shekarchizadeh M. 2004. Optimizing Mix Proportions of Normal Weight Reactive Powder Concrete with Strengths of 200–350 MPa, Ultra High Performance Concrete (UHPC). International Symposium on Ultra High Performance Concrete, Kassel, Germany.

Tasdemir MA, Bayramov F, Kocaturk N, Yerlikaya M. 2004. Betonun Performansa Gore Tasariminda Yeni Gelismeler. Beton 2004 Kongresi Bildiriler, İstanbul.

Topçu IB, Karakurt C. 2005. Reaktif Pudra Betonlari. TMH-Turkiye Muhendislik Haberleri, 437 (3).

Tokyap Inşaat Ltd. Sti. http://www.pomza.net (12.01.2018).

TS EN 12390-3: 2010. Beton-Sertlesmis Beton Deneyleri-Bolum 3: Deney Numunelerinin Basinc Dayaniminin Tayini. TSE, Ankara.

TS EN 12390-5: 2010. Beton – Sertlesmis Beton Deneyleri – Bolum 5: Deney Numunelerinin Egilme Dayaniminin Tayini. TSE, Ankara.

Tunc A. 2007. Yol Malzemeleri ve Uygulamalari. 2. Baski, Nobel Yayin Dagitim.

Turkmenoglu ZF, Kilic AM, Depci T. 2015. Van Yoresi Pomzasi ile Uretilmis Kendiliginden Yerlesen Hafif Betonlarin Mekanik Ozelliklerinin Incelenmesi. Cukurova Universitesi Muhendislik-Mimarlik Fakultesi Dergisi, 30: 105-116.

Uygunoglu T, Unal O. 2007. Buhar Kuru Uygulanmis Pomzali Hafif Betonun Ozellikleri. Politeknik Dergisi, 10 (1), 111-116.

Yazici H. 2007. The Effect of Curing Conditions on Compressive Strength of Ultra High Strength Concrete with High Volume Mineral Admixtures. Building and Environment, 42 (5), 2083–2089.

Yazici H, Deniz E, Baradan B. 2013. The Effect of Autoclave Pressure, Temperature and Duration Time on Mechanical Properties of Reactive Powder Concrete. Construction and Building Materials, 42, 53–63.

Zheng W, Luo B, Wang Y. 2013. Compressive and Tensile Properties of Reactive Powder Concrete with Steel Fibers at Elevated Temperatures. Construction and Building Materials, 41, 844–851.

SPLITTING TENSILE STRENGTH TEST FOR IGNIMBRITE ROCKS USED IN THE PRODUCTION OF NATURAL PAVING STONE

Abdulrezzak BAKİS[1]

CHAPTER 3

1 Bitlis Eren University, Faculty of Engineering and Architecture, Department of Civil Engineering, Bitlis, E-mail: arezzakbakis@gmail.com

SPLITTING TENSILE STRENGTH TEST FOR IGNIMBRITE ROCKS USED IN THE PRODUCTION OF NATURAL PAVING STONE

Abdulrezzak BAKİS[1]

1. INTRODUCTION

Concrete paving stones, which are widely used in urban roads, tretuvar, and recreation areas [1], are fabricated by mixing cement, aggregate, water, and additives in certain ratios [2]. Concrete paving stones are produced in different grades, such as square cobblestones, tombstones, and paving stones, the third one being the most common [3]. The most common materials employed in the fabrication of pavement stones are crushed limestone aggregates. Relatively, this study investigates the use of Ahlat stone rock.

Originally known as ignimbrites, Ahlat stone rock is widely used in Bitlis Province of the Ahlat region. Ahlat stone rock is one of the pyroclastic rocks that contain abundant pumice and volcanic glass due to the explosion of Nemrut crater. On this basis, Ahlat stone rock has limited applicability in the construction sector [4]. Ahlat stone rock is rather used mainly as a wall stone in structures. The author of this paper realizes that no study has been carried out yet regarding the use of ignimbrite rocks like Ahlat stone in the production of natural paving stones.

Specifically, this paper investigates the usability of Ahlat stone rock in the production of natural paving stones. Two different types of paving stones are produced, under two different types of curing applications. Splitting tensile strength tests of different types of natural paving

1 Bitlis Eren University, Faculty of Engineering and Architecture, Department of Civil Engineering, Bitlis, E-mail: arezzakbakis@gmail.com

stones were carried out, and the results were compared with specification limits of TS 2824 EN 1338 standard [5].

2. Materials and Method

2.1. Materials

2.1.3. Natural Ahlat Stone Rock

Two different types of paving stones were manufactured for the purpose of this study, as depicted in Table 1. ASRWC was produced from natural Ahlat stone rock and obtained after 3 days at 20 ± 2 °C standard water curing application. ASRCC was obtained from a curing application combined to that for ASRWC.

Table 1. *Paving stone type and natural Ahlat stone size*

Paving stone type	Natural Ahlat stone rock size (mm)
ASRWC	165 × 200 × 80 mm
ASRCC	165 × 200 × 80 mm

Figure 1 describes the appearance of the Ahlat stone rocks used in the production of ASRWC and ASRCC, which were retrieved from the Ahlat Ovakisla quarry.

Fig. 1. *Ahlat stone rocks used for ASRWC and ASRCC production*

Table 2. *Chemical properties of Ahlat stone*

Component	Na_2O	MgO	Al_2O_3	SiO_2	K_2O	CaO	TiO_2	Fe_2O_3
Percentage, %	5.51	0.24	16.01	64.11	4.78	1.64	0.44	4.91

Tables 2 and Table 3 provide a list of the chemical, physical, and mechanical properties of the Ahlat stone [6].

Table 3. *Chemical and mechanical properties of Ahlat stone*

Specific gravity (g/cm^3)	Porosity (%)	Water absorption by weight (%)	Surface abrasion loss (cm^3/50 cm^2)	Unit weight (g/cm^3)	Compressive strength (MPa)	Bending strength (MPa)
2.60	27.31	20	29	1.89	10.6	1.59

2.2. Method

The usability of Ahlat stone rock in the fabrication was validated in the fabricated two different types of paving stones. Two curing applications were applied to the stones. Moreover, each stone type was subjected to splitting tensile strength tests. Results of the tests were compared with specification limits TS 2824 EN 1338 standard.

2.2.1. Curing types

Two curing types, namely, standard water curing and combined curing, were applied for the paving stones. The literature did not specify any standard for the combined curing of hardened concrete. Accordingly, the types of curing are shown in Table 4.

Table 4. *Curing type for the paving stones*

Paving stone type	**Curing type**
ASRWC	Standard water curing
ASRCC	Combined curing

From Table 4, the standard curing was for 3 days at 20 ± 2 °C, whereas the combined curing involved 3 days at 20 ± 2 °C of the standard water curing, followed by 2 days at 180 ± 2 °C of drying oven curing.

2.2.2. Test Methods

Splitting tensile strength tests for the natural paving stones were performed in accordance to TS 2824 EN 1338 standard [5].

2.2.2.1. Splitting tensile strength test method

A load was applied by increasing the tension per second (0.05 ± 0.01 MPa). The test results were calculated using Eqs. (1) to (4) [5]:

$$S = L \times t; \quad (1)$$

$$T = 0.637 \times k \times P / S; \quad (2)$$

$$F = P / L; \quad (4)$$

where:

S = Splitting area, mm^2

L = Splitting section length, mm

T = Paving stone thickness, mm

T = Splitting tensile strength, MPa

P = Splitting load, N

K = Correction coefficient

F = Splitting load per unit area, N/mm

As mentioned in the earlier sections, each paving stone had dimensions of 165 × 200 × 80 mm. For each specimen, the calculated values for L, t, S, and k were 200 mm, 80 mm, 16000 mm^2, and 1.00, respectively. Following TS 2824 EN 1338 standard, eight samples were broken for each type of paving stones. The splitting tensile strength was calculated as the average of the values.

3. Results and Discussion

3.1. Results of the Splitting Tensile Strength Test

Accordingly, the results of the splitting tensile strength test are indicated in Table 5.

Table 5. *Results of the splitting tensile strength test*

Paving stone type	Splitting tensile strength $T_{(average)}$ (MPa)	Splitting load per unit area $F_{(average)}$ (N/mm)	TS 2824 EN 1338 Specification limits	
			$T_{(average)}$ (MPa)	$F_{(average)}$ (N/mm)
ASRWC	1.2	120	$T_{(average)}$ ≥3.6 MPa	$F_{(average)}$ ≥250 N/mm
ASRCC	1.6	180		

4. Conclusions

The usability of Ahlat stone rock in fabricating natural paving stones was the focal subject of investigation for this study. Two different types of paving stones were fabricated under two curing types. Tests of splitting tensile strength for each paving stone type were carried out. Test results were compared with the specification limits of TS 2824 EN 1338 standard. The findings of this study can be generalized as follows:

- Ahlat stone rocks cannot used in the production of natural paving stones.

- Combined curing increases the splitting tensile strength of paving stones at 33.3%, on average.

- Two types of natural paving stones were produced from the Ahlat stone rocks. Of these, ASRWC achieved the lowest splitting tensile strength. ASRCC achieved the highest splitting tensile strength.

Acknowledgments

The author would like to thank Bitlis Eren University Rector and its staff, Ultra Building Materials and Quality Control Concrete Laboratory Industry and Trade Limited Company, and Van Lake Building Quality Control Laboratory Construction Industry Trade Limited Company.

REFERENCES

[1] Semiz M. Research of the physical characteristics of concrete keystone and alternative production. Master Thesis, Gazi University, Graduate School of Natural and Applied Sciences, Ankara 2006;1-20.

[2] Acikgoz Y. Research in usage of fly ashes in the production of interlocking concrete pave. Master Thesis, Gazi University, Graduate School of Natural and Applied Sciences, Ankara 2008;1-60.

[3] MEGEP. Covering in Sidewalk and Parks. Construction Technology, Ankara 2012;8-10.

[4] Bakis A. Usability of ahlat stone in rigid pavement construction. BEU Journal of Science 2016;5:164-71. http://dergipark.gov.tr/download/article-file/264097

[5] TS 2824 EN 1338. Concrete paving blocks-Requirements and test methods. TSE, Ankara 2005.

[6] Simsek O, Erdal M. Investigation of some mechanical and physical properties of the ahlat stone (Ignimbrite). GU J Sci 2004;17:71-8.

http://gujs.gazi.e.,du.tr/article/view/1060000425

RECENT DEVELOPMENTS IN TROMBE-WALL SYSTEMS: SOLUTION FOR ZERO ENERGY BUILDINGS

Kazım KUMAŞ[1], Ali Özhan AKYÜZ[2], Azim Doğuş TUNCER[3], Ceylin ŞİRİN[4], Afşin GÜNGÖR[5]

CHAPTER 4

1 Burdur Mehmet Akif Ersoy University, Bucak Emin Gülmez Vocational School of Technical Sciences, 15300, Bucak, Turkey
2 Burdur Mehmet Akif Ersoy University, Bucak Emin Gülmez Vocational School of Technical Sciences, 15300, Bucak, Turkey
3 Burdur Mehmet Akif Ersoy University, Istiklal Campus, Faculty of Engineering and Architecture 15030, Burdur, Turkey
4 Burdur Mehmet Akif Ersoy University, Istiklal Campus, Faculty of Engineering and Architecture 15030, Burdur, Turkey
5 Burdur Mehmet Akif Ersoy University, Bucak Technology Faculty, 15300, Burdur, Turkey. (Akdeniz University, Engineering Faculty, Antalya, Turkey)

RECENT DEVELOPMENTS IN TROMBE-WALL SYSTEMS: SOLUTION FOR ZERO ENERGY BUILDINGS

Kazım KUMAŞ[1], Ali Özhan AKYÜZ[2], Azim Doğuş TUNCER[3], Ceylin ŞİRİN[4], Afşin GÜNGÖR[5]

INTRODUCTION

An important contributor to sustainable and clean electricity supply, solar energy systems are one of the fastest developing energy sources among renewable sources for generating both electrical and thermal energy [1-3]. Building applications are the major energy consumers globally and the big portion of the electrical energy is utilized for HVAC systems. Because of environmental concerns and limited fossil fuel resources, buildings are expected to use energy efficiently, by utilizing sustainable energy completely or partially [4]. As known, integration of passive solar technologies for cooling and heating applications are cost effective. Accordingly, the utilization of passive-solar systems in residential and commercial buildings is one of the main key aspects for meet the requirements for sustainable development goals. Passive-solar approaches could reduce yearly heating demand almost 25% [5-7].

1 Burdur Mehmet Akif Ersoy University, Bucak Emin Gülmez Vocational School of Technical Sciences, 15300, Bucak, Turkey
2 Burdur Mehmet Akif Ersoy University, Bucak Emin Gülmez Vocational School of Technical Sciences, 15300, Bucak, Turkey
3 Burdur Mehmet Akif Ersoy University, Istiklal Campus, Faculty of Engineering and Architecture 15030, Burdur, Turkey
4 Burdur Mehmet Akif Ersoy University, Istiklal Campus, Faculty of Engineering and Architecture 15030, Burdur, Turkey
5 Burdur Mehmet Akif Ersoy University, Bucak Technology Faculty, 15300, Burdur, Turkey. (Akdeniz University, Engineering Faculty, Antalya, Turkey)

Solar architecture proposes to plan a house that provide big part of its energy demand from solar energy. In the solar houses, the southern facades are glazed with plenty of space and are planned to be larger than the western/eastern facades. Thus, in the winter more energy can be captured from south facade of the house all day long. Since the sun passes more steeply in summer in comparison to winter, the roof and eaves can prevent the house from staying under extreme sun. To strengthen this benefit from the sun, there are thermal masses (stones that can store heat), such as stones, bricks or concrete, in places where direct sunlight is available, allowing them to release the heat they gained during the day, and to compensate for domestic heat at night. Another passive (indirect) method is to build a greenhouse in front of the southern facade of the house, which is narrower than the wall length and height. In this method heated air between the greenhouse and the wall through the holes above the wall and to provide the cold air flow through the house through the holes left below the wall. If there is a thermal mass such as wall, stone, filled brick or concrete behind the cover, it continues its heating function by releasing the heat it stores during the day.

These processes, which are utilized in passive solar technologies, are heat energy currents and consist of conduction, radiation, and natural convection. When sunlight incident on the building materials, the building material transmits, reflects, or absorbs solar radiation. In an air duct to be formed, it is obvious that the heat generated by the sun will cause an air movement. From this point of view, the heating of the buildings can be done thanks to the sun, which is a natural energy resource. One of the passive heating techniques is Trombe-walls. Trombe-walls are known as storage walls and are extensively utilized technologies because of advantages such as high performance and zero operating cost.

Working principle of a classic Trombe-wall application for heating process is illustrated in Fig. 1. The external area of the building wall is black colored to enhance the absorption rate and the classic Trombe-wall surface is glazed. The channel (duct) is left between the glass and wall. Classic Trombe-wall can absorb solar radiation utilizing greenhouse effect generated in a glazed cavity, and gain and store heat utilizing a massive wall. Part of the thermal energy is transferred into the interior space (heated space) through the wall by conduction. Concurrently, the air with lower temperature enters the cavity from the heated space through the lower vent, heated up by the wall and flows upward due to buoyancy effect. The heated air goes back to the building space through the upper vent. Heat transfer between Trombe-wall and the indoor environment is performed partly by transmission through the wall and partly by ventilation through the vents [4,8].

Trombe-wall systems could be classified in two class: heating-based and cooling-based. Classification of Trombe-wall systems is given in Fig. 2. As it can be seen, this two class have various configurations. These configurations are specified considering the utilized materials, structures and auxiliary units. In this study, Trombe-wall applications which are used as passive heating systems have been introduced and the developments in this technology have been explained. Improvement possibilities have been discussed and trending technologies that can be integrated into these applications have been presented.

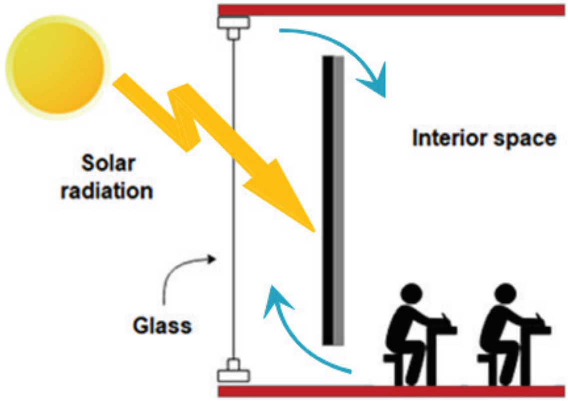

Fig. 1. Working principle of a classic Trombe-wall application for space heating

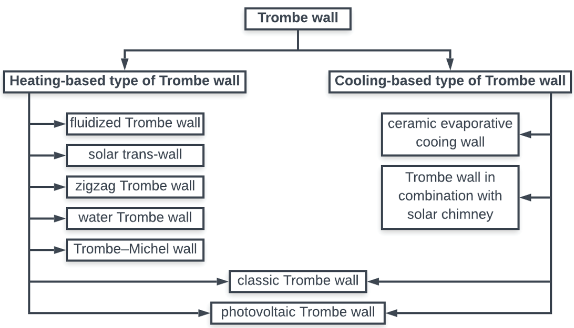

Fig. 2. Classification of Trombe-wall systems [4]

THEORETICAL CALCULATIONS

Air change per hour (ACH) is an important parameter for cooling-based Trombe-walls and is found with following equations [9-10]:

$$\dot{V} = \dot{m}/\rho \quad (1)$$

ACH=$(\dot{V}.3600)$/total volume of the room (2)

Here, is volumetric flow rate of air (m³/s) and is density of air (kg/m³). Useful energy gained by heating-based Trombe wall is calculated as follows:

$$Q_u = \dot{m}C_p(T_o - T_i) \quad (3)$$

Thermal efficiency of the heating-based Trombe-wall is defined as [11]:

$$\eta_{th} = Q_u/(Q_r + Q_u) \quad (4)$$

In Eq. 3, is outlet temperature (°C) and is inlet temperature (°C). In Eq. 4, is the radiation heat obtained by glass (W).

RECENT DEVELOPMENTS IN TROMBE WALL SYSTEMS

Trombe-wall technology is an important application for highlighting sustainability and the use of sustainable and renewable energy sources. First studies related to the Trombe-wall began to be examined in two categories. The first is the work of natural convection between two parallel plates modeled as solar chimneys, and the other is the investigation of the heat transfer in the whole system. Previous researches were investigated the performance of this technology. Various modifications have been proposed for these applications, some of them are shown in Table 1. By investigating the studies, it can be seen that insulation, fans and vents have remarkable effect on the performance of the Trombe-wall systems. Mentioned Trombe-wall components should be utilized meticulously to obviate reverse flow in the system. In addition, dimensions, wall materials and its color, coating and glazing materials and specifications should be carefully chosen for the specific climate conditions. Also, thickness of the massive wall is another important metric that specifies transmitting cycle of the stored useful heat from ambient to indoor air.

Table 1. *Some studies about Trombe-wall systems*

Ref.	Trombe-wall type	Application	Change of parameter(s)
[12]	Photovoltaic Trombe-wall	w/ and w/o fan, glass and porous surface	Daily efficiency: 6.28-49.9%
[13]	Photocatalytic thermal-catalytic Trombe wall	Comparison of photocatalytic-thermal-catalytic, photocatalytic and thermal-catalytic Trombe walls	Total reduced heat loads: 309.8- 296.1 MJ/m^2 Generated clean air: 4764.9- 9482.2 m^3/m^2
[14]	Thermal-catalytic Trombe-wall	w/ brick material and thermal insulation material	Total thermal load reduction: 270.6 MJ/m^2 Generated clean air: 8328.7 m^3/m^2, 10068.4 m^3/m^2
[15]	Semi-transparent photovoltaic Trombe-wall	Mathematical modeling of direct and indirect gain systems	Optimum wall thickness: 0.3-0.4 m
[16]	Composite Trombe-wall	Simulation and thermal optimization, application w/ and w/o air supply	Heat demand reduce rate with air supply: 3.7%
[17]	-	Trombe wall with extra window modification	Average increase in indoor temperature: 0.5 K
[18]	Trombe-Michel wall	Models with sharp edge, rounded edge and guided flow	Glaze spacing: 0.1-0.5 m Rayleigh number: 5.2610^6-6.5710^8
[19]	Trombe-wall integrated with reflection layer and collector	Combined with collector and storage unit	Collector temperature: 45.5-84.8 ^{o}C Temperature gradient of the wall: 0.148-0.401 ^{o}C mm

When the researches are examined, it can be seen that heat transfer and flow analysis has a great importance in terms of to better understand thermal behaviour of the system. These approaches are critical to the efficient use of energy. In addition, it can be allowed to optimize the Trombe-wall system. Moreover, integrating photovoltaic modules can help to produce electrical energy as well as thermal energy. The use of phase change materials will help to utilize latent heat and increase the thermal period.

CONCLUSION

Trombe-wall applications are receiving significant attention and proven to be highly advantageous and considerable in the present energy conservation and environment protection. It is seen that higher efficiency values were obtained for Trombe wall applications with larger wall area. Also, integrating the porous medium inside the air duct of the photovoltaic Trombe-wall system rises the heat transfer area, which increases its electrical and thermal efficiencies. To better understand thermal and flow behavior of the Trombe-wall systems, Computational Fluid Dynamics (CFD) can be utilized effectively as a powerful tool. There are a limited number of studies on CFD analysis in the literature. Using of this approach will help to develop sustainable and promising applications. For future works, it is recommended to replace the porous medium by phase change material and integrating a cooling coil for further Trombe-wall system improvement.

REFERENCES

[1] Khanlari, A., Güler, H.Ö., Tuncer, A. D., Şirin, C., Bilge, Y. C., Yılmaz, Y., Güngör, A. (2020). Experimental and numerical study of the effect of integrating plusshaped perforated baffles to solar air collector in drying application, Renewable Energy, 145, 1677-1692.

[2] Tuncer, A. D., Mavuş, R., Gökçe, C., Koşan, M., Aktaş, M. (2019). Efficient Energy Systems Models for Sustainable Food Processing, Turkish Journal of Agriculture - Food Science and Technology, 7(8), 1138-1145.

[3] Aktaş, M., Koşan, M., Arslan, E., Tuncer, A. D. (2019). Designing a novel solar-assisted heat pump system with modification of a thermal energy storage unit. Proceedings of the Institution of Mechanical Engineers, Part A: Journal of Power and Energy 233(5), 588-603.

[4] Hu, Z., He, W., Ji, J., Zhang, S. (2017). A review on the application of Trombe wall system in buildings, Renewable and Sustainable Energy Reviews, 70, 976-987.

[5] Chan, H. Y., Riffat, S. B., Zhu, J. (2010). Review of passive solar heating and cooling technologies, Renewable and Sustainable Energy Reviews, 14, 781–789.

[6] Hami, K., Draoui, B., Hami, O. (2012). The thermal performances of a solar wall, Energy,39(1),11–16.

[7] Saadatian, O., Sopian, K., Lim C. H., Asim, N., Sulaiman M Y. (2012). Trombe walls: a review of opportunities and challenges in research and development, Renewable and Sustainable Energy Reviews,16(8),6340–6351.

[8] Smolec, W., Thomas A. (1991). Some aspects of Trombe wall heat transfer models, Energy Conversion and Management, 32(3),269–77.

[9] Burek, S. A. M., Habeb, A. (2007). Air flow and thermal efficiency characteristics in solar chimneys and Trombe Walls, Energy and Buildings, 39 (2), 128–135.

[10] Rabani, M., Kalantar, V., Dehghan, A. A., Faghih, A. K. (2015). Empirical investigation of the cooling performance of a new designed Trombe wall in combination with solar chimney and water spraying system, Energy and Buildings, 102(1), 45–57.

[11] Li, Y., Liu S. (2014). Experimental study on thermal performance of a solar chimney combined with PCM, Applied Energy, 114, 172–178.

[12] Ahmed, O. K., Hamada, K. I., Salih, A. M. (2019). Enhancement of the performance of Photovoltaic/Trombe wall system using the porous medium: Experimental and theoretical study, 171, 14-26.

[13] Yu, B., Yang, J., He, W., Qin, M., Zhao, X., Chen, H., (2019). The performance analysis of a novel hybrid solar gradient utilization photocatalyticthermal-catalytic-Trombe wall system, Energy, 174, 420-435.

[14] Hu, B., Jiang, Q., He, W., Hu, Z., Chen, H., Ji, J., Xu, G. (2018). The performance analysis of a novel TC-Trombe wall system in heating seasons, Energy Conversion and Management, 164, 242-261.

[15] Taffese, F., Verma, A., Singh, S., Tiwari, G. N. (2016). Periodic modeling of semi-transparent photovoltaic thermal-trombe wall (SPVT-TW), Solar Energy, 135, 265-273.

[16] Ma, Q., Fukuda, H., Wei, X., Hariyadi, A. 2019. Optimizing energy performance of a ventilated composite Trombewall in an office building, Renewable Energy, 134, 1285-1294.

[17] Bellos, E., Tzivanidis, C., Zisopolou, E., Mitsopoulos, G., Antonopoulos, K. A. (2016). An innovative Trombe wall as a passive heating system for a building in Athens − A comparison with the conventional Trombe wall and the insulated wall, Energy and Buildings, 133, 754-769.

[18] Corasaniti, S., Manni, L., Russo, F., Gori, F. (2017). Numerical simulation of modified Trombe-Michel

Walls with exergy and energy analysis. International Communications in Heat and Mass Transfer, 88, 269-276.

[19] Long, J., Yongga, A., Sun, H. (2018). Thermal insulation performance of a Trombe wall combined with collector and reflection layer in hot summer and cold winter zone, Energy and Buildings, 171, 144-154.

MODEL DESIGN OF AN IN-WHEEL BLDC MOTOR USING MATLAB/SIMULINK FOR LIGHT ELECTRIC VEHICLES

Ali Sinan ÇABUK

CHAPTER 5

MODEL DESIGN OF AN IN-WHEEL BLDC MOTOR USING MATLAB/SIMULINK FOR LIGHT ELECTRIC VEHICLES

Ali Sinan ÇABUK

1. INTRODUCTION

Countries leading in technology are working on projects to prevent environmental pollution and decrease consumption of fossil fuels. One of the most common methods is using environmental friendly electrical motors in transportation [1-4]. Increasing use of small sized vehicles especially in residential areas is taught to be an environmental friendly transportation target [3-5]. Energy planning is one of the critical concepts in electrical vehicle (EV) technology. In energy planning, energy management electric motors are crucial [4-7]. Due to positive features such as high torque, efficiency and low volume-weight structure, automotive manufacturers have begun to produce EV and light electric vehicles based on in-wheel brushless direct current (BLDC) motors [8-10]. The BLDC motor structure has been subject to research in recent years because of the innovations in the materials used in its and the power electronics elements used in the drive circuits of such motor components [11-13]. Increasing efficiency and reducing losses to minimum should be a goal of priority in EV where energy planning is important. This provides two elemental benefits such as decreasing the energy consumption per km and increasing the distance to be travelled [14-17]. Therefore research on in-wheel BLDC motor, which is a new technology, has increased. The most important problem of in-wheel BLDC motor needs to be well modeled to achieve realistic results. One of the most preferred methods for solving that problem is MATLAB software.

MATLAB can be used in many types of mathematical and engineering problems. MATLAB and Simulink can be used to provide framework based on magnetic, electric and electronic devices and quantities are modelled, simulated and post-processed [18,19].

Among other programming software, Simulink gives opportunity of building the simulation allocate by means of fundament function blocks. Thus a group of differential equations can be modelled by interconnectedness of convenient function blocks, each of those execution a particular mathematical operation. This did not only decrease programming efforts but also debugging of errors is made easy. The model of simulation can be developed handily by adding new sub-models that can be used for various control functions, because Simulink is a model operation programmer. Less number of data tables and less time of simulation are needed for the proposed model because Simulink is based on graphical coding environment. Furthermore different mode of operating of machine is possible under the same conditions, with very little addition [20, 21].

MATLAB/Simulink which is useful for providing accurate results of electric machines can be used in developing of a dynamic model of the BLDC motor [18-21].

The driving system must be defined by considering the basic criteria of estimating of losses during operation of an inverter, which supplies a BLDC motor type. Only mathematical modelling and computer simulation can provide estimation of losses as well as the response of the entire system to load changes when driving is addressed to a small vehicle with different operating regimes. A driving model created in MATLAB/Simulink can usually be used for such simulation [20, 21].

2. MATLAB/SIMULINK MODEL OF IN-WHEEL BLDC MOTOR

MATLAB-Simulink was created for numerical calculation, modelling and simulation with high performance. Realistic approaches through modelling with software is possible to be approached. This chapter of New Horizons in Engineering book aims to explain the MATLAB/Simulink software used in the design of the in-wheel brushless direct current motor for light electric vehicles. MATLAB/Simulink software can be beneficial to the design process of the electric motor, especially for in-wheel BLDC motor.

2.1. In-Wheel BLDC Motor Design

An in-wheel BLDC motor used in solar car races and light electric vehicles studied with its dynamic model is chosen for this study. The equations of the state system and that are connected to the rotor position were used from (2.1) to (2.6) and the mathematical model of the structure is designed with MATLAB/Simulink. In addition, following points were taken into consideration during modelling:

- Magnetic circuit saturations were ignored,
- Stator resistance, self-inductance and mutual conductance of all phases were taken as equal and fixed,
- Current characteristics and Eddy currents were ignored
- All semi-conductive materials considered to be in control system assumed as ideal

Phase voltages and back e.m.f. are given below

$$V_A = R_{iA} + (L - M)\frac{d_{iA}}{d_t} + E_A \tag{2.1}$$

$$V_B = R_{iB} + (L - M)\frac{d_{iB}}{d_t} + E_B \tag{2.2}$$

$$V_C = R_{iC} + (L - M)\frac{d_{iC}}{d_t} + E_C \tag{2.3}$$

$$E_A = K_e \omega_m F(\theta_e) \tag{2.4}$$

$$E_B = K_e \omega_m F(\theta_e - \frac{2\pi}{3}) \tag{2.5}$$

$$E_C = K_e \omega_m F(\theta_e + \frac{2\pi}{3}) \tag{2.6}$$

where A, B, C statements given determine the phases V_A, V_B and V_C are phase voltages and E_A, E_B, E_C are phase back e.m.f., R is resistance of each phase of in-wheel BLDC motor, L is inductance of each phase of in-wheel BLDC motor, M is mutual inductance, K_e is back e.m.f. constant, ω_m angular velocity of rotor, θ_e is electrical angle of rotor, $F(\theta_e)$ is reference function of back e.m.f. according to rotor position.

Electrical torque generated by phases and electrical moment of the in-wheel BLDC motor

$$T_A = K_t i_A F(\theta_e) \tag{2.7}$$

$$T_B = K_t i_B F(\theta_e - \frac{2\pi}{3}) \tag{2.8}$$

$$T_C = K_t i_C F(\theta_e + \frac{2\pi}{3}) \tag{2.9}$$

$$T_e = T_A + T_B + T_C \tag{2.10}$$

$$T_e - T_L = J\frac{d^2\theta_m}{dt^2} + \beta\frac{d\theta_m}{dt} \tag{2.11}$$

$$\theta_e = \frac{p}{2}\theta_m \tag{2.12}$$

$$\omega_m = \frac{d\theta_m}{dt} \tag{2.13}$$

where *A, B, C* statements given determine the phases T_A, T_B and T_C are electrical torque, i_A, i_B and i_C are phase currents, K_t is torque constant, T_e is electrical moment of the in-wheel BLDC motor, θ_m is mechanical angle of rotor, T_L is load torque. The mechanical angle of the rotor is related with the angular velocity of the rotor, which can be seen in equation 2.13.

Phase to phase voltage between V_{AB} and V_{BC} phases:

$$V_{AB} = R(i_A - i_B) + (L - M)\frac{d}{dt}(i_A - i_B) + E_{AB} \tag{2.14}$$

$$V_{BC} = R(i_B - i_C) + (L - M)\frac{d}{dt}(i_B - i_C) + E_{BC} \tag{2.15}$$

where E_{AB} and E_{BC} are back e.m.f.

In accordance with the formula given above; since $(i_A + i_B + i_c) = 0$, if mutual inductance are ignored in equations (2.14) and (2.15), then equations (2.16) and (2.17) are obtained.

$$\frac{di_A}{dt} = -\frac{R}{L}i_A + \frac{2}{3L}(V_{AB} - E_{AB}) + \frac{1}{3L}(V_{BC} - E_{BC}) \tag{2.16}$$

$$\frac{di_B}{dt} = -\frac{R}{L}i_B - \frac{1}{3L}(V_{AB} - E_{AB}) + \frac{1}{3L}(V_{BC} - E_{BC}) \tag{2.17}$$

According to equations shown above, state space model of in-wheel BLDC motor is follows:

$$\begin{bmatrix} i'_A \\ i'_B \\ \omega'_m \end{bmatrix} = \begin{bmatrix} -\frac{R}{L} & 0 & 0 \\ 0 & -\frac{R}{L} & 0 \\ 0 & 0 & -\frac{\beta}{J} \end{bmatrix} \begin{bmatrix} i_A \\ i_B \\ \omega_m \end{bmatrix} + \begin{bmatrix} \frac{2}{3L} & \frac{1}{3L} & 0 \\ -\frac{1}{3L} & \frac{1}{3L} & 0 \\ 0 & 0 & \frac{1}{J} \end{bmatrix} \begin{bmatrix} V_{AB} - E_{AB} \\ V_{BC} - E_{BC} \\ T_e - T_L \end{bmatrix} \quad (2.18)$$

$$\begin{bmatrix} i_A \\ i_B \\ i_C \\ \omega_m \end{bmatrix} = \begin{bmatrix} 1 & 0 & 0 \\ 0 & 1 & 0 \\ -1 & -1 & 0 \\ 0 & 0 & 1 \end{bmatrix} \begin{bmatrix} i_A \\ i_B \\ \omega_m \end{bmatrix} \quad (2.19)$$

J is motor inertia and T_L is load torque.

According to the formula sets given above, MATLAB/Simulink model of in-wheel BLDC motor can be began.

Firstly transfer function of each phase voltage with torque constant can be created as given Figure 2.1.

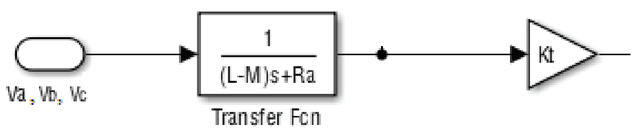

Figure 2.1. *MATLAB/Simulink Model of transfer function of phase voltage*

Each K_e back e.m.f. constant should be linked up interpose with transfer function of each phase voltage. Then transfer functions of phase voltages can linked up each other as given Figure 2.2.

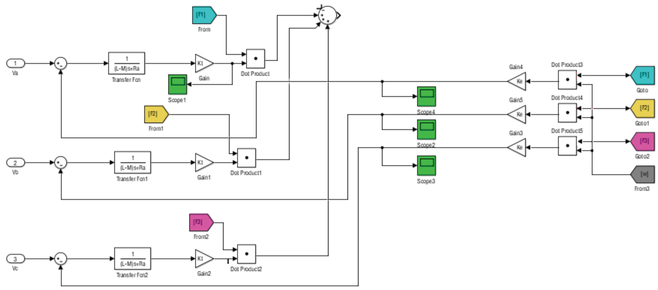

Figure 2.2. *MATLAB/Simulink Model of transfer functions of phase voltages*

In order for MATLAB/Simulink Model of in-wheel BLDC motor to work it needs a signal from hall sensors. Therefore Hall Effect truth table and accordingly electrical angel truth table must be created. The signals assumed to be appropriate to be produced by the hall-effect sensors can be designed as of each are effective in 60° electrical angle and formed in compliance with the information mentioned above as shown in Table 2.1.

Table 2.1. *Rotor position power of hall-effect sensor signal [15]*

Electrical Degree	Hall Sensor "A"	Hall Sensor "B"	Hall Sensor "C"
0-60	1	0	1
60-120	0	0	1
120-180	0	1	1
180-240	0	1	0
240-300	1	1	0
300-360	1	0	0

MATLAB/Simulink Model of Hall Effect block and electrical angel block can be created by means of Table 1 as given Figure 2.3.

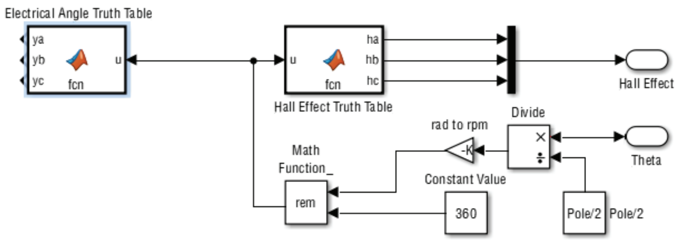

Figure 2.3. *MATLAB/Simulink Model of Hall Effect and electrical angel blocks*

Then MATLAB/Simulink Model of transfer functions of phase voltages and Hall Effect and electrical angel blocks can be combined for create MATLAB/Simulink Model of in-wheel BLDC motor. As given before can be seen the electrical and mechanical equations for in-wheel BLDC motor that has three-phase trapezoidal feeding. MATLAB/Simulink with equation 2.1 to 2.19 components was used in the modelling the system. MATLAB/Simulink Model of in-wheel BLDC motor is shown in Figure 2.4 can be created with the equations given before.

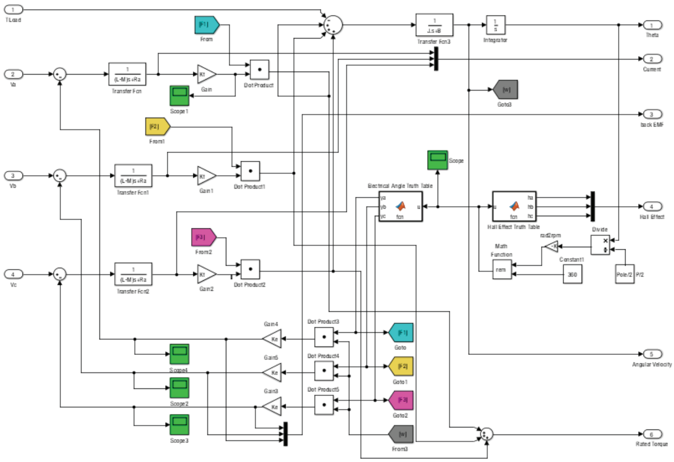

Figure 2.4. *MATLAB/Simulink Model of in-wheel BLDC motor*

Figure 2.4 shows three different phase groups created in MATLAB/Simulink model with V_A, V_B and V_C voltage inputs and T_L load torque. The current has outputs for back EMF measurements and torque. Armature current values of the model are determined separately from each phase winding. Torque is determined as the total value, which is created by each phase winding. Half-effect sensor outputs are used to provide the rotating movement of rotor by determining the position. Rotor angular speed (ω_m) output is used to control if required speed is provided or not.

The truth table is formed by benefiting from the data indicated in the literature of the signals produced by the hall-effect sensors, in order to determine the rotor position and produce the appropriate signal [15].

MATLAB/Simulink Model of in-wheel BLDC motor, as given Figure 2.4, should be transformed as sub-block for used in control system. Figure 2.5 shown the sub-block of in-wheel BLDC motor.

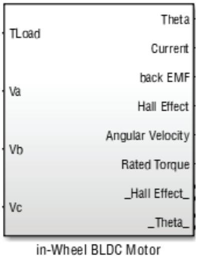

Figure 2.5. *Sub-block of in-wheel BLDC motor*

2.2. Controller Design

Controller of the motor modelled is the most important part of in-wheel BLDC motor design. Controller is added in order for output variables to be at the required values. The operating principle of the controller is based on measuring the variable of interest, comparing it to the reference signal and obtaining the error with feedback. According to this error controller, system produces an improving signal. Figure 2.6 shows the principals of the feedback driver system. In this figure, the abbreviation PPU stands for power propulsion electronic unit.

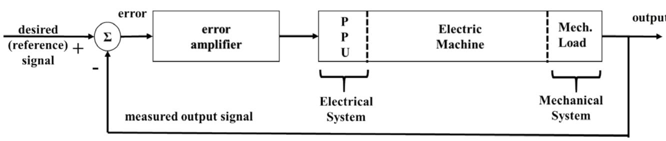

Figure 2.6. *Feedback driver system*

Most of the time controlling one single variable is not sufficient in electrical machine applications. In such cases multiple error signals can be produced and multiple controllers can be added. Figure 2.7 shows that the setting consists of speed and torque, therefore the position is at the outer part, speed is in the middle and torque is at the inner part. In cascade controls, response time increases while moving towards the inner loop.

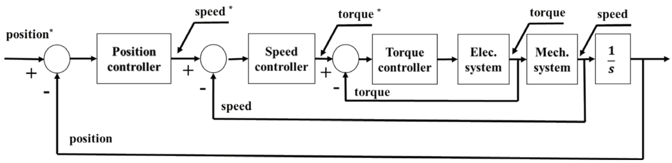

Figure 2.7. *Principle schema of controller*

Non-linear system must be linearized firstly when designing a controller. The steady state operating point of the system must be determined. Linearization is carried out by using fundamental linear control theory, where change in input reference signal and change in load can be easily ignored at the steady state zone. After controller is designed using linear control theory, the whole system is simulated in order to test the controller for the signal values. It is thought that for system design controller may need to be adjusted.

The PI controller is most extensively accepted in industrial application due to its effective, simple design, easy structure and low cost. It is more often used as controller, especially when response speed is not a trouble. PI controller can be eliminated steady state error forced and oscillations resulting in operation of on-off controller and P controller respectively. For this reason, PI controller can be designed according to Figure 2.8 in order to resolve the problems mentioned above.

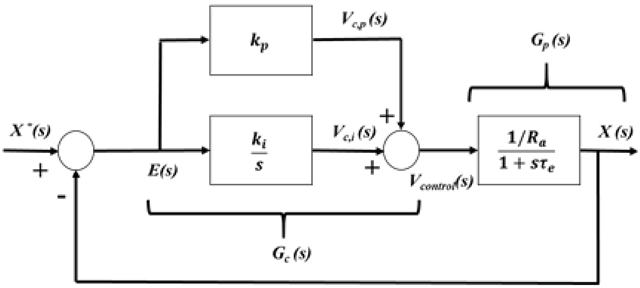

Figure 2.8. *Principle schema of PI controller*

The PI controller given in Figure 2.8 eliminates the steady state error. While it does this it brings a slowness to the system. We can express this as in equations 2.20, 2.21 and 2.23.

$$\frac{V_c(s)}{E(s)} = k_p + \left(\frac{k_i}{s}\right) = \left(\frac{k_i}{s}\right)(1 + \frac{s}{k_i/k_p}) \quad (2.20)$$

$$V_{c,i}(s) = \frac{k_i}{s} E(s) \quad (2.21)$$

$$V_{c,p}(s) = k_p\, E(s) \quad (2.22)$$

While system design is built, integral control alone takes integral of error according to time therefore slows the response of the system. Therefore it is used together with P (proportional) control. Furthermore when P controller step input is given alone, it gives an error at steady state. Therefore it is used together with I (integral) controller. Integral controller works continuously until the error reaches zero at the steady state step input, which finally leads to error value zero. In motion control systems P controller is usually used in control loops, and PI controller is usually used in speed and torque. D (derivative) controller is usually not preferred in motion control systems. Controller can be modelled primarily for torque and current. Speed controller can be designed after torque controller is assumed to be optimal. If necessary, the slowest loop controller can be designed for the conditions where speed controller and torque controller can be ideal [22, 23].

In-wheel BLDC motor controlled is equipped with Proportional Integral (PI) controller in order to improve in-wheel BLDC motor speed by means of response and stability. PI (Proportional-Integral) method is applied provide process control and stability in this system that is realized by MOSFET triggering circuit [22]. The feature of this method to follow errors proportionally enables it to respond quickly in order to increase the static accuracy, dynamic response and reduce the error to zero in the system. PI speed control block diagram used in MATLAB/ Simulink model designed for in-wheel BLDC motor is shown in Figure 2.9.

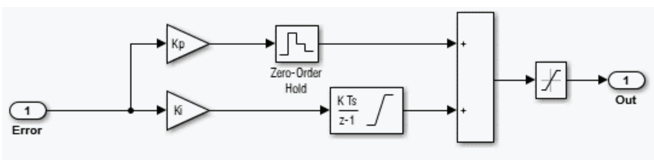

Figure 2.9. *PI speed control*

Figure 2.10 shows below the design of control and driver model of in-wheel BLDC motor, where MATLAB/ Simulink dynamic model is created.

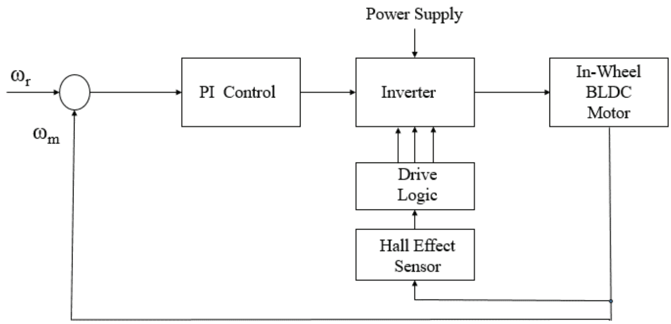

Figure 2.10. *Dynamic model block diagram of in-wheel BLDC motor*

Six step MOSFET was used as inverter in MATLAB/Simulink Model which was produced based on the block diagram created for speed control of in-wheel BLDC motor shown in Figure 2.10. Here, in which order the MOSFETs should be transmitted, the rotor position and generate coded signals are carried out for control with the three Hall Effect sensors. Control with six step driver is considered for the form of which model was created with MATLAB/Simulink.

The rotor position must be defined to enable electronic communication and therefore in order for in-wheel BLDC motor to operate. Using physical position sensors such as Hall Effect (HE) magnetic sensors, encoders or another sensor-free method fed to the controller to trigger the sequential electronic control of the inverter circuit helps detecting the rotor position. The controller carries out the switching sequence to the three-phase inverter, using six power semiconductor transistors in order to commutate the power electronically to the motor phase from the DC voltage source [22].

The frequency of the three-phase power which is fed to the in-wheel BLDC motor and the output depend on the switching state of the inverter. Various control methods can be used in order to carry out controlling of inverter switches [22].

Sub-control blocks stated in Figure 2.11 were formed in order for Hall Effect sensors stated in Table 2.2 to carry out proper and appropriate MOSFET triggering.

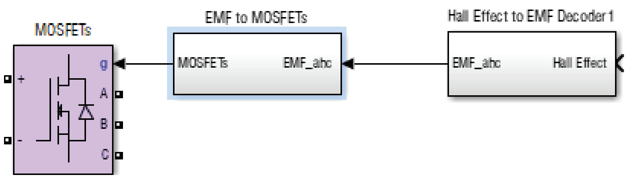

Figure 2.11. *MOSFET triggering logic circuit scheme*

Table 2.2. *Rotor position with e.m.f. [15]*

Electrical Degree	EMF "A"	EMF "B"	EMF "C"
0-60	1	-1	0
60-120	0	-1	1
120-180	-1	0	1
180-240	-1	1	0
240-300	0	1	-1
300-360	1	0	-1

Hall Effect sensors are used in order to digitally code the angle information obtained from the rotor position. In order to effect an energy transfer in compliance with motor winding couples and direction of rotation the coding is conducted. Codes from the Hall Effect sensors trigger the power electronic elements through which armature voltage is applied to the motor windings.

MATLAB/Simulink model is frequently used to design with a 6-step drive. For this reason, the markings deemed appropriate to produce field effect sensors are designed to be effective at each 60° electrical angle and are accordingly formed as in Table 2.3.

Table 2.3. *MOSFET switching for clockwise rotation [15]*

EMK "A"	EMK "B"	EMK "C"	Q1	Q2	Q3	Q4	Q5	Q6
0	0	0	0	0	0	0	0	0
0	-1	1	0	0	0	1	1	0
-1	1	0	0	1	1	0	0	0
-1	0	1	0	1	0	0	1	0
1	0	-1	1	0	0	0	0	1
1	-1	0	1	0	0	1	0	0
0	1	-1	0	0	1	0	0	1
0	0	0	0	0	0	0	0	0

Digital codes from the Hall Effect sensors are required for the sequential switching of the MOSFETs given in Table 2.3. The logic circuit for switching the MOSFETs is as shown in Figure 2.12.

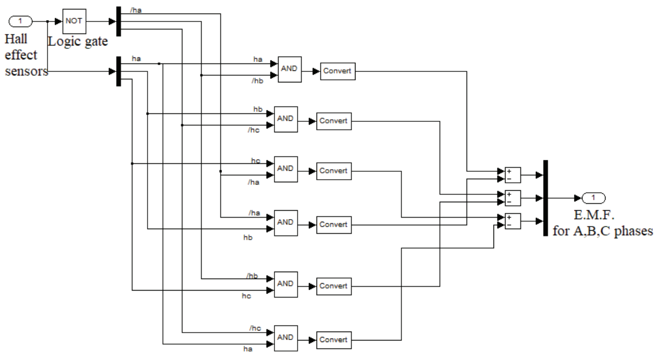

(a)

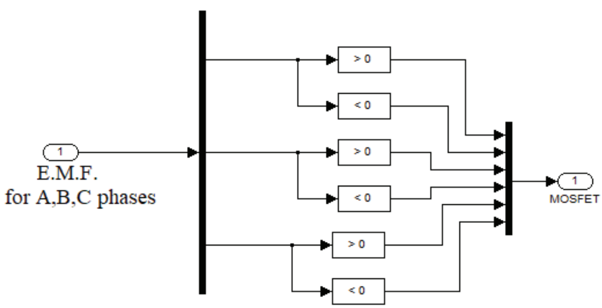

(b)

Figure 2.12. *(a) Hall effect sensor - Electromotive force logic circuit (b) Electromotive force - MOSFET logic circuit*

Armature inductance is variable on d and q axes because of the in-wheel BLDC motor reluctance. While determining the parameters of the required variable controller, BLDC motor is assumed to have a single inductance value. In order to simplify calculations of the inductance value, average of d and q axes inductance values are taken. There is 10 folds difference between crossover frequencies of moment and speed controllers. Torque loop is usually selected to be one tenth of the bandwidth switching frequency. As rotor flux is constant in-wheel BLDC motor, current and moment are directly proportional to each other by a constant k_T. Figure 2.13 shows torque controller design.

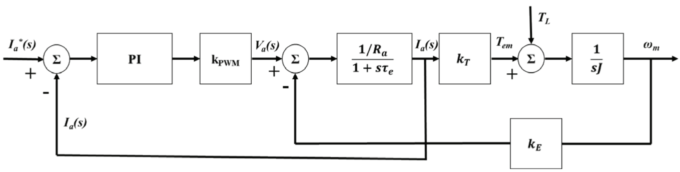

Figure 2.13. *Torque controller design.*

Figure 2.13 shows feedback from output speed to the torque controller loop. This shows a back-EMF caused by the speed in the feedback system. $E_a(s)$ is determined by terms of $I_s(s)$ where load torque (T_L) is ignored and the current is output signal. Here feedback term is inversely proportional to the torque of inertia (J_{eq}). When assuming the torque is large, feedback term can be ignored.

MATLAB/Simulink PI controller model of in-wheel BLDC motor is shown in Figure 2.14 can be created with detail information given before.

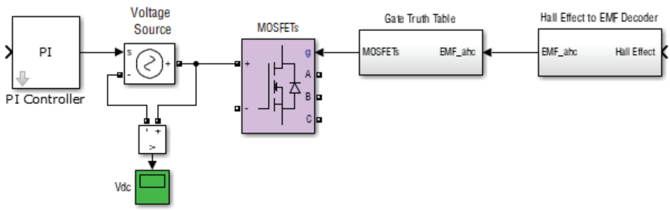

Figure 2.14. *PI controller of In-wheel BLDC motor.*

2.3. MATLAB/Simulink model of the system

In-wheel BLDC motor speed control MATLAB/Simulink model which was obtained with all these abovementioned components is shown in Figure 2.15. The model involves MATLAB/Simulink Model of in-wheel BLDC motor and PI controller. In-wheel BLDC motor and controller MATLAB/Simulink Model requires input reference speed, bus bar voltage value and power, pole number of the motor. Also phase resistance, phase inductance, motor inertia, e.m.f. constant and torque constant values need to enter as data in the sub-system.

The parameters of system parts modelling is determined to be very important besides a graphical results from MATLAB/Simulink Model. The graphical results can be seen in measurement component as given green box in Figure 2.15. In particular, the placement of hall-effect sensors and the codes they generate must be well monitored by the driver circuit, otherwise the motor is not working. Especially the position of Hall-Effect otherwise the monitor will not work.

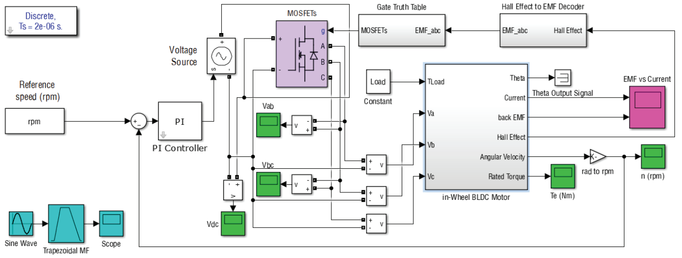

Figure 2.15. *In-wheel BLDC motor and controller MATLAB/Simulink Model*

Thereby an in-wheel BLDC motor and drive system can be modelled in MATLAB/Simulink for light electric vehicles due to the fact that it can provide more accurate dynamic modelling results.

REFERENCES

[1] Zhu S., Hu Y., Liu C., & Wang K. (2018). Iron Loss and Efficiency Analysis of Interior PM Machines for Electric Vehicle Applications. *IEEE Transactions on Industrial Electronics*, 65(1), 114-124.

[2] Zarko, D., Ban, D., & Lipo, T. A. (2007). Analytical solution for cogging torque in surface permanent-magnet motors using conformal mapping. *IEEE Transactions on Magnetics*, 44(1), 52-64.

[3] CheshmehBeigi, H. M. (2018). An adaptive nonlinear internal-model control for the speed control of homopolar salient-pole BLDC motor. *International Journal of Electronics*, 105 (5), 848-865.

[4] Cabuk, A. S., Saglam, S., & Ustun, O. (2017). Impact of various slot-pole combinations on an in-wheel BLDC motor performance. *I.U.-Journal of Electrical & Electronics Engineering*, 17 (2), 3369-3375.

[5] Kim, S., Lee, J., & Lee, K. (2018). Robust speed control algorithm with disturbance observer for uncertain PMSM. *International Journal of Electronics*, 105 (8), 1300-1318.

[6] Zhang, Z., Fan, Y., Lorenz, R. D., Nied, A., & Cheng, M. (2018). Design and comparison of three-phase and five-phase FTFSCW-IPM motor open-end winding drive systems for electric vehicles applications. *IEEE Transactions on Vehicular Technology,* 67 (1), 385-396.

[7] Li, S., Sarlioglu, B., Jurkovic, S., Patel, N., & Savagian, P. (2017). Comparative analysis of torque compensation control algorithms of interior permanent magnet machines for automotive applications considering the effects of temperature variation. *IEEE Transactions on Transportation Electrification*, 99, 1-13.

[8] Bernat, J., Stepien, S. J., Stranz, A., & Superczynska, P. (2017). Infinite-time linear–quadratic optimal control of the BLDC motor exploiting a nonlinear finite element model. *The International Journal for Computation and*

Mathematics in Electrical and Electronic Engineering, 36(3), 633-648.

[9] Salehifar, M., Arashloo, R. S., Moreno-Equilaz, J. M., Sala, V., & Romeral, L. (2014). Fault detection and fault tolerant operation of a five phase PM motor drive using adaptive model identification approach. *IEEE J. Emerg. Sel. Topics Power Electron*, 2 (2), 212-223.

[10] Krykowski, K., Hetmanczyk, J., Gałuszkiewicz, Z., & Miksiewicz, R. (2011). Computer analysis of high-speed PM BLDC motor properties. *The International Journal for Computation and Mathematics in Electrical and Electronic Engineering*, 30(3), 941-956.

[11] Tuncay, R. N., Ustun, O., Yılmaz, M., Gökce, C., & Karakaya, U. (2011, Sept.). *Design and implementation of an electric drive system for in-wheel motor electric vehicle applications*. 7th IEEE Vehicle Power and Propulsion Conference, Chicago, IL, USA, 1-6.

[12] Nair, S. S., Nalakath, S., & Dhinagar, S. J. (2011, May). *Design and analysis of axial flux permanent magnet BLDC motor for automotive applications*. IEEE International Electric Machines & Drives Conference, Niagara Falls, Canada, 1615-1618.

[13] Carpiuc, S. C. (2017). Rotor temperature detection in permanent magnet synchronous machine-based automotive electric traction drives. *IEEE Transactions on Power Electronics*, 32(3), 2090-2097.

[14] Rubaai, A., & Young, P. (2016). Hardware/Software implementation of fuzzy- neural-network self-learning control methods for brushless DC motor drives. *IEEE Transactions on Industry Applications*, 52(1), 414-424.

[15] Cabuk, A. S. (2016). *A Novel Approach to Optimized Design of In-Wheel BLDC Motors* (Doctoral dissertation). Retrieved from https://tez.yok.gov.tr/UlusalTezMerkezi/giris.jsp (425881)

[16] Singh, B., & Kumar, R. (2016). Solar PV array fed water pump driven by BLDC motor using landsman converter. *IET Renewable Power Generation*, 10(4), 474-484.

[17] Prabu, M.J., Poongodi, P., & Premkumar, K. (2016). Fuzzy supervised online coactive neuro-fuzzy inference system-based rotor position control of brushless DC motor. *IET Power Electronics*, 9(11), 2229-2239.

[18] Ghorbanian, V., & Lowther, D. D. (2017). A Statistical solution to efficiently optimize the design of an inverter-fed permanent-magnet motor. *IEEE Transactions on Industry Applications*, 53(6), 5315-5326.

[19] Maraaba, L., Al-Hamouz, Z., Milhem, A., & Abido, M. (2018). Modelling of interior-mount LSPMSM under asymmetrical stator winding. *IET Electric Power Applications,* 12 (5), 693-700.

[20] Memon, A. A., Shah, S. A. A., Shah, W., Baloch, M. H., Kaloi, G. S., & Mirjat, N. H. (2018). A Flexible mathematical model for dissimilar operating modes of a switched reluctance machine. *IEEE Access*, 6, 9643-9649.

[21] Kumar, R., & Singh, B. (2017). Single stage solar PV fed brushless DC motor driven water pump. *IEEE Journal of Emerging and Selected Topics in Power Electronics*, 5(3), 1377-1385.

[22] Singh J., & Singh, M. (2016). Comparison and analysis of different techniques for speed control of brushless DC motor using MATLAB simulink. *International Journal of Engineering Trends and Technology (IJETT)*, 38 (7), 373-379.

[23] Rao K.S., & Mishra R. (2014). Comparative study of P, PI and PID controller for speed control of VSI-fed induction motor. *International Journal of Engineering Development and Research*, 2(2), 2740-2744.

RECOGNİTİON OF EEG SİGNALS WİTH DECİSİON TREE CLASSİFİER

Furkan ESMERAY[1]

CHAPTER 6

1 Electric and Energy Department Munzur University Tunceli, Turkey
furkanesmeray@munzur.edu.tr

RECOGNİTİON OF EEG SİGNALS WİTH DECİSİON TREE CLASSİFİER

Furkan ESMERAY[1]

1. INTRODUCTION

The body that controls the nervous system, stores all the information, intelligently, understands, thinks and decides on emotional functions is brain. For centuries the work on the brain has been a research field that has dragged the brain, doctors and scientists into a complex structure. Because the brain; many uncertainties, unknown and complex structures. The human brain produces a variety of signals that have been analyzed over the years and proved to be proven at the same time. These signals are also called EEG or Electroencephalogram in medicine [1]. Signs with a lower amplitude than the brain surface detected by the electrodes are called EEG signals. The EEG signals produced by the neurons are in the cerebral cortex. These signals give many different warnings. On the other hand, EEG signals; rhythms created by rhythm centers located deep in the brain. These potentials are recorded with irregular variations and reflected in the sea. These signals obtained in the human brain keep a lot of information, but not yet used as a whole. Since the EEG signals have a low amplitude, this information is difficult to reach. EEG measurement today; headache and sleep related diseases, to determine the level of anesthesia of an anesthetized patient, to detect epilepsy, to be cheap, and to avoid pain in many areas. However, the evaluation of this information leads to certain limitations due to the lack of certain values. Thus, the use of EEG markers in clinical diagnosis has become possible thanks to the analysis of EEG signals in the light of increasing technological developments. Çol has

1 Electric and Energy Department Munzur University Tunceli, Turkey furkanesmeray@munzur.edu.tr

a bad influence on human life because of the diseases that may arise in the brain which is an important organ. The use of these markers in the diagnosis and treatment of diseases is the reason for resolving the signs taken from the brain during treatment, which is an intense research topic in the scientific field in the near future [2]. Because of this reaso**n**, EEG signals can be analyzed by different methods and an objective evaluation can be made. In statistical analysis of the signal, some of these methods have been developed in recent years and other methods have been used to determine specific waveforms during the decomposition and examination phase[3]. EEG recording and analysis methods are one of the most commonly used methods in the treatment of brain diseases as well as in treatment. In particular, it is possible to increase the recording times of EEG devices, to record a fixed discrete data by connecting to a computer, to record the data of patients' EEGs for one or more days or even weeks, thus achieving a healthier result than EEG analyzes. Karkov (1875), one of the earliest stages of EEG use, was the subject of a more than 150-year literature search and showed that there was a change in the amplitude of cortex muscle signals in spite of acoustic stimulation [4]. These methods have been applied based on the use of EEG signals in determining the depth of anesthesia by referring to many methods. Li X et al. have obtained a successful outcome using an experimental Kip decomposition-situated method of epileptic EEG signals. The results obtained can be achieved into numerical and small Numerical Mode Functions of non-stationary complex signs [5]. Soo-young Ye et al. in their study, 20-50 value of Bispectrum index ranged between 0-100 value, anesthesia was stated, the wariness of 60-100 value and EEG frequency range in determining the depth of anesthesia was reported to be below 8 Hz [6]. In a study on the anesthesia grade of Rüştü Güntürk, 30 neurons in the middle stage and 60 neurons in the input stage were trained using the Power Spectral Intensities of the Elman network EEG signals in the 1-50 Hz frequency range, and the level of anesthesia was found. At the end of the study, 95% success was achieved [7]. Laxman Tawade et al. the detection of epilepsy disarray was investigated by using the Discrete Wavelet Transform method in EEG signs. They were arrested with a success rate of 96% [8]. Maan M. Shaker reported that as a result of using Discrete Wavelet Transform and Fourier transforms in his studies on EEG signals, he obtained very successful results of alpha, beta, delta, tetra classes by classifying noise canceling EEG signals with Discrete Wavelet Transform and separating EEG waves [9]. V. Esmaeilia et al. developed a fuzzy logic structure based on EEG to determine the depth of anesthesia and conducted a study to achieve the goal of 4 grouping (awake anesthesia compliance, intraoperative anesthesia, and isolation) on single-channel EEG data [10]. C.M. Sweeney-Reed et al. used the Empirical Mode Decomposition method to demonstrate that it is possible to reach the desired frequency band on EEG signals. With the method they used, the desired bandwidth IQ functions were synchronized with the EEG signals [11]. Zhang X et al. They proposed an EEG derivative model (Lembel-Ziv Complexity Analysis) based on the relationship between depth of anesthesia and brain activity, and this model, which was proposed to determine the depth of anesthesia, succeed a real-time success rate of 93% [12].

2.THEORY AND METHODS

The aim of this study is to analyze the EEG signals obtained from different groups of patients and healthy people with some machine learning techniques. In this way, it is aimed to provide automatic estimation of classes with a computer-aided system. EEG signals used in this study were used as 5 different groups.

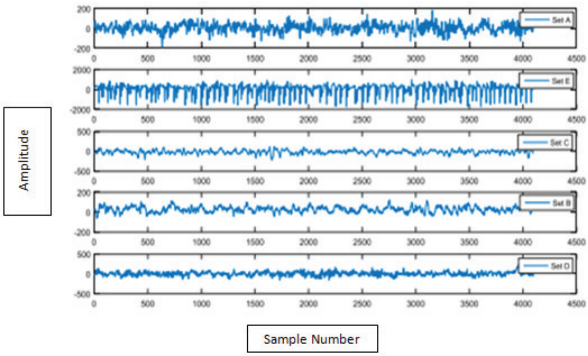

Figure 1.1: *EEG signals in the 5 different group [13]*

The signals of Set A and Set B in Figure 1.1 were applied to healthy people. In addition, Set A - Set B are signals from healthy eyes. Set C, Set D and Set E are signals for epilepsy patients. Set C and Set D are signals from the damaged hemisphere and the undamaged hemisphere, even if they are not on epileptic seizures. Set E is the signal obtained during an epileptic seizure. Each set has 100 sample signals. In this study, a total of 500 EEG signal samples were used.

2.1.Sym3 Wavelet Family

Discrete wavelet transform is a widely used method for property extraction in many different domains such as signal engraving, biomedical signal engraving, and data mining [14,15]. The Discrete Wavelet Transform (DWT) is the sum of the signal that is multiplied by its stabilize values and scaled over the time range of the wavelet. The DWT function is used at the wanted level for the signal and image [14, 15]. The DWT method allows to obtain the distinguishing characteristics of the signal by analyzing the low frequency component at a lower band gap and the higher frequency component at a narrow range. The mathematical expression of the subbands obtained using DWT is indicated in Equation (1) [14, 16].

$$F_{BF}(u, v) = DWT\{F(x, y), B \in \{CA, Y \quad (1)$$

where, in the decomposition process of these subbands, *CA* expresses the approximate coefficients of the operation, while *YA, AY, YY* expresses the detail coefficients of the operation [14, 16-18]. Detail coefficients are horizontal, vertical and diagonal. DWT can be resumed by decomposing the approach data again in similar way. Approximate coefficients are used in this study. There is no algorithm in determining the wavelet family that should be selected in the studies. In the time domain, the main wavelet is visually more similar to the signal to be processed, resulting in greater efficiency than the wavelet transform method. But it seems almost impossible to make a choice like this. For this reason, all wavelet family types should be tried..In this study, sym3 wavelet family is used [14, 18].

2.2. Decision Tree (DT)

Decision tree has begun from a roots and operation at decree loops and finally finished in labeled let a classifier and inspected learning certainment. In the best case, for n number nodes decide reached the result [19, 20]. The function in Equation (2) has been expressed as entropy in the form of the amount of all the probabilities in a *H* unit.

$$K(H) = -\sum_{i=1}^{b} s_i . \log_2 s_i \quad (2)$$

The *H* unit in the equation denotes the class property and entropy is used for the *H* class property. As shown in Equation (3), weighted averages of each classified feature is calculated.

$$K(W,H) = -\sum_{i=1}^{b} \frac{|H_i|}{H} . K(H_i) \quad (3)$$

Here, entropy is calculated for each *W* characteristic of *H* class. The entropy value calculated for the i value of *H* is the number of values , which is the total number of *H* values. The information gain calculated for each property is shown in Equation (4).

$$Gain(W,H) = K(H) - H(W,H) \quad (4)$$

In this way, the feature that capacity the highest gain is evaluate as the root node of the tree. The remaining values are recalculated to form the other nodes and branches of the decision tree, and each sub node is added as the highest earning property. While the ID3 algorithm only implements to category-based classification, the C4.5 algorithm, which is the developed version of the same algorithm, allows the use of properties with digital values in decision nodes. The threshold value is used in decision mechanisms in which numerical features are used. Decision trees are obtained by calculating gains separately for divided values [20].

3.RESULTS

Machine learning techniques are known to be applied in many areas [23,14, 21-37]. This article describes the application of EEG signals using some machine learning techniques. The aim of this study is to analyze EEG signals taken from healthy or sick people in different groups with some machine learning techniques and to automatically predict the classes of these patients with a computer aided system. In this study, EEG signals were used in 5 different groups. In this article, sym3 Wavelet Family and Decision Tree (DT) are used. The classification success rate for this article is low. The classification result was 39.2%. The Decision Tree classifier has not been found to be a suitable classifier method to recognize these EEG signals.

REFERENCES

[1] Demir, Ö., "EEG Dalgalarının Dalgacık (Wavelet) Dönüşümü İle Değerlendirilmesi", Yüksek Lisans Tezi, *Dumlupınar Üniversitesi Fen Bilimleri Enstitüsü,* Elektrik-Elektronik Mühendisliği Anabilim Dalı, Kütahya, (2008).

[2] Batar, H., "EEG İşaretlerinin Dalgacık Analizi Yöntemleri Kullanılarak Yapay Sininr Ağlarıyla Sınıflandırılması", Yüksek Lisans Tezi, *Sütçü İmam Üniversitesi Fen Bilimleri Enstitüsü,* Elektrik-Elektronik Mühendisliği Anabilim Dalı, Kahramanmaraş, (2005).

[3] Alkan, A., "Eeg İşaretlerinin Ayrıştırılmasında, Altuzay Yöntemlerinin Kullanılması", *Journal of Yaşar University*, 1(3), 211-213, (2006).

[4] Tosun, M., "Yapay Sinir Ağları yardımı ile EEG Tabanlı Anestezi Derinliği Tahmini için Yöntemler", Fen Bilimleri Enstitüsü, Balıkesir Üniversitesi, 2013.

[5] Li, X., Chu, M., Qiu, T. and Bao, H., "An EMD based time-frequency distribution and its application in EEG analysis", *Sheng Wu Yi Xue Gong Cheng Xue Za Zhi.*, 24(5), 990-995, (2007).

[6] Ye, S., Park, J., Kim, J., Jung, J., Jeon, A., Kim, I., et al., "Development for the Evaluation Index of an Anesthesia Depth using the Bispectrum Analysis", *International Journal of Biological and Medical Sciences*, 4, 67-70, (2009).

[7] Gunturkun, R., "Using Elman Recurrent Neural Networks with Conjugate Gradient Algorithm in Determining the Anesthetic the Amount of Anesthetic Medicine to be Applied", *J Med Syst*, 34, 479–484, (2010).

[8] Tawade, L. and Warpe, H., "Detection of Epilepsy Disorder Using Discrete Wavelet Transforms Using Matlabs", *International Journal of Advanced Science and Technology*, 28 , March (2011).

[9] Shaker, M.M., "EEG Waves Classifier using Wavelet Transform and Fourier Transform", *International Journal of Biological and Life Sciences,* 1:2, 85-90, (2005).

[10] Esmailie, V. and Assareh, A., “Estimating the depth of anesthesia using fuzzy soft computation applied to EEG Features”, *Intelligent Data Analysis,* 12, 393-407, (2008).

[11] Sweeney-Reed, C.M., Andrade, A.O. and Nasuto, S.J., “Empirical mode decomposition of EEG signals for synchronization analysis.”, *3rd IEEE EMBSS UK and RI postgradute conference in Biomedical Engineering and Medical Physics*, IEEE EMB Student Society UKRI, 15-16, (2004).

[12] Zhang, X., Roy, R.J. and Jensen, E.W. “EEG complexity as a measure of depth of anesthesia for patients”, *IEEE Transactions on Biomedical Engineering,* 48, (12), 1424-1433, (2011).

[13]Alçin,ÖmerF.,etal.“Multi-categoryEEGsignalclassification developing time-frequency texture features based Fisher Vector encoding method.” *Neurocomputing* 218 (2016): 251-258.

[14] Korkmaz, S. A., & Esmeray, F. (2018). Quality lignite coal detection with discrete wavelet transform, discrete fourier transform, and ANN based on k-means clustering method. 2018 6th International Symposium on Digital Forensic and Security (ISDFS,1-6, IEEE.

[15] Korkmaz, S. A., & Poyraz, M. (2014). A New Method Based for Diagnosis of Breast Cancer Cells from Microscopic Images: DWEE—JHT. Journal of medical systems, 38(9), 92.

[16] Karhan Z., Ergen B. (2016). Content based medical image classification using discrete wavelet and cosine transforms. (2015). *23nd Signal Processing and Communications Applications Conference (SIU)*, (pp:1445-1448)

[17] Sengur, A., Turkoglu, I., & Ince, M. C. (2007). Wavelet packet neural networks for texture classification. Expert systems with applications, **32(2),** 527-533.

[18] Sengur, A., Turkoglu, I., & Ince, M. C. (2008). Wavelet oscillator neural networks for texture segmentation. Neural Network World, **18(4),** 275.

[19] AKI M.O., Sürücü uykululuğunun gerçek Zamanlı Görüntü İşleme ve Makine Öğrenmesi Teknikleri ile Tespitine Yönelik Bir Sistem Tasarımı ve Uygulaması, Trakya Üniversitesi, Fen Bilimleri Enstitüsü.

[20] Özkan, Y., Veri madenciliği yöntemleri. 2008: Papatya Yayıncılık Eğitim.

[19] Korkmaz, Sevcan Aytac, and Hamidullah Binol. "Classification of molecular structure images by using ANN, RF, LBP, HOG, and size reduction methods for early stomach cancer detection." Journal of Molecular Structure 1156 (2018): 255-263..

[20] Korkmaz, S. A., Bínol, H., Akçiçek, A., & Korkmaz, M. F. (2017, September). A expert system for stomach cancer images with artificial neural network by using HOG features and linear discriminant analysis: HOG_LDA_ANN. In 2017 IEEE 15th International Symposium on Intelligent Systems and Informatics (SISY) (pp. 000327-000332). IEEE.

[21] Korkmaz, Sevcan Aytaç, and Furkan Esmeray. "A New Application Based on GPLVM, LMNN, and NCA for Early Detection of the Stomach Cancer." Applied Artificial Intelligence 32.6 (2018): 541-557.

[22] Korkmaz, Sevcan Aytac, and Mehmet Fatih Korkmaz. "A new method based cancer detection in mammogram textures by finding feature weights and using Kullback–Leibler measure with kernel estimation." Optik 126.20 (2015): 2576-2583.

[23] Korkmaz, S. A., Esmeray, F. (2018). "Classification with Random Forest Based on Local Tangent Space Alignment and Neighborhood Preserving Embedding for MSER features: MSER_DFT_LTSA-NPE_RF." International Journal of Modern Research in Engineering and Technology, 3.2:31-37.

[24] Korkmaz, Sevcan Aytaç, and Haluk Eren. "Cancer detection in mammograms estimating feature weights via Kullback-Leibler measure." 2013 6th international congress on image and signal processing (CISP). Vol. 2. IEEE, 2013.

[25] Korkmaz, Sevcan Aytac, Mehmet Fatih Korkmaz, and Mustafa Poyraz. "Diagnosis of breast cancer in light microscopic and mammographic images textures using relative entropy via kernel estimation." Medical & biological engineering & computing 54.4 (2016): 561-573.

[26] Korkmaz, Sevcan Aytac, et al. "Diagnosis of breast cancer nano-biomechanics images taken from atomic force microscope." Journal of Nanoelectronics and Optoelectronics 11.4 (2016): 551-559.

[27] Korkmaz, Sevcan Aytac, and Mustafa Poyraz. "Least square support vector machine and minumum redundacy maximum relavance for diagnosis of breast cancer from breast microscopic images." Procedia-social and behavioral sciences 174 (2015): 4026-4031.

[28] Korkmaz, Sevcan AYTAÇ. "Detecting cells using image segmentation of the cervical cancer images taken from scanning electron microscope." The Online Journal of Science and Technology-January 8.1 (2018): 47-53.

[29] Korkmaz, Sevcan Aytaç, et al. "Recognition of the stomach cancer images with probabilistic HOG feature vector histograms by using HOG features." 2017 IEEE 15th International Symposium on Intelligent Systems and Informatics (SISY). IEEE, 2017.

[30] Korkmaz, Sevcan Aytaç, et al. "New methods based on mRMR_LSSVM and mRMR_KNN for diagnosis of breast cancer from microscopic and mammography images of some patients." International Journal of Biomedical Engineering and Technology 19.2 (2015): 105-117.

[31] KORKMAZ, Sevcan AYTAÇ. "Variation of Driving Concentration with Driver Perceptionn through In-Car

View Road Scene as Visual Stimulant." The Online Journal of Science and Technology-July 7.3 (2017).

[32] Korkmaz, S. A., and F. Esmeray. "Classification with Random Forest Based on Local Tangent Space Alignment and Neighborhood Preserving Embedding for MSER features: MSER_DFT_LTSA-NPE_RF." International Journal of Modern Research in Engineering and Technology 3 (2018): 31-37.

[33] Korkmaz, S. Aytac, and Mustafa Poyraz. "Path planning for rescue vehicles via segmented satellite disaster images and GPS road map." 2016 9th International Congress on Image and Signal Processing, BioMedical Engineering and Informatics (CISP-BMEI). IEEE, 2016.

[34] Korkmaz, Sevcan Aytaç. "LBP Özelliklerine Dayanan Lokasyon Koruyan Projeksiyon (LPP) Boyut Azaltma Metodunun Farklı Sınıflandırıcılar Üzerindeki Performanslarının Karşılaştırılması." Sakarya University Journal of Science 22.4 (2018): 1101-1108.

[35] Korkmaz, Sevcan Aytaç. "Recognition of the Gastric Molecular Image Based on Decision Tree and Discriminant Analysis Classifiers by using Discrete Fourier Transform and Features." Applied Artificial Intelligence 32.7-8 (2018): 629-643.

CLASSIFICATION OF EEG SIGNALS BY ARTIFICIAL NEURAL NETWORKS

Furkan Esmeray[1]

CHAPTER 7

1 Electric and Energy Department Munzur University Tunceli, Turkey
furkanesmeray@munzur.edu.tr

CLASSIFICATION OF EEG SIGNALS BY ARTIFICIAL NEURAL NETWORKS

Furkan ESMERAY[1]

1. INTRODUCTION

The brain that controls the nervous system, stores all information, performs intelligence, comprehends, thinks, and decides emotional functions. Although the work on the brain has been going on for centuries, it has been a research field that forces the brain, doctors and scientists with a complex structure. Because the brain; many uncertainties, unknown and complicated structures. The human brain produces a variety of signals and these signals have been analyzed for many years, and at the same time, they have been proven to be proven. These signals are also called EEG or Electroencephalogram in the field of medicine [1]. Signs with low amplitude from the brain surface, which are detected by the electrodes, are called EEG signals. EEG signals produced by neurons are located in the cerebral cortex. Many different stimuli are responded by these signals. On the other hand, EEG signals; rhythms created by the rhythm centers located in the depths of the brain. These potentials are recorded with irregular variation and reflected on the skin. These signals obtained in the human brain store a lot of information, but are not yet fully exploited in unity. Because EEG signals have a low amplitude, it is difficult to reach this information. EEG examination today; is a method that is used to detect head trauma and sleep related illnesses, to determine the level of anesthesia of an anesthetized patient, to detect epilepsy, and to be cheap and not to suffer in many areas. However, evaluation of this information is limited due to the lack of certain values. Hence, the use of EEG markers in clinical

1 Electric and Energy Department Munzur University Tunceli, Turkey furkanesmeray@munzur.edu.tr

diagnostics has been made possible due to the analysis of EEG signals in the light of increasing technological developments. Brain; is a very important organ as well as diseases that can occur in the brain is affecting human life in a bad way. The use of these markers in the diagnosis and treatment of diseases in the brain is the reason for the resolution of the signs taken from the brain during treatment, which is a matter of intensive research in the scientific field in the near future [2]. Therefore, an objective evaluation can be made by analyzing the EEG signals by different methods. In the statistical analysis of signals some of these methods have been developed in recent years and others have been used to determine specific waveforms at the stage of decomposition and examination [3]. EEG recording and analysis methods are one of the most used methods in diagnosis and treatment of brain related diseases. In particular, increasing the recording times of EEG devices, recording a fixed disc by connecting to a computer, recording patients' EEG for one or more days or even weeks, and thus achieving healthier results than EEG analyzes is now possible. One of the earliest stages of the use of EEG, Karkov (1875) was the subject of more than 150 years of literature research, demonstrating a change in the amplitude of brain signals in the cortex despite an acoustic stimulus [4].

These methods have been applied based on the use of EEG signals in determining the depth of anesthesia by referring to many methods.

Mustafa Tosun and his colleagues designed an artificial neural network model using the entire frequency range covered by EEG signals (1-50 Hz). He also trained 94% of the level of successful anesthesia with heart rate with this model [4].

Laxman Tawade et al. the detection of epilepsy disorder was investigated by using the Discrete Wavelet Transform method in EEG signals. They were arrested with a success rate of 96% [5].

Soo-young Ye et al. in their study, 20-50 value of Bispectrum index ranged between 0-100 value, anesthesia was specified, the alertness of 60-100 value and EEG frequency range in determining the depth of anesthesia was reported to be below 8 Hz [6].

Li X et al. have achieved a successful outcome using an experimental Kip decomposition-based method of epileptic EEG signals. The results obtained can be divided into numerical and small Numerical Mode Functions of non-stationary complex signs [7].

C.M. Sweeney-Reed et al. used the Empirical Mode Decomposition method to demonstrate that it is possible to reach the desired frequency band on EEG signals. With the method they used, the desired bandwidth IQ functions were synchronized with the EEG signals [8].

Maan M. Shaker reported that as a result of using Discrete Wavelet Transform and Fourier transforms in his studies on EEG signals, he obtained very successful results of delta, tetra, alpha and beta classes by classifying noise canceling EEG signals with Discrete Wavelet Transform and separating EEG waves [9].

Zhang X et al. They proposed an EEG derivative model (Lembel-Ziv Complexity Analysis) based on the relationship between depth of anesthesia and brain activity, and this model, which was proposed to determine the depth of anesthesia, achieved a real-time success rate of 93% [10].

In a study on the anesthesia level of Rüştü Güntürk, 30 neurons in the middle layer and 60 neurons in the input layer were trained using the Power Spectral Intensities of the Elman network EEG signals in the 1-50 Hz frequency range, and the level of anesthesia was found. At the end of the study, 95% success was achieved [11].

V. Esmaeilia et al. Developed a fuzzy logic structure based on EEG to determine the depth of anesthesia and conducted a study to achieve the goal of 4 grouping (awake anesthesia compliance, intraoperative anesthesia, and isolation) on single-channel EEG data [12].

2. THEORY AND METHODS

In this study; The aim of this course is to analyze EEG signals belonging to healthy and sick people in different groups with some machine learning techniques and also to be able to predict which classes they belong to with a computer aided system. In this study, EEG signals were used in 5 different groups.

2.1. Rbio5.5 Wavelet Family

Discrete wavelet transform, signal processing, biomedical signal processing, and data mining are widely used to extract many different field features [14,15]. The Discrete Wavelet Transform (DWT) is the sum of the signal that is multiplied by its offset values and scaled over the time domain of the wavelet. The DWT function is used at the desired level for the signal and image [14, 15]. The DWT method allows to obtain the distinguishing characteristics of the signal by analyzing the low frequency component in the low frequency range and the high frequency component in a narrower range. The mathematical expression of the subbands obtained using DWT is given by Equation (1) [14, 16].

$$F_{BF}(u,v) = DWT\{F(x,y), B \in \{CA, YA, AY, YY\}, 1 < F < 4\} \quad (1)$$

YA, AY, YY express the detail coefficients of the operation, while in the decomposition of these sub-bands, express the approximate coefficients of the operation [14, 16-18]. The coefficient of detail is horizontal, vertical and diagonal. The DWT approach data can be resumed in a similar way. Approximate coefficients are used in this article. There is no algorithm in determining the wavelet family that should be selected in the studies. In the time domain, the main wavelet is more visually similar to the signal to be processed, resulting in greater efficiency than the wavelet transform method. But it seems almost impossible to make a choice like this. For this reason, all wavelet family types should be tried.In this study, the rbio5.5 wavelet family was used [14, 18].

2.2. Artificial Neural Network

ANN has the ability to respond to samples that are not encountered during training by training the ANN. Even if only part of the access to a trained network is provided, the network can select the one closest to the access from memory. So it assumes that it has received full logon data. Finally, it produces a uniform output value. Even if the data is corrupted, incomplete; the network that has never been seen before will provide optimal output. This feature is due to the generalization of the network. Depending on the neural network, simulation and distortion calculations can be tested by applying them in MATLAB or MEX programs. In this study, the calculations were tested using MEX. The structure of ANN used in this study consists of Cross Entropy and Scaled Conjugate Grade.

Cross-Entropy

In this article, cross-entropy method is used for the suitability of performance of artificial neural network classifier. Cross Entropy is used to calculate the network performance of a specific target and output. Reducing cross entropy to the smallest size provides good classification requirements. Cross-entropy is a method used for each pair of output-target elements. Total cross-entropy performance is calculated by averaging individual data [19,21].

Scaled Conjugate Gradient Method

In this article, the Scaled Conjugate Gradient method is used to train an artificial neural network classifier. Depending on the weight of the network and a versatile function; Minimizing the function of cosmic error, neural network learning be attached to on the optimization perspective. The gradient descent algorithm is based on the use of most training algorithms [19-20].

3.RESULTS

It has been applied to many areas using machine learning techniques [14,22-35]. In this study, some machine learning techniques have been applied to EEG signals. As a result of this study, EEG signals from different groups of healthy and sick people were analyzed with some machine learning techniques. Thus, it is aimed to automatically classify with a computer aided system. In this study, EEG signals in 5 different groups were used. The rbio5.5 Wavelet Family and Artificial Neural Network classifier were used as the method of this study. The classification success rate was 84.21%.

REFERENCES

[1] Demir, Ö., "EEG Dalgalarının Dalgacık (Wavelet) Dönüşümü İle Değerlendirilmesi", Yüksek Lisans Tezi, *Dumlupınar Üniversitesi Fen Bilimleri Enstitüsü,* Elektrik-Elektronik Mühendisliği Anabilim Dalı, Kütahya, (2008).

[2] Batar, H., "EEG İşaretlerinin Dalgacık Analizi Yöntemleri Kullanılarak Yapay Sininr Ağlarıyla Sınıflandırılması", Yüksek Lisans Tezi, *Sütçü İmam Üniversitesi Fen Bilimleri Enstitüsü,* Elektrik-Elektronik Mühendisliği Anabilim Dalı, Kahramanmaraş, (2005).

[3] Alkan, A., "Eeg İşaretlerinin Ayrıştırılmasında, Altuzay Yöntemlerinin Kullanılması", Journal of Yaşar University, 1(3), 211-213, (2006).

[4] Tosun, M., "Yapay Sinir Ağları yardımı ile EEG Tabanlı Anestezi Derinliği Tahmini için Yöntemler", Fen Bilimleri Enstitüsü, Balıkesir Üniversitesi, 2013.

[5] Tawade, L. and Warpe, H., "Detection of Epilepsy Disorder Using Discrete Wavelet Transforms Using Matlabs", International Journal of Advanced Science and Technology, 28 , March (2011).

[6] Ye, S., Park, J., Kim, J., Jung, J., Jeon, A., Kim, I., et al., "Development for the Evaluation Index of an Anesthesia Depth using the Bispectrum Analysis", International Journal of Biological and Medical Sciences, 4, 67-70, (2009).

[7] Li, X., Chu, M., Qiu, T. and Bao, H., "An EMD based time-frequency distribution and its application in EEG analysis", Sheng Wu Yi Xue Gong Cheng Xue Za Zhi., 24(5), 990-995, (2007).

[8] Sweeney-Reed, C.M., Andrade, A.O. and Nasuto, S.J., "Empirical mode decomposition of EEG signals for synchronization analysis.", 3rd IEEE EMBSS UK and RI postgradute conference in Biomedical Engineering and Medical Physics, IEEE EMB Student Society UKRI, 15-16, (2004).

[9] Shaker, M.M., "EEG Waves Classifier using Wavelet Transform and Fourier Transform", International Journal of Biological and Life Sciences, 1:2, 85-90, (2005).

[10] Zhang, X., Roy, R.J. and Jensen, E.W. "EEG complexity as a measure of depth of anesthesia for patients", IEEE Transactions on Biomedical Engineering, 48, (12), 1424-1433, (2011).

[11] Gunturkun, R., "Using Elman Recurrent Neural Networks with Conjugate Gradient Algorithm in Determining the Anesthetic the Amount of Anesthetic Medicine to be Applied", J Med Syst, 34, 479–484, (2010).

[12] Esmailie, V. and Assareh, A., "Estimating the depth of anesthesia using fuzzy soft computation applied to EEG Features", Intelligent Data Analysis, 12, 393-407, (2008).

[13] Alçin, Ömer F., et al. "Multi-category EEG signal classification developing time-frequency texture features based Fisher Vector encoding method." Neurocomputing 218 (2016): 251-258.

[14] Korkmaz, S. A., & Esmeray, F. (2018). Quality lignite coal detection with discrete wavelet transform, discrete fourier transform, and ANN based on k-means clustering method. 2018 6th International Symposium on Digital Forensic and Security (ISDFS,1-6, IEEE.

[15] Korkmaz, S. A., & Poyraz, M. (2014). A New Method Based for Diagnosis of Breast Cancer Cells from Microscopic Images: DWEE—JHT. Journal of medical systems, **38(9),** 92.

[16] Karhan Z., Ergen B. (2016). Content based medical image classification using discrete wavelet and cosine transforms. (2015). 23nd Signal Processing and Communications Applications Conference (SIU), (pp:1445-1448)

[17] Sengur, A., Turkoglu, I., & Ince, M. C. (2007). Wavelet packet neural networks for texture classification. Expert systems with applications, **32(2),** 527-533.

[18] Sengur, A., Turkoglu, I., & Ince, M. C. (2008). Wavelet oscillator neural networks for texture segmentation. Neural Network World, **18(4),** 275.

[19] Korkmaz, Sevcan Aytac, and Hamidullah Binol. "Classification of molecular structure images by using ANN, RF, LBP, HOG, and size reduction methods for early stomach cancer detection." Journal of Molecular Structure 1156 (2018): 255-263..

[20] Korkmaz, S. A., Bínol, H., Akçiçek, A., & Korkmaz, M. F. (2017, September). A expert system for stomach cancer images with artificial neural network by using HOG features and linear discriminant analysis: HOG_LDA_ ANN. In 2017 IEEE 15th International Symposium on Intelligent Systems and Informatics (SISY) (pp. 000327-000332). IEEE.

[21] Turkoglu, I. (2007). Hardware implementation of varicap diode's ANN model using PIC microcontrollers. Sensors and Actuators A: Physical, 138(2), 288-293.

[22] Korkmaz, Sevcan Aytac, and Mehmet Fatih Korkmaz. "A new method based cancer detection in mammogram textures by finding feature weights and using Kullback–Leibler measure with kernel estimation." Optik 126.20 (2015): 2576-2583.

[23] Korkmaz, Sevcan Aytaç, and Furkan Esmeray. "A New Application Based on GPLVM, LMNN, and NCA for Early Detection of the Stomach Cancer." Applied Artificial Intelligence 32.6 (2018): 541-557.

[24] Korkmaz, Sevcan Aytac, et al. "Diagnosis of breast cancer nano-biomechanics images taken from atomic force microscope." Journal of Nanoelectronics and Optoelectronics 11.4 (2016): 551-559.

[25] Korkmaz, Sevcan Aytac, Mehmet Fatih Korkmaz, and Mustafa Poyraz. "Diagnosis of breast cancer in light microscopic and mammographic images textures using relative entropy via kernel estimation." Medical & biological engineering & computing 54.4 (2016): 561-573.

[26] Korkmaz, Sevcan Aytaç, and Haluk Eren. "Cancer detection in mammograms estimating feature weights via Kullback-Leibler measure." 2013 6th international congress on image and signal processing (CISP). Vol. 2. IEEE, 2013.

[27] Korkmaz, Sevcan Aytac, and Mustafa Poyraz. "Least square support vector machine and minumum redundacy maximum relavance for diagnosis of breast cancer from breast microscopic images." Procedia-social and behavioral sciences 174 (2015): 4026-4031.

[28] Korkmaz, Sevcan AYTAÇ. "Detecting cells using image segmentation of the cervical cancer images taken from scanning electron microscope." The Online Journal of Science and Technology-January 8.1 (2018): 47-53.

[29] KORKMAZ, Sevcan AYTAÇ. "Variation of Driving Concentration with Driver Perceptionn through In-Car View Road Scene as Visual Stimulant." The Online Journal of Science and Technology-July 7.3 (2017).

[30] Korkmaz, Sevcan Aytaç, et al. "New methods based on mRMR_LSSVM and mRMR_KNN for diagnosis of breast cancer from microscopic and mammography images of some patients." International Journal of Biomedical Engineering and Technology 19.2 (2015): 105-117.

[31] Korkmaz, Sevcan Aytaç. "LBP Özelliklerine Dayanan Lokasyon Koruyan Projeksiyon (LPP) Boyut Azaltma Metodunun Farklı Sınıflandırıcılar Üzerindeki Performanslarının Karşılaştırılması." Sakarya University Journal of Science 22.4 (2018): 1101-1108.

[32] Korkmaz, Sevcan Aytaç, et al. "Recognition of the stomach cancer images with probabilistic HOG feature vector histograms by using HOG features." 2017 IEEE 15th International Symposium on Intelligent Systems and Informatics (SISY). IEEE, 2017.

[33] Korkmaz, S. Aytac, and Mustafa Poyraz. "Path planning for rescue vehicles via segmented satellite disaster images and GPS road map." 2016 9th International Congress on

Image and Signal Processing, BioMedical Engineering and Informatics (CISP-BMEI). IEEE, 2016.

[34] Korkmaz, Sevcan Aytaç. "Recognition of the Gastric Molecular Image Based on Decision Tree and Discriminant Analysis Classifiers by using Discrete Fourier Transform and Features." Applied Artificial Intelligence 32.7-8 (2018): 629-643.

[35] Korkmaz, S. A., and F. Esmeray. "Classification with Random Forest Based on Local Tangent Space Alignment and Neighborhood Preserving Embedding for MSER features: MSER_DFT_LTSA-NPE_RF." International Journal of Modern Research in Engineering and Technology 3 (2018): 31-37.

PRODUCTION METHODS OF DISCONTINUOUS AND CONTINUOUS ELECTROSPUN NANOFIBER YARNS

Behzat YILDIRIM[1], Halil İbrahim İÇOĞLU[2], Ali KILIÇ[3], Mehmet TOPALBEKİROĞLU[4]

CHAPTER 8

1 Department of Textile Engineering, Gaziantep University, Gaziantep, 27310, Turkey
2 Department of Metallurgical and Materials Engineering, Gaziantep University, Gaziantep, 27310, Turkey
3 Department of Mechanical Engineering, Gaziantep University, Gaziantep, 27310, Turkey
4 Department of Textile Engineering, Gaziantep University, Gaziantep, 27310, Turkey

PRODUCTION METHODS OF DISCONTINUOUS AND CONTINUOUS ELECTROSPUN NANOFIBER YARNS

Behzat YILDIRIM[1], Halil İbrahim İÇOĞLU[2], Ali KILIÇ[3], Mehmet TOPALBEKİROĞLU[4]

1. INTRODUCTION

Nanofibers can be defined as the fibers having a diameter under 100 nm. The fibers having a diameter under 1 μm are also accepted as nanofibers. Nanofibers have advantageous characteristics such as high specific surface area, excellent porosity [1]. Although nanofibers can be produced by various methods, electrospinning is the most common method due to its simplicity, set up flexibility and suitability to production in mass scale [2].

In electrospinning method polymer fluid is drawn as a thin filament under high electrical field and is collected randomly on a collector in nonwoven mat formation. When the applied voltage overcomes the surface tension of the polymer fluid at the tip of the needle, firstly Taylor cone then a thin jet are formed. This jet reaches to the collector by following firstly straight route then spiral route under high electrical field [3]. Various polymers can be used in this method. Basic electrospinning set up is given in Figure 1.

1 Department of Textile Engineering, Gaziantep University, Gaziantep, 27310, Turkey
2 Department of Metallurgical and Materials Engineering, Gaziantep University, Gaziantep, 27310, Turkey
3 Department of Mechanical Engineering, Gaziantep University, Gaziantep, 27310, Turkey
4 Department of Textile Engineering, Gaziantep University, Gaziantep, 27310, Turkey

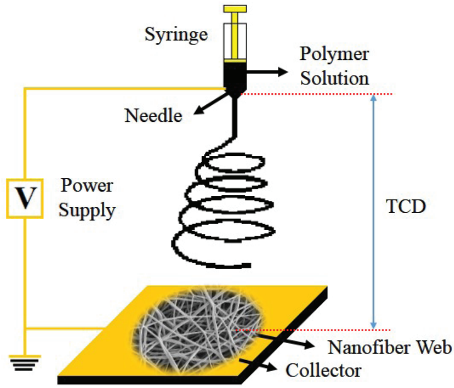

Figure 1. *Schematic diagram of a basic electrospinning set-up*

The recent studies about electrospinning have focused on especially nanofiber characterization using of new materials and new application areas of nanofibers. Furthermore, it is very important that electrospinning device can be manufactured in different set-ups for revealing all of the potential of nanofibers. Because the set-up has critical effect on the performance of nanofibers [4]. Electrospinning method principally comes from the study of Formhals in 1934. Several patents about electrospinning set-ups for nanofiber production by using electrostatic forces were obtained [5-8]. There has been a tremendous increase on the nanofiber studies since 2000s.

There are some limitations in applications of nanofibers because of the production of nanofibers as nonwoven mat formation. Nanofibers couldn't be used in the areas of conventional yarns. Hence, the idea about production of nanofiber yarn has emerged. Some researchers applied various modifications on electrospinning set-up to improve application areas of nanofibers. Some reviews were published on the production of electrospun nanofiber yarns by Zhou and Gong [9], Ali et al. [10], Abbasipour and Khavaji [11], Shuakat and Lin [12], O'conner et al. [13], Wei and Qin [14] and Göktepe and Mülayim [15].

When electrospun nanofiber yarn studies are investigated, the nanofiber yarns can be classified as continuous and discontinuous in terms of the winding mechanism and also classified as twisted and non-twisted in terms of twisting mechanism. In this study, nanofiber yarns are investigated according to the properties of modified electrospinning set-ups instead of the product that focused on the previous review studies. How to produce of different type of nanofiber yarns by using the related modified electrospinning set up is focused on in this study instead of type of nanofiber yarn such as continuous-discontinuous or twisted-non-twisted form. If the modified set up has an integrated twisting and winding mechanisms, that system is classified as continuous and twisted. However, if there is an additional winding or twisting mechanism, those studies are classified as discontinuous or non-twisted. Concisely, classification is made by the type of yarn produced by electrospinning set up without additional process. Totally 120 recent research studies about electrospun nanofiber yarns are comparatively analyzed in terms of countries, years and product types.

2. NANOFIBER BUNDLES

Nanofiber yarns are linear form of merging of numerous nanofibers. This process can be divided as two parts: the production of uniaxially aligned nanofiber bundles, the drawing of those bundles with or without twisting. Mechanical performance dramatically increases after twisting of uniaxially aligned nanofibers similar to conventional yarns. Low twist adversely affects the strength of nanofiber yarns like that of conventional yarns [11].

Although nanofiber bundles were accepted as nanofiber yarns in some early studies, they have to be classified in different manner due to increase of the related studies. Because, yarns are generally defined as twisting of uniaxially aligned fibers. Concisely, nanofiber yarns and nanofiber bundles have actually different meanings [12]. Figure 2 shows the general classification of nanofiber bundles. Nanofiber bundles are firstly divided into two groups as continuous and discontinuous. Also each of the group is classified as twisted and non-twisted forms according to the presence of twisting unit in electrospinning set-up.

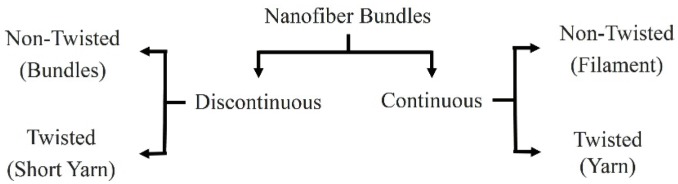

Figure 2. *Classification of nanofiber bundles*

2.1. Discontinuous Methods

There has been a great effort to produce nanofiber yarns in electrospinning system in the recent studies. The early studies were focused on short nanofiber bundles with or without twisting. Although they described that forms as yarns, those forms are actually out of general yarn definition [12]. Nanofibers are generally collected as randomly aligned mat formation on fixed flat collector in electrospinning method. However, discontinuous nanofiber bundles or short twisted yarns instead of nanofiber mats can be produced by manipulation of electrical field, moving collector or twisting mechanisms [10].

2.1.1. Discontinuous and non-twisted short nanofiber bundles

The earliest studies on nanofiber yarn production in electrospinning method were focused on uniaxially alignment of nanofibers. Nanofiber bundles can be produced by modification of electrical field or using different type of collector. This system is based on the principle of collection of nanofibers on a specific pattern or parallel alignment. The electrospinning set-ups, the nanofiber bundle morphologies and other important properties of those studies are given by years in Table 1.

Table 1. *Discontinuous and non-twisted nanofiber bundles*

Author(s)	Electrospinning System	Yarn Morphology	Technical Specifications
Deitzel et al. [16]	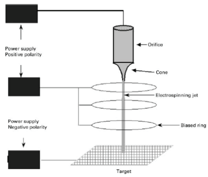	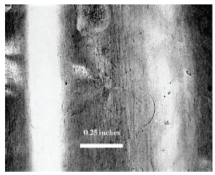	*Polymer;* PEO *App. vol.;* 20 kV *Feed rate;* 0.125 mL/h *TCD;* 20 cm
Theron et al. [17]	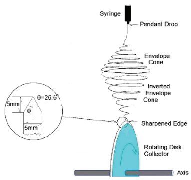	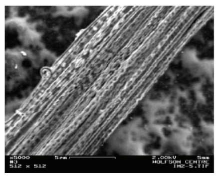	*Polymer;* PEO *App. vol.;* 8.5 kV *TCD;* 15 cm
El-Aufy [18]	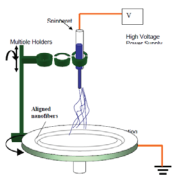	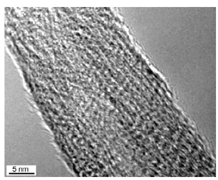	*Polymer;* PEDT/PSS *App. vol.;* 25 kV *TCD;* 15-20 cm
Fennessey et al. [19]	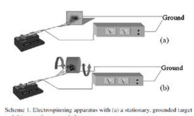	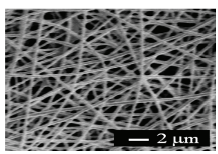	*Polymer;* PAN *App. vol.;* 8-16 kV *Feed rate;* 1.18 g/mL *TCD;* 13-16 cm
Teo et al. [20]	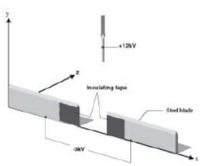	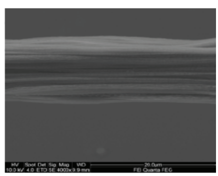	*Polymer;* PCL *App. vol.;* 14 kV *Feed rate;* 1 mL/h *TCD;* 12 cm

Okuzaki et al. [21]	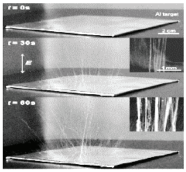	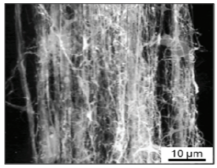	*Polymer;* PXTC *App. vol.;* 20 kV *TCD;* 20 cm
San Choi et al. [22]	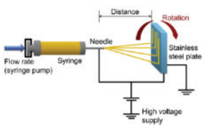	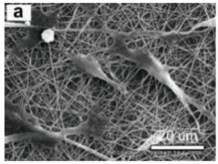	*Polymer;* PCL *App. vol.;* 20 kV *Feed rate;* 3 mL/h *TCD;*10 cm
Maheshwari et al. [23]	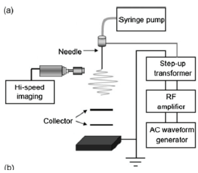	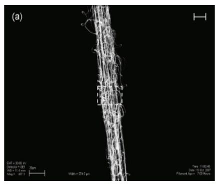	*Polymer;* PVP *App. vol.;* 2.23-3.3 kV *Feed rate;* 0.15-0.5 mL/h *TCD;* 2-4 cm
Chvojka et al. [24]	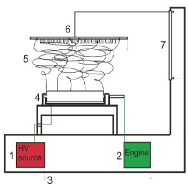	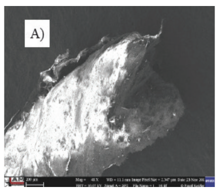	*Polymer;* PVA *App. vol.;* 45 kV *TCD;* 12 cm
Tsai [25] Bae et al. [26]	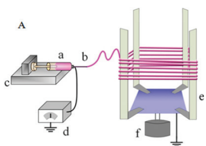	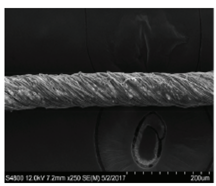	*Polymer;* CA, PMMA, PAN, PVDF, PEO, PLGA *App. vol.;* 10-12 kV *Feed rate;* 0.25–0.30 mL/h *TCD;* 20-30 cm
Chawla et al. [27]	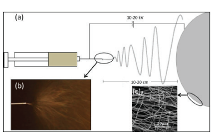	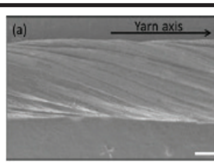	*Polymer;* PAN *App. vol.;* 16 kV *Feed rate;* 1 mL/h *TCD;* 20 cm

Bosworth [28]	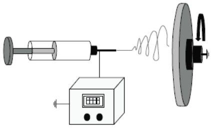	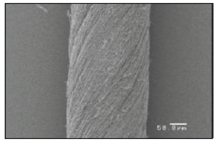	*Polymer;* PCL, PLGA *App. vol.;* 20 kV *Feed rate;* 1 mL/h *TCD;* 20 cm
Barua [29] Barua et al. [30]	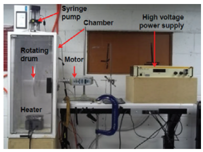	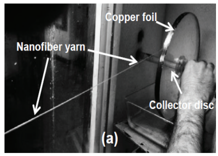	*Polymer;* PAN *App. vol.;* 15 kV *Feed rate;* 10-32 µL/min *TCD;* 18 cm
Baniasadi et al. [31]	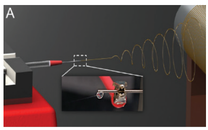	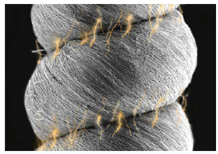	*Polymer;* PVDF-TrFE *Conc.;* %20 *App. vol.;* 25 kV *TCD;* 25 cm
Mehrpouya et al. [32] Chen et al. [33]	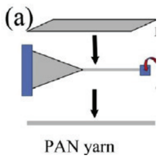	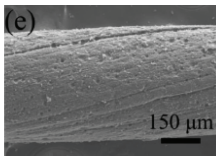	*Polymer;* PAN, PVA *App. vol.;* 15-18 kV *TCD;* 15 cm *Feed rate;* 0-1 mL/h
Kim et al. [34]	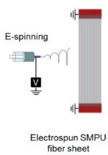	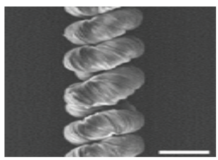	*Polymer;* PU *App. vol.;* 18 kV *TCD;* 20 cm *Feed rate;* 13 µl/min

Deitzel et al. [16] was used three rings with equal distances between needle and collector to control the electrical field. While positive voltage was applied to the rings and the needle, negative voltage was applied to the collector. Hence they controlled the electrical field due to the rings and directed nanofibers to the specific area on the collector.

Theron et al. [17] was used a rotating disc for alignment of the nanofibers. When they reached enough amount of aligned nanofibers on the disc, they took up the nanofiber bundles. The studies of Chawla et al. [27], Barua [29] and Barua et al. [30] are similar to that method. However Chawla [27], Barua [29] and Barua et al. [30] were used smoother edged disc while Theron et al. [17] was used sharp edged disc. Chawla et al. [27] was also used an additionally twisting apparatus. Barua [29] and Barua et al. [30] were used an additionally winding apparatus. Bosworth et al. [24] was also used a horizontally rotating disc. Rotation of the disc provides alignment of nanofibers. Similarly El-Aufy [18] was used a horizontally rotating disc but with vertical edges. The nanofibers are firstly collected on rotating disc then is directed to the edges of the disc under centrifugal force. Hence parallel aligned nanofiber bundles are obtained. Fennessey et al. [19] used a rotating drum collector instead of disc in their study. The drum rotates continuously to align nanofibers collected. The nanofibers are taken up when they reach enough amount by cutting and nanofiber bundles are obtained. Similar study was performed by Baniasadi et al. [31]. Teo et al. [20] used sharp edged knives as collectors to align nanofibers. The nanofibers are collected between two knives located at the same level with a particular gap distance. When the nanofibers reach enough amount, they are taken up as nanofiber bundles. Okuzaki et al. [21] used poly(p-xylenetetrahydrothiophenium chloride) (PXTC) polymer to align nanofibers. PXTC nanofibers are collected on collectors as vertically unlike other polymers which are collected as horizontally. The nanofiber bundles at specific length depending on the tip to collector distance are obtained. San Choi et al. [22] used rotating plate collector for alignment of nanofibers. The plate rotates right and left to collect the nanofibers in specific positions during electrospinning. Maheshwari et al. [23] used AC power supplier instead of DC one. The researchers reported that AC overcome the limitations of DC on alignment of the nanofibers collected in electrospinning. They mentioned that the nanofibers escaped from electrical field control after a certain distance during electrospinning and they were able to get aligned easily by manually or pneumatically. Also they collected nanofibers as uniaxially aligned by using parallel electrode collectors in their study. Kim et al. [34] used also parallel electrode collectors but with DC power supplies. The nanofibers collected uniaxially aligned between parallel electrodes were taken up and were twisted additionally. Chvojka et al. [24] used a copper saw-like collector in the needleless electrospinning set-up. Saw-like collector both provides the alignment of the nanofibers and facilitates taken up the nanofibers collected on the collector. Tsai [25] and Bae et al. [26] used four aluminum rods vertically mounted on the corners of a constantly rotating plate as collector. The nanofibers are collected around the rods. When the nanofibers reach enough amount, they are taken up by cutting and then twisting is applied additionally. Mehrpouya et al. [32] and Chen et al. [33] used the electrospinning set-up with a drum collector. They applied additionally twisting after taking up the nanofiber bundles collected on the drum at the end of the electrospinning. Chen et al. [33] used also aluminum foil on the surface of the drum to facilitate to take up the nanofibers. In this simple method, the length of the nanofiber bundles is depended on the diameter of the drum.

2.1.2. Discontinuous and twisted short nanofiber yarns

Mechanical properties of yarns are enhanced by twisting. Before twisting, nanofibers have to be uniaxially aligned formation. In this group of nanofiber yarns, twisting is both applied during electrospinning and controllable. Twist level can be increased or decreased in different directions. The electrospinning set-ups, the nanofiber yarn morphologies and other important properties of those studies are given by years in Table 2. The twisting in these systems are applied by rotating of ring collectors, hollow hemisphere collector, needle collector, disc plate collector, needle as feeding unit and manipulation of electrical field.

Table 2. *Discontinuous and twisted nanofiber bundles*

Author(s)	Electrospinning System	Yarn Morphology	Specifications
Dalton et al. [35]	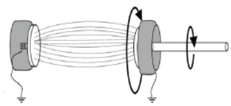	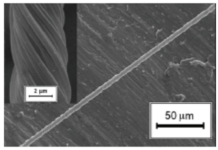	*Polymer;* PCL *App. vol.;* 15 kV *Feed rate;* 0,1 mL/h *TCD;* 15 cm
Liu et al. [36]	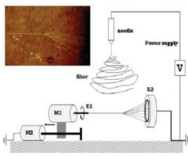	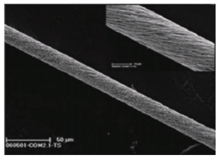	*Polymer;* PMMA *App. vol.;* 6,4 kV *TCD;*; 10 cm
Gu et al. [37]	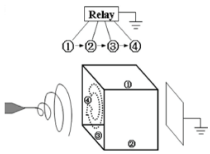	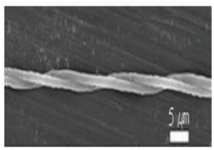	*Polymer;* PEO *App. vol.;* 8 kV *Feed rate;* 7 mL/min *TCD;* 13 cm
Lotus et al. [38]	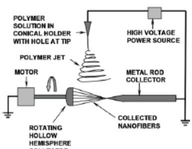	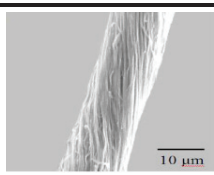	*Polymer;* PVP *App. vol.;* 10-15 kV *TCD;* 25 cm
Chang et al. [39]	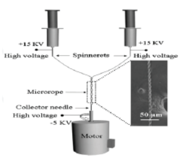	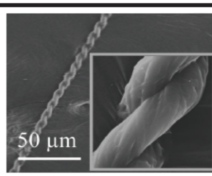	*Polymer;* PVP *App. vol.;* 20 kV *TCD;* 10 cm
Paneva et al. [40]	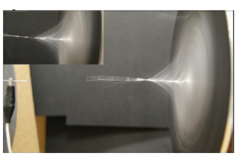	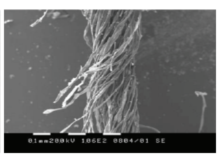	*Polymer;* Chitosan *App. vol.;* 38 kV *Feed rate;* 1,1 mL/h *TCD;* 15 cm
Chang et al. [41]	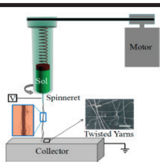	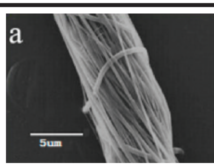	*Polymer;* PVP, PES *App. vol.;* 20 kV *TCD;* 5 cm

Dalton et al. [35] used a pair of ring collectors to collect and twist of electrospun nanofibers. The nanofibers collected between the rings are twisted by continuously rotating motion of one of the rings. The gap distance between rings affects the properties of the nanofiber yarn. Liu et al. [36] used a rotating funnel type collector in their study. Nanofibers are firstly collected on the inner surface of the cone shape collector, then get aligned with due to the structure of the collector which is getting narrower and are also twisted by rotation of the funnel collector. Gu et al. [37] used two conjugate pairs of electrodes in a rectangular formation between the tip and the collector to twist the nanofibers. During electrospinning, one of the electrodes is activated with power supply for a period of moment, then the activation passes the next electrode and go on in a regular pattern. Hence, a spiral electrostatic field is obtained and that twist nanofibers. In this method, controlling of nanofibers are difficult due to the complicated system. Lotus et al. [38] used rotating hollow hemisphere collector for alignment and twisting of nanofibers. Chang et al. [39] used positively charged two feeding systems and negatively charged needle collector. The nanofiber pairs are merged on the needle collector and twisted nanofibers are obtained by rotation of the collector. Paneva et al. [40] used a rotating disc collector horizontally located in the electrospinning set-up. The nanofibers are twisted while being collected by rotation of the disc. The disc speed defines the twist level of the nanofiber yarn. Chang et al. [41] used a rotating needle in the feeding system while using of a fixed collector unlike the other studies. Twisting is obtained by rotation of the feeding needle. The limitation of this system is the low rotation speed of the feeding needle.

2.2. Continuous Methods

Two types of continuous nanofiber bundles are produced with the electrospinning set-up. Non-twisted nanofiber bundles are also referred to herein as filament yarns, while twisted continuous nanofiber bundles meet all the characteristics of conventional yarns. Having a winding apparatus integrated into the system has taken the electrospinning device to the continuous nanofiber yarn class. Depending on the presence or absence of a twisting unit in the system, twisted/non-twisted classification is made. The system is suitable for a continuous nanofiber yarn production if the twisting unit twists the fiber bundles during electrospinning.

2.2.1. Continuous and non-twisted filament nanofiber bundles

Continuous nanofiber bundles can be defined as non-twisted uniaxially aligned nanofibers [10]. The electrospinning set-ups, the nanofiber yarn morphologies and other important properties of those studies are given by years in Table 3. The main feature of these techniques is fiber alignment and winding. While continuous form is advantage, non-twist form is a disadvantage because it is very difficult to hold together of nanofibers. Different techniques are applied in the studies to ensure that the system is continuous. In these studies, liquid bath, double or multiple needles, rollers, discs, funnels, conveyors are used to provide a continuous nanofiber production.

Table 3. *Continuous and non-twisted nanofiber filament bundles*

Author(s)	Electrospinning System	Yarn Morphology	Specifications
Smit et al. [42] Khil et al. [43]	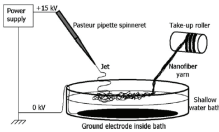	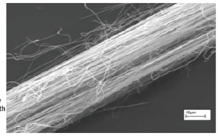	*Polymer;* PCL, PVDF, PAN, PVAc *App. vol.;* 15 kV *Feed rate;* 1 mL/h *TCD;* 18 cm
Pan et al. [44] Yao et al. [45] Ma et al. [46]	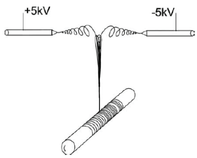	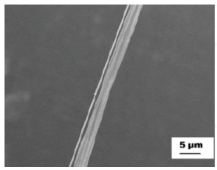	*Polymer;* PVA, PVP, PLLA, P(LLA-CL) *App. vol.;* 10-20 kV *Feed rate;* 5-15 mL/h *TCD;* 10-20 cm
Li et al. [47]	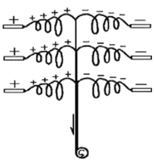	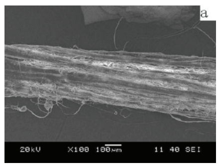	*Polymer;* PLLA *App. vol.;* 10 kV *Feed rate;* 5 mL/h *TCD;* 40 cm
Wang et al. [48] Wang et al. [49] Zhang et al. [50]	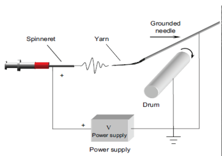	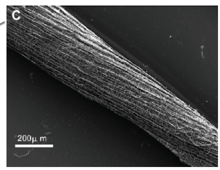	*Polymer;* PHBV, PAN, PLLA, PMIA *App. vol.;* 9-18 kV *Feed rate;* 8-20 mL/min *TCD;* 15 cm
Mondal et al. [51]	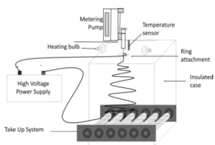	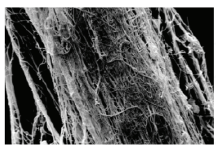	*Polymer;* PAN *App. vol.;* 40 kV *Feed rate;* 0.2 mL/h *TCD;* 10 cm
Kim et al. [52]	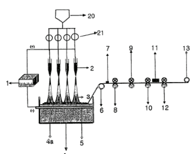	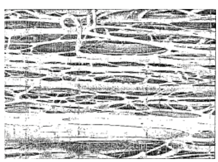	*Polymer;* PCL, PA6, PES, PVA, PU *App. vol.;* 20-30 kV *TCD;* 5-10 cm

Kim [53]	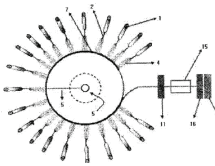	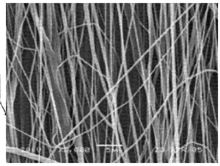	*Polymer;* PA6, PA66 *App. vol.;* 35 kV *TCD;* 12 cm
Kim et al. [54]	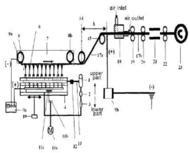	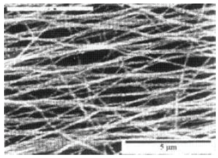	*Polymer;* PU *App. vol.;* 28-35 kV *Feed rate;* 1.2-2.0 mL/h *TCD;* 16-20 cm
Li et al. [55]	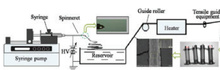	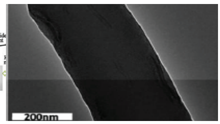	*Polymer;* PA6 *App. vol.;* 16-24 kV *TCD;* 6 cm
Pokorny et al. [56]	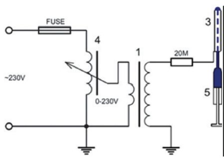	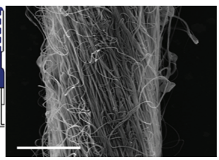	*Polymer;* PVP, PAN *App. vol.;* 30 kV *Feed rate;* 80-180 mL/h *TCD;* 15 cm
Tian et al. [57]	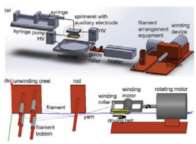	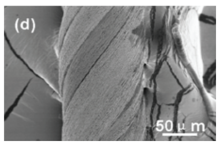	*Polymer;* PA6 *App. vol.;* 26 kV *Feed rate;* 1.5 mL/h *TCD;* 6 cm
Mouthuy et al. [58] Abhari et al. [59]	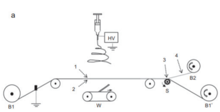	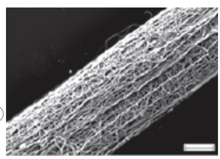	*Polymer;* PDO *App. vol.;* 7.2-8.6 kV *Feed rate;* 0.8 mL/h *TCD;* 20 cm
Wang et al. [60] Wu et al. [61]	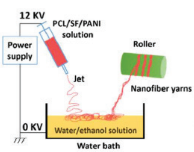	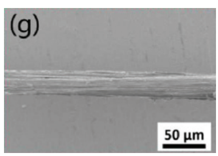	*Polymer;* PCL, SF, PANI *App. vol.;* 12 kV *TCD;* 15 cm *Feed rate;* 1 mL/h

Yan et al. [62] Yan et al. [63] Yan et al. [64] Yan et al. [65] Wang et al. [66]	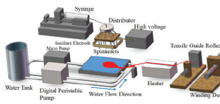	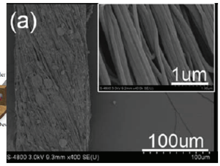	*Polymer;* PAN *App. vol.;* 17-35 kV *TCD;* 9 cm *Feed rate;* 4-100 mL/min
Jiang et al. [67]	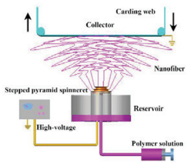		*Polymer;* PAN *App. vol.;* 50 kV *Feed rate;* 3 mL/min *TCD;* 15 cm
Kangazian Kangazi et al. [68]	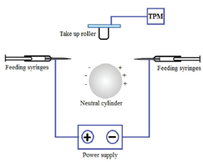	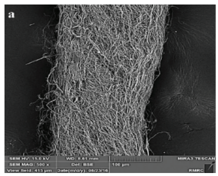	*Polymer;* PVA *App. vol.;* 40 kV *TCD;* 19 cm *Feed rate;* 10 mL/h
Song et al. [69]	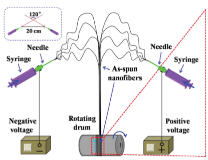	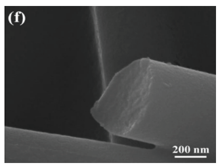	*Polymer;* PVP *App. vol.;* 7 kV *Feed rate;* 0.45 mL/h *TCD;* 20 cm

Smit et al. [42] and Khil et al. [43] used a water bath to continuously collect nanofibers. When the nanofibers accumulate in the liquid bath, they are designed to be drawn with a shaft and wound on the cylinder. Wang et al. [60] and Wu et al. [61] used a similar method but used a water/ethanol mixture in the bath.

Pan et al. [44], Yao et al. [45] and Ma et al. [46] used two oppositely placed needles in their studies. Both needles are oppositly charged and the nanofibers move towards to each other during electrospinning. At the midpoint, the two nanofibers are taken up with a yarn and continuously wound onto a cylinder. Song et al. [69] conducted a similar study. However, in this study, the needle positions were placed at a specific angle, unlike the other studies. Li et al. [47] used six needles instead of two needles. In this way, they have increased the production speed. Kangazian Kangazi et al. [68] placed a cylinder between two opposing needles. In this design, the nanofibers are sprayed from the opposite needles and collected in the middle cylinder. Then, the nanofibers taken over the cylinder are wound onto the bobbin.

In the studies of Wang et al. [48], Wang et al. [49] and Zhang et al. [50], when the polymer coming out of the needle tip is took nanofiber form by pulling, it comes onto a grounded needle on the opposite side. The nanofibers at the grounded needle end are then continuously wound onto a drum.

Mondal et al. [51] used multiple cylinders to collect and align the nanofibers. The electrospun nanofibers are collected on continuously rotating drums. With the movement of the drums, the nanofibers are directed and taken out of the electric field and wound on a roller.

Kim et al. [52] used the multi feed system. The nanofibers spun from the needles are collected on a continuously rotating conveyor. The nanofibers moving on the conveyor are picked up by rollers and wound onto the winding roller. Kim [53] made a similar design and increased the number of needles. In addition, the multiple spinner has reversed their positions. It is wound on the winding cylinder by drawing and paralleling the nanofiber bundles carried by cylinders and air. Kim et al. [54] positioned multiple needles around a disc. Nanofibers are collected on the edge of the continuously rotating disc. The nanofiber bundle formed on the edge of the disc is taken up by the rollers and transferred to a bucket.

In the study of Li et al. [55], the similarity of the electrospinning set-up to the wet spinning method is remarkable. The needle is located on a water bath. The sprayed nanofibers come to the water bath and pass through the guide roller and heater. It is aimed to remove the water on the heater. As a final process, the continuous nanofiber bundle is transferred to the winding unit. Tian et al. [57] instead of using a single needle, they have used multiple needles. In addition, more than one nanofiber bundle is combined and twisted with a separate system. Yan et al. [62], Yan et al. [63], Yan et al. [64], Yan et al. [65] and Wang et al. [66] have done similar design of Tian et al. [57]. In these studies, unlike the previous studies, they installed a pump to circulate in the water bath. Thus, nanofibers are more easily directed.

Pokorny et al. [56] designed a needleless electrospinning set-up with a rod placed at the tip of the syringe. They used both DC and AC power supplies in the design. Multiple jets are formed at the rod end and the feed rate of the polymer increases at the same time. In this way, nanofiber bundles are quickly formed and twisted by a separate rotating unit.

Mouthuy et al. [58] and Abhari et al. [59] used stainless steel wire as collector in their study. Nanofibers are collected on a steel wire which is wound from one cylinder to another. After a certain point, the nanofiber bundle and the steel wire are separated from each other and wound into separate cylinders.

Jiang et al. [67] used a needleless pyramid-shaped feeding apparatus and a conveyor as a collector. In the study, the researchers reported that they use a different feeding system to increase production speed. However, nanofibers are collected on the conveyor. The nanofibers are wound on the conveyor and then separated.

2.2.2. Continuous and twisted nanofiber yarn

Yarns can be obtained by spinning of fibers together. Obtaining yarn from nanofibers has been a featured topic in recent years. Producing yarns from nanofibers by electrospinning is not only used in many places where conventional yarns are used, but also opens up innovative and special fields of use. Nanofibers are usually used as nonwovens. After, making yarn from nanofibers, they can be used in fields such as knitting and weaving. Produced nanofibers have much larger surface area than traditional yarns. The electrospinning mechanisms, morphology and other features of these methods are given by years in Table 4.

Table 4. *Continuous and twisted nanofiber yarn*

Author(s)	Electrospinning System	Yarn Morphology	Specifications
Ko et al. [70]	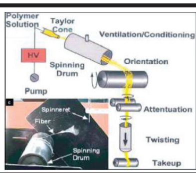	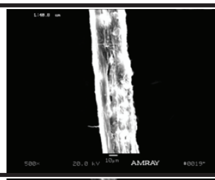	*Polymer;* PLA, PAN *App. vol.;* 25 kV *TCD;* 15 cm
Dabirian et al. [71] Dabirian et al. [72]	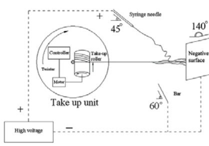	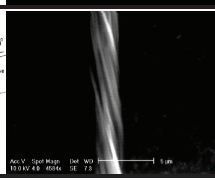	*Polymer;* PAN *App. vol.;* 8-11.4 kV *TCD;* 12-13 cm
Teo et al. [73] Yousef. et al. [74] Wu et al. [75] Wu et al. [76] Jian-Feng et al. [77]	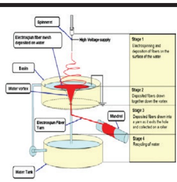	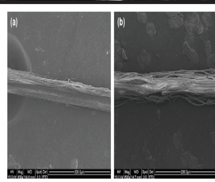	*Polymer;* PVDF, PAN, PLLA, PLCL *App. vol.;* 12-15 kV *Feed rate;* 1-15 mL/h *TCD;* 12-15 cm
Sun et al. [78] Zhang et al. [79] Wu et al. [80] Zhang et al. [81]	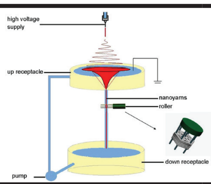	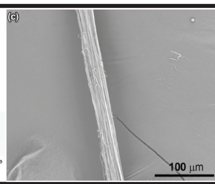	*Polymer;* PVDF, PAN, PLLA, PLCL *App. vol.;* 12-15 kV *Feed rate;* 1-15 mL/h *TCD;* 12-15 cm

Lee et al. [82] Lee et al. [83] Lee et al. [84]	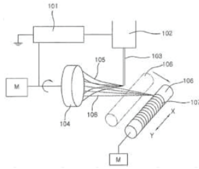	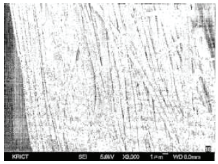	*Polymer;* PI, PA, PE, PU, PP, PVDF, PAN, PSF, PEO *App. vol.;* 1-1.5 kV/cm *Feed r;* 0.3 mL/min *TCD;* 10 cm
Bazbouz et al. [85]	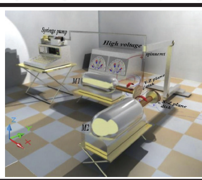	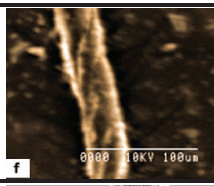	*Polymer;* Nylon 6 *App. vol.;* 15 kV *Feed rate;* 0.2 mL/h *TCD;* 8 cm
Lotus [86] Afifi et al. [87]	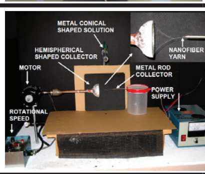	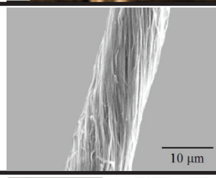	*Polymer;* PVP, PLLA *App. vol.;* 10-15kV *TCD;* 25 cm
Dabirian et al. [88]	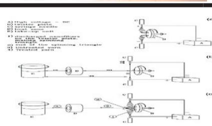	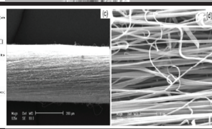	*Polymer;* PAN *App. vol.;* 9 kV *TCD;* 18 cm
Yan et al. [89]	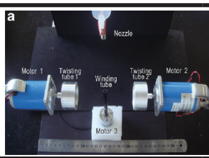	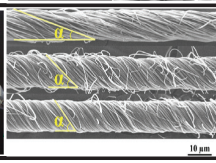	*Polymer;* PAN *App. vol.;* 10 kV *TCD;* 10 cm
Ali et al. [90] Lin et al. [91] Xie [92] Yang et al. [93] Levitt et al. [94] Jin et al. [95] Yang et al. [96]	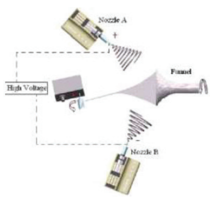	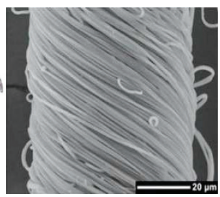	*Polymer;* PVDF, PCL, PVDF, PAN, PS, PSA, PLCL *App. vol.;* 10-30 kV *Feed rate;* 0.4-2.2 mL/h *TCD;* 12-25 cm
Fan et al. [97] Demir et al. [98] Jin et al. [99] Wu et al. [100] Levitt et al. [101] Kruse et al. [102]	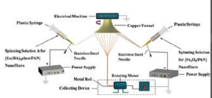	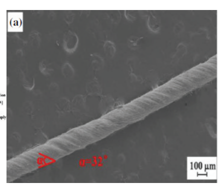	*Polymer;* PLA, PEG *App. vol.;* 24 kV *TCD;* 23 cm *Feed rate;* 2.5 mL/h

Li et al. [103]	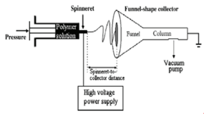	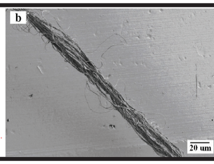	*Polymer;* PAN *App. vol.;* 12 kV *Feed rate;* 0.005 mg/min *TCD;* 0-9 cm
Hajiani et al. [104] Memarian [105] Ravandi [106] Memarian [107] Najafi [108] Ahmadloo [109] Amini et al. [110]	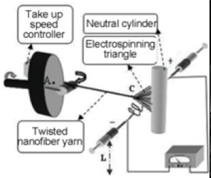	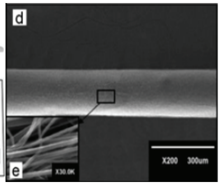	*Polymer;* PA66, PVAc, PAN, PVA/PU *App. vol.;*10.5-26 kV *Feed rate;* 0.2-0.75 mL/h *TCD;* 15-21 cm
Maleki et al. [111] Maleki et al. [112] Fakhrali [113] Maleki et al. [114] Fakhrali [115]	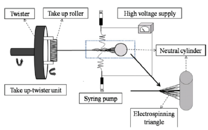	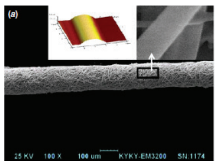	*Polymer;* PLLA, PVA/PA6 *App. vol.;* 9-25 kV *Feed rate;* 0.3 mL/h *TCD;* 18-38 cm
Wu et al. [116] Liu et al. [117] Wu et al. [118] Wu et al. [119]	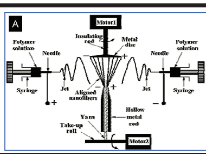	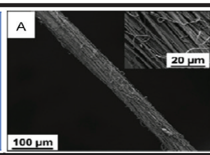	*Polymer;* PAN, PANI/PAN, PCL *App. vol.;* 10-20 kV *Feed rate;* 0.8 mL/h *TCD;* 12-20 cm
He et al. [120] He et al. [121] He et al. [122] He et al. [123] He et al. [124]	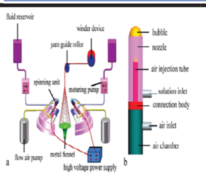	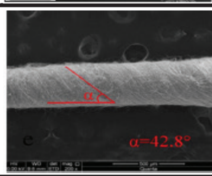	*Polymer;* PAN, PAN/PMMA, PLA *App. vol.;* 14-38 kV *Feed rate;* 0.1-48 mL/h *TCD;* 12-24 cm
Zhou et al. [125] Gao et al. [126] Nan et al. [127]	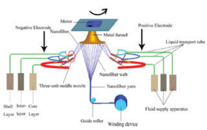	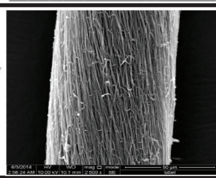	*Polymer;* PAN, PAN/PMMA, PLA *App. vol.;* 14-38 kV *Feed rate;* 0.1-48 mL/h *TCD;* 12-24 cm

Zhuang et al. [128]	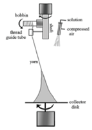	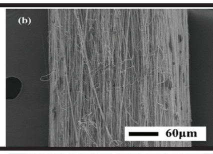	*Polymer;* PAN *App. vol.;* 5 mV (AC) *Feed rate;* 12 mL/h *TCD;* 10 cm
Shuakat et al. [129] Shuakat et al. [130]	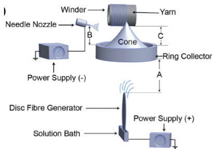	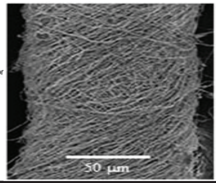	*Polymer;* PVDF/HFP *App. vol.;* 38-57 kV *TCD;* 6 cm
Lee et al. [131]	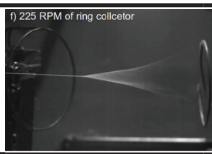	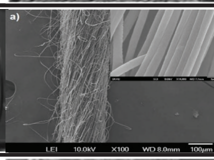	*Polymer;* PAN *App. vol.;* 8-22 kV *Feed rate;* 0.35 mL/h *TCD;* 10 cm
Ma et al. [132]	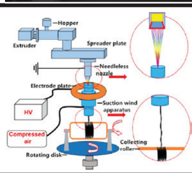	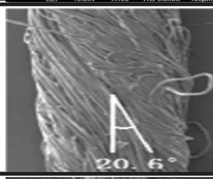	*Polymer;* PP *App. vol.;* 15-40 kV *Feed rate;* 1-100 g/h *TCD;* 10 cm
Wu et al. [133]	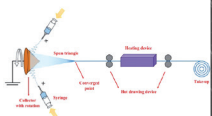	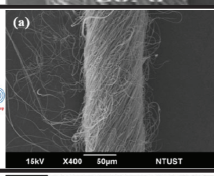	*Polymer;* PAN *App. vol.;* 20 kV *TCD;* 25 cm *Feed rate;* 3-7 mL/h
Javazmi et al. [134]	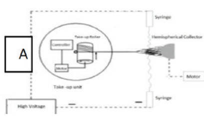	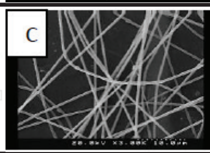	*Polymer;* PAN *App. vol.;* 13 kV *TCD;* 20 cm *Feed rate;* 0.085 mL/h
Zhou et al. [135]	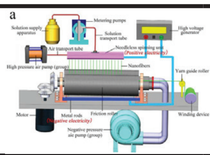	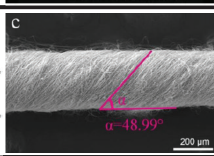	*Polymer;* PAN *App. vol.;* 30-38 kV *TCD;* 32-48 cm *Feed rate;* 36-60 mL/h

Ko et al. [70] used a method similar to conventional spinning systems for the alignment of nanofibers in the electrospinning set-up. The nanofibers aligned by the rollers are twisted in a spinning apparatus and wound onto the winding cylinder.

Dabirian et al. [71-72] placed the needle at a certain angle to the collector. They have developed a unit that turns and twists to wind the nanofiber from the collector. The system design is very simple and the resulting yarns are uniform. Similar design was performed by Hajiani et al. [104], Memarian et al. [105], Ravandi et al. [106], Memarian et al. [107], Najafi et al. [108], Ahmadloo et al. [109], Amini et al. [110], Maleki et al. [111], Maleki et al. [112], Fakhrali et al. [113], Maleki et al. [114] and Fakhrali et al. [115]. However, cylinder instead of plate was used as collector in these studies. Javazmi et al. [134] used hemispheres instead of cylinders. The design of the systems is simple. It is advantageous that the twist and winding can be controlled.

Teo et al. [73] collected the nanofibers into a water bath with a center hole. The polymer jet in contact with water solidify and form nanofibers. Vortex is formed in the water bath with air and water is transferred from the bath with hole in the middle to another bath below. Thanks to the vortex, the nanofibers are twisted, and the nanofibers enter the vortex according to the flow of water and move from the hole in the center of the bath to the following bath. Twisted nanofibers from the first bath are drawn and wrapped in a cylinder before reaching the following bath. The water in the following bath is continuously pumped to the upper bath with pipes. This system is described in Yousefzadeh et al. [74], Wu et al. [75], Wu et al. [76], Jian-Feng et al. [77], Sun et al. [78], Zhang et al. [79], Wu et al. [80] and Zhang et al. [81]. The system is simple, but another process is required to remove water from the yarns. However, it is very difficult to control the twist in the yarns in the system.

Lee et al. [82-84] used rotating discs as collectors. In this study, one or two needles are placed around the rotating disc at certain angles. The nanofibers are collected on the disc and wound by twisting onto the cylinder by rotating of the disc. The twist value of the yarn can be controlled by the speed of the disc.

Bazbouz et al. [85] used rotating discs as collectors. The nanofibers are electrospun from a needle placed at an angle to the rotating disc. While the nanofibers on the rotating disc are taken up and wound, it also gains twist. A similar study is described in Zhuang et al. [128]. However, the AC power is used instead of DC power. Wu et al. [116], Liu et al. [117], Wu et al. [118] and Wu et al. [119] used a rotary disc collector in their studies. However, two needles were used in these studies. The needles are oppositely charged and placed opposite each other. The design is simple. Twisting and winding can be controlled.

Lotus et al. [86] and Afifi et al. [87] used a hollow metallic funnel as a collector. In these studies, nanofibers are electrospun from one or two needles placed at an angle to the continuously rotating metallic funnel. The nanofibers formed on the cone are simultaneously drawn by a winding system and are twisted by the rotation of the cone. The system is simple and twist level can be controlled by the speed of the funnel. If the funnel rotates slowly or fastly, twist level will be low or high, respectively. Dabirian et al. [88] used two needles facing each other on a rotating disc collector. The nanofibers are pulled over the rotating collector disc to take up the twist and wind on a roller. Yan et al. [89] placed a plastic winding tube in front of an arrangement and metallic twist tubes on both sides. During electrospinning, the nanofibers come onto metallic twist tubes, where they are twisted and wound into the winding tube. Although the system design is complex, the researchers have reported that the twist and winding of nanofiber yarns can be controlled by speed of the tube.

Ali et al. [90] used a hollow rotating funnel as the collector. The nanofibers are collected on the funnel by using two opposing needles positioned opposite each other. In the meantime, the nanofibers are both wound and twisted. Similar studies have done by Lin et al. [91], Xie [92], Yang et al. [93], Levitt et al. [94], Jin et al. [95], Yang et al. [96], Fan et al. [97], Demir et al. [98], Jin et al. [99], Wu et al. [100], Levitt et al. [101] and Kruse et al. [102]. It can be said that the number of these studies, havig simple design and easy control of twist, has increased in recent years.

Li et al. [103] used a metallic funnel as collector. The middle point of the funnel is connected to an empty pipe and vacuuming is carried out at one point of the pipe. The nozzle and funnel are placed opposite each other. The nanofibers are collected onto the inner surface of the funnel and are directed to the center because of the surface slope. Meanwhile, the nanofibers under the control of the vacuum in the pipe gain some twist due to rotation and pass through the pipe. While this system is simple, the control difficulty of vacuum can lead to variation in twist.

He et al. [120] used two positively cahrged needles and two negatively charged needles. The needles are fed with the polymer solution by pumps. The nanofibers are collected in a continuously rotating metallic funnel. While the nanofibers drawn from the metallic funnel are wound into a winding cylinder, the continuous rotation of the funnel gains twist to the nanofibers. He et al. [121-124], Zhou et al. [125], Gao et al. [126] and Nan et al. [127] performed similar studies. Although the set-up is relatively complicated, it can be said that the control of twisting and winding in the system is quite easy.

Shuakat et al. [129-130] used two different feeding systems, needle and rotating disc. The nanofibers are collected on a rotating ring collector for both feeding units. The collected nanofibers are drawn and wound. The system is simple and twist can be controlled by ring speed. Lee et al. [131] used a fixed metallic ring as collector. The nanofibers are collected on the ring then are drawn by a unit. This system gives both twist and continuous yarn winding. Ma et al. [132] in their studies, the melt electrospinning set-up was designed. The melt thermoplastic polymer is fed through the feed chamber and dispensed on a plate. The polymer is then electrospun from the needleless feeding system into a suction apparatus. Here, the polymer mixed with both the electric field and the air pressure solidifies to the nanofiber form. The nanofiber bundle is taken up and continuously wound onto a cylinder. The winding cylinder gains twist to the nanofiber bundle by rotating around itself.

Wu et al. [133] used a cone-shaped apparatus as a collector. The sharp end of the cone is positioned with the yarn facing the direction of drafting. The nanofibers electrospun from oppositely charged needles are collected on the cone, and then drawn from this section. A heating system is integrated in the set-up before winding. It is similar to the studies using funnel as a collector.

The set-up of Zhou et al. [135] is similar to the Dref-2000 spinning machine. In the system, nanofibers are collected on two suction drums by using a needleless feeding unit. With the rotation of the drums, the nanofibers collected are twisted. The nanofibers, which are twisted into yarn form, are continuously drawn and wound. It can be said that it is an advantageous design in the production of nanofiber yarns with both yarn fineness and twist control.

2. RESULTS AND DISCUSSION

120 studies about nanofiber yarn production of all types done in 2001-2018 are examined in this study. Figure 3 shows those studies by years. The number of the studies is generally increased. While 2 studies were done in 2001-2002, 39 studies were done in 2017-2018. Higher amount of number of studies are predicted in future years. The studies examined according to the type of the electrospun nanofiber yarns are given in Figure 4.

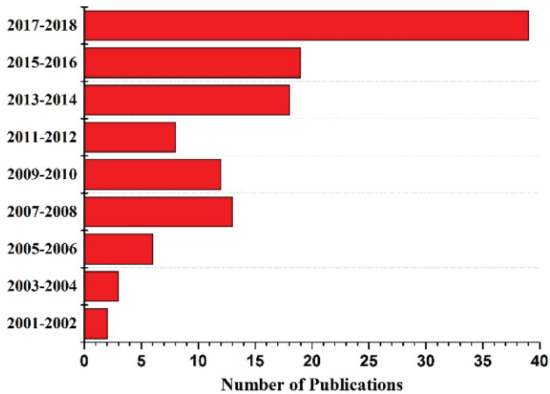

Figure 3. *Number of studies about electrospun nanofiber yarn production by years*

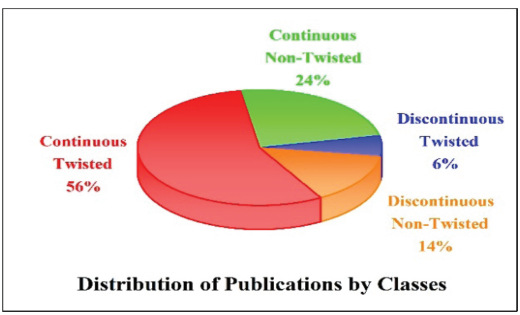

Figure 4. *Percentages of the studies according to the type of the electrospun nanofiber yarns*

56% of the studies at the greatest ratio is related to continuous twisted nanofiber yarns. The ratio of continuous nanofiber yarns is totally 80% (Figure 4). This number reveals that the researchers are focused on continuous systems. Among them, the researchers are especially focused on twisted nanofiber yarn production. When discontinuous systems are examined, non-twisted systems (14%) are more common than twisted ones (6%). When these numbers were calculated, the systems having additional twisting unit were accepted as non-twisted ones. Also, it is very difficult to twist nanofibers during electrospinning in discontinuous systems due to the short length of nanofiber bundles and discontinuity of the system. Figure 5 shows the percentages of the nanofiber yarn studies according to feeding, twisting and collector types.

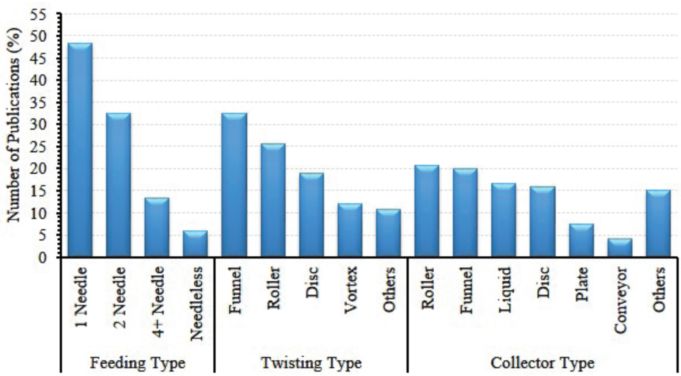

Figure 5. *Percentages of the studies according to feeding, twisting and collector types*

According to Figure 5, the studies using one needle feeding system are more common. Also the number of studies decreases with increasing number of needles. The reason is directly related to simplicity of the set-up. Although the number of the studies using needleless feeding systems are the lowest due to the complicated set-up, they are more advantageous in mass scale production.

The most common twisting units in the studies are funnel, roller, disc and vortex type mechanisms. The reason of that is related to simplicity of the mechanism and easily controlling of twist. Specifically in funnel systems twist level is easily controlled and the system has a simple design. Roller, funnel, liquid bath, disc, plate and conveyor are common collector types used in the nanofiber yarn studies. Liquid bath collector has a limitation that the liquid on the nanofiber yarn surface need to be removed. However liquid bath collector are preferred in the production of hollow nanofiber yarns. Collector type directly affects nanofiber yarn structure and diameter.

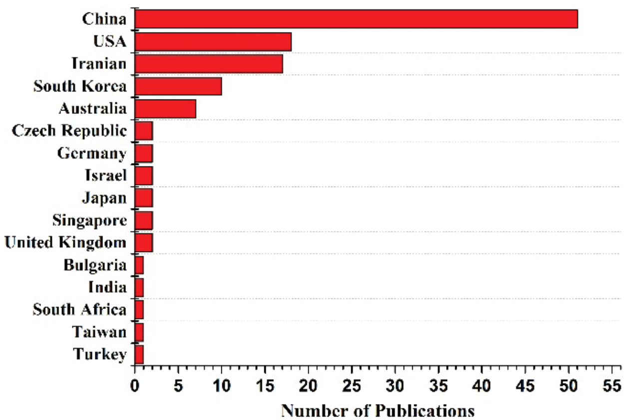

Figure 6. *Number of studies about electrospun nanofiber yarn production by countries*

The number of studies about electrospun nanofiber yarn production by countries are given in Figure 6. China with 51 studies is in the top position in electrospun nanofiber yarn production subject. USA, Iran and South Korea are the other important countries about the subject. It is seen that the studies were done by a specific group of researchers especially in China, Iran and South Korea. They investigated various polymers by using same modified electrospinning set-ups.

3. CONCLUSIONS

Electrospinning is a promising method in mass scale production of nanofibers. Modified electrospinning set-ups produce aligned nanofibers and converts them into nanofiber yarns instead of randomly aligned fibers. Hence, new potential application areas reveal because of transferring of advantageous properties of nanofibers to the nanofiber yarns such as high specific surface area, excellent hydrophility, very low fiber diameter, filtration performance, enhanced mechanical properties, biodegradability, wide range of polymer usage etc. The characteristics of the nanofiber yarns are strongly depended on the electrospinning set-up and the polymer used. In the production of nanofiber yarns two goals have to be achieved. The first goal is that nanofibers has to be collected in uniaxially aligned formation. The other one is twisting and winding of the nanofibers. The early studies were only focused on uniaxially alignment of nanofibers. Twisting and winding have been focused on in later studies. Hence there is a need of classification of different types of nanofiber yarns produced in various studies. Today, continuous and twisted nanofiber yarn production are more important than discontinuous nanofiber bundles due to suitability in mass scale production. This separation is critical for the future researches to produce nanofiber yarns conventionally. When we consider in mass scale production, producing of twisted nanofiber yarns continuously during the process of electrospinning is a requirement. Hence the recent studies are focused on controlling of nanofiber yarns with fully automated systems to reach the properties of conventional yarns. We can easily mention that the future of the nanofiber yarn studies will be focused on multiple needles or needleless systems in feeding units, manipulation of electrical field to facilitate the alignment of nanofibers, using of collectors more efficiently, fully controlling of twisting and using of various advanced polymers. On the other hand, there are limited studies on nanofiber yarns using polymer melts due to critical limitations for mass scale production.

When nanofiber yarns and conventional yarns are compared, it can be easily seen that electrospun nanofiber yarns have advantageous properties just like the fabrics to be woven and knitted by using of nanofiber yarns. To see the various potential application areas of nanofiber yarns, the fabric forms have to be produced and the relationship between structure and properties has to be understood very well. Nano materials are one of the most important technological step in human history and, they will be critical in textile industry, too.

REFERENCES

1. Zdraveva E., Fang J., Mijovic B., Lin T., Electrospun Nanofibers, Structure and Properties of High-Performance Fibers, Editor: Bhat G., Woodhead Publishing Series in Textiles, Duxford, UK, 267-300, 2017.

2. Haider, A., Haider, S., Kang, I.K., A comprehensive review summarizing the effect of electrospinning parameters and potential applications of nanofibers in biomedical and biotechnology, Arabian J. Chem., 11 (8), 1165-1188, 2018.

3. Teo, W.E., Ramakrishna, S., A review on electrospinning design and nanofibre assemblies. Nanotechnology, 17 (14), R89, 2006.

4. Xu C.Y., Inai R., Kotaki M., Ramakrishna S., Aligned biodegradable nanofibrous structure: a potential scaffold for blood vessel engineering, Biomaterials, 25 (5), 877-886, 2004.

5. Anton F., Process and apparatus for preparing artificial threads, U.S. Patent No. 1,975,504, U.S. Patent and Trademark Office, Washington, DC, 1934.

6. Anton F., Artificial fiber construction, U.S. Patent No. 2,109,333, U.S. Patent and Trademark Office. Washington, DC, 1938a.

7. Anton F., Method and apparatus for the production of fiber. U.S. Patent No. 2,116,942, U.S. Patent and Trademark Office, Washington, DC, 1938b.

8. Anton F., Method and apparatus for spinning. U.S. Patent No. 2,349,950., U.S. Patent and Trademark Office, Washington, DC, 1944.

9. Zhou, F. L., Gong, R. H., Manufacturing technologies of polymeric nanofibres and nanofibre yarns, Polym. Int., 57 (6), 837-845, 2008.

10. Ali U., Zhou Y., Wang X., Lin T., Electrospinning of continuous nanofiber bundles and twisted nanofiber yarns, Nanofibers production, properties and functional

applications, Vol. 8, Editor: Lin T., IntechOpen, Centre for Material and Fibre Innovation, Deakin University, Australia, 153-174, 2011.

11. Abbasipour M., Khajavi R., Nanofiber bundles and yarns production by electrospinning: a review, Adv. Polym. Tech., 32 (3), 21363 (1-9), 2013.

12. Shuakat M.N., Lin T., Recent developments in electrospinning of nanofiber yarns, J. Nanosci. Nanotechnol., 14 (2), 1389-1408, 2014.

13. O'Connor R.A., McGuinness G.B., Electrospun nanofibre bundles and yarns for tissue engineering applications: A review, Proc Inst Mech Eng H Title, 230 (11), 987-998, 2016.

14. Wei, L., Qin, X., Nanofiber bundles and nanofiber yarn device and their mechanical properties: A review, Text. Res. J., 86 (17), 1885-1898, 2016.

15. Göktepe, F., Mülayim, B.B., Long path towards to success in electrospun nanofiber yarn production since 1930's: a critical review, Autex Research Journal, 18 (2), 87-109, 2018.

16. Deitzel J.M., Kleinmeyer J.D., Hirvonen J.K., Tan N.B., Controlled deposition of electrospun poly(ethylene oxide) fibers, Polymer, 42 (19), 8163-8170, 2001.

17. Theron A., Zussman E., Yarin A.L., Electrostatic field-assisted alignment of electrospun nanofibers. Nanotechnology, 12 (3), 384–390, 2001.

18. El-Aufy A.K., Nanofibers and nanocomposites poly (3,4-ethylene dioxythiophene)/poly (styrene sulfonate) by electrospinning, Doctoral Thesis, Drexel University, Materials Science and Engineering, Philadelphia, 2004.

19. Fennessey S.F., Farris R.J., Fabrication of aligned and molecularly oriented electrospun polyacrylonitrile nanofibers and the mechanical behavior of their twisted yarns, Polymer, 45 (12), 4217-4225, 2004.

20. Teo W.E., Ramakrishna S., Electrospun fibre bundle made of aligned nanofibres over two fixed points, Nanotechnology, 16 (9), 1878–1884, 2005.

21. Okuzaki H., Takahashi T., Hara Y., Yan H., Uniaxially aligned carbon nanofibers derived from electrospun precursor yarns, J. Polym. Sci., Part B: Polym. Phys., 46 (3), 305-310, 2008.

22. San Choi J., Lee S.J., Christ G.J., Atala A., Yoo J.J., The influence of electrospun aligned poly(ε-caprolactone)/collagen nanofiber meshes on the formation of self-aligned skeletal muscle myotubes, Biomaterials, 29 (19), 2899-2906, 2008.

23. Maheshwari S., Chang H.C., Assembly of Multi-Stranded Nanofiber Threads through AC Electrospinning, Adv. Mater., 21 (3), 349-354, 2009.

24. Chvojka J., Hinestroza J.P., Lukas D., Production of poly(vinylalcohol) nanoyarns using a special saw-like collector, Fibres Text. East. Eur, 2 (98), 28-31, 2013.

25. Tsai C.C., Electrospun Nanofiber Yarns for Nanofluidic Applications, Doctoral Thesis, Clemson University, Materials Science and Engineering, South Carolina, 2013.

26. Bae, S., DiBalsi, M.J., Meilinger, N., Zhang, C., Beal, E., Korneva, G., Brown, R.O., Kornev, K.G., Lee, J.S., Heparin-eluting electrospun nanofiber yarns for antithrombotic vascular sutures. ACS Appl. Mater. Interfaces, 10 (10), 8426-8435, 2018.

27. Chawla S., Naraghi M., Davoudi A., Effect of twist and porosity on the electrical conductivity of carbon nanofiber yarns, Nanotechnology, 24 (25), 255708, 2013.

28. Bosworth L.A., Travelling along the clinical roadmap: developing electrospun scaffolds for tendon repair, UK Society for Biomaterials Annual Conference, Birmingham-United Kingdom, 304974 (1-6), 24-25 June, 2013.

29. Barua B., Investigation of electrospinning process parameters and studies of stabilization kinetics of polyacrylonitrile-based electrospun carbon nanofibers, Doctoral Thesis, University of Oklahoma, Aerospace and Mechanical engineering, Oklahoma, 2015.

30. Barua, B., Saha, M.C., Studies of reaction mechanisms during stabilization of electrospun polyacrylonitrile carbon nanofibers, Polym. Eng. Sci., 58 (8), 1315-1321, 2018.

31. Baniasadi M., Huang J., Xu Z., Moreno S., Yang X., Chang J., Minary-Jolandan, M. High-performance coils and yarns of polymeric piezoelectric nanofibers, ACS applied materials & interfaces, 7 (9), 5358-5366, 2015.

32. Mehrpouya, F., Foroughi, J., Naficy, S., Razal, J., Naebe, M., Nanostructured electrospun hybrid graphene/ polyacrylonitrile yarns, Nanomaterials, 7 (10), 293, 2017.

33. Chen, L., Li, D., Chen, L., Si, P., Feng, J., Zhang, L., Li, Y., Lou, J., Ci, L., Core-shell structured carbon nanofibers yarn@ polypyrrole@ graphene for high performance all-solid-state fiber supercapacitors, Carbon, 138, 264-270, 2018

34. Kim, S.H., Sim, H.J., Hyeon, J.S., Suh, D., Spinks, G.M., Baughman, R. H., Kim, S.J., Harvesting electrical energy from torsional thermal actuation driven by natural convection, Sci. Rep., 8 (1), 8712, 2018.

35. Dalton P.D., Klee D., Möller M., Electrospinning with dual collection rings, Polymer, 46 (3), 611-614, 2005.

36. Liu L.Q., Eder M., Burgert I., Tasis D., Prato M., Daniel Wagner H., One-step electrospun nanofiber-based composite ropes, Applied physics letters, 90 (8), 083108 (1-3), 2007.

37. Gu B.K., Shin M.K., Sohn K.W., Kim S.I., Kim S.J., Kim S.K., Lee H., Park, J.S., Direct fabrication of twisted nanofibers by electrospinning, Appl. Phys. Lett., 90 (26), 263902 (1-3), 2007.

38. Lotus A.F., Bender E.T., Evans E.A., Ramsier R.D., Reneker D.H., Chase G.G., Electrical, structural, and chemical properties of semiconducting metal oxide nanofiber yarns, J. Appl. Phys., 103 (2), 024910 (1-6), 2008.

39. Chang G., Li A., Xu X., Wang X., Xue G., Twisted polymer microfiber/nanofiber yarns prepared via direct fabrication, Industrial & Engineering Chemistry Research, 55 (25), 7048-7051, 2016.

40. Paneva D., Manolova N., Rashkov I., Penchev H., Mihai M., Dragan E.S, Self-organization of fibers into yarns during electrospinning of polycation/polyanion polyelectrolyte pairs, Dig J Nanomater Biostruct., 5 (4), 811-819, 2010.

41. Chang G., Shen J., Fabrication of Microropes via Bi-electrospinning with a Rotating Needle Collector, Macromol. Rapid Commun., 31 (24), 2151-2154, 2010.

42. Smit E., Bűttner U., Sanderson R.D., Continuous yarns from electrospun fibers, Polymer, 46 (8), 2419-2423, 2005.

43. Khil M.S., Bhattarai S.R., Kim H.Y., Kim S.Z., Lee K.H., Novel fabricated matrix via electrospinning for tissue engineering, Journal of Biomedical Materials Research Part B: Applied Biomaterials, 72 (1), 117-124, 2005.

44. Pan H., Li L., Hu L., Cui X., Continuous aligned polymer fibers produced by a modified electrospinning method, Polymer, 47 (14), 4901-4904. 2006.

45. Yao C., Li X., Song T., Preparation and characterization of zein and zein/poly-L-lactide nanofiber yarns, J. Appl. Polym. Sci., 114 (4), 2079-2086, 2009.

46. Ma J., He Y., Liu X., Chen W., Wang A., Lin C.Y., Mo X., Ye X., A novel electrospun-aligned nanoyarn/three-dimensional porous nanofibrous hybrid scaffold for annulus fibrosus tissue engineering, Int. J. Nanomed., 13, 1553-1567, 2018.

47. Li X., Yao C., Sun F., Song T., Li Y., Pu Y., Conjugate electrospinning of continuous nanofiber yarn of poly(L-

lactide)/nanotricalcium phosphate nanocomposite, J. Appl. Polym. Sci., 107 (6), 3756-3764, 2008.

48. Wang X., Zhang K., Zhu M., Hsiao B.S., Chu B., Enhanced mechanical performance of self-bundled electrospun fiber yarns via post-treatments, Macromol. Rapid Commun., 29 (10), 826-831, 2008a.

49. Wang X., Zhang K., Zhu M., Yu H., Zhou Z., Chen Y., Hsiao B.S., Continuous polymer nanofiber yarns prepared by self-bundling electrospinning method, Polymer, 49 (11), 2755-2761, 2008b.

50. Zhang K., Wang X., Yang Y., Wang L., Zhu M., Hsiao B.S., Chu B., Aligned and molecularly oriented semihollow ultrafine polymer fiber yarns by a facile method, J. Polym. Sci., Part B: Polym. Phys., 48 (10), 1118-1125, 2010.

51. Mondal A., Borah R., Mukherjee A., Basu S., Jassal M., Agrawal A.K., Electrospun self-assembled nanofiber yarns, J. Appl. Polym. Sci., 110 (1), 603-607, 2008.

52. Kim H.Y., Gil M.S., Jung Y.H., Kim H.J., Lee B.S., Process of preparing continuous flament composed of nano fiber, U.S. Patent No. 7,354,546, U.S. Patent and Trademark Office, Washington, DC, 2008.

53. Kim H.Y., Method of manufacturing a continuous filament by electrospinning and continuous filament manufactured thereby, U.S. Patent Application No. 12/554,784, U.S. Patent and Trademark Office, Washington, DC, 2009.

54. Kim H.Y., Park J.C., Process of preparing continuous flament composed of nanofibers, U.S. Patent No. 7,807,094, U.S. Patent and Trademark Office, Washington, DC, 2010.

55. Li J., Tian L., Pan N., Pan Z.J., Mechanical and electrical properties of the PA6/SWNTs nanofiber yarn by electrospinning, Polymer Engineering & Science, 54 (7), 1618-1624, 2014.

56. Pokorny P., Kostakova E., Sanetrnik F., Mikes P., Chvojka J., Kalous T., Bilek M., Pejchar K., Valtera J., Lukas D., Effective AC needleless and collectorless electrospinning

for yarn production, Phys. Chem. Chem. Phys., 16 (48), 26816-26822, 2014.

57. Tian L., Yan T., Pan Z., Fabrication of continuous electrospun nanofiber yarns with direct 3D processability by plying and twisting, J. Mater. Sci., 50 (21), 7137-7148, 2015.

58. Mouthuy P.A., Zargar N., Hakimi O., Lostis E., Carr A., Fabrication of continuous electrospun filaments with potential for use as medical fibres, Biofabrication, 7 (2), 025006 (1-13), 2015.

59. Abhari R.E., Mouthuy P.A., Vernet A., Schneider J.E., Brown C.P., Carr A.J., Using an industrial braiding machine to upscale the production and modulate the design of electrospun medical yarns, Polym. Test., 69, 188-198, 2018.

60. Wang, L., Wu, Y., Guo, B., Ma, P.X., Nanofiber yarn/hydrogel core–shell scaffolds mimicking native skeletal muscle tissue for guiding 3D myoblast alignment, elongation, and differentiation, ACS nano, 9 (9), 9167-9179, 2015.

61. Wu, Y., Wang, L., Guo, B., Ma, P.X., Interwoven aligned conductive nanofiber yarn/hydrogel composite scaffolds for engineered 3D cardiac anisotropy, Acs Nano, 11 (6), 5646-5659, 2017.

62. Yan, T., Tian, L., Pan, Z., Structures and mechanical properties of plied and twisted polyacrylonitrile nanofiber yarns fabricated by a multi-needle electrospinning device, Fibers Polym., 17 (10), 1627-1633, 2016.

63. Yan, T., Pan, Z., High conductivity electrospun carbon/ graphene composite nanofiber yarns, Polym. Eng. Sci., 58 (6), 903-912, 2017.

64. Yan, T., Wang, Z., Pan, Z.J. A highly sensitive strain sensor based on a carbonized polyacrylonitrile nanofiber woven fabric, J. Mater. Sci., 53 (16), 11917-11931, 2018.

65. Yan, T., Wang, Z., Wang, Y.Q., Pan, Z.J., Carbon/graphene composite nanofiber yarns for highly sensitive strain sensors, Mater. Des., 143, 214-223, 2018.

66. Wang, Y.Q., Zhang, X., Pan, Z.J., A novel method to fabricate high strength nanofiber filaments: morphology, crystalline structure, and thermal and mechanical properties, Fibers Polym., 19 (6), 1245-1254, 2018.

67. Jiang G., Zhang J., Ji D., Qin X., Ge Y., Xie S., A novel approach for fabricating antibacterial nanofiber/cotton hybrid yarns, Fibers and Polymers, 18 (5), 987-992, 2017.

68. Kangazi, M.K., Gharehaghaji, A.A., Montazer, M., Glass nanofibrous yarn through electrospinning along with in situ synthesis of silver nanoparticles, J. Sol-Gel Sci. Technol., 88 (3), 528-540, 2018.

69. Song X., Liu W., Wang J., Xu S., Liu B., Cai Q., Ma, Y., Highly aligned continuous mullite nanofibers: Conjugate electrospinning fabrication, microstructure and mechanical properties, Materials Letters, 212, 20-24, 2018.

70. Ko F., Gogotsi Y., Ali A., Naguib N., Ye H., Yang G.L., Li C., Willis P., Electrospinning of continuous carbon nanotube-filled nanofiber yarns, Advanced materials, 15 (14), 1161-1165, 2003.

71. Dabirian F., Hosseini Y., Ravandi S.H., Manipulation of the electric field of electrospinning system to produce polyacrylonitrile nanofiber yarn, J. Text. Inst., 98 (3), 237-241, 2007.

72. Dabirian F., Hosseini S.A., Novel method for nanofibre yarn production using two differently charged nozzles, Fibres Text. East. Eur, 17 (3), 45-47, 2009.

73. Teo W.E., Gopal R., Ramaseshan R., Fujihara K., Ramakrishna S., A dynamic liquid support system for continuous electrospun yarn fabrication, Polymer, 48 (12), 3400-3405, 2007.

74. Yousefzadeh M., Latifi M., Teo W.E., Amani-Tehran M., Ramakrishna S., Producing continuous twisted yarn from well-aligned nanofibers by water vortex, Polymer Engineering & Science, 51 (2), 323-329, 2011.

75. Wu J., Liu S., He L., Wang H., He C., Fan C., Mo, X., Electrospun nanoyarn scaffold and its application in tissue engineering, Materials Letters, 89, 146-149, 2012.

76. Wu J., Huang C., Liu W., Yin A., Chen W., He C., Wang H., Liu S., Fan C., Bowlin G.L., Mo, X. Cell infiltration and vascularization in porous nanoyarn scaffolds prepared by dynamic liquid electrospinning, J. Biomed. Nanotechnol., 10 (4), 603-614, 2014.

77. Jian-feng C., Wei L., Tong W., Da-wei L., Jian-guang Z., Nan-ping Z., Xiu-mei. M., Fabrication of a bi-layer tubular scaffold consisted of a dense nanofibrous inner layer and a porous nanoyarn outer layer for vascular tissue engineering. Journal of Donghua University, 31 (5), 718-722, 2014.

78. Sun B., Li J., Liu W., Aqeel B.M., El-Hamshary H., Al-Deyab S.S., Mo X., Fabrication and characterization of mineralized P(LLA-CL)/SF three-dimensional nanoyarn scaffolds, Iran. Polym. J., 24 (1), 29-40, 2015.

79. Zhang K., Guo X., Li Y., Fu Q., Mo X., Nelson K., Zhao W., Electrospun nanoyarn seeded with myoblasts induced from placental stem cells for the application of stress urinary incontinence sling: An in vitro study, Colloids Surf., B, 144, 21-32, 2016.

80. Wu, T., Zhang, J., Wang, Y., Sun, B., Yin, M., Bowlin, G.L., Mo, X., Design and fabrication of a biomimetic vascular scaffold promoting in situ endothelialization and tunica media regeneration, ACS Appl. Bio Mater., 1 (3), 833-844, 2018.

81. Zhang K., Cao N., Guo X., Zou Q., Zhou S., Yang R., Zhao W., Mo X., Liu W., Fu Q., The fabrication of 3D surface scaffold of collagen/poly (L-lactide-co-caprolactone) with dynamic liquid system and its application in urinary incontinence treatment as a tissue engineered sub-urethral sling: In vitro and in vivo study, Neurourology and urodynamics, 37 (3), 978-985, 2018.

82. Lee J.R., Jee S.Y., Kim H.J., Hong Y.T., Kim S., Park S.J., Filament bundle type nano fiber and manufacturing

method thereof. U.S. Patent Application No. 11/570,663, U.S. Patent and Trademark Office, Washington, DC, 2008.

83. Lee J.R., Jee S.Y., Kim H.J., Hong Y.T., Kim S., Park S.J., Filament bundle type nano fiber and manufacturing method thereof. U.S. Patent Application No. 11/920,495, U.S. Patent and Trademark Office, Washington, DC, 2009.

84. Lee J.R., Jee S.Y., Kim H.J., Hong Y.T., Kim S., Park S.J., Filament bundle type nano fiber and manufacturing method thereof, U.S. Patent No. 7,803,460, U.S. Patent and Trademark Office, Washington, DC, 2010.

85. Bazbouz M.B., Stylios G.K., Novel mechanism for spinning continuous twisted composite nanofiber yarns, Eur. Polym. J., 44 (1), 1-12, 2008.

86. Lotus A.F., Synthesis of semiconducting ceramic nanofibers, development of p-n junctions, and bandgap engineering by electrospinning, Doctoral Thesis, The University of Akron, Chemical Engineering, Ohio, 2009.

87. Afifi A.M., Nakano S., Yamane H., Kimura Y., Electrospinning of continuous aligning yarns with a 'funnel' target, Macromol. Mater. Eng., 295 (7), 660-665, 2010.

88. Dabirian F., Ravandi S.H., Sanatgar R.H., Hinestroza J.P., Manufacturing of twisted continuous PAN nanofiber yarn by electrospinning process, Fibers and Polymers, 12 (5), 610-615, 2011.

89. Yan H., Liu L., Zhang Z. Continually fabricating staple yarns with aligned electrospun polyacrylonitrile nanofibers, Materials Letters, 65 (15-16), 2419-2421, 2011.

90. Ali U., Zhou Y., Wang X., Lin T., Direct electrospinning of highly twisted, continuous nanofiber yarns, J. Text. Inst., 103 (1), 80-88, 2012.

91. Lin, T., Niu, H., Wang, X., Ali, U., Wang, X., Needleless electrospinning and direct electrospinning of nanofiber

yarns, In Proceedings of the International Symposium on New Frontiers in Fiber Materials Science (AATCC 2011) American Association of Textile Chemists and Colorists, 52-53, 2011.

92. Xie Z., Polyacrylonitrile nanofibre yarn; electrospinning and their post-drawing behaviour, Master Thesis, Deakin University, Geelong, 2013.

93. Yang C., Deng G., Chen W., Ye X., Mo X., A novel electrospun-aligned nanoyarn-reinforced nanofibrous scaffold for tendon tissue engineering, Colloids Surf., B, 122, 270-276, 2014.

94. Levitt A.S., Knittel C.E., Vallett R., Koerner M., Dion G., Schauer C.L., Investigation of nanoyarn preparation by modified electrospinning setup, J. Appl. Polym. Sci., 134 (19), 44813 (1-13), 2017.

95. Jin S., Xin B., Zheng Y., Preparation and characterization of polysulfone amide nanoyarns by the dynamic rotating electrospinning method, Text. Res. J., 0 (00), 1-11, 2017.

96. Yang E., Xu Z., Chur L.K., Behroozfar A., Baniasadi M., Moreno S., Huang J., Giligan J., Minary-Jolandan M., Nanofibrous Smart Fabrics from Twisted Yarns of Electrospun Piezopolymer, ACS Appl. Mater. Interfaces, 9 (28), 24220-24229, 2017.

97. Fan L., Ma Q., Tian J., Li D., Xi X., Dong X., Yu W., Wang J., Liu G., Conjugate electrospinning-fabricated nanofiber yarns simultaneously endowed with bifunctionality of magnetism and enhanced fluorescence, J. Mater. Sci., 53 (3), 2290-2302, 2018.

98. Demir, A., Acikabak, B., Ahan, Z., Development of carbon nanofiber yarns by electrospinning, In IOP Conference Series: Mater. Sci. Eng (Vol. 460, No. 1, p. 012027), IOP Publishing, December, 2018.

99. Jin S., Xin B., Zheng Y., Liu S., Effect of Electric Field on the Directly Electrospun Nanofiber Yarns: Simulation and Experimental Study, Fibers and Polymers, 19 (1), 116-124, 2018.

100. Wu T., Zhang J., Wang Y., Li D., Sun B., El-Hamshary H., Yin M., Mo X., Fabrication and preliminary study of a biomimetic tri-layer tubular graft based on fibers and fiber yarns for vascular tissue engineering, Mater Sci Eng C, 82, 121-129, 2018.

101. Levitt A.S., Vallett R., Dion G., Schauer C.L., Effect of electrospinning processing variables on polyacrylonitrile nanoyarns, J. Appl. Polym. Sci., 135 (25), 46404 (1-9), 2018.

102. Kruse, M., Greuel, M., Kreimendahl, F., Schneiders, T., Bauer, B., Gries, T., Jockenhoevel, S., Electrospun PLA-PEG-yarns for tissue engineering applications, Biomedical Engineering/Biomedizinische Technik, 63 (3), 231-243, 2018.

103. Li N., Hui Q., Xue H., Xiong J., Electrospun Polyacrylonitrile nanofiber yarn prepared by funnel-shape collector, Materials Letters, 79, 245-247, 2012.

104. Hajiani F., Jeddi A.A., Gharehaghaji A.A., An investigation on the effects of twist on geometry of the electrospinning triangle and polyamide 66 nanofiber yarn strength, Fibers and Polymers, 13 (2), 244-252, 2012.

105. Memarian F., Latifi M., Amani-Tehran M., Innovative method for electrospinning of continuous TiO2 nanofiber yarns: Importance of auxiliary polymer and solvent selection, J. Ind. Eng. Chem., 20 (4), 1886-1891, 2014.

106. Ravandi S.H., Tork R.B., Dabirian F., Gharehaghaji A.A., Sajjadi A., Characteristics of yarn and fabric made out of nanofibers, Materials Sciences and Applications, 6 (01), 103-110, 2015.

107. Memarian, F., Tehran, M.A., Latifi, M., Characterization of photocatalytic composite nanofiber yarns with respect to their tensile properties, J. Ind. Text., 47 (5), 921-937, 2016.

108. Najafi S.J., Gharehaghaji A.A., Etrati S.M., Fabrication and characterization of elastic hollow nanofibrous PU yarn, Materials & Design, 99, 328-334, 2016.

109. Ahmadloo E., Gharehaghaji A.A., Latifi M., Mohammadi N., Saghafi H., How fracture toughness of epoxy-based nanocomposite is affected by PA66 electrospun nanofiber yarn, Eng. Fract. Mech., 182, 62-73, 2017.

110. Amini G., Banitaba S.N., Gharehaghaji A.A. Imparting strength into nanofiberous yarn by adhesive bonding, Int. J. Adhes. Adhes., 75, 96-100, 2017.

111. Maleki H., Gharehaghaji A.A., Moroni L., Dijkstra P.J., Influence of the solvent type on the morphology and mechanical properties of electrospun PLLA yarns, Biofabrication, 5 (3), 035014 (1-7), 2013.

112. Maleki H., Gharehaghaji A.A., Criscenti G., Moroni L., Dijkstra P.J., The influence of process parameters on the properties of electrospun PLLA yarns studied by the response surface methodology, J. Appl. Polym. Sci., 132 (5), 41388 (1-13), 2015.

113. Fakhrali A., Ebadi S.V., Gharehaghaji A.A., Latifi M., Moghassem A., Analysis of twist level and take-up speed impact on the tensile properties of PVA/PA6 hybrid nanofiber yarns, e-Polymers, 16 (2), 125-135, 2016.

114. Maleki H., Gharehaghaji A.A., Dijkstra P.J., Electrospinning of continuous poly (L-lactide) yarns: Effect of twist on the morphology, thermal properties and mechanical behavior, J. Mech. Behav. Biomed. Mater., 71, 231-237, 2017.

115. Fakhrali A., Ebadi S.V., Gharehaghaji A.A., Latifi M., Moghassem, A., Interactions between PA6 Ratio and Tensile Properties in PVA/PA6 Hybrid Nanofiber Yarns, Nano Hybrids and Composites, 14, 25-37, 2017.

116. Wu S.H., Qin X.H., Uniaxially aligned polyacrylonitrile nanofiber yarns prepared by a novel modified electrospinning method, Materials Letters, 106, 204-207, 2013.

117. Liu P., Wu S., Zhang Y., Zhang H., Qin X., A fast response ammonia sensor based on coaxial PPy–PAN nanofiber yarn, Nanomaterials, 6 (7), 121 (1-10), 2016.

118. Wu S., Liu P., Zhang Y., Zhang H., Qin X., Flexible and conductive nanofiber-structured single yarn sensor for smart wearable devices, Sens. Actuators, B, 252, 697-705, 2017a.

119. Wu S., Wang Y., Streubel P.N., Duan B., Living nanofiber yarn-based woven biotextiles for tendon tissue engineering using cell tri-culture and mechanical stimulation, Acta biomaterialia, 62, 102-115, 2017b.

120. He J., Zhou Y., Qi K., Wang L., Li P., Cui S., Continuous twisted nanofiber yarns fabricated by double conjugate electrospinning, Fibers and Polymers, 14 (11), 1857-1863, 2013.

121. He J.X., Qi K., Zhou Y.M., Cui S.Z., Fabrication of continuous nanofiber yarn using novel multi-nozzle bubble electrospinning, Polymer International, 63 (7), 1288-1294, 2014a.

122. He J.X., Zhou Y.M., Wu Y.C., Liu R.T., Nanofiber coated hybrid yarn fabricated by novel electrospinning-airflow twisting method, Surf. Coat. Technol., 258, 398-404, 2014b.

123. He J., Qi K., Zhou Y., Cui S., Multiple conjugate electrospinning method for the preparation of continuous polyacrylonitrile nanofiber yarn, J. Appl. Polym. Sci., 131 (8), 40137 (1-6), 2014c.

124. He J., Qi K., Wang L., Zhou Y., Liu R., Cui, S., Combined application of multinozzle air-jet electrospinning and airflow twisting for the efficient preparation of continuous twisted nanofiber yarn, Fibers and Polymers, 16 (6), 1319-1326, 2015.

125. Zhou Y., He J., Wang H., Qi K., Ding B., Cui S., Carbon nanofiber yarns fabricated from co-electrospun nanofibers, Materials & Design, 95, 591-598, 2016.

126. Gao, Y., Shao, W., Qian, W., He, J., Zhou, Y., Qi, K., Wang, L., Cui, S.,Wang, R., Biomineralized poly (l-lactic-co-glycolic acid)-tussah silk fibroin nanofiber fabric with

hierarchical architecture as a scaffold for bone tissue engineering, Mater. Sci. Eng., C, 84, 195-207. (2018).

127. Nan, N., He, J., You, X., Sun, X., Zhou, Y., Qi, K., Shao, W., Liu, F., Chu, Y., Ding, B., A stretchable, highly sensitive, and multimodal mechanical fabric sensor based on electrospun conductive nanofiber yarn for wearable electronics, Advanced Materials Technologies, 4 (3), 1800338, 2018.

128. Zhuang X., Jia K., Cheng B., Feng X., Shi S., Zhang B., Solution blowing of continuous carbon nanofiber yarn and its electrochemical performance for supercapacitors, Chem. Eng. J., 237, 308-311, 2014.

129. Shuakat M.N., Lin T., Highly-twisted, continuous nanofibre yarns prepared by a hybrid needle-needleless electrospinning technique, RSC advances, 5 (43), 33930-33937, 2015.

130. Shuakat M.N., Lin T., Direct electrospinning of nanofibre yarns using a rotating ring collector, J TEXT I. Journal, 107 (6), 791-799, 2016.

131. Lee J.H., Gim Y., Bae S., Oh C., Ko H.S., Baik S., Oh T.S., Yoo J.B., Determination of twisting angle of electrospun nanofiber bundle for continuous electrospinning system, J. Appl. Polym. Sci., 134 (48), 45528 (1-7), 2017.

132. Ma X., Zhang L., Tan J., Qin Y., Chen H., He W., Yang W., Li H., Continuous manufacturing of nanofiber yarn with the assistance of suction wind and rotating collection via needleless melt electrospinning, J. Appl. Polym. Sci., 134 (20), 44820 (1-7), 2017.

133. Wu, C.M., Hsu, C.H., Su, C.I., Liu, C.L., Lee, J.Y., Optimizing parameters for continuous electrospinning of polyacrylonitrile nanofibrous yarn using the Taguchi method, J. Ind. Text., 48 (3), 559-579, 2018.

134. Javazmi, L., Hosseini Ravandi, S.A., Sharifkhani, M.E., Effect of TiO2 nanoparticle on wicking phenomenon in PAN nanofiber yarns, In Proceedings of the 2018 International Conference on Nanoscience

and Nanotechnology (ICONN 2018), University of Wollongong, January, 2018.

135. Zhou, Y., Wang, H., He, J., Qi, K., Ding, B., Cui, S., Investigation of parameters for preparing nanofiber yarn via a stepped airflow-assisted electrospinning, Fibers Polym., 19 (10), 2169-2177, 2018.

A SAFE DRIVING APPLICATION FOR DYNAMIC WEATHER CONDITIONS: DR.FALCON DRIVING SAFETY APP

Hasan ŞAHIN[1]

CHAPTER 9

1 Mechanical Engineering Department , Istanbul Technical University, Istanbul, Turkey, sahinhasan@itu.edu.tr

A SAFE DRIVING APPLICATION FOR DYNAMIC WEATHER CONDITIONS: DR.FALCON DRIVING SAFETY APP

Hasan ŞAHIN[1]

I. Introduction

Mobile devices especially mobile phones are one of the most used devices in human's daily life. Many devices can be controlled and integrated via mobile phones. For example, in automotive environment, integration of mobile devices are also possible nowadays (Diewald et al., 2011). Using mobile phones while driving may cause an accident because of texting or making a phone call (Walsh et al., 2008). However, if the mobile phone is used as a driver assistant during driving, it may also prevent texting and making a phone call. As a driver assistant, one of the most important data which could be observed during driving is the positioning of the vehicle via GPS signals (Zito et al., 1995). By using global positioning system (GPS) signals, the corresponding velocity and acceleration values of the vehicle could be also observed. On the other hand, most vehicles are already equipped with an electronic control unit (ECU) and corresponding sensors to detect the same values (Ruta et al., 2010). The most significant advantage of the assistance of mobile phones is the usage of INTERNET and GPS together which is still not common for ECU to do it alone in most vehicles. There are also other sensons in mobile phones which could be used effectively for driving safety, such as three-axis accelerometer (Fazeen et al., 2012). Inter-vehicle communication is also another challenging point in driving assistance (Aoki, 1996). INTERNET connection is also used for inter-vehicle communication (Hartenstein et al., 2001). INTERNET

1 Mechanical Engineering Department , Istanbul Technical University, Istanbul, Turkey, sahinhasan@itu.edu.tr

could be also provided by mobile phones seperately for inter-vehicle communication. The location determination could be done via GPS alone or by the assistance of INTERNET together (Zhao, 2000). Moreover, INTERNET provides additional location information parameters such as local weather conditions. The originality of this study comes from detecting local weather conditions to calculate the local maximum road friction coefficient. By calculating the maximum road friction coefficient, the driver could be warned either during accelerating and decelerating. To generate a reasonable warning, the vehicle acceleration/deceleration values should be observed and compared to the calculated ones from maximum road friction coefficient. In this study, these values are calculated directly from the derivative of the real-time velocity value taken via GPS signal. To crosscheck the acceleration values, a three-axis accelerometer application was used which is significant to observe driving behaviour (Paefgen et al., 2012 ; Singh et al., 2013).

II. Methodology

First of all, the mobile application was coded in Swift 2.0 language and its suitable for most vehicles on road such as cars, trucks and etc. GPS signal is required for velocity, acceleration and distance calculations. INTERNET connection is also required for local weather detection. In Fig. 1 below, a snapshot of hard-braking warning of the application could be seen as an example. Hard braking, traction and speed limit warnings will be explained in detail in this section.

Fig. 1. *Hard-braking warning of the application during hard braking*

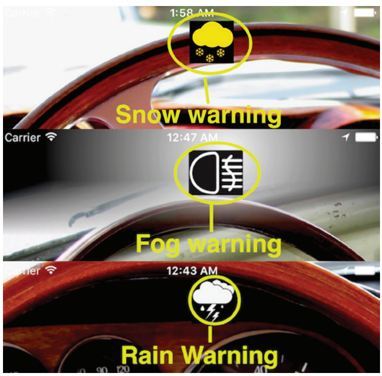

Fig. 2. *Weather conditions and their representations in the application*

Before explaining the warning types, the weather conditions will be mentioned. As it is illustrated in Fig. 2 above, snow, fog and rain warning signs are active depending on the real-time weather. If the weather is clear or cloudy, no specific sign is active in the application.

TABLE I. *Warning activation conditions*

Warning Types	Weather Conditions		
	Dry Asphalt	Wet Asphalt	Snowy Asphalt
Hard Braking (ON)	if (a_x < -mu*g) [mu = 1]	if (a_x < -mu*g) [mu = 0.5]	if (a_x < -mu*g) [mu = 0.3]
Traction Loss (ON)	if (a_x >mu* t*g) [mu = 1]	if (a_x > mu*t*g) [mu = 0.5]	if (a_x > mu*t*g) [mu = 0.3]
Speed Limit (ON)	if (set speed > actual speed)	if (set speed > actual speed)	if (set speed > actual speed)

a_x = longitudinal acceleration , mu = maximum road coefficient friction, t = traction coefficient, g = 9.81 m/s2

According to the real-time weather data taken via INTERNET connection locally, the maximum road friction coefficient (mu) is calculated as illustrated in Table 1 above. The whole decision making is also illustrated in Fig. 3. For dry asphalt, mu is 1; for wet asphalt, mu is 0.5; for snowy asphalt mu is 0.3. The longitudinal acceleration of the vehicle is calculated from the derivative of the actual velocity of the vehicle via GPS signal. To enable hard-braking warning, the actual longitudinal acceleration of the vehicle must be at least equal or below the gravitational force multiply by mu. To enable traction warning, the actual longitudinal acceleraton of the vehicle must be at least equal or above the traction coefficient multiply by mu and gravitational force. The traction coefficient depends on the slope of the road, the differential type (front, rear or 4 wheel) and some other specifications of the vehicle. The experiments done with Audi A3 (2012 model – front differential) vehicle and therefore the traction coefficient was defined as 0.5 (by assuming zero slope) for this car in this study. In the speed limit warning, the driver sets the maximum speed by manually. If the vehicle exceeds that speed value, the speed limit warning is enabled automatically.

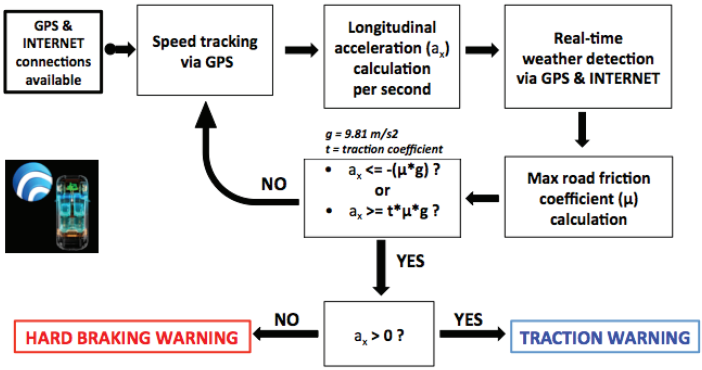

Fig. 3. *Decision making of the application*

As its illustrated in Fig. 3 above, the decision making flowchart for the activation of the traction and hard-braking warnings are clear. The speed limit warning is not represented in the flowchart because it is just set by the driver manually as mentioned before.

III. Results and Discussion

Before representing the measured results from three axis accelerometer, the examples of warning screenshots will be mentioned shortly. The speed limit warning (yellow), the traction warning (blue) and the hard-braking warning (red) screenshots in the application are illustrated in Fig. 4 below. In the speed limit warning screenshot in Fig. 4, the maximum speed set by the driver is 40 km/h, the acceleration of the vehicle is almost zero, the average speed is 15 km/h, the actual speed is 41 km/h and the distance taken is 2 km. In the traction warning screenshot in Fig. 4 , the acceleration of the vehicle is almost 4 m/s2, the average speed is 13 km/h, the actual speed is 38 km/h and the distance taken is 2 km. Finally, in the hard-braking warning screenshot in Fig. 4, the deceleration of the vehicle is almost 6 m/s2, the average speed is 25 km/h, the actual speed is 29 km/h and the distance taken is 11 km/h.

The real-time acceleration values calculated from the actual speed data via GPS signal, must be crosschecked by a second local sensor. Another sensor, a three-axis accelerometer was used to crosscheck. Three cases were chosen for crosshecking during hard-braking such as hard-braking on dry, wet and showy asphalts.

Fig. 4. *Examples of the warning screenshots from the application*

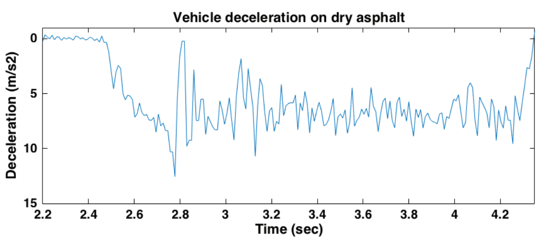

Fig. 5. *The deceleration data taken by a three-axis accelerometer sensor during hard braking on dry asphalt.*

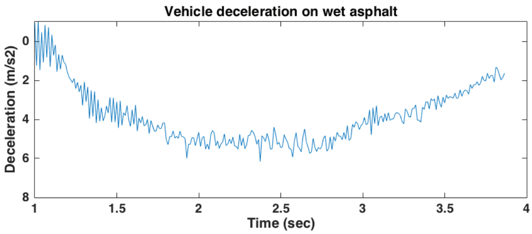

Fig. 6. *The deceleration data taken by a three-axis accelerometer sensor during hard braking on wet asphalt.*

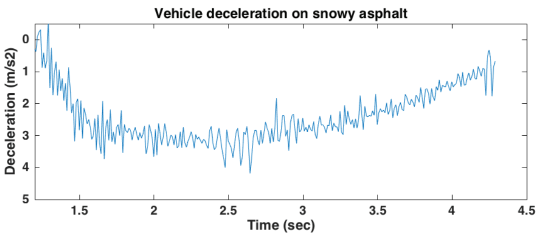

Fig. 7. *The deceleration data taken by a three-axis accelerometer sensor during hard braking on snowy asphalt.*

In the first case, a full braking maneuver was performed on a dry asphalt. The peak value of the deceleration is just above the defined maximum road friction coefficient multiply by gravitational force on a dry asphalt as shown in Fig. 5 and Table 1. In the second case, a full braking maneuver was perfomed on a wet asphalt. This case is also presented in Fig. 4 as a hard braking screenshot from the application. Therefore, a crosscheck was performed on a wet asphalt so that the hard braking warning was enabled in the correct time zone by reaching more than 5 m/s2 deceleration as shown in Fig. 4 and Fig. 6. The peak value of the deceleration is also above the threshold value according to the defined maximum road friction coefficient on a wet asphalt as shown in Fig. 6 and Table 1. In the last case, a full braking maneuver was performed on a snowy asphalt. The peak value of the deceleration is also above the threshold value according to the defined maximum road friction coefficient on a snowy asphalt as shown in Fig. 7 and Table 1.

The measured hard-braking results from a three-axis accelerometer confirms the logic of the activation principle of the hard-braking warning in the application. So that, hard-braking warnings are reliable depending on the real-time weather. The traction warning activation directly depends on the vehicle specifically as mentioned in the methodology. The speed limit warning is also reliable as it is set manually by the driver. The activation principles of traction and hard-braking warnings are almost similar to the activation principles of Anti-lock Braking System (ABS) and Traction Control System (TCS). The aim of the warnings is adopting the driver to the vehicle stability limits in changing weather conditions.

IV. Conclusion

The application includes two major warnings such as hard-braking and traction warnings. Actually, the activation warnings of ABS and TCS in the vehicles are almost similar to the hard-braking and traction warnings in the application. However, the warnings in the application may provide drivers to improve their driving style by observing vehicle stability limits clearly in changing weather conditions. The hard-braking warning of the application is almost valid for all vehicles on road as it directly depends on braking. On the other hand, the traction warning of the application is not valid for all vehicles. For a valid traction warning, the vehicle options (such as differential type) should be added into the application as a future study. Moreover, a speed limit warning is also included in the application. This warning is also valid for all vehicles as the set speed is defined by the driver manually and the actual speed is observed via GPS signal in the application. As a future study, a driving experiment should be also done with enough participants to observe the benefits of the application on driving styles.

REFERENCES

Diewald, S., Möller, A., Roalter, L. and Kranz, M. (2011). Mobile Device Integration and Interaction in the Automotive Domain. *Automotive UI Adjunt Proceedings*, Salzburg, Austria.

Walsh, S.P., White, K.M., Hyde, M.K. and Watson, B. (2008). Dialling and driving: Factors influencing intentions to use a mobile phone while driving. *Accident Analysis and Prevention,* vol. 40 1893–1900, Elsevier.

Zito, R., D'este, G. and Taylar, M.A.P. (1995). Global positioning systems in the time domain: How useful a tool for intelligent. *Transp. Res.-C*. Vol. 3, No. 4, pp. 193-209.

Ruta, M., Scioscia, F., Gramegna, F. and Sciascio, E.D. (2010). A Mobile Knowledge-based System for On-Board Diagnostics and Car Driving Assistance. *UBICOMM 2010 : The Fourth International Conference on Mobile Ubiquitous Computing, Systems, Services and Technologies*, Bari, Italy.

Fazeen, M., Gozick, B., Dantu, R., Bhukhiya, M. and Gonzales, M.C. (2012). Safe Driving Using Mobile Phones. *IEEE Transactions On Intelligent Transportation Systems*, Vol. 13, No. 3.

Aoki, M. (1996). Inter vehicle communication: Technical Issues on Vehicle Control Application. *IEEE Communications Magazine*.

Hartenstein, H., Bochow, B. and Ebner, A. (2001). Position-Aware Ad Hoc Wireless Networks for Inter-Vehicle Communications: the Fleetnet Project. *ACM MobiHOC*, Long Beach, CA, USA.

Zhao, Y. (2000). Mobile Phone Location Determination and Its Impact on Intelligent Transportation Systems. *IEEE Transactions On Intelligent Transportation Systems*, Vol. 1, No. 1.

Paefgen, J., Kehr, F., Zhai, Y. and Michahelles, F. (2012). Driving Behavior Analysis with Smartphones: Insights from a Controlled Field Study. *MUM '12*, Ulm, Germany.

Singh, P., Juneja, N. and Kapoor, S. (2013). Using Mobile Phone Sensors to Detect Driving Behavior. *DEV '13*, ACM 978-1-4503-1856.

CARBON PAPER AS A BINDER-FREE ELECTRODE IN ENERGY APPLICATIONS

Meltem YANILMAZ[1]

CHAPTER 10

1 Dr Meltem Yanilmaz, Istanbul Technical University, yanilmaz@itu.edu.tr

CARBON PAPER AS A BINDER-FREE ELECTRODE IN ENERGY APPLICATIONS

Meltem YANILMAZ[1]

INTRODUCTION

Considering growing population and excessive consumption of fossil fuels, renewable and green energy technologies are vital for future energy generation, storage, and usage. Electrochemical energy storage devices have been receiving great interest owing to the fact that they have great potential to reduce fossil fuel energy consumption in transportation and store renewable energy. Lithium ion batteries have been used in many portable electronics including cell phones, laptop computers, digital cameras, power tools, electrical bicycles, etc. Lithium ion batteries have been studied as electric energy storage devices due to their advantages such as high energy density, and long cycle life. However, high performance and low cost materials are needed to improve performance of the cells for future applications. Moreover, sodium ion batteries have been considered alternative to lithium ion batteries due to their low cost and comparable energy density (Komaba, Murata et al. 2011, Liu, He et al. 2014, Chen and Deng 2015, Gao, Zhang et al. 2017, Wang, Nie et al. 2017).

Na-ion batteries have similar mechanism to that of lithium ion batteries. However, ionic volume of Na-ions is almost double that of Li-ions, and thus some Li-ion hosts cannot be used in sodium ion batteries including graphite. Hard carbon structures and amorphous carbon have been extensively investigated in Na-ion batteries. Electrode structure and properties directly affect the performance of electrochemical energy storage devices and carbon

1 Dr Meltem Yanilmaz, Istanbul Technical University, yanilmaz@itu.edu.tr

based structures are widely applied in these devices owing to their good chemical stability, high surface area, good mechanical integrity, high ionic conductivity and tunable physical properties (Zhao, Zhao et al. 2013, Wang, Nie et al. 2017).

Carbon structures with high specific surface area are promising for next generation energy storage. However, the techniques that have used to prepare high quality carbon materials are complex and time consuming and expensive precursor like polyacrylonitrile have been used (Dutta, Bhaumik et al. 2014, Liu, He et al. 2014).

Biomass is an abundant and sustainable source for production of carbon and using biomass could significantly reduce carbon prices. Biomass-derived carbon materials have been gaining tremendous attention as electrode materials for energy storage devices because of their adjustable physical and chemical properties, environmentally friendly and low-cost features (Jiang, Nelson et al. 2015, Wang, Nie et al. 2017). Carbon materials synthesized from carbonization of biomass could also be used in sensors, energy storage, and water purification. Martins et al (Martins, Huang et al. 2016) used porous carbon papers as electrocatalysts and they reported that carbon materials synthesized from cellulosic paper showed better catalytic activity in direct hydrazine fuel cells. Zhang et al (Zhang, Li et al. 2014) prepared carbon material to be used in Li-sulfur batteries and cycling and C-rate performance was significantly improved by using carbon paper interlayer in Li-sulfur cells. The discharge capacity of 800 mAh/g was reached in 200 cycles by using biomass derived carbon interlayer and the discharge capacity of 600 mAh/g was presented at high current density of 1C (Zhang, Li et al. 2014). Liu et al (Liu, He et al. 2014) synthesized supercapacitor electrodes by using filter paper and high specific capacitance of 334 F g^{-1} with good cycling stability as well as excellent rate capability was achieved owing to high porosity. In another study, filter paper was carbonized and used in electrochemical supercapacitors and the flexible electrode showed an areal specific capacitance of 1900 mF/cm^2 at a scan rate of 5 mV/s and maintains its capacity up to 85.1% over 1000 cycles (Zhang, Zhu et al. 2015). Jiang et al (Jiang, Nelson et al. 2015) investigated the effect of different carbonization temperature on the electrochemical performance of filter paper based carbon electrodes. The filter paper carbonized at 1500 ^{0}C exhibited the best performance with high capacitance and excellent capacitance retention, >87%, after 3000 charge–discharge cycles was achieved. Hong et al (Hong, Qie et al. 2014) synthesized porous hard carbon by using pomelo peels. Bacterial cellulose was used to create porous carbon for supercapacitors in another study (Shan, Yang et al. 2016). Berenguer reported lignin based carbon materials for supercapacitors (Berenguer, García-Mateos et al. 2016). Cheng et al (Cheng, Li et al. 2016) used cotton to fabricate carbon electrode for supercapacitors. Sudhan et al (Sudhan, Subramani et al. 2016) achieved high capacitance of 156 F/g by carbonizing rice straw in supercapacitors.

Cellulose and its derivatives is the most abundant renewable polymer resource and it has an annual production that is over 7.5×10^{10} tons. Cellulose is a fibrous, tough, water-insoluble polymer that plays an essential role in maintaining the structure of plant cell walls. It is a high molecular weight homopolymer of β-1,4-linked anhydro-D-glucose units in which every unit is corkscrewed 180° with respect to its neighbors, and the repeat segment is a dimer of glucose, known as cellobiose (Habibi, Lucia et al. 2010). In this study, filter paper was carbonized and as-prepared porous carbon paper was used as a binder free electrode in Na-ion and Li-ion batteries.

Experimental

Cellulosic filter paper was used to prepare carbon paper. Cellulosic paper was carbonized at 800 ^{0}C with a temperature ramp of 1 C/min for 2h under argon atmosphere to synthesize highly porous fibrous carbon paper. The morphology was investigated by using scanning electron microscopy. The obtained carbon paper directly used as an electrode in Li-ion and Na-ion batteries.

Results and discussion

Figure 1 shows the SEM image of carbon paper and it is seen from the image that carbon paper is composed of highly porous carbon fibers. Zhang et al (Zhang, Li et al. 2014) also prepared carbon papers to be used in Li-sulfur batteries and highly porous carbon papers with high conductivity was reported after pyrolyzing the cellulosic paper. The conductivity of 3.52 Sm^{-1} with the BET surface area of 534 m^2 g^{-1} was reported and the high conductivity and surface area led to enhanced cycling and C-rate performance (Zhang, Li et al. 2014). Similar morphology was also reported by Liu et al (Liu, He et al. 2014) and higher porosity after carbonization was reported in their study.

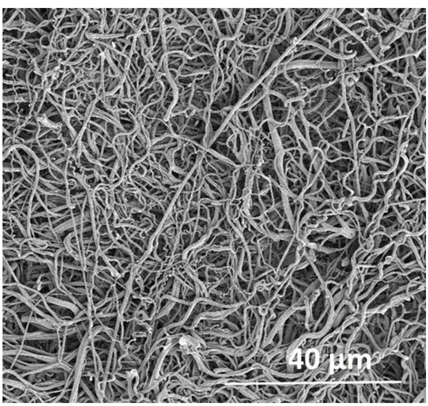

Figure 1 *SEM images of carbon paper*

Production of battery electrodes without addition of any carbon black conductor, polymer binder or use of current collectors help simplify fabrication process (Jin, Yu et al. 2014). In this study, filter paper was pyrolysed and used directly as a biner free electrode in coin cells. The as-prepared carbon paper with high porosity could be good candidate in electrochemical energy storage devices. Figure 2 shows charge-discharge profiles of binder free carbon paper electrode over a potential window 0.01–2.5 V vs Na/Na^{+}. The first cycle discharge capacity is 386 mAh/g, and the first cycle charge capacity is 71 mAh/g. Due to the high porosity and conductivity, high capacity is achieved from binder free carbon paper. This value is higher than that of graphite and activated carbon which was reported in previous studies (Wenzel, Hara et al. 2011). The large first cycle irreversible capacity loss is ascribed to irreversible formation of solid-electrolyte interphase (SEI) and the trapping of inserted sodium ion (Chen and Deng 2015).

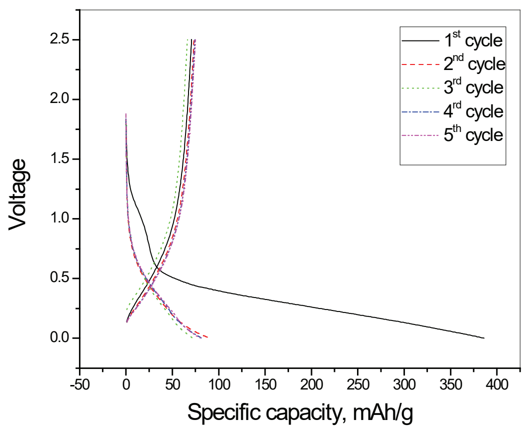

Figure 2 *The charge-discharge profiles for the first five cycles*

Figure 3 shows the cycling and efficiency of Na-ion cell containing highly porous carbon paper. After the first cycle, efficiency is increased to 81% and the efficiency over 98% is reached at the end of first ten cycles. The reversible capacity of 78 mAh/g is reported and the capacity of 67 is reached after 200 cycles.

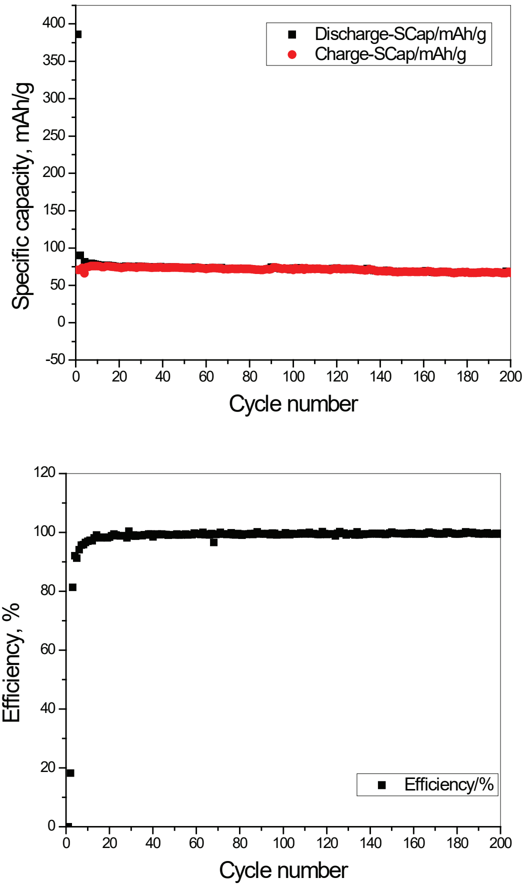

Figure 3 *Cycling performance and efficiency*

In lithium ion batteries, fast kinetics and high capacity could be reached by introducing nanoporosity and a hierarchical pore system (Wenzel, Hara et al. 2011). Figure 4 shows charge discharge profiles of binder free carbon paper electrode over a potential window 0.01–2.5 V vs Li/Li$^+$. The first discharge capacity is 502 mAh/g and charge capacity is 194 mAh/g with the initial Columbic efficiency of 38%. The large initial irreversible capacity of the composite electrode is seen because of the formation of the SEI film on the electrode surface and the generation of lithium oxides and lithium silicates.

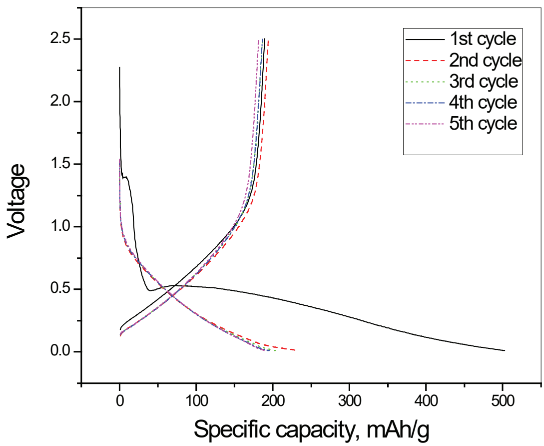

Figure 4 *The charge-discharge profiles for the first five cycles*

The cycling performance and Coulombic efficiency are presented in Figure 5 and the reversible capacity is seen as 150 mAh g^{-1}. The capacity of 143 mAh/g is seen during 200 cycles with the Coulombic efficiency of over 99%. The activated carbon synthesized by using shells of broad beans was reported and similar capacity of 150 mAh/g was reported by Xu et al (Xu, Han et al. 2015). The unique three dimensional porous network structure and the high surface area help increase the electrode–electrolyte contact and facilitate the electron transfer upon the discharge/charge processes. Thus, good electrochemical performance is observed.

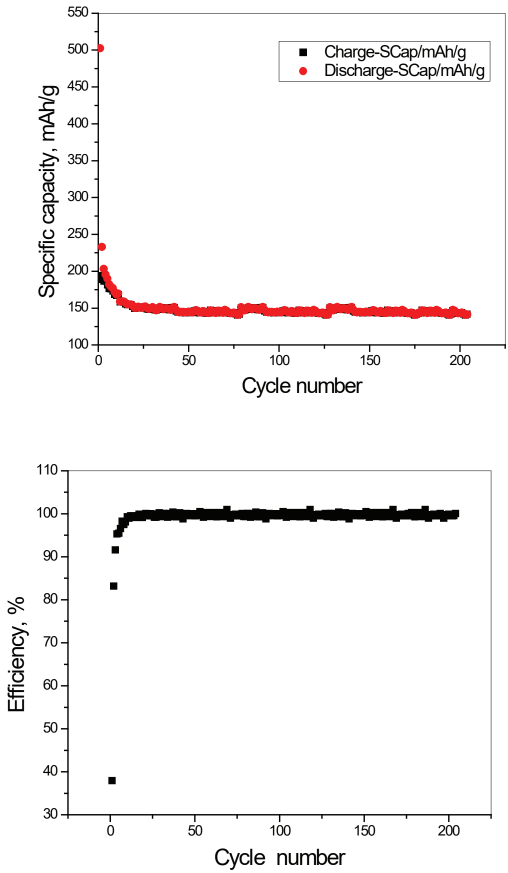

Figure 5 *Cycling performance and efficiency for lithium ion batteries*

Conclusions

Highly porous carbon paper was synthesized and as-prepared highly porous fibrous carbon material used in Na-ion and Li-ion batteries as binder free electrodes. The capacity of 78 and 150 mAh/g was achieved in Na-ion and Li-ion batteries, respectively. Therefore, carbon papers derived from cellulosic paper could be a promising candidate in next generation energy storage systems.

REFERENCES

BERENGUER, R., et al. (2016). "Biomass-derived binderless fibrous carbon electrodes for ultrafast energy storage." Green Chemistry **18**(6): 1506-1515.

CHEN, W. and D. Deng (2015). "Carbonized common filter paper decorated with Sn@ C nanospheres as additive-free electrodes for sodium-ion batteries." Carbon **87**: 70-77.

CHENG, P., et al. (2016). "Biomass-derived carbon fiber aerogel as a binder-free electrode for high-rate supercapacitors." the Journal of Physical Chemistry C **120**(4): 2079-2086.

DUTTA, S., et al. (2014). "Hierarchically porous carbon derived from polymers and biomass: effect of interconnected pores on energy applications." Energy & Environmental Science **7**(11): 3574-3592.

GAO, Z., et al. (2017). "Biomass-derived renewable carbon materials for electrochemical energy storage." Materials Research Letters **5**(2): 69-88.

HABIBI, Y., et al. (2010). "Cellulose nanocrystals: chemistry, self-assembly, and applications." Chemical reviews **110**(6): 3479-3500.

HONG, K.-l., et al. (2014). "Biomass derived hard carbon used as a high performance anode material for sodium ion batteries." Journal of Materials Chemistry A **2**(32): 12733-12738.

JIANG, L., et al. (2015). "Cellulose-Derived Supercapacitors from the Carbonisation of Filter Paper." ChemistryOpen **4**(5): 586-589.

JIN, J., et al. (2014). "Lignin-based electrospun carbon nanofibrous webs as free-standing and binder-free electrodes for sodium ion batteries." Journal of Power Sources **272**: 800-807.

KOMABA, S., et al. (2011). "Electrochemical Na insertion and solid electrolyte interphase for hard-carbon electrodes and application to Na-Ion batteries." Advanced Functional Materials **21**(20): 3859-3867.

LIU, M., et al. (2014). "Filter paper-derived carbon fiber/polyaniline composite paper for high energy storage applications." Composites science and technology **101**: 152-158.

MARTINS, A. C., et al. (2016). "Fibrous porous carbon electrocatalysts for hydrazine oxidation by using cellulose filter paper as precursor and self-template." Carbon **102**: 97-105.

SHAN, D., et al. (2016). "Biomass-derived three-dimensional honeycomb-like hierarchical structured carbon for ultrahigh energy density asymmetric supercapacitors." Journal of Materials Chemistry A **4**(35): 13589-13602.

SUDHAN, N., et al. (2016). "Biomass-derived activated porous carbon from rice straw for a high-energy symmetric supercapacitor in aqueous and non-aqueous electrolytes." Energy & Fuels **31**(1): 977-985.

WANG, J., et al. (2017). "Biomass derived carbon for energy storage devices." Journal of Materials Chemistry A **5**(6): 2411-2428.

WENZEL, S., et al. (2011). "Room-temperature sodium-ion batteries: improving the rate capability of carbon anode materials by templating strategies." Energy & Environmental Science **4**(9): 3342-3345.

XU, G., et al. (2015). "Biomass-derived porous carbon materials with sulfur and nitrogen dual-doping for energy storage." Green Chemistry **17**(3): 1668-1674.

ZHANG, K., et al. (2014). "From filter paper to carbon paper and toward Li–S battery interlayer." Materials Letters **121**: 198-201.

ZHANG, L., et al. (2015). "Flexible asymmetrical solid-state supercapacitors based on laboratory filter paper." ACS nano **10**(1): 1273-1282.

ZHAO, J., et al. (2013). "Electrochemical and thermal properties of hard carbon-type anodes for Na-ion batteries." Journal of Power Sources **244**: 752-757.

UAV-UNMANNED AERIAL VEHICLE COMPOSITE PROPELLER DESIGN:

INTEGRATED MODEL OF STRUCTURAL VON MISES AND SHEAR STRESSES UNDER PRESSURE/ VELOCITY, AND ENGINEERING ANALYSIS OF AEROACOUSTIC AND AERODYNAMIC FLOW EFFECT BY FEA-CFD-CFX

Özdoğan KARAÇALI[1]

CHAPTER 11

1 Department of Mechanical Engineering,Engineering faculty, İstanbul University-Cerrahpaşa, Avcılar, Istanbul, 34320 Turkey, ozdogank@istanbul.edu.tr

UAV-UNMANNED AERIAL VEHICLE COMPOSITE PROPELLER DESIGN:

INTEGRATED MODEL OF STRUCTURAL VON MISES AND SHEAR STRESSES UNDER PRESSURE/VELOCITY, AND ENGINEERING ANALYSIS OF AEROACOUSTIC AND AERODYNAMIC FLOW EFFECT BY FEA-CFD-CFX

Özdoğan KARAÇALI[1]

1. Brief Introduction to Unmanned Aerial Vehicle Technology

The Unmanned Air Vehicle-UAV is a remote control aircraft. UAVs are divided into two as remote operation or as a flight plan and automatic flight. Recently, UAVs have been used for a variety of civil and military i.e. fire fighting purposes. These tools are often used in difficult, dirty and dangerous missions for normal combat aircraft.

Today, many different shape, size, confusion and character vehicles are produced. Historically, UAVs are simply drones. However, independent control systems have been developed. The aim of this article is to reveal the differences UAVs propeller. First of all, UAVs can be reused. It can fly without stopping at a certain altitude. In addition, these vehicles fly with the help of a jet engine or two-stroke engine. Besides, cruise missiles are not classified as UAVs even if they are unmanned and controlled by remote control.

1 Department of Mechanical Engineering,Engineering faculty, İstanbul University-Cerrahpaşa, Avcılar, Istanbul, 34320 Turkey, ozdogank@istanbul.edu.tr

In some cases, the abbreviation for UAV has been extended to the UAVS (unmanned aerial vehicle systems). The American Federal Aviation Department has defined a general class as unmanned flight systems (IUS). In fact, this class was first used by the United States Navy to reflect not only planes but also ground systems and other elements [1].

It is also widely employed as an experimental platform in various research groups at the university to test and approve UAV, navigational guidance, dynamic simulation modeling and control purposes [1-6]. Unclassified unmanned aircraft have no standard. However, UAVs can be distinguished from each other by their weight, altitude, durability, size range, task and design proceses. This article focuses on the development of a new structural and flow engineering analysis approach based on the strength of the main structure, structural analysis, air speed and pressure reliability assessment in propeller design. The mini class is summarized in this study to develop a propeller for a universal aircraft. This article focuses on the strength calculations and weight and strength optimization of the body of this advanced UAV system. Figure 1 shows the researched UAV and the prototype solid model developed.

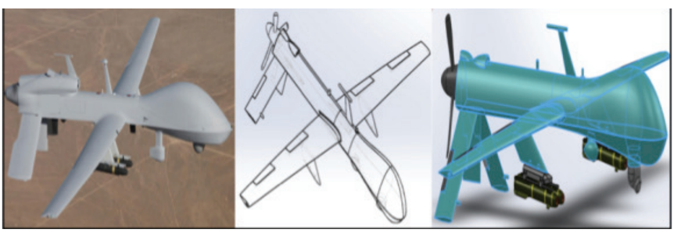

Figure 1: *Researched UAV and prototype solid model developed*

2. Propeller Design in UAV

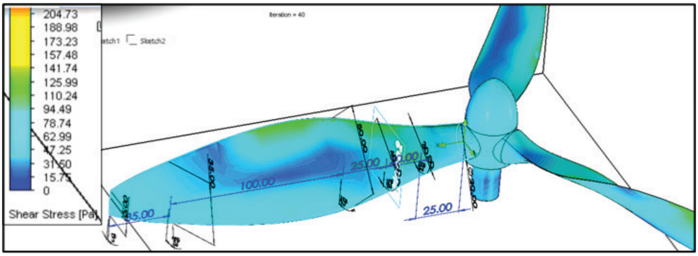

Figure 2: *Propeller dimansions*

In general, aerodynamic problems are often difficult to solve by analytical analysis. Experimental or numerical simulation can be used to analyze these calculation models as can be seen in Figure 2. However, the numerical method is more preferred because of the large expenses required in the test method. This article presents the modeling and simulation mesh operations of the computational fluid dynamic (CFD) problem in the UAV propeller model using the UAV propeller profile shown in Figure 3. ANSYS Fluent is used to analyze the pressure and velocity distribution on the propeller surface. Lifting and pulling forces were also determined by ANSYS structural analysis.

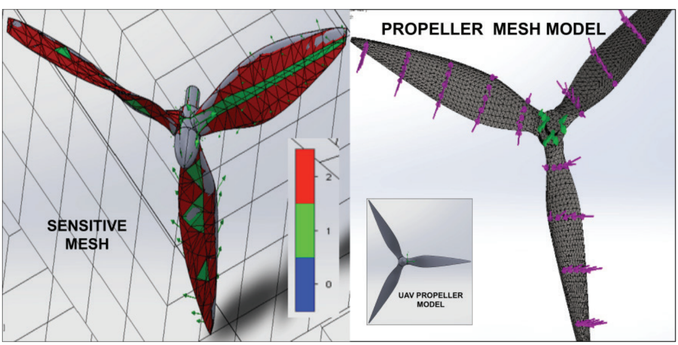

Figure 3: *UAV propeller model*

Figure 4 shows the position on the UAV propeller and UAV. Entirely tetrahedral formless meshes were realized for rotating flow and continuous flow areas. The use of free mesh is only as to the ability to parse multifaceted geometries quicker. The mesh becomes additionally sensitive nearby the propeller area and progressively increases to the fixed area. Mesh grid production affects the precision of the analysis, the required calculation time and the speed of convergence. The overall quantity of cells produced was 465521 with 943538 faces and 81853 nodes. Figure 3 displays the surface mesh of the propeller blade and more sensitive mesh analysis of the blades.

The reliability problem of the UAVs has become extremely important in recent years, such as maintenance and safety issues: the engines have become more robust, the avionics have been improved, and the propellers are able to withstand the loads and stresses of the main structures and materials of UAVs as they operate at high speed and pressure. [4-5]. Therefore, in this article, load and stress analysis of propeller structure of UAVs were studied.

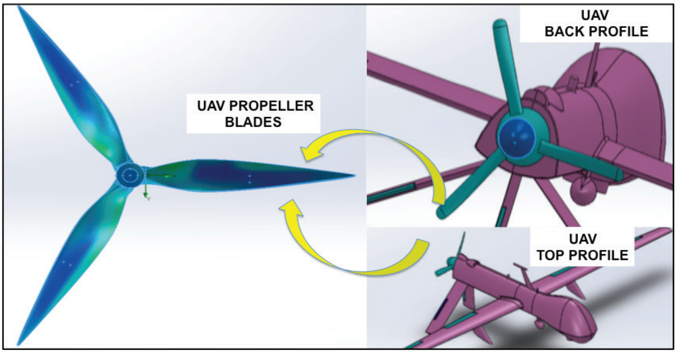

Figure 4: *UAV and propeller solid model in SOLIDWORKS*

3. Unmanned Aerial Propeller Literature

Today, as the emerging modern technology, UAVs are being used in many areas of daily life from the defense industry. Method of development of UAV propellers selection Numerical and experimental researches are summarized below, depending on the strength of the UAV and the altitude at which it will fly:

• Aerodynamic effects on corrugated and devastating wind blade in UAV propeller object: Analysis is performed both experimentally and numerically that the investigational data gathered is expended to verify numerical or computational data. The result demonstrates that design of the blade improves the total functioning of the propeller blade in low wind speed conditions compared to the flat and tubercle design [6].

• Experimentally designed wind tunnel design to measure propeller performance, including experimental and numerical methods: Experimentally performed in a low-noise wind tunnel to advance the impeller of the low Reynolds number propellers to undertake the analysis of the propeller blade. The properties of Reynolds numeral were analyzed with RPM variation varying from 1,600 to 8,000. The outcome displays that Reynolds number choices have significantly influenced complete aircraft work [7-8].

• Determining the performance of the numerical impeller: ANSYS CFD-Fluent was employed during the analysis of the UAV propeller. A chamber housing as the airflow area is input from the distance of the propeller blade. The outcome of the analysis related to pressures du to velocity displays that the presented CFD flow modeling method was able to deliver some reliable data for a margin of 0.001 to 0.013, correspondingly [9].

• Aeroacoustic effect on the UAV propeller: Broadband noise is produced by forces' random distribution on the propeller blade faces and may be triggered by an input of air turbulent [10]. The oscillating pressure zone may also be activated spontaneously while the boundary of developing turbulent layer cooperates with the impeller rear edges. The estimation of the rotating propellers theory, in particular the harmonic noise generated by the velocity of the spin propellers, is founded on analysis of the Fowcs-Williams/Hawkings [11]. The tonal additive to the acoustic pressure is associated with a source of propeller thickness and aerodynamic loading.

4. UAV Propeller Material Selection Survey: Composite Propellers

In this research, combining propeller design technology with synthetic fiber production, optimization of the air foils from the navel to the end is provided. The performance of the propeller increased some of the noise profile. The impeller is made of a hollow carbon and glass shell with excellent strength / weight, durability and very low inertia. Adjustable hubs provide individual blade replacement and infinite step adjustment. The electric variable pitch core is therefore adjusted in the flight analysis of the propeller angle for maximum climbing or discharging performance. UAV was designed using the minimum induced loss method for the primary design point in propeller research [12]

5. Material and Method for UAV Propeller Survey

The UAV propeller is a device that converts mechanical energy to the force that we call thrust and is used to push the UAV vehicle to which it is attached. The impeller of the UAV is the most powerful part of the entire system within the building frame. This has been designed with great care through SOLIDWORKS solid modeling, which allows the structural investigation and evaluation of the loads of the structure. In Figure 3, SOLIDWORKS has been meshed with solid modeling and an impeller mounted to the UAV is given. There are many factors to consider when choosing the right UAV propeller blades. UAV is the propeller material, power, speed, air density, maximum noise as factors determining propeller design [13]. UAV propeller blades have a significant impact on power and can affect the flight of an UAV softly. Therefore, one of the most important aspects is flight efficiency. The question to be answered as a research question is: uçuş how will the new UAV propeller blades increase the flight efficiency in the UAV? This article will answer these questions in the technical sense, how the velocity and pressure distribution on the surface of propeller affect the structural design of the propeller and the behavior of the material, the deformation rates, the effect of relative pressure and acoustic effect on the flight performance will be examined. Shear stress analysis of the UAVs was displayed in Figure 5. Figure 6 presents structural von Mises stresses on the UAV propeller. The von Mises stresses according to the air pressure vortex result in red coloration analysis. Figure 7 shows modal analysis of UAV propeller at different frequencies.

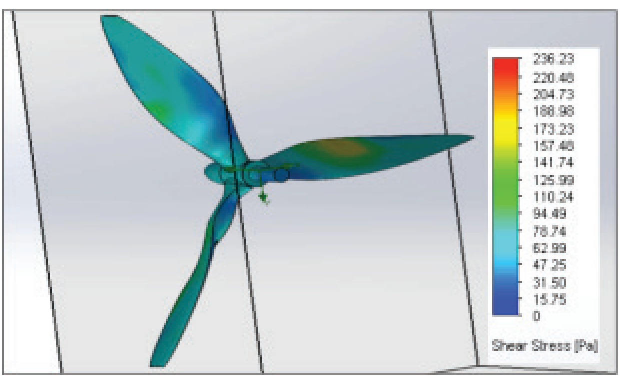

Figure 5: *Shear stress analysis of the UAVs*

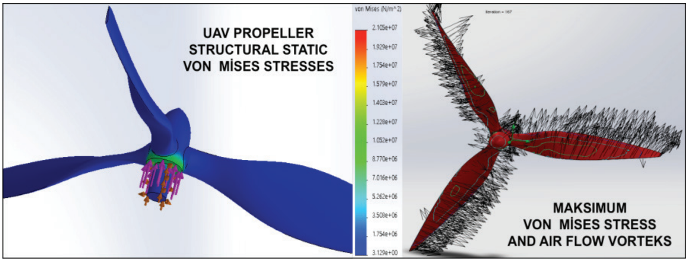

Figure 6: *Structural von Mises stresses on UAV propeller*

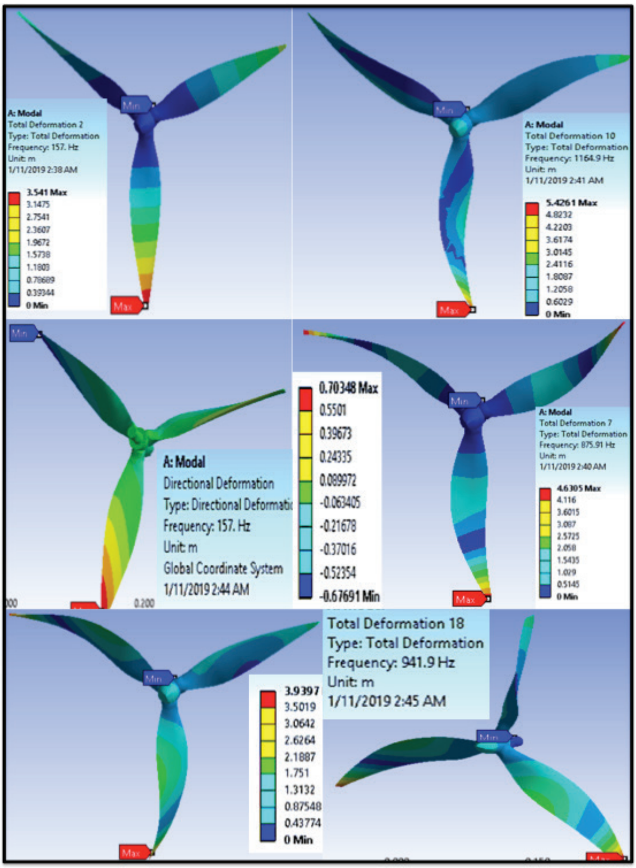

Figure 7: *Modal analysis of UAV propeller at different frequencies*

Number of blades and size of blades The number of blades required in the blades of the UAV varies depending on the platform, usage and handling load requirements. The length of this propeller blade selected to be 0.65 m long and 0.17 m wide was used to transport heavy transport loads. The UAV propeller blade constructed in SOLIDWORKS was analyzed by finite element method (SEY) in ANSYS. The pressure on the propeller surface was tested during take-off and flight and was in parallel with computational analysis. Figure 8 shows the pressure on the surface of the UAV propeller [Pa].

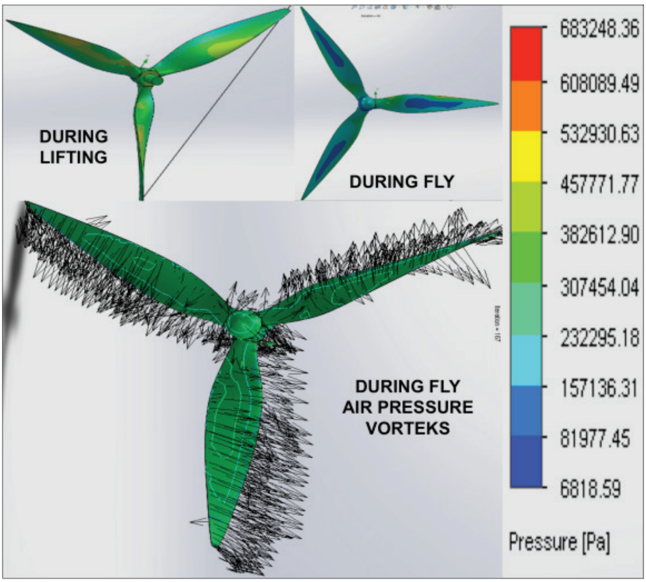

Figure 8: *Pressure on the surface of the UAV propeller [Pa]*

The pitch is defined as the movement or distance of the propeller for a single revolution (1 full turn). The correct pitch will usually depend on the specific application for an iha platform. The low slope causes more torque and less turbulence for frequent lifting, and as a result, the engines do not have to work too hard to carry heavy transport loads that can lead to a prolonged flight time (the motors draw less current than the battery). High-thrust propellers carry more air, but generally generate more turbulence and less torque [14].

Figure 9 shows the relative pressure focal points at the high altitude to the UAV propeller, deformation and a model of the wings to accurately predict the deformation. The relationship between the internal pressure and stiffness of the material UAV propeller and external loads effect on the surface were demonstrated. One of the benefits of the test tool is that the mechanical alternative state of the UAV propeller shape has proved to be a useful and necessary instrument for verification and control of the aerodynamic efficiency.

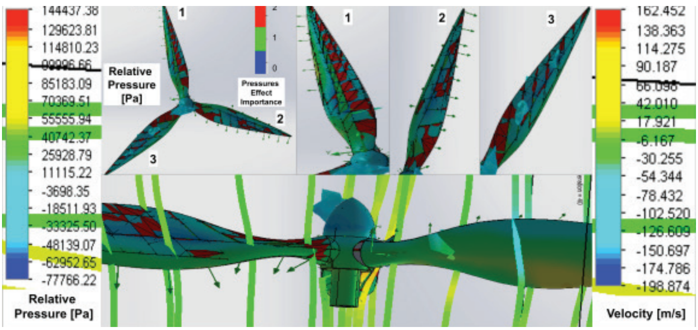

Figure 9: *Relative pressure from UAV propeller [Pa]*

This study analyzes the propeller performance on the flat propeller blade using ANSYS Fluent. The flow area is divided into the global stationary region and the rotating region. The numerical algorithm developed in this study was built on a finite volume method with pressure and velocity co-located in the propeller cell center. Figure 10 shows the structural and CFD flow analysis of the propeller in the y-axis direction. It was observed that the air pressure of the airborne UAV formed on the propeller formed shear stress on propeller blades. The shear stress obtained from the propeller surface was found to be a maximum of 21903 Pa.

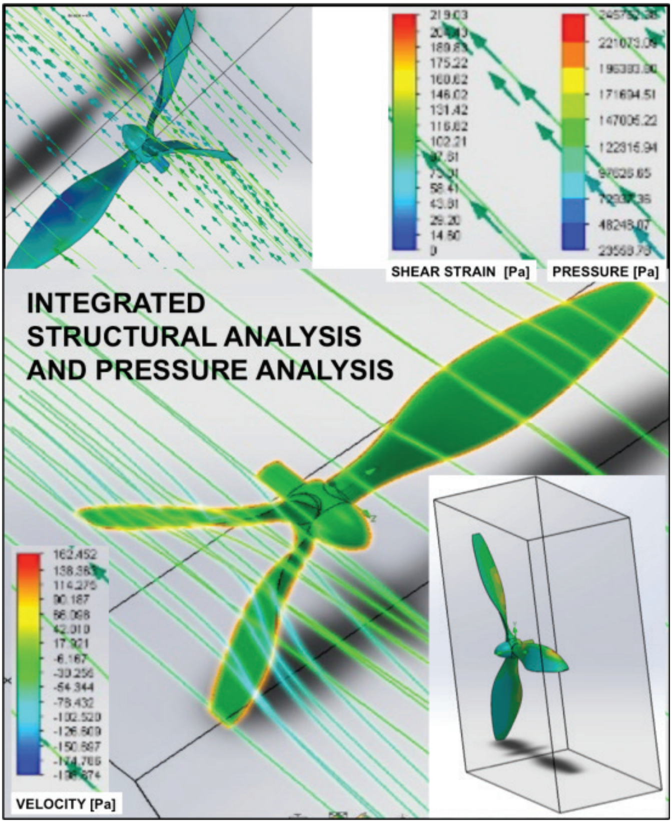

Figure 10: *Structural and CFD flow analysis in the y-axis direction of the UAV propeller*

The CFD analysis of Figure 10 provided knowledge established on the objectives of the analysis - such as torque, thrust, air flow line information, pressure distribution, air velocities and additional data. Determining the boundary conditions in the order of the problem has determined the altering circumstances for evaluation. These UAV propeller integrated design CFD and structural analysis research space of boundary conditions incorporate with the air flow speed to the working region, the integrated air and surface temperature and the rotation of the UAV propeller caused by pressure in space. The UAV propeller CFD analysis program, calculated as the pressure, speed information, during the operation of the flying vehicle depending on the model of the finite element model is placed in the new model to determine the strain and stress needed to determine the load was also used.

To ensure that the UAV propeller can resist the forces affected when working at the greatest engine speed, results of the pressure analysis at highest level of engine speed have been transferred to the ANSYS simulation program to perform a FEA analysis. FEA analysis was established to produce stress information values and their position or places on the appointed execurive model, deformation amount and value of safety factor. In Figure 11, the effect of acoustic power on the surface of UAV is given by ANSYS analysis. The UAV, which is expected to operate silently, is especially related because of the intense growth in the number of issues for civilian and military reasons. The silence and effectiveness of the propulsion structure are important elements in advanced aircraft design and may often extend to the success or breakdown of the duty [9].

The analysis of the aerodynamic behaviours activity is the initial move in experimental and theoretical investigations of sound output from propellers. In addition to evaluating the efficiency required to estimate the performance of impulse, torque and impeller, aerodynamic computations may specify load distribution across the aperture of the UAV propellers, which are straightforwardly dependable for the entire noise [10-14].

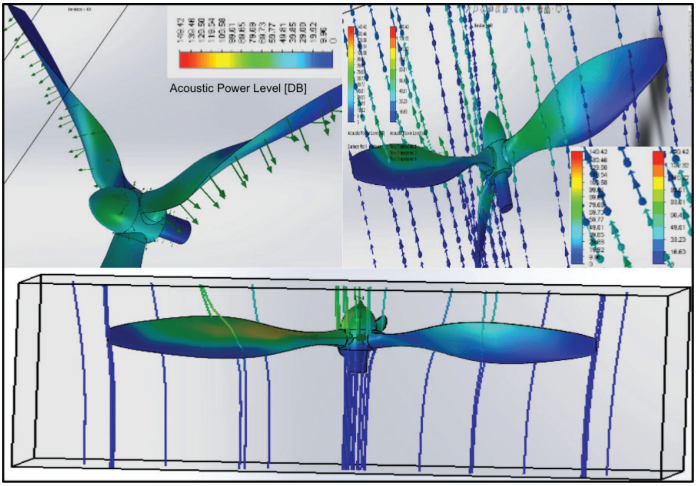

Figure 11: *Acoustic power effect on surface of UAV [dB]*

It is a necessary input for consecutive acoustic calculations. From the results of the aerodynamic analysis, it can be easily understood that its precision deeply affects the reliability of the latest aeroacoustic effect results in research findings.

Figure 12 shows the density strength deformation analysis of the UAV propeller. In the ongoing flight repetitions, the deformation of the UAV propeller surface significantly reduced the aerodynamic efficiency and increased the noise level. Figure 13 shows deformation of UAV propeller ANSYS analysis results are given. Functional structure in flow area measurementscan be seen, where deformation occurs on the surface as in Figure 12.

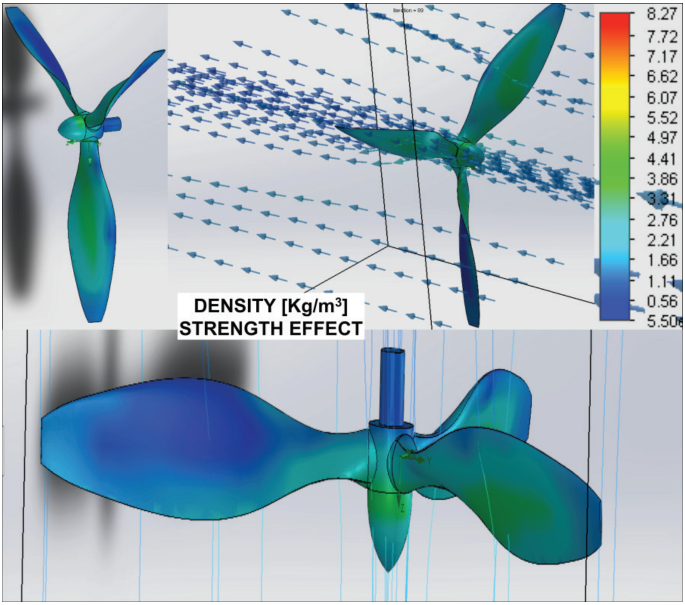

Figure 12: *Density strength deformation analysis of UAV propeller*

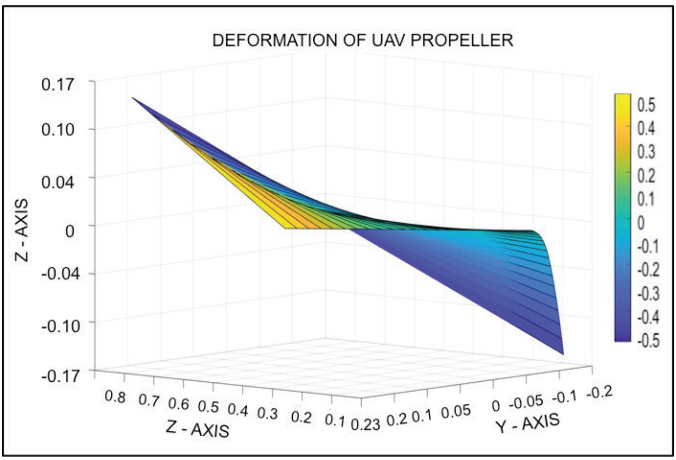

Figure 13: *Deformation of UAV propeller [mm]*

6. Results and Discussion

In this study, propeller design and physical details of the UAV are presented. The aerodynamic, aeroacoustic and structural multi-disciplinary design and analysis strategy of the unmanned combat air vehicle has been proposed. In the implementation of the strategy, after the initial dimensions of the UAV propeller have been defined, a structural analysis model generator with the ANSYS computer program is used to construct the finite element model for solid model and structural analysis. As shown in Figure 3 and Figure 4, both static and flight stress analysis of the solid model and von Mises torsion analysis were performed. In the finite element model of the structure, shear stresses, density strength, deformations on the surface of the UAV propeller are modeled. By combining CFD flow analysis with ANSYS structural UAV propeller modeling, both the effect of air pressure and surface deformations resulting from the composite material were measured as in Figure 10 and the surface was protected without reaching the deformation.

This aerodynamic-structural integrated design optimization for the UAV propeller is the most complex problem in this research. In the UAV propeller analysis, it was seen that the results were obtained with computational method. Further research will focus on more disciplined impacts such as impulse, flight performance, stability, and controls for UAV performance.

7. Conclusions

A computational simulation research was accomblished out to determine the aerodynamic and aeroakustic features of the aircraft UAV and the effect of air flow and structural analysis. In this study, an UAV design and structural analysis, air flow analysis were investigated. The propeller is an important part of the unmanned aircraft, and it has been observed in this study that the performance directly affects the safety of the UAV. ANSYS analysis results show that the static strength of the impeller meets the design requirements. This study will be confirmed by the flight test in future studies.

8. Acknowledgements

Istanbul University-Cerrahpaşa this study was to provide tangible support, BAP (Scientific Research Projects) No. 29286, Avcılar, Istanbul, Turkey

9. KAYNAKLAR

[1]U. Ozdemir, Y. O. Aktas, A. Vuruskan, Y. Dereli, A. Farabi, T. K. Demirbag, A. Erdem "Design of a Commercial Hybrid VTOL UAV System" J Intell Robot Syst (2014) 74:371–393 doi: 10.1007/s10846-013-9900-0

[2]W. A.J. Anemaat, M. Schuurman, W. Liu, A. Karwas "Aerodynamic Design, Analysis And Testing of Propellers For Small Unmanned Aerial Vehicles" American Institute Of Aeronautics And Astronautics DOI: 10.2514/6.2017-0721

[3]L. Cambiera, S. Heib, S. Plot "The Onera Elsa Cfd Software: Input From Research And Feedback From Industry" Mechanics & Industry 14, 159–174 (2013) Afm, Edp Sciences 2013 Mechanics doi: 10.1051/Meca/2013056

[4]Z. Ning, R. Wlezien, H Hu "An Experimental Study On Small UAV Propellers With Serrated Trailing Edges" AIAA Aviation Forum 5-9 June 2017, Denver, Colorado 47th Aiaa Fluid Dynamics Conference

[5]M. I. Khan, M. A. Salam1, M. R. Afsar, M. N. Huda, D) T. Mahmud "Design, Fabrication & Performance Analysis Of An Unmanned Aerial Vehicle" International Conference On Mechanical Engineering Aip Conf. Proc. 1754, 060007-1–060007-7; Doi: 10.1063/1.4958448

[6]S. Kumar, P. C. Mishra "Finite Element Modeling For Structural Strength Of Quadcoptor Type Multi Mode Vehicle" Aerospace Science and Technology 53 (2016) 252–266, doi: 10.1016/J.Ast.2016.03.020

[7]F. Mazhar, A. M. Khan, I. A. Chaudhry, M. Ahsan "On Using Neural Networks In UAV Structural Design For Cfd Data Fitting and Classification" Aerospace Science And Technology 30 (2013) 210–225 doi: 10.1016/j.ast.2013.08.005

[8]D. Park, Y. Lee, T. Cho, C Kim "Design And Performance Evaluation of Propeller For Solar-Powered High-Altitude Long-Endurance Unmanned Aerial Vehicle" Hindawi

International Journal Of Aerospace Engineering Volume 2018, Article Id 5782017, doi: 10.1155/2018/5782017

[9]S. Gaggero, C. M. Rizzo, G. Tani, M Viviani "EFD and CFD Design And Analysis Of A Propeller In Decelerating Duct" International Journal of Rotating Machinery Volume 2012, Article Id 823831, Doi:10.1155/2012/823831

[10]G. Sinibaldi, L. Marino "Experimental analysis on the noise of propellers for small UAV" Applied Acoustics 74 (2013) 79–88 doi: 10.1016/j.apacoust.2012.06.011

[11]S. Rajappa, M. Ryl, H. Bu "Modeling, control and design optimization for a fully-actuated hexarotor aerial vehicle with tilted propellers" 2015 IEEE International Conference on Robotics and Automation (ICRA) Washington State Convention Center, Seattle, Washington, May 26-30, 2015

[12]A. T. Mushynski, T. J. Johnson "Analysis And Design ff A Low Reynolds Propeller For Optimal Unmanned Aerial Vehicle (Uav) Flight" Proceedings Of The ASME 2017 International Mechanical Engineering Congress And Exposition IMECE2017 November 3-9, 2017, Tampa, Florida, USA IMECE2017-71164

[13]T. Vogeltanz "A Survey of Free Software for the Design, Analysis, Modelling, and Simulation of an Unmanned Aerial Vehicle" Arch Computat Methods Eng (2016) 23:449–514 doi:10.1007/s11831-015-9147-y

[14]M. Felli1,M. Falchi" Propeller wake evolution mechanisms in oblique flow conditions" J. Fluid Mech. (2018), vol. 845, pp. 520–559. Cambridge University Press 2018 doi:10.1017/jfm.2018.232

NEW FINDINGS ON SEISMITES IN THE UPPER MIOCENE-PLIOCENE DEPOSITS, DENİZLİ BASIN, SW TURKEY

Savaş TOPAL[1]

CHAPTER 12

1 Department of Geological Engineering, Pamukkale University, Turkey, savastopal@pau.edu.tr

NEW FINDINGS ON SEISMITES IN THE UPPER MIOCENE-PLIOCENE DEPOSITS, DENİZLİ BASIN, SW TURKEY

Savaş TOPAL [1]

INTRODUCTION

Soft-sediment deformation structures (SSDS) expose as a result of liquefaction or fluidization in water-saturated and unconsolidated sediments. Those liquefaction or fluidization caused by different natural processes (Owen, 1987). SSDS are named as seismites related to seismically-induced liquefaction or fluidization. Deformation structures formed by shakes produced by earthquakes caused by faults are defined as seismites (Seilacher, 1969). Seismites are a type of SSDS that can be proved as a result of shaking. Seismic activity is generally thought to be the cause of this event.

Seismites have been observed in many geological environments as streams, delta and lake (Topal and Özkul, 2014). Denizli basin in the SW Turkey is one of the principal seismic areas of Aegean Graben System (Koçyiğit, 2005). The area was affected much possible historical earthquakes although it has a low-moderate seismic index. Although some historical seismic records were provided from a few antique cities such as Hierapolis, Tripolis and Laodikea in the basin (Altunel, 2000), there is no information about the earthquakes in the prehistoric period since Miocene.

The SSDS defined in this study were formed in the lake deposits. Lake environments are the sedimentation areas that reflect the results of seismic and tectonic activity as the deformation structure during sedimentation. The aim

1 Department of Geological Engineering, Pamukkale University, Turkey, savastopal@pau.edu.tr

of this study; to define the seismites observed in lacustrine rocks in the Miocene-Pliocene sequence in the Denizli basin and to interpret the trigger mechanisms.

Geological Setting

NW-trending Denizli basin is one of the grabens of the Aegean extensional province and bounded by normal faults from both southern and northern margins (Westaway, 1993). The basin was filled by Neogene alluvial, lacustrine and fluvial deposits (Fig. 1). The Neogene succession unconformably is underlain by the pre-Neogene rock units that include Paleozoic marble, quartzite and schist and Mesozoic crystalline limestones. The basement units are covered by Upper Miocene sediments which was defined Kızılburun, Sazak, Sakızcılar and Kolankaya formation from base to top respectively. These four units together are named as Denizli group in the previous studies (Sun, 1990). This study has been performed in Kolankaya formation comprising seismites (Fig. 1).

Kolankaya formation which is a typical lacustrine fan delta succession thickening and coarsening upward, mainly consisting of poorly consolidated sand and gravely sand and interlayered with claystone, siltstone, limestone and marl. At the north part of the basin the formation passes laterally into Sakızcılar formation at the base and covered unconformably by Quaternary Asartepe formation, travertine, slope waste and alluvium at the top. In the studied area, the dominant color of the formation is yellowish brown. In addition, rather frequently quartz pebbles are observed in the unit. The pebbles are usually rounded to subrounded and well cemented in some levels. Although age of the Kolankaya formation is offered as evaluated lower Pliocene according to the fossil assemblage by Taner (1974), It is recently ascribed to the Upper Miocene-Pliocene (Alçiçek et al., 2007).

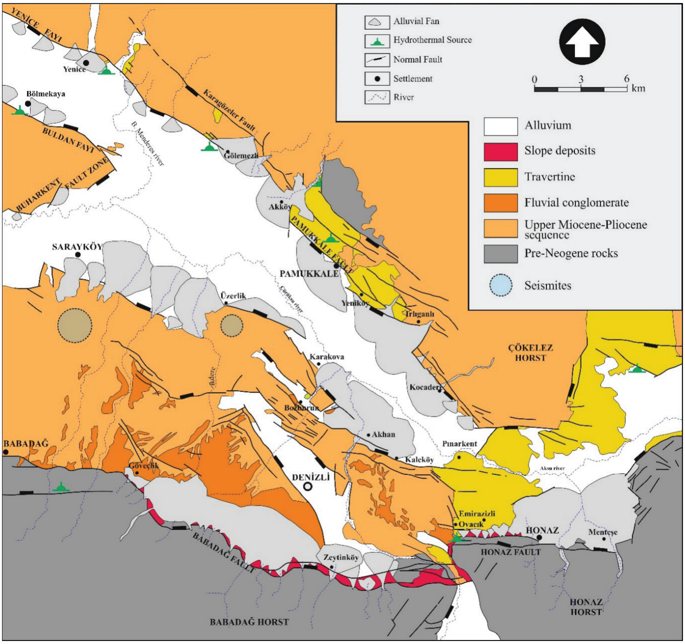

Figure 1. *Geological map of Denizli basin (Koçyiğit, 2005).*

Seismites in the Study Area

SSDS encountered during field studies; clastic dykes, water escape structures and load casts and flame structures.

Clastic dykes: These structures are formed by the upward transport of sediments with pore water (Lowe, 1975). Such clastic dykes may also occur as a result of the upward movement of the flowing sediment under the pressure of the upper layer. The dykes observed in the study area; developed in relation to the upward and lateral movement of the sands as a result of liquefaction and fluidization (Fig. 2).

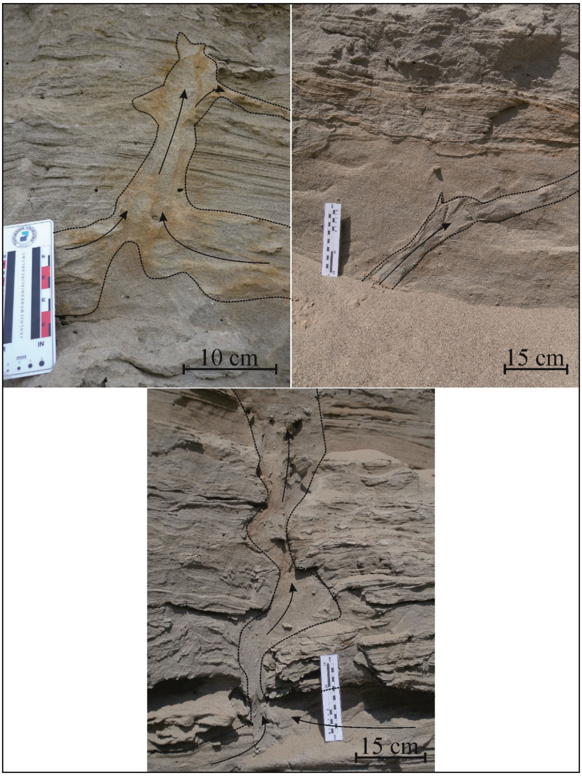

Figure 2. *Different sizes of clastic dykes in the study area.*

Water escape structures: These structures are the best indicators of liquefaction and water leakage processes as a SSDS (Fig. 3). Water escape structures are the structures formed as a result of liquefaction and fluidization of water limited to sand with low permeability layers (Owen, 1987).

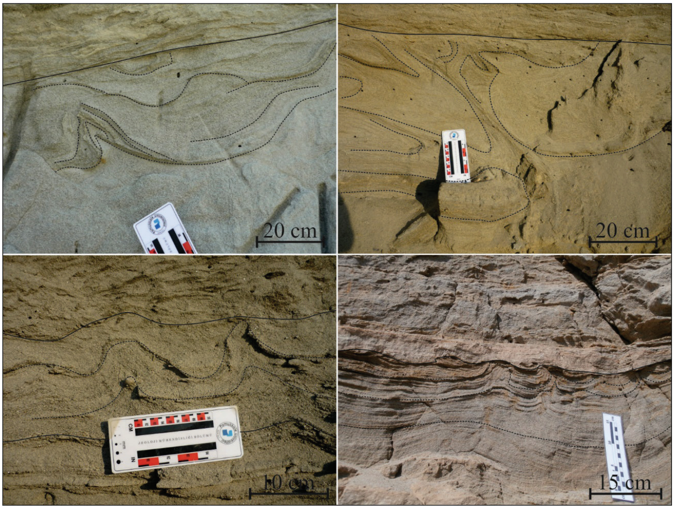

Figure 3. *Water escape structures in the study area.*

Load casts-flame structures: Flame structures develop between sediment layers with a high kinematic viscosity ratio (Anketell et al., 1970). Flame structures arise from the diapiric inlet of fine sediments (Mills, 1983). Similar to those described by Moretti and Sabato (2007), it was most likely triggered by seismic activity in the study area. In response to gravitational differences between the two sediment layers, load patterns are formed due to liquefaction (Fig. 4). The size and shape of the charge plates are controlled by the vertical density gradient and the ratio of kinematic viscosities of the liquefaction layer (Mills, 1983).

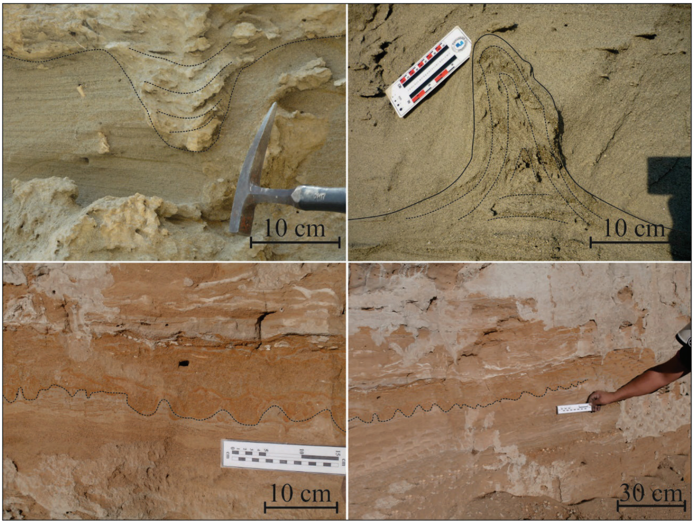

Figure 4. *Load casts and flame structures in the study area.*

Discussion

SSDS are a term used to change the fabric and layers of newly deposited sediments (Nichols, 2009). Generally, SSDS occur as a result of loss of shear strength in water-saturated granular sediments. This loss of strength is associated with liquefaction and / or fluidization of water resulting from increased pore pressure (Allen, 1982; Owen, 1987).

The most common forms of deformation structures in lacustrine sediments are; sediment load that creates upper pressure (Lowe, 1975), storm effect (Molina et al., 1998) and seismic shaking (Seilacher, 1969; Rodriguez-Pascua et al., 2000). The deformation structures observed in the lacustrine sediments of Denizli basin were evaluated in terms of the triggering mechanisms mentioned above. No data showing the effects of sediment load or storm waves caused pressure on the layers. The most effective mechanism in the formation of such structures is seen as seismic vibrations.

Conclusions

When the prehistoric, historical and instrumental seismic data of the Denizli basin is analyzed, it is seen that it is a very seismically active basin and the opening is still continuing. The Neogene and Quaternary sedimentary deposits in the basin were cut by many normal faults and took the current topographic form.

The stratigraphic record of the old earthquakes in the Neogene sequence can be seen in many different ways. These records are called seismites structures. In this study, earthquake-related deformation structures, clastic dykes, water escape structures and load casts-flame structures identified in the Upper Miocene - Pliocene sequence were collected in three different groups.

As a result of the studies, Upper Miocene-Pliocene sequence and hence the region is frequently affected by Miocene and subsequent earthquakes greater than 5.

REFERENCES

Alçiçek, H., Varol, B. and Özkul, M. 2007. Sedimentary facies, depositional environments and palaeogeographic evolution of the Neogene Denizli Basin of SW Anatolia, Turkey. Sedimentary Geology, 202, 596-637.

Allen, J.R.L. 1982. Sedimentary structures: their character and physical basis. Developments in Sedimentology. Elsevier, Amsterdam (663 p.).

Altunel, E. 2000. Historical earthquake activity in and around Hierapolis. Ricerche Archeologiche Turche Nella Valle Del Lykos, Eds: D'Andria F, Silvestrelli F. 299-325, (in Italian and Turkish).

Anketell, J.M., Cegla, J. and Dzulynsky, S. 1970. On the deformational structures in systems with reversed density gradients. Ann. Soc. Geol. Pol., 40(1): 3-30.

Koçyiğit, A. 2005. The Denizli graben-horst system and the eastern limit of western Anatolian continental extension: basin fill, structure, deformational mode, throw amount and episodic evolutionary history, SW Turkey. Geodinamica Acta 18, 167-208.

Lowe, D.R. 1975. Water escape structures in coarse grained sediments. Sedimentology, 22, 157-204.

Mills, P.C. 1983. Genesis and diagnostic value of soft-sediment deformation structures -a review. Sedimentary Geology 35, 83–104.

Molina, J.M., Alfaro, P., Moretti, M., Soria, J.M. 1998. Soft-sediment deformation structures induced by cyclic stress of storm waves in tempestites (Miocene, Guadalquivir Basin, Spain). Terra Nova 10, 145-150.

Moretti, M., Sabato, L. 2007. Recognition of trigger mechanisms for soft-sediment deformation in the Pleistocene lacustrine deposits of the Sant'Arcangelo Basin (Southern Italy): seismic shock vs. overloading. Sedimentary Geology 196, 31-45.

Nichols, G. 2009. Sedimentology and Stratigraphy, Wiley-Blackwell, 419p.

Owen, G. 1987. Deformation processes in unconsolidated sands, in: Jones, M.E., Preston, R.M.F. (Eds.), Deformation of Sediments and Sedimentary Rocks. Geol. Soc. London Spec. Publ. 29, pp. 11–24.

Rodriguez-Pascua, M.A., Calvo, J.P., De Vicente, G., Gomez-Gras, D. 2000. Soft-sediment deformation structures interpreted as seismites in lacustrine sediments of the Prebetic Zone, SE Spain, and their potential use as indicators of earthquake magnitudes during the Late Miocene. Sedimentary Geology 135, 117-135.

Seilacher, A. 1969. Fault-graded beds interpreted as seismites. Sedimentology 13, 155–159.

Sun, S. 1990. Denizli-Uşak Arasının Jeolojisi ve Linyit Olanakları, MTA Rapor no: 9985, Ankara.

Taner, G. 1974. Denizli Bölgesi Neojeninin Paleontolojik ve Stratigrafik Etüdü, MTA. Dergisi, 82, 89-127.

Topal, S. and Özkul, M. 2014. Soft-Sediment Deformation Structures Interpreted as Seismites in the Kolankaya Formation, Denizli Basin (SW Turkey). The Scientific World Journal, Article ID: 352654, http://dx.doi.org/10.1155/2014/3526.

Westaway, R. 1993. Neogene evolution of the Denizli region, of western Turkey. Journal of Structural Geology, 15, 37-53.

BASİC COMPONENT ANALYSİS AND DİSCRİMİNANT ANALYSİS METHOD TO DİSTİNGUİSH EEG SİGNALS

Sevcan AYTAÇ KORKMAZ[1]

CHAPTER 13

1 Electronic and Automation Department, Fırat University, Elazığ, Turkey
sevcanaytackorkmaz@gmail.com

BASİC COMPONENT ANALYSİS AND DİSCRİMİNANT ANALYSİS METHOD TO DİSTİNGUİSH EEG SİGNALS

Sevcan AYTAÇ KORKMAZ[1]

1. INTRODUCTION

The name of the organ that controls the nervous system, stores all information and builds intelligent building, understands, thinks and decides on emotional functions is called the brain. Although the studies on the brain continue for a long time, the brain; doctors, and scientists, many uncertainties include unknown and complex structures. In addition, the human brain produces a variety of signals, and these signals have been analyzed over the years and at the same time proved to be usable signals. These signals are also referred to as EEG or Electroencephalograms [1]. Signs with low amplitude defined by the electrodes from the brain surface are called EEG signals. EEG signals produced by neurons are located in the cerebral cortex. These signals give many different notices. On the other hand, EEG signals; as rhythms formed by the rhythm centers located in the depths of the brain. These potentials are registered in an irregular attitude and externalized in the sea. These signals acquired in the human brain keep a lot of information, but not yet used as a whole. Since EEG signals have a low amplitude, this information is difficult to succeed. EEG signals are now available; to define head trauma and sleep interested disease, to determine the level of anesthesia of an anesthetized patient, to define epilepsy, to be cheap, and to intercept suffering in many areas. However, the evaluation of this information is limited by the deficiency of clear criteria. For this reason, the use of EEG sşgnals in clinical identification has become possible

1 Electronic and Automation Department, Fırat University, Elazığ, Turkey sevcanaytackorkmaz@gmail.com

thanks to the analysis of EEG signals in the light of increasing technological developments. Brain; besides the disease that may come into being, it can affect the human life in a bad way because it is a very important organ. The use of these signals in the identification and handling of diseases is an intense research topic in the scientific domain in the near future, as well as the resolution of problems with the help of the signs received from the brain during disease treatment [2]. Because of this reason, EEG signals can be analyzed by different methods and an objective estimation can be made. In statistical analysis of the signal, some of these methods have been improved in recent years and other methods have been used to determine specific waveforms during the resolution and examination stage[3]. EEG recording and analysis methods have become one of the most used methods in the identification and treatment of brain diseases. In particular, it is possible to increase the recording times of EEG devices, to registry a fixed diskette by connecting to a computer, to registry patients' EEG for one or more days, or even for a long period of time, thus achieving well results than EEG analyzes. Karkov (1875), one of the earliest stages of EEG use, has also shown that there is a change in the amplitude of cortex muscle signals in spite of acoustic stimulation, as well as being a subject of more than 150 years of literature research [4]. These methods have been applied based on the use of EEG signals in determining the depth of anesthesia by referring to many methods. Mustafa Tosun and colleagues designed an artificial neural network model using the whole frequency range covered by the EEG signals (1-50 Hz) and trained this model with heart rate in this model and as a result 94% of the successful anesthesia level [4]. Soo-young Ye et al. Reported that 20-50 values of the Bispectrum index range between 0-100 values in the study they conducted indicated anesthesia, indicating a wakefulness for 60-100 values, and indicated that the EEG frequency range was below 8 Hz in determining the depth of anesthesia [5]. Laxman Tawade et al. Investigated the detection of epilepsy disorder by using the Discrete Wavelet Transform method on EEG signals. They were arrested at the end of a 96% success in detecting epilepsy [6]. Maan M. Shaker reported that using the Discrete Wavelet Transform and Fourier transforms in his work on EEG signals and at the end of the study he achieved very successful results by classifying the noise canceled EEG signals with the Discrete Wavelet Transform and splitting the EEG waves into delta, tetra, alpha and beta classes [7]. C.M. Sweeney-Reed and colleagues demonstrated using the Empirical Mode Decomposition method that it is possible to reach the desired frequency band on the EEG signals. In this study, the desired band interval IQ functions were obtained synchronized with the EEG signals [8]. Li X and colleagues successfully analyzed the epileptic EEG signals using an empirical Kip decomposition based method, since they can be divided into numerical and minor Numerical Kip Functions of non-stationary complex signals [9]. Zhang X et al. Proposed an EEG-derived model (Lembel-Ziv Complexity Analysis) based on the relation of anesthesia depth to brain activity and found that it achieved a real-time success rate of 93% thanks to the model proposed in determining the depth of anesthesia [10]. V. Esmaeilia and colleagues developed an EEG based fuzzy logic structure to detect the depth of anesthesia and performed a study to achieve the goal of 4 grouping (awake anesthesia compliance, operation sequence anesthesia and isolation) on single channel EEG data [11]. In a study performed by Rüştü Güntürkün anesthesia level, Elman network structure in the 1-50 Hz frequency range including 30 in the middle layer and 60 neurons in the entrance layer was trained using the Power Spectral Densities of the EEG signals and found an anesthesia level with a 95% success rate at the end of the study [12].

2.THEORY AND METHODS

In this study; to analyze EEG signals from healthy and sick people in different groups with some machine learning techniques and to automatically classify these signals with a computer assisted system. EEG signals in 5 different groups were used in this study. These groups are called Set A, Set B Set C, Set D, and Set E classes.

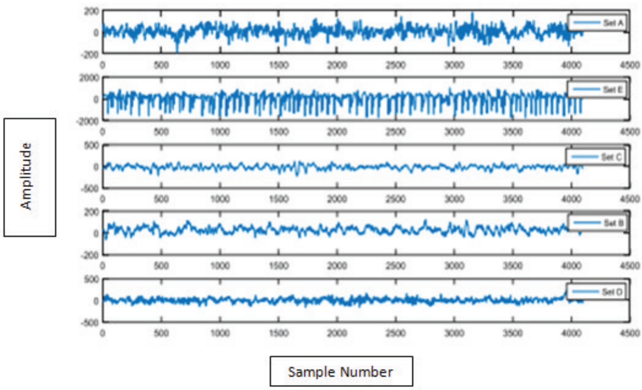

Figure 1.1: *EEG signals in the 5 different group [13]*

The signals of Set A and Set B in Figure 1.1 are given to healthy persons. However, Set A is the signal from the healthy eyes. Set C, Set D, and Set E belong to the epilepsy patients. Set C and Set D are signals from the damaged half-curette and the undamaged half-curette when not in the epileptic seizure. Set E is the signal taken while in epileptic seizure. Each set has 100 sample signals. In other words, a total of 500 EEG signal samples were used because there were 5 groups in this study.

Table 1.1: *Feature-Success Rate Table*

Feature	Success Rate(%)	Feature	Success Rate(%)
5	30,4	**60**	34,8
10	24,8	**65**	40,8
15	28,0	**70**	39,2
20	34,0	**75**	41,2
25	32,8	**80**	38,0
30	32,8	**100**	39,2
35	31,2	**200**	38,0
40	31,2	**300**	32,4

2.1 Basic Component Analysis For Dimension Download (PCA)

Basic component analysis studies initiated by Karl Pearson in 1901 were developed by Hotelling in 1933 [14]. Basic Component Analysis (PCA) is a method that is widely used in image recognition studies, also called prime component analysis or Karhunen-Loeve transformation. PCA is a transformation technique that allows the reduction of size to a smaller size, preserving the values of the dimensions that contain multiple data sets [15]. This analysis aims to determine the best transformation that can be expressed with fewer variables. These variables obtained after the transformation are called the basic components of the initial variables. The first principal component is the largest variance value, and the other major components are the sequential ones with the variance values decreasing. The basic components are perpendicular to each other. PCA's advantages include low sensitivity to noise, reduced memory and capacity requirements, and more efficient operation in less space [16]. PCA is used because it provides ease of understanding mathematical elements such as matrix, eigenvalue, eigenvector, and complex computation algorithms because it forms the basic solution model for the new techniques required [17]. Basic component analysis is a multivariate statistical method that provides size reduction by describing the variance-covariance structure of a data set consisting of variables with the help of linear combinations of these variables [18].

2.2. Discriminant Analysis (DA)

The analysis used in the derivative of the Fisher Discriminant is extended to find a subspace which is observed to contain changeability belonging to all classes if there are more than one class. Let's assume that each class *f* has a mean of one δ and the same *Σ* covariance. Class variability is described as the example covariance of class averages.

$$\Sigma_b \frac{1}{f} \Sigma_{i=1}^{f} (\delta - \delta).(\delta_i - \delta)^T \tag{1}$$

Where "δ" is the average of the class averages. The "y" r-oriented class distinction is expressed as follows.

$$S = \frac{\vec{y}^T \, \Sigma_b \, \vec{y}^T}{\vec{y}^T \, \Sigma \, \vec{y}} \tag{2}$$

The eigenvalue vector for   is the eigenvalue corresponding to the difference between the classes. Since rank has these nonzero eigenvalues, the features of the vectors contain a vector that describes the subspace. These vectors are used especially for vector reduction. The eigenvalues with the smallest value will be very sensitive to the good choice of the training data and may need a regulation. There are a number of alternative methods, if classification is needed instead of size reduction, For example, after classes have been separated, the standard

Fisher Discriminant or discriminant analysis method is used to classify each difference. Usually used in an example, a class is placed in a group and everything else is placed in another group and the discriminant analysis is implemented [19].

3. RESULTS

Machine learning techniques have been applied to many fields [20-27]. In this study, some machine learning techniques have been implemented to EEG signals. The aim of this study is to analyze EEG signals from healthy and sick people in different groups with some machine learning techniques and to predict their class as an automat with a computer-assisted system. In this study, 5 different groups of EEG signals were used in a size of 4097x500. In this study, Basic Component Analysis for Dimension Download (PCA) and Discriminant Analysis (DA) were used as methods. In this study, the success rate of classification was low. In this study, the classification success rate is high as seen from the number of the feature-success rate in Table 1.1. The classification result was found to be 41.2%. Classification by methods used for this reason is not a suitable classifier to recognize these EEG signaling.

REFERENCES

[1] Demir, Ö., "EEG Dalgalarının Dalgacık (Wavelet) Dönüşümü İle Değerlendirilmesi", Yüksek Lisans Tezi, *Dumlupınar Üniversitesi Fen Bilimleri Enstitüsü,* Elektrik-Elektronik Mühendisliği Anabilim Dalı, Kütahya, (2008).

[2] Batar, H., "EEG İşaretlerinin Dalgacık Analizi Yöntemleri Kullanılarak Yapay Sininr Ağlarıyla Sınıflandırılması", Yüksek Lisans Tezi, *Sütçü İmam Üniversitesi Fen Bilimleri Enstitüsü,* Elektrik-Elektronik Mühendisliği Anabilim Dalı, Kahramanmaraş, (2005).

[3] Alkan, A., "Eeg İşaretlerinin Ayrıştırılmasında, Altuzay Yöntemlerinin Kullanılması", *Journal of Yaşar University*, 1(3), 211-213, (2006).

[4] Coşkun, M., "Yapay Sinir Ağları yardımı ile EEG Tabanlı Anestezi Derinliği Tahmini için Yöntemler", Fen Bilimleri Enstitüsü, Balıkesir Üniversitesi, 2013.

[5] Ye, S., Park, J., Kim, J., Jung, J., Jeon, A., Kim, I., et al., "Development for the Evaluation Index of an Anesthesia Depth using the Bispectrum Analysis", *International Journal of Biological and Medical Sciences*, 4, 67-70, (2009).

[6] Tawade, L. and Warpe, H., "Detection of Epilepsy Disorder Using Discrete Wavelet Transforms Using Matlabs", *International Journal of Advanced Science and Technology*, 28 , March (2011).

[7] Shaker, M.M., "EEG Waves Classifier using Wavelet Transform and Fourier Transform", *International Journal of Biological and Life Sciences,* 1:2, 85-90, (2005).

[8] Sweeney-Reed, C.M., Andrade, A.O. and Nasuto, S.J., "Empirical mode decomposition of EEG signals for synchronization analysis.", *3rd IEEE EMBSS UK and RI postgradute conference in Biomedical Engineering and Medical Physics*, IEEE EMB Student Society UKRI, 15-16, (2004

[9] Li, X., Chu, M., Qiu, T. and Bao, H., "An EMD based time-frequency distribution and its application in EEG

analysis", *Sheng Wu Yi Xue Gong Cheng Xue Za Zhi.*, 24(5), 990-995, (2007).

[10] Zhang, X., Roy, R.J. and Jensen, E.W. "EEG complexity as a measure of depth of anesthesia for patients", *IEEE Transactions on Biomedical Engineering,* 48, (12), 1424-1433, (2011).

[11] Esmailie, V. and Assareh, A., "Estimating the depth of anesthesia using fuzzy soft computation applied to EEG Features", *Intelligent Data Analysis,* 12, 393-407, (2008).

[12] Gunturkun, R., "Using Elman Recurrent Neural Networks with Conjugate Gradient Algorithm in Determining the Anesthetic the Amount of Anesthetic Medicine to be Applied", *J Med Syst*, 34, 479–484, (2010).

[13]Alçin, Ömer F., et al. "Multi-category EEG signal classification developing time-frequency texture features based Fisher Vector encoding method." *Neurocomputing* 218 (2016): 251-258.

[14]Yazar, I., 2008. Temel Bileşen Analizi ve Bağımsız Bileşen Analizi Yöntemlerini Temel Alan Bazı Görüntü Tanıma Uygulamaları ve Karşılaştırmaları, *Yüksek Lisans Tezi*, Eskişehir Osmangazi Üniversitesi Fen Bilimleri Enstitüsü.

[15]Sengur, A., 2008. An expert system based on principal component analysis, artificial immune system and fuzzy k-NN for diagnosis of valvular heart diseases, *Computers in Biology and Medicine*, 38.3, 329-338.

[16]Abdi, H. and Lynne J., 2010. Principal component analysis, *Wiley Interdisciplinary Reviews: Computational Statistics*, 2.4,433-459.

[17]Jolliffe, I., 2005. Principal component analysis, *John Wiley & Sons*, Ltd.

[18] Saraswat, M., Wadhwani, A. K. and Manish, D., 2013. Compression of Breast Cancer Images by Principal Component Analysis, *International journal of Advanced Biological and Biomedical Research,* 1, 767-776.

[19] Karakitsos, P., Megalopoulou, T. M., Pouliakis, A., Tzivras, M., Archimandritis, A., & Kyroudes, A. (2004). Application of discriminant analysis and quantitative cytologic examination to gastric lesions. Analytical and quantitative cytology and histology/the International Academy of Cytology [and] American Society of Cytology, 26(6), 314-322.

[20] Korkmaz, S. A., & Esmeray, F. (2018, March). Quality lignite coal detection with discrete wavelet transform, discrete fourier transform, and ANN based on k-means clustering method. In *2018 6th International Symposium on Digital Forensic and Security (ISDFS)* (pp. 1-6). IEEE.

[21] ESMERAY, F., & ÖZERCAN, İ. H. (2018). Mini-Review: THE CLASSIFICATION STUDIES DONE FOR EARLY DIAGNOSIS OF THE STOMACH CANCER. *The Online Journal of Science and Technology-October*, *8*(4).

[22] ESMERAY, F., & ÖZERCAN, İ. H. (2018). MACHINE LEARNING APPLICATIONS IN DETECTION OF THE BREAST CANCER: MINI-REVIEW. *The Online Journal of Science and Technology-April*, *8*(2).

[23] Korkmaz, S. A., & Esmeray, F. (2018). A New Application Based on GPLVM, LMNN, and NCA for Early Detection of the Stomach Cancer. *Applied Artificial Intelligence*, *32*(6), 541-557.

[24] Esmeray F, Korkmaz SA (2018) Electricity Affecting the Production of Artificial Neural Network Classification by Value. Computer Trends Inf Sci Technol 3 (1): 001-004.

[25]Korkmaz, S. A., & Esmeray, F. (2018). Rastgele Orman Bazlı Sınıflandırma ile MSER özellikleri için Yerel Teğet Alan Hizalama ve Mahalle Koruma Yerleşimi: MSER_DFT_LTSA-NPE_RF. International Journal of Modern Research in Engineering and Technology, 3(2), 31-37.

[26] ESMERAY, F., & ÖZERCAN, İ. H. (2018). Sağlık Bilimleri Örnek Alıştırmalar Kitabı. NOBEL Akademik Yayıncılık, Kasım, 1. Baskı, 433-436.

[27] ESMERAY, F., & ÖZERCAN, İ. H. (2018). Sağlık Bilimleri Örnek Alıştırmalar Kitabı. NOBEL Akademik Yayıncılık, Kasım, 1. Baskı, 439-442.

CLASSIFICATION OF EEG SIGNALS BY STOCHASTIC PROXIMITY EMBEDDING AND RANDOM FOREST METHODS

Sevcan AYTAÇ KORKMAZ[1]

CHAPTER 14

1 Electronic and Automation Department Fırat University Elazığ, Turkey
sevcanaytackorkmaz@gmail.com

CLASSIFICATION OF EEG SIGNALS BY STOCHASTIC PROXIMITY EMBEDDING AND RANDOM FOREST METHODS

Sevcan AYTAÇ KORKMAZ[1]

1.INTRODUCTION

It is the brain that controls the nervous system, stores all information, and at the same time builds intelligent structure, understands, thinks and decides on emotional functions. Although the work on the brain lasts for centuries, the brain; physicians and scientists into a complex structure. Because the brain; Many uncertainties include unknown and complex structures. The human brain produces a variety of signals and these signals have been analyzed over the years and at the same time proved to be usable signals. These signals are also called EEG or Electroencephalogram in medicine. [1]. Signs with low amplitude detected by the electrodes from the brain surface are called EEG signals. EEG signals produced by neurons are located in the cerebral cortex. These signals give many different warnings. On the other hand, EEG signals; as rhythms formed by the rhythm centers located in the depths of the brain. These potentials are recorded in an irregular manner and reflected in the sea. These signals obtained in the human brain keep a lot of information, but not yet used as a whole. Since EEG signals have a low amplitude, this information is difficult to achieve. EEG signals are now available; to detect head trauma and sleep related illnesses, to determine the level of anesthesia of an anesthetized patient, to detect epilepsy, to be cheap, and to avoid suffering in many areas. However, the evaluation of this information is limited by the lack of certain criteria. For this reason, the use of EEG markers in clinical diagnosis

1 Electronic and Automation Department Fırat University Elazığ, Turkey sevcanaytackorkmaz@gmail.com

has become possible thanks to the analysis of EEG signals in the light of increasing technological developments. Brain; besides the illnesses that may come into being, it can affect the human life in a bad way because it is a very important organ. The use of these signals in the diagnosis and treatment of diseases is an intense research topic in the scientific field in the near future, as well as the resolution of problems with the help of the signs received from the brain during disease treatment [2]. Because of this reason, EEG signals can be analyzed by different methods and an objective evaluation can be made. In statistical analysis of the signal, some of these methods have been developed in recent years and other methods have been used to determine specific waveforms during the decomposition and examination phase[3]. EEG recording and analysis methods have become one of the most used methods in the diagnosis and treatment of brain diseases. In particular, it is possible to increase the recording times of EEG devices, to record a fixed diskette by connecting to a computer, to record patients' EEG for one or more days, or even for a long period of time, thus achieving healthier results than EEG analyzes. Karkov (1875), one of the earliest stages of EEG use, has also shown that there is a change in the amplitude of cortex muscle signals in spite of acoustic stimulation, as well as being a subject of more than 150 years of literature research [4].

These methods have been applied based on the use of EEG signals in determining the depth of anesthesia by referring to many methods.

Maan M. Shaker have used Fourier Transform and Discrete Wavelet Transform in their studies on EEG signals. and as a result of the study, the noise was canceled and classified EEG signals by Discrete Wavelet Transform and very successful results were obtained for delta, tetra, alpha and beta classes by separating EEG waves [4].

Li X et al have been successfully analyzed epileptic EEG signals using an experimental Mode decomposition-based method. In addition, they have stated that these can be divided into small numerical modes and numerical functions of non-stationary complex signals [5].

C.M. Sweeney-Reed and colleagues have indicated using the Empirical Mode Decomposition method that it is possible to reach the desired frequency band on the EEG signals. In study, the requested band interval IQ functions have been obtained synchronized with the EEG signals [6].

Mustafa Tosun et al. Have designed an artificial neural network model that uses the entire frequency range covered by EEG signals (1-50 Hz). and this model has been trained with the heart rate. and success rate of anesthesia level was found to be 94% [7].

Laxman Tawade et al. The detection of epilepsy disorder was investigated by using the Discrete Wavelet Transform method in EEG signals. Epilepsy detected, the 96% success rate was obtained [8].

In the study conducted by Soo-young Ye et al., It was reported that 20-50 values of Bispectrum index ranged between 0-100 values, that they were awake at 60-100 values and that the EEG frequency range has been below 8 Hz in determining the depth of anesthesia [9].

In a study conducted with Rüştü Güntürk's anesthesia level, 30 neurons in the middle layer and 60 neurons in the input layer were trained using the Power Spectral Intensities of the Elman network EEG signals in the 1-50 Hz frequency range. and 95% success rate was obtained at the end of the study [10].

V. Esmaeilia et al. have developed an EEG-based fuzzy logic to determine the depth of anesthesia. In study, it have been executed a study to achieve its goal on single-channel EEG data [11].

Zhang X et al. An EEG model based on the relationship between depth of anesthesia and brain activity has been proposed. and a real-time success rate of 93% has been achieved with the proposed model for determining the depth of anesthesia [12].

2.THEORY AND METHODS

Main purpose of this study is to analyze EEG signals from sick and healthy people in different groups with some machine learning techniques and to automatically classify these signals with a computer aided design. EEG signals in 5 different classes have been used in this study. These classes are called Set A, Set B Set C, Set D, and Set E groups [13]. Each set has 100 sample signals. In other words, a total of 500 EEG signal samples have been used. Because, there are 5 classes in this study.

Table 1.1: *Feature-Success Rate Table*

Feature	Success Rate(%)	Feature	Success Rate(%)
5	41,2	**60**	67,2
10	48,4	**65**	69,6
15	49,6	**70**	64,4
20	51,6	**75**	68,4
25	56,4	**80**	65,2
30	57,6	**85**	70,4
35	59,2	**90**	64,8
40	60,0	**95**	66,0
45	64,4	**100**	65,2
50	63,2	**200**	71,6
55	66,0	**300**	65,2

2.1.Stochastic Proximity Embedding (SPE)

SPE uses a self-organizing scheme that embarks to bring each individual stress $(d_{ij} - r_{ij})^2$ rapidly to zero. The method starts with an initial configuration and iteratively refines it by repeatedly selecting two points at random, and adjusting their coordinates so that their Euclidean distance on the map d_{ij} matches more closely their corresponding proximity r_{ij}. The verification is proportional to the disparity λ $\frac{|r_{ij} - d_{ij}|}{d_{ij}}$, where is a learning rate parameter that decreases during the course of the refinement to avoid oscillatory behavior [14]. The detailed algorithm is as follows:

1. Initialize the coordinates x_i . Select an initial learning rate .

2. Select a pair of points, i and j, at random and compute their distance$d_{ij} = \|x_i - x_j\|$. If $d_{ij} \neq r_{ij}$, update the coordinates x_i and x_j by:

$$x_i \leftarrow x_i + \lambda \frac{1}{2} \frac{r_{ij} - d_{ij}}{d_{ij} + \varepsilon} (x_i - x_j) \qquad (1)$$

And

$$x_j \leftarrow x_j + \lambda \frac{1}{2} \frac{r_{ij} - d_{ij}}{d_{ij} + \varepsilon} (x_j - x_i) \qquad (2)$$

where ε is a small number to avoid division by zero.

3. Repeat (2) for a prescribed number of steps S.

4. Decrease the learning rate λ by prescribed decrement δλ.

5. Repeat (2)–(4) for a prescribed number of cycles C.

2.2. Random Forest (RF)

RF is a wood type classifier method. Also Gini indexide can be used in RF classifier. The division position according to the smallest Gini index can be determined by Gini index. To create a tree with an RF classifier, two separate parameters must be entered. These parameters are m and N parameters. m represents the number of variables used in each node. N represents the number of trees to be developed to determine the best part [15,16]. The initial value M must be entered randomly from the outside. Subsequent m's are reduced or increased according to the overall error rate. Classification accuracy is determined by generalized error data. Taking into account the P training data, a new P training data is generated.

Tree-type classifiers in the RF classifier are used in the $\{h(x, \theta_p) P = 1, \dots\}$ type. where, *x* is the input data; θ_P showes the random vector. The $h(x, F_p)$ classifier is constructed using the new training data set. The *x* and *y* are not found in F_k. When a random pixel is choosed for a given training F data set, this pixel belongs to class M_i .Thus, the Gini index is expressed as below.

$$\sum \sum_{j \neq i} (f(M_i, F)/|F|)(f(M_j, F)/|F|) \tag{3}$$

Here, F is the training data set, M_i is the class to which a randomly selected pixel belongs, $f(M_i, F)/|F|)$ indicates the possibility of belonging. to the M_i class of the selected example.

3. RESULTS

Machine learning models were applied to many fields [17-24]. In this study, some machine learning techniques have been applied to EEG signals. The purpose of this study is to analyze EEG signals from healthy and sick people. EEG signals in 5 different groups were used in this study. Stochastic Proximity Embedding (SPE) and Random Forest (RF) were used in this study. In this study, the classification success rate is high as seen from the number of the feature-success rate in Table 1.1. Classification result was found as 71.6%. For this reason, the methods used in this study are suitable classifiers to recognize these EEG signaling.

REFERENCES

[1] Demir, Ö., "EEG Dalgalarının Dalgacık (Wavelet) Dönüşümü İle Değerlendirilmesi", Yüksek Lisans Tezi, *Dumlupınar Üniversitesi Fen Bilimleri Enstitüsü,* Elektrik-Elektronik Mühendisliği Anabilim Dalı, Kütahya, (2008).

[2] Batar, H., "EEG İşaretlerinin Dalgacık Analizi Yöntemleri Kullanılarak Yapay Sininr Ağlarıyla Sınıflandırılması", Yüksek Lisans Tezi, *Sütçü İmam Üniversitesi Fen Bilimleri Enstitüsü,* Elektrik-Elektronik Mühendisliği Anabilim Dalı, Kahramanmaraş, (2005).

[3] Alkan, A., "Eeg İşaretlerinin Ayrıştırılmasında, Altuzay Yöntemlerinin Kullanılması", *Journal of Yaşar University*, 1(3), 211-213, (2006).

[4] Shaker, M.M., "EEG Waves Classifier using Wavelet Transform and Fourier Transform", *International Journal of Biological and Life Sciences,* 1:2, 85-90, (2005).

[5] Li, X., Chu, M., Qiu, T. and Bao, H., "An EMD based time-frequency distribution and its application in EEG analysis", *Sheng Wu Yi Xue Gong Cheng Xue Za Zhi.*, 24(5), 990-995, (2007).

[6] Sweeney-Reed, C.M., Andrade, A.O. and Nasuto, S.J., "Empirical mode decomposition of EEG signals for synchronization analysis.", *3rd IEEE EMBSS UK and RI postgradute conference in Biomedical Engineering and Medical Physics*, IEEE EMB Student Society UKRI, 15-16, (2004)

[7] Coşkun, M., "Yapay Sinir Ağları yardımı ile EEG Tabanlı Anestezi Derinliği Tahmini için Yöntemler", Fen Bilimleri Enstitüsü, Balıkesir Üniversitesi, 2013.

[8] Tawade, L. and Warpe, H., "Detection of Epilepsy Disorder Using Discrete Wavelet Transforms Using Matlabs", *International Journal of Advanced Science and Technology*, 28 , March (2011).

[9] Ye, S., Park, J., Kim, J., Jung, J., Jeon, A., Kim, I., et al., "Development for the Evaluation Index of an Anesthesia Depth using the Bispectrum Analysis", *International*

Journal of Biological and Medical Sciences, 4, 67-70, (2009).

[10] Gunturkun, R., “Using Elman Recurrent Neural Networks with Conjugate Gradient Algorithm in Determining the Anesthetic the Amount of Anesthetic Medicine to be Applied”, *J Med Syst*, 34, 479–484, (2010).

[11] Esmailie, V. and Assareh, A., “Estimating the depth of anesthesia using fuzzy soft computation applied to EEG Features”, *Intelligent Data Analysis,* 12, 393-407, (2008).

[12] Zhang, X., Roy, R.J. and Jensen, E.W. “EEG complexity as a measure of depth of anesthesia for patients”, *IEEE Transactions on Biomedical Engineering,* 48, (12), 1424-1433, (2011).

[13]Alçin,ÖmerF.,etal.“Multi-categoryEEGsignalclassification developing time-frequency texture features based Fisher Vector encoding method.” *Neurocomputing* 218 (2016): 251-258.

[14] Agrafiotis, Dimitris K. “Stochastic proximity embedding.” *Journal of computational chemistry* 24.10 (2003): 1215-1221.

[15] Iakovidis, Dimitrios K., et al. “zz.” Computer-Based Medical Systems, 2005. Proceedings. 18th IEEE Symposium on. IEEE, 2005.

[16]Korkmaz, S. A., & Binol, H. (2017). Analysis of Molecular Structure Images by using ANN, RF, LBP, HOG, and Size Reduction Methods for early Stomach Cancer Detection. Journal of Molecular Structure.

[17] Korkmaz, S. A., & Esmeray, F. (2018, March). Quality lignite coal detection with discrete wavelet transform, discrete fourier transform, and ANN based on k-means clustering method. In *2018 6th International Symposium on Digital Forensic and Security (ISDFS)* (pp. 1-6). IEEE.

[18] ESMERAY, F., & ÖZERCAN, İ. H. (2018). Mini-Review: THE CLASSIFICATION STUDIES DONE FOR EARLY

DIAGNOSIS OF THE STOMACH CANCER. *The Online Journal of Science and Technology-October*, *8*(4).

[19] ESMERAY, F., & ÖZERCAN, İ. H. (2018). MACHINE LEARNING APPLICATIONS IN DETECTION OF THE BREAST CANCER: MINI-REVIEW. *The Online Journal of Science and Technology-April*, *8*(2).

[20] Korkmaz, S. A., & Esmeray, F. (2018). A New Application Based on GPLVM, LMNN, and NCA for Early Detection of the Stomach Cancer. *Applied Artificial Intelligence*, *32*(6), 541-557.

[21] Esmeray F, Korkmaz SA (2018) Electricity Affecting the Production of Artificial Neural Network Classification by Value. Computer Trends Inf Sci Technol 3 (1): 001-004.

[22]Korkmaz, S. A., & Esmeray, F. (2018). Rastgele Orman Bazlı Sınıflandırma ile MSER özellikleri için Yerel Teğet Alan Hizalama ve Mahalle Koruma Yerleşimi: MSER_DFT_LTSA-NPE_RF. International Journal of Modern Research in Engineering and Technology, 3(2), 31-37.

[23] ESMERAY, F., & ÖZERCAN, İ. H. (2018). Sağlık Bilimleri Örnek Alıştırmalar Kitabı. NOBEL Akademik Yayıncılık, Kasım, 1. Baskı, 433-436.

[24] ESMERAY, F., & ÖZERCAN, İ. H. (2018). Sağlık Bilimleri Örnek Alıştırmalar Kitabı. NOBEL Akademik Yayıncılık, Kasım, 1. Baskı, 439-442.

6 TH INTERNATIONAL, MULTICONGRESS GAZIANTEP, 26 - 27 APRIL 2019

A SOFTWARE APPLICATION OF SERVICE ORIENTED COMPUTING

Ali Evren GÖKSUNGUR[1]

CHAPTER 15

1 Department of Computer Engineering, Nişantaşı University, İstanbul, Turkey

6 TH INTERNATIONAL, MULTICONGRESS GAZIANTEP, 26 - 27 APRIL 2019

A SOFTWARE APPLICATION OF SERVICE ORIENTED COMPUTING

Ali Evren GÖKSUNGUR[1]

1. INTRODUCTION

According to developing technologies smart solutions become more important at big data operations. Since complex software operations need to be reduced to execute too many different transactions quickly. Service Oriented computing method provides to simplify computer programs operations by using associate web service solutions. Service Oriented Computing SOAP uses web services to produce any kind of complex multiple data solutions. In this paper, a software application of service oriented computing is explained in details. By using Soap method instead of too many software programs many problem may solve with quick web service solutions.

2. Service Oriented Computing - Related Literature

Previous Research on Service Oriented Computing

Service Oriented Computing method is based on web services as fundamental elements to develop software solutions to any kind of business process. By using this method complex transactions are completed easily with composite web services. (M.P. Papazoglou, 2003, p.2.) Instead of too many software program operations ; The

1 Department of Computer Engineering, Nişantaşı University, İstanbul, Turkey

advantage of service Oriented computing is directly to send a request and to get a response and this method provides a way to create a new architecture that will define a quick solution to software problems. (M.N. Huhns, M.P. Singh, 2005, p. 75-81.) Before to decide to use Service Oriented Computing method Organizations should consider about value of service level and quality in addition to the cost and duration of delivered services. So if any organization need to solve a big data software problem then according to its infrastructure, service needs should define and according to service needs s quick solution may develop by using Service Oriented Computing Method. (Demirkan, Delen, April 2013, p. 412-421). Servie Oriented Architecture (SOA) is an architectural style in building Web applications based on services. Also security is very important and secure connection according to trust logic of any kind of software operations it is possible to define a trust-based SOA solution based on an identified trust definition. Because trust is an important factor in successful online operations, it is a major criterion for service selection. (Zainab M.Aljazzaf, Miriam A.M.Capretz, MarkPerry, 2016, p.470-480).

For each software problem, individual solutions should develop by using web service solutions. To define a web service solution: Three basic standard is in use: These are: (Simple Object Access Protocol) SOAP: Communication: how services can be used. WSDL: Description: How services can be published. UDDI: Discovery: how services can be discovered. According to these standards effective solutions may be proceed to manage web services easily. (Nathan Griffiths, Kuo-Ming Chao, 2010, p. 24-25.)

3. Methods

Service-oriented architecture (SOA) is a style of software design where services are provided to the other components by application components, through a communication protocol over a network.

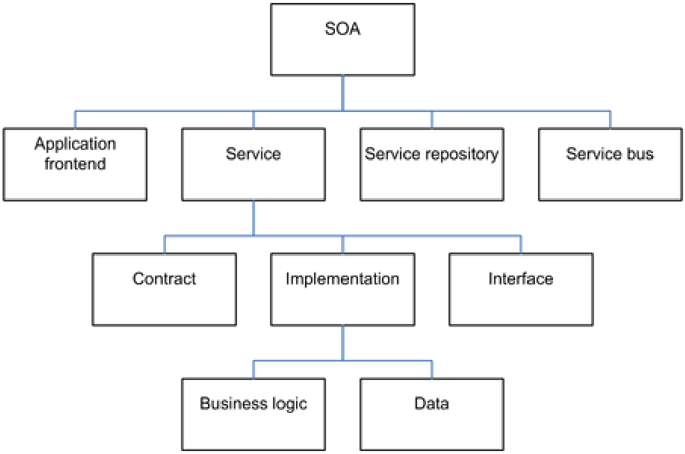

Fig. 1. *Service Oriented Architecture (SOA)*

Service Oriented Computing is also include;

- Service Based Solutions
- Uses an iterative process
- Component Based Development
- Business Process Management
- Web services composition
- API/Service Design

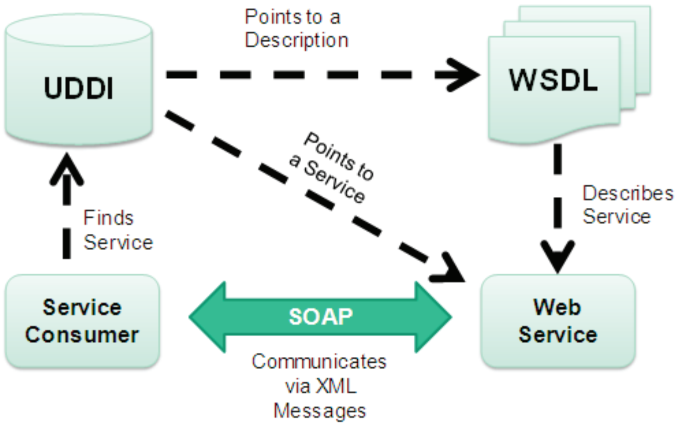

Fig.2. *Web Services - Basic Architecture (SOAP, WSDL, UDDI)*

SOAP: (Simple Object Access Protocol)

SOAP is an XML-based protocol for exchanging information between computers.

SOAP is a communication protocol.

SOAP is for communication between applications.

SOAP is a format for sending messages.

SOAP is designed to communicate via Internet.

SOAP is platform independent.

SOAP is language independent.

SOAP is simple and extensible.

SOAP allows you to get around firewalls.

SOAP will be developed as a W3C standard.

WSDL:

WSDL is an XML-based language for describing web services and how to access them.

WSDL stands for Web Services Description Language.

WSDL was developed jointly by Microsoft and IBM.

WSDL is an XML based protocol for information exchange in decentralized and distributed environments.

WSDL is the standard format for describing a web service.

WSDL definition describes how to access a web service and what operations it will perform.

WSDL is a language for describing how to interface with XML-based services.

WSDL is an integral part of UDDI, an XML-based worldwide business registry.

WSDL is the language that UDDI uses.

UDDI:

UDDI is an XML-based standard for describing, publishing, and finding web services.

UDDI stands for Universal Description, Discovery, and Integration.

UDDI is a specification for a distributed registry of web services.

UDDI is platform independent, open framework.

UDDI can communicate via SOAP, CORBA, and Java RMI Protocol.

UDDI uses WSDL to describe interfaces to web services.

UDDI is seen with SOAP and WSDL as one of the three foundation standards of web services. UDDI is an open industry initiative enabling businesses to discover each other and define how they interact over the Internet. SOAP provides a mechanism that can be used to exchange messages between Web service clients and servers.

UDDI using SOAP, and its interface is described using WSDL.

4. Results and Discussion

According to develop a Software Application of Service Oriented Computing. A health insurance software application is examined. Three basic standard is used to develop the best web service solution for this application. These three basic standards are: (Simple Object Access Protocol) SOAP: WSDL and UDDI. Also, health insurance web service is analyze with 3 method related the data structure as compute method to calculate the policy firstly. Then secondly approve method is used to approve the policy and finally print out method is used to get the pdf document of the policy.

According to develop an application of web service based solution. By using SOAP platform and WSDL methods the health insurance data set is defined as input and according to this solution.

Approve function:

Input:

```
<soapenv:Envelope xmlns:soapenv=”http://schemas.xmlsoap.org/soap/envelope/” xmlns:for=”ForeignersHealth”>
   <soapenv:Header/>
   <soapenv:Body>
      <for:Approve>
         <!--Optional:-->
         <for:Input>
            <for:PrintType>1</for:PrintType>
            <for:IsTestMode>0</for:IsTestMode>
            <for:Channel>30806</for:Channel>
            <!--Optional:-->
            <for:Username>30806001</for:Username>
            <!--Optional:-->
            <for:TrackingCode>2019-03-22-000518-59518093</for:TrackingCode>
            <!--Optional:-->
            <for:CitizenshipNumber>0</for:CitizenshipNumber>
            <!--Optional:-->
            <for:TaxNumber>6368806578</for:TaxNumber>
            <for:UnitNo>11266123</for:UnitNo>
            <for:PolicyNo>22756878</for:PolicyNo>
```

Output:


```
<soap:Envelopexmlns:soap="http://schemas.xmlsoap.org/soap/envelope/" xmlns:xsi="http://www.w3.org/2001/XMLSchema-instance" xmlns:xsd="http://www.w3.org/2001/XMLSchema">
  <soap:Body>
    <ComputeResponse xmlns="ForeignersHealth">
      <ComputeResult>
        <IsSuccess>true</IsSuccess>
        <StatusCode>status-success</StatusCode>
    <StatusDescription>Teklif alma süreci tamamlandı. (Hesaplanan Brüt Prim: 789,11 ₺)</StatusDescription>
     <TrackingCode>2019-03-22-000518-59518093</TrackingCode>
        <UnitNo>11266123</UnitNo>
         <Premium>789.11</Premium>
     <BeginDate>2019-05-01T00:00:00</BeginDate>
        <EndDate>2020-05-01T00:00:00</EndDate>
        <PolicyNo>22756878</PolicyNo>
```


5. Conclusion

To develop dynamic software applications by using service oriented computing method. Each software solution should analyze according to define firstly its service oriented architecture and then its data structure should analyze to develop effective web service solutions. In this paper, an application is analyze and according to web service standards, the problem is defined in three stage for a health insurance software application. Compute, Approve and Print web services are defined then a software program is developed to combine these web services and effective software solution is applied according to service oriented computing method.

6. REFERENCES

[1] M.P. Papazoglou, Service-oriented computing: concepts, characteristics and directions, **Published in:** Proceedings of the Fourth International Conference on Web Information Systems Engineering, 2003. WISE 2003.. **Print ISBN:** 0-7695-1999-7, p.2 (https://ieeexplore.ieee.org/abstract/document/1254461)

[2] M.N. Huhns , M.P. Singh , Service-oriented computing: key concepts and principles , Published in: IEEE Internet Computing (Volume: 9 , Issue: 1 , Jan-Feb 2005), p. 75-81. https://ieeexplore.ieee.org/document/1407782

[3] Haluk Demirkan , Dursun Belen , Decision Support Systems , Published by Elsevier B.V. , Volume 55, Issue 1, April 2013, Pages 412-421 https://www.sciencedirect.com/science/article/pii/S0167923612001595

[4] Zainab M.Aljazzaf , Miriam A.M.Capretz , MarkPerry, Trust-based Service-Oriented Architecture , Journal of King Saud University - Computer and Information Sciences, Volume 28, Issue 4, October 2016, Pages 470-480https://www.sciencedirect.com/science/article/pii/S1319157816300064?via%3Dihub

[5] Nathan Griffiths , Kuo-Ming Chao, Agent-Based Service-Oriented Computing , Published by Springer-Verlag London Limited 2010 , ISBN 978-1-84996-040-3 , p. 24-25 .

NUMERICAL ANALYSIS OF PBLI^{17} FLUID FLOW IN A 3D CIRCULAR CHANNEL UNDER A MAGNETIC FIELD

Murat ERDEM[1], Yasin VAROL[2]

CHAPTER 16

1 Vocational School of Technical Sciences, Firat University, Elazig, Turkey., muratrdm01@gmail.com,

2 Department of Automotive Engineering, Technology Faculty, Firat University, Elazig, Turkey., yvarol@gmail.com

NUMERICAL ANALYSIS OF PBLI[17] FLUID FLOW IN A 3D CIRCULAR CHANNEL UNDER A MAGNETIC FIELD

Murat ERDEM[1], Yasin VAROL[2]

Nomenclature

B	magnetic field induction (T)
c_p	specific heat (J/kg. K)
D	diameter (mm)
E	electric field
Ha	hartmann number
P	pressure (Pa)
k	thermal conductivity of fluid (W/m k)
j	electrical current density (A/m^2)
Re	Reynolds number
L	length (mm)
T	temperature (K)
T_i	inlet temperature (K)
T_o	outlet temperature (K)
T_w	wall temperature (K)
U	flow velocity (m/s)

1 Vocational School of Technical Sciences, Firat University, Elazig, Turkey., muratrdm01@gmail.com,

2 Department of Automotive Engineering, Technology Faculty, Firat University, Elazig, Turkey., yvarol@gmail.com

μ dynamic viscosity (kg/m s)

ρ density (kg/m^3)

σ electrical conductivity (S/m)

W_f friction loss (W)

Δ Laplace operator

Del operator for cylindrical coordinates

1. Introduction

Magneto-hydrodynamics (MHD), associated with heat transfer and fluid behavior, have received considerable attention for the last decades since there is a growing interest of understanding the underlying physical processes occurring. This is due to their wide variety of application in engineering areas, such as crystal growth in liquid, cooling of nuclear reactor, electronic package, microelectronic devices, and solar technology. There has been an increasing interest to understand the flow behavior and the heat transfer mechanism of enclosures that are filled with electrically conducting fluids under the influence of a magnetic field force [1-5]. There are many study related to the subject in the literature. Some of which are explained below.

Erdem [6], examined experimentally and numerically the fluid motion and heat transfer by applying external magnetic field strength to different fluid types in a three dimensional pipe. In his study, it has been tried both the cooling and heating parameters. It stated that the magnetic field force applied reduces the velocity of fluid, but increases the pressure and heat transfer. Erdem et al. [7] investigated the behavior of the fluid by applying an external magnetic field to the liquid lithium fluid in a circular channel.

Here, the lithium liquid has been cooled. Authors stated that the magnetic field has a significant effect on the fluid movement. Recebli et al. [8] the effect of perpendicularly applied magnetic field on steady state laminar liquid lithium flow in a horizontal circular pipe theoretically analyzed with three dimensional computer based program (ANSYS-Fluent). They examined the forced convective heat transfer. It explained that the increase of magnetic field induction has enhanced the convective heat transfer and pressure. Afify [9] investigated the analysis of non-Darcy free convection flow of an electrically conducting fluid over an impermeable vertical plate embedded in a thermally stratified, fluid saturated porous medium for the case of power-law surface temperature. It presented some results for velocity values and local Nusselt number for representative values of different controlling parameters. It explained that the magnetic field is effective on flow. Ellahi [10] studied some effects of MHD and temperature dependent viscosity on the flow of non-Newtonian nano fluid in a cylindrical channel for some analytical solutions. He illustrated the effects of various physical parameters on velocity, temperature and nano concentration, which are discussed by using graphical approach. He claimed that homotopy analysis method (HAM) provides us with a convenient way to control the convergence of approximation series; that is fundamental difference between the HAM and other methods for finding approximate solution. Also, it was specified that the MHD parameter decreases the velocity profile is larger than that of temperature profile even in the presence of variable viscosities. Ki [11] investigated a level set method for two-phase incompressible flows in the effect of magnetic field force. It explained that the examples tested have demonstrate the validity and effectiveness of the approach. When flow field is under magnetic field, the heat transfer and fluid flow analysis in a straight channel utilizing nano-fluid is numerically investigated by Heidary et al. [12]. They analyzed the effect of different Hartmann number and Reynolds numbers on the Nusselt number (Nu). It stated that Ha number have increased significantly Nu number. With related to subject, Rahimi - Gorji et al. [13] studied the heat transfer and fluid flow analysis for a nan fluid in a fin shaped micro channel. They are focused on geometry in general. Zaloğlu and Yalçınkaya [14], magneto-hydrodynamic flow of a viscous fluid having electrical conductivity studied between the two plates. In the study, they analyzed the results of changes in radial velocities with the number of Ha.

The main aim of this study is to numerically examine the magneto hydrodynamic flow behavior of $PbLi^{17}$ fluid in a three-dimensional pipe. The analysis was carried out in laminar conditions (Re = 1000).

2. Material and Method

The mesh quality properties of this geometry are given in Table 1. It is clear that the orthogonal quality of the mesh structure is of appropriate value. This value increases the quality as it approaches to number 1. The boundary conditions of the geometry are also presented in Table 2. The thermo-physical properties of the working fluid are obtained from Ref. [15].

Table 1. Mesh quality

Mesh size	0.0005 m
Mesh number	280825
Orthogonal quality	0.9871
Size function	Uniform

Table 2. *Boundary conditions of the problem*

Ti (K)	573
Tw (K)	473
To (K)	293
U (m/s)	0.0185

The 3D pipe used in this numerical study is given in Figure 1. The pipe is under the influence of external magnetic field. Pipe temperature and wall temperature are different. The fluid temperature is greater than the wall temperature (Ti>Tw) and the fluid passes through the channel in laminar conditions and the pipe has finite thickness. The mesh structure is shown in Figure 2 and mesh type is quadratic.

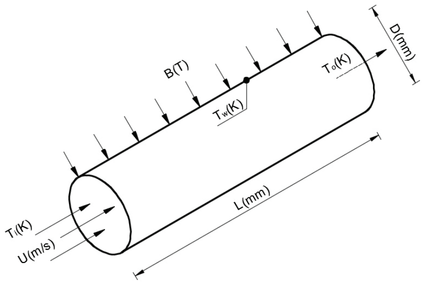

Fig. 1. *Circular 3D pipe model*

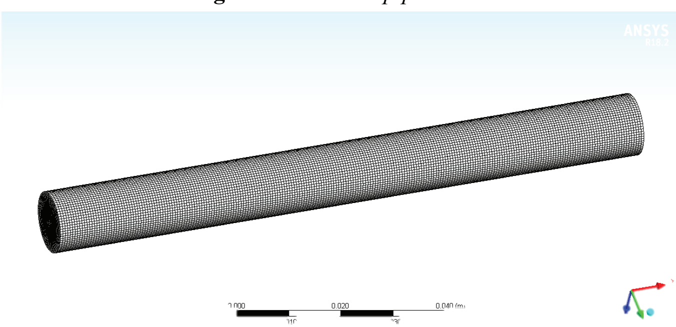

Fig. 2. *Grid structure*

Analysis was performed with using the momentum Eq. (1), Ohm law Eq. (2), continuity Eq. (3), and energy Eq. (4) equations [5, 8]. Calculations were performed using ANSYS-Fluent commercial software.

$$\rho * (U.\nabla)U = -\nabla P + \mu * \Delta U + [j\text{x}B] \tag{1}$$

$$j = \sigma * [E + U\text{x}B] \tag{2}$$

$$\nabla.U = 0 \tag{3}$$

$$\rho * c_p * (U.\nabla)T = k * \Delta T + \frac{j^2}{\sigma} + W_f \tag{4}$$

3. Results and Discussion

This study deals with the numerical investigation of the flow behavior of PbLi[17] fluid in a three-dimensional circular channel. External magnetic field strength has applied perpendicularly to the channel. The study was carried out for Re = 100. The obtained results are presented graphically and discussed.

Along the pipe diameter, the change in the fluid velocity with the magnetic field force is shown in Figure 3. As shown in the figure, the magnetic field strength has decreased the fluid velocity. That is, as the magnetic field strength increases, the fluid velocity has fallen due to the retarding effect of the Lorentz force. When there is no magnetic field, the fluid velocity is about 0.029 m/s, when the magnetic field strength is B = 0.08T, the fluid velocity is about 0.025 m/s and when the magnetic field strength is B = 0.16T, the fluid velocity is about 0.022 m/s.

Figure 4 gives the fluid velocity variations occurring by the magnetic field strength along the center length of pipe. As understood from this, the fluid velocity was reduced by the magnetic field. The fluid velocity values at the end of the channel are the same as in Figure 3. Namely, the maximum velocity values in Fig. 3 and Fig. 4 are the same.

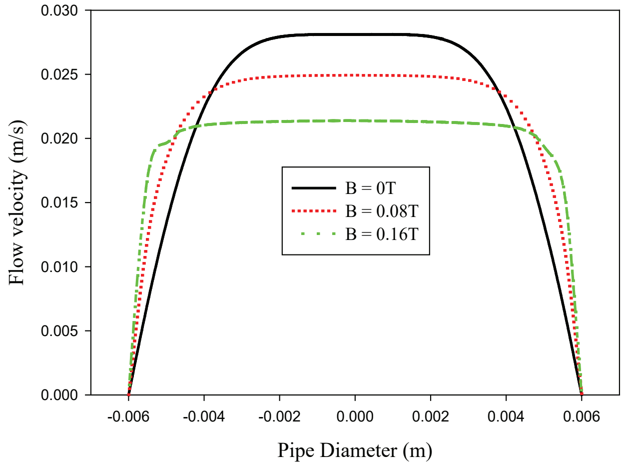

Fig. 3. *Change of flow velocity with pipe diameter*

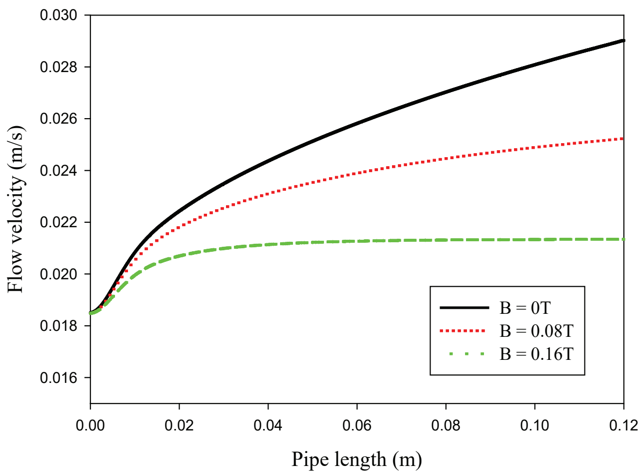

Fig. 4. *Change of flow velocity with pipe center length*

The variation of the pressure values with magnetic field along the center of the channel is illustrated in Figure 5. It is understood that the pressure is clearly increased with the magnetic field. Similar results can be found in the literature. The pressure values were for B = 0, B = 0.08 and B = 0.16T, approximately P = 2.5, 9 and 31 Pa, respectively.

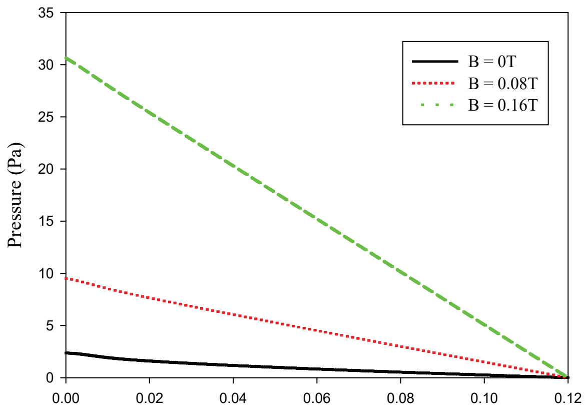

Fig. 5. *Change of flow pressure with pipe center length*

The change in the fluid temperature with the magnetic field along the length of the pipe is shown in Figure 6. As the wall temperature has lower than the fluid temperature, the fluid is tended to cool down. At first sight, it is observed that the fluid temperature does not change much with the application of magnetic field. However, when the figure is examined very closely, it is understood that the magnetic field increases the fluid temperature. For this, Figure 7 has examined to better understand the effect of the magnetic field on the fluid temperature. In fact, Figure 6 and Figure 7 are the same. The magnetic field effect has been seen more clearly in a small scale range in Figure 6. Temperature values in the range X = 0.0046 - 0.0060 m on Figure 6 were investigated. Therefore, the effect of magnetic field on temperature values is understood more clearly. In the Figure 7, it is clear that the magnetic field increases the fluid temperature. As mentioned earlier, the wall temperature is lower. As the wall temperature is lower, the increased temperature indicates that the heat transfer rate is growing. Therefore, the heat transfer of the fluid under cooling is increased by the magnetic field.

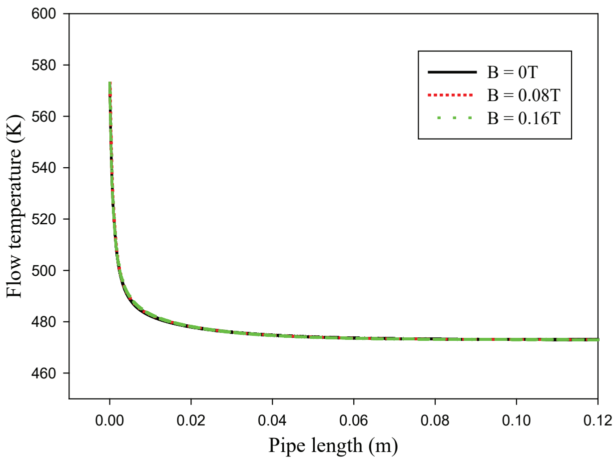

Fig. 6. *Change of temperature with magnetic field through pipe length (Y = 0.0055 m)*

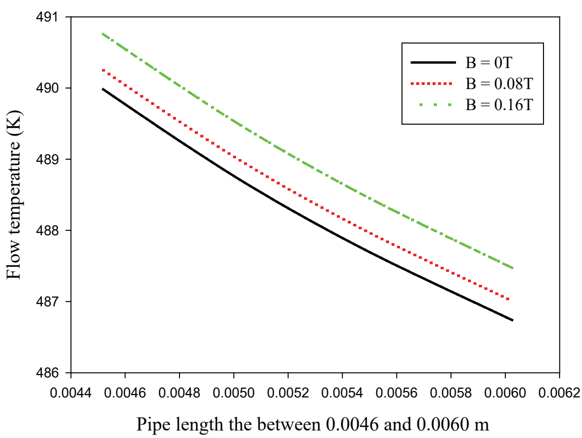

Fig. 7. *Temperature changes with magnetic field through pipe length* (X = 0.0046 – 0.0060 m, Y = 0.0055 m)

The change in velocity contours with magnetic field strength is shown in Figure 8. As is known, the magnetic field strengths are B = 0, 0.08 and 0.16T, respectively. These forces are shown in the figure from top to bottom. Namely, the magnetic field strength from top to bottom is increased in the Figure. Here, fluid velocity values are seen on the scales next to the Figure. It is seen clearly that the flow velocity values in the scales decreases with the magnetic field strength. These values were V = 0.0029 m/s for B = 0T, V = 0.00253 for B = 0.08T and 0.00221 m/s for B = 0.16T, respectively. At the same time, these values are found in Figure 3 and Figure 4. Here (Fig. 8), when there was no magnetic field, the first shape became completely round (B = 0T), after the applied magnetic field it became an ellipse image (B = 0.08T), and then the vortices began to be for maximum magnetic field strength (B=0.16T).

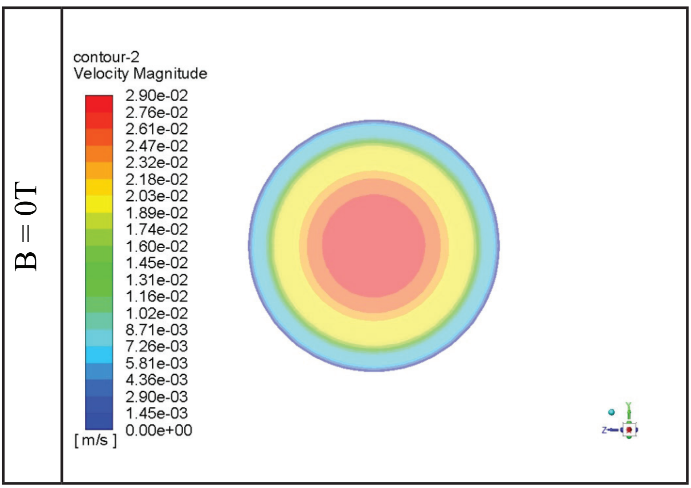

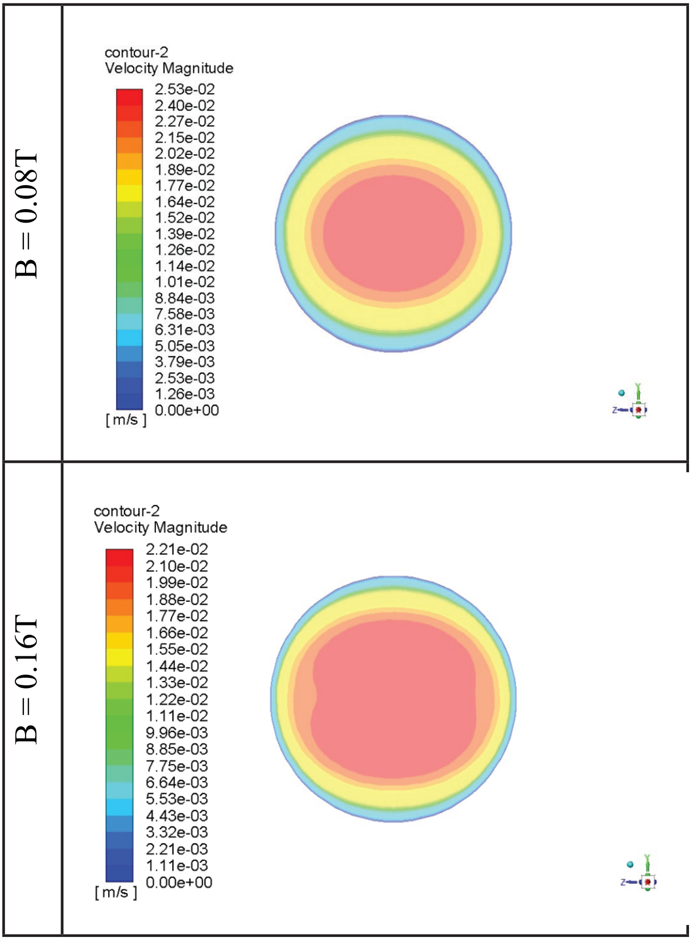

Fig. 8. *Changes of velocity contours with magnetic field through pipe diameter*

4. Conclusion

In this study, MHD behavior of PbLi[17] liquid metal has been investigated numerically in a three dimensional pipe exposed to magnetic field strength. The obtained speed, pressure and temperature values are presented graphically.

In the study scope, the following results have been obtained.

- The magnetic field force significantly has reduced the fluid speed.
- The magnetic field strength has increased the fluid pressure.
- Fluid temperature has increased with magnetic field strength. So, heat transfer is increased.
- Along the diameter of the pipe, in the fluid velocity contours have occurred changes with the magnetic field. As the magnetic field strength increases, the inner cylindrical shape deteriorates.

As a results, fluid behavior can be controlled with magnetic field force.

REFERENCES

1. Bourantas, G.C. and Loukopoulos, V.C. 2014. MHD natural-convection flow in an inclined square enclosure filled with a micropolar-nanofluid, International Journal of Heat and Mass Transfer, vol. 79, pp. 930-944.

2. Rudraiah, N., Barron, R.M., Venkatachalappa, M. and Subbaraya, C.K. 1995. Effect of a magnetic field on free convection in a rectangular enclosure, International Journal of Engineering Science, vol. 33, pp. 1075–1084.

3. Alchaar, S. Vasseur, P. and Bilgen, E. 1995. Natural convection heat transfer in a rectangular enclosure with a transverse magnetic field, Journal of Heat Transfer, vol. 117 pp. 668–673.

4. Garandet, J.P., Alboussiere, T. and Moreau, R. 1992. Buoyancy driven convection in a rectangular enclosure with a transverse magnetic field, Int. J. Heat Mass Transfe*r*, 35, 741–748.

5. Erdem, M., Firat, M. and Varol, Y. 2017. Numerical Investigation of Mhd Forced Flow In a Three-Dimensional Cylindrical Pipe, International Conference on Engineering Technology and Innovation, 99-105, Sarajevo, Bosnian and Herzegovina.

6. Erdem, M. 2019. Experimental and Numerical Investigation of Nanoparticles Added Magnetohydrodynamics Flow, PhD Thesis, Fırat University, The Institute of Natural and Applied Sciences, pp. 197, Elazig, Turkey.

7. Erdem, M., Firat, M. and Varol, Y. 2018. Numerically investigation of MHD liquid lithium flow under cooling conditions in a circular channel, Pamukkale University Journal of Engineering Sciences, 24 (1), 30-35.

8. Recebli, Z., Selimli, S. and Gedik, E. 2013. Three dimensional numerical analysis of magnetic field effect on Convective heat transfer during the MHD steady state laminar flow of liquid lithium in a cylindrical pipe, Computers & Fluids, 88, 410-417.

9. Afify, A.A. 2007. Effects of variable viscosity on non-Darcy MHD free convection along a non-isothermal vertical surface in a thermally stratified porous medium, Applied Mathematical Modelling, vol. 31, pp.1621–1634.

10. Ellahi, R. 2013. The effects of MHD and temperature dependent viscosity on the flow of non-Newtonian nanofluid in a pipe: Analytical solutions, Applied Mathematical Modelling, vol. 37, pp. 1451-1467.

11. Ki, H. 2010. Level set method for two-phase incompressible flows under magnetic fields, Computer Physics Communications, 181, 999-1007.

12. Heidary, H., Hosseini, R., Pirmohammadi, M. and Kermani. M.J. 2015. Numerical study of magnetic field effect on nano-fluid forced convection in a channel, Journal of Magnetism and Magnetic Materials, 374, 11-17.

13. Rahimi-Gorji, M. Pourmehran, O. Hatami M and. Ganji D.D. 2015 Statistical optimization of microchannel heat sink (MCHS) geometry cooled by different nanofluids using RSM analysis, Eur Phys J Plus, 2015,130 (2), 1–21.

14. Zaloğlu A, Yalçınkaya G. 2003. Paralel iki levha arasındaki viskoz akışkanın MHD radyal titreşimli akışı. İTÜ Journal/d Engineering, 2(5), 53-60.

15. Müller, U. and Buhler, L. 2001. Magnetofluiddynamics in Channels and Containers, 1st edition, Springer-Verlag Berlin Heidelbeng.

AT IDLE SPEED OF DIFFERENT SPARK PLUG TYPES; EMISSION, NOISE AND VIBRATION EFFECT

Nurullah GÜLTEKİN[1]

CHAPTER 17

1 Program of Automotive Technology, Karamanoğlu Mehmetbey University, Vocational School of Technical Sciences, TURKEY (ngultekin@kmu.edu.tr)

AT IDLE SPEED OF DIFFERENT SPARK PLUG TYPES; EMISSION, NOISE AND VIBRATION EFFECT

Nurullah GÜLTEKİN[1]

1. INTRODUCTION

In the gasoline engine, spark plugs are used to ignite the air fuel mixture inside the cylinder as a result of compression. In order for the combustion to be of good quality, the ignition must be of good quality. High quality ignition in petrol engines is of great importance for a good combustion process. The firing process depends on a number of variables such as the arc formed by the spark plug, the picvoltage, the firing speed, the spark plug nail range and the design of the spark plug being placed in the combustion chamber [1].Spark plugs are the most important part of the ignition system that affects the quality of ignition.It also has a certain cost, as Spark Plugs are replaced more often than other ignition system parts. Since there are many brands and models of spark plugs on the market, users are faced with many spark plug options when they take their tools into care. Users can choose from these options with either manufacturer's advice, master's advice or ear-filling knowledge. Since manufacturers ' recommendations are generally in line with their own brands, the cost of these types of spark plugs is higher than that of other brands. But when viewed functionally, there is no difference between most of them. In additıon to they use diffrent spark plug, because they believe their are performance that increases, fuel, emision, noise reduces.

1 Program of Automotive Technology, Karamanoğlu Mehmetbey University, Vocational School of Technical Sciences, TURKEY (ngultekin@kmu.edu.tr)

Spark plugs are the most important part of gasoline engines that affect combustion quality. If the spark plugs do not form the required arc for good combustion, engine operation is adversely affected. Deterioration in engine operation; decrease in engine power, increase in emission values, increase in noise and increase vibration.

1.1. Emision

Exhaust emissions from motor vehicles; incomplete combustion, unsuitable air-fuel mixture, fuel properties and different engine operating conditions. Exhaust gases, which occur due to the lack of proper conditions of combustion, cause air pollution in residential areas where motor vehicles are used extensively, especially in metropolitan cities and threaten human health significantly. engine cylinder volume, engine setting, usage, fuel composition varies depending on many parameters such as [2-3]. In internal combustion engines, unburned hydrocarbons (HC), carbon monoxide (CO) and nitrogen oxides (NOx) are important components that cause air pollution depending on the combustion conditions.

Temperature, pressure, oxygen concentration and time in the combustion chamber; are important factors affecting combustion and combustion products [4-5]. In particular, the incomplete combustion event causes unburned HC in the exhaust gases. Lack of oxygen in rich mixtures; Decrease in combustion chamber temperature is another factor that causes increase in HC emissions. In addition, the extinction of the flame, which occurs due to heat losses in the cylinder walls and reaches the so-called flame extinction zone, causes HC emission formation [6, 7-8, 9].

Hydrocarbons released from the exhaust of internal combustion engines; These are emissions that are partially burned or not involved in combustion due to faulty air-fuel ratio, low compression, valve thrust and inhomogeneous temperature distribution within the cylinder. Hydrocarbon emissions suspended in the atmosphere react with nitrogen oxides to form a fog layer known as 'photochemical sis-smog,, causing adverse effects on the respiratory system and living organisms [10]. Emissions, in terms of their negative effects on human health, according to respiration time and intake amounts; long-term, mild headaches if left in the environment containing 100 ppm carbon monoxide, severe headaches if left in the environment containing 500 ppm carbon monoxide, dizziness and fainting, respiratory weakness, loss of consciousness and death at values of 2000 ppm. Emission control in vehicles is of great importance in order to minimize harmful gases that affect human health at these levels. A motor vehicle with no emission control can make a person's need of 15 m^3 of fresh air daily to be inhaled in as little as 10 minutes [11-12].

Many international agreements have been made on reducing emissions, protecting nature and human health, and the European Union is at the heart of these agreements. In the light of these agreements, companies also carry out many R & D studies in order to reduce their emission values. These technologies include direct injection engine design, stepped filled engines, reduced engine sizes in recent years, and the application of overfilling systems to prevent power loss in small stroke volume engines [13]. In addition, it is known that these technological efforts to reduce emissions significantly increase vehicle costs.

Another measure taken to reduce emissions is; countries require emissions to a certain standard to allow the use of manufactured vehicles. During the use of the vehicles, measurements are made at regular intervals and the emission values of the vehicles are tried to be controlled. However, in our country, emission measurement stations are given to private enterprises and economic concerns of these enterprises cause emission controls to be far from the desired standard. On the other hand; vehicle users who are not aware of the fact that the emission values are higher than the standard values, as well as damaging the nature and human health, increase the fuel consumption, only want to have the formal process and ensure the adequacy [11].

1.2. Noise

Noise; unpleasant, unwanted, disturbing sound. But not every sound is defined as noise. Calling sound is not only dependent on the intensity of the sound, its treble and fullness and its continuity. It also changes depending on the physical and mental state of the person exposed to the sound. However, it is clear that many types of sound will be regarded by everyone as undisputed noise. The more meaningless a noise, the more violent, the more irregular and the more sudden the more disturbing it is [14].

Noise on people; muscle stress, stress, increase in blood pressure, heart and blood circulation changes, pupil growth and insomnia have been found to have some physiological effects. Stress and insomnia are long-term effects of noise. Also; migraine, ulcer, gastritis and so on. Noise may also have a significant effect on the emergence of diseases. One of the growing problems of developing and especially developed countries is traffic noise [13,14,15]. it consists of components such as noise from the engine, chassis and bodywork, braking, and noise from wheel contact with the road surface and air friction generated by the vehicle [16]. In addition, a well-designed exhaust system is also an important source of noise [17]. It is known that the share of exhaust noise to total noise emitted from vehicles varies depending on the vehicle and the type of muffler used, but is 40%. Therefore, one of the important issues that need to be worked on in order to reduce the noise emitted from motor vehicles is the exhaust system [18].

1.3. Vibration

Vibration is another factor caused by vehicles and has a negative impact on human health. For drivers using vehicles with excessive vibration; distractions, stress, irritability and fatigue [19]. According to the studies, both physical health problems and psychological disorders are observed in people working in vehicles that are continuously exposed to broad spectrum low frequency in degraded terrain [21]. In this case, the possibility of an accident increases. In addition, vibrations in the vehicle may cause the systems on the vehicle to be subjected to impacts, material fatigue, frictions and thermal stresses and cause failure in a short time [22,23].

The main causes of vibrations in vehicle engines; pressure forces caused by combustion, irregularity of engine parts operating with accelerated motion, centrifugal force caused by flywheel and movements in valve mechanism [24]. Forcing forces generated by unbalanced movements in linearly and cyclically accelerated parts cause increased motor vibration. Another reason for engine vibrations; the flexibility of the parts, inter-part gaps and non-continuous contact [11,20]. In addition, the sudden pressure pulse caused by the combustion event in the engine cylinder causes the cylinder walls and engine side walls to vibrate. These vibrations in different parts of the engine cause pressure oscillations of the air and noise. In today’s technology it is impossible to eliminate vibration in internal combustion engines; but it is possible to reduce. In particular, advances in material technology have a positive effect on motor vibration. In addition, optimizing the operation of the motor will reduce the vibration factor. In order to minimize these vibrations and sounds in vehicles;

measures such as reducing the engine speed, increasing the number of cylinders and thickening the engine body should be taken. But these measures; fuel consumption, cost, performance and purchase and sale costs due to the additional load is not preferred by the manufacturer and users [18].

In this study; The effect of spark plug nail gap on exhaust emission, noise and vibration was investigated in a gasoline engine with different types of spark plugs. In the experiment, Tofaş group engine, which has a single silencer in the exhaust system with engine volume of 1581 cm^3, exhaust gas measurements measuring instrument, noise measuring instrument and acceleration measuring instrument. As a result of the study, the effects of different spark plug types and spark plug nail spacing on engine operation (emission, noise, vibration) were determined.

Other parts of the study are organized as follows: Chapter 2 describes the materials and methods used in the experiment, Chapter 3 presents the findings, Chapter 4 explains the results and discussion.

2. Material and method

Experimental setup was established and the experiments were carried out in the laboratory. In the experimental setup; gasoline engine, three different types of spark plugs (single-ended spark plugs, three-nail spark plugs, iridium spark plugs), emission measuring device, noise measuring device and vibration measuring device were used.

The manufacturer's recommendation for the engine used in the experiments is a single-ended spark plug. The spark plug ended spacing of the spark plug types used was set to their original values.

In this study, the BOSH BEA 250 exhaust gas emission measurement device shown in Figure 1 was used to perform the emission measurements. The noise generated by the engine was measured by the Figure 2 CEM DT-8820 volume meter, calibrated by the OMKA calibration Center. Values are in decibels (dBA). The noise measurement for noise measurements is saved at a distance of 1m and the measurements are indoors.

Figure1. *Exhaust emission device* **Figure2.** *Noise level measurement device.*

In the studies, PCE-VD3 model accelerometer vibration device shown in Figure 3 was used to determine the vibration data generated by the motor. This device is a miniature universal data logger with an integrated triaxial (X, Y, Z axes) acceleration sensor. The internal sensor of this device has a measuring range of ± 18 per axis. In the X, Y, Z axes and total resultant acceleration, four different types of acceleration are measured in units of g. Vibration data were recorded by computer. The vibration data is automatically recorded by the software over a 500 ms interval. The measurement time for each selected experiment was assumed to be 45s. At the end of each measurement, mean and maximum resultant acceleration values were recorded.

The experiments were carried out with the Tofaş group engine, which has a 1581 cm^3 engine volume, shown in

Figure 4, with a single silencer in the exhaust system. The motor is on the coffee table.

Figure 3. *Accelerometer device.*

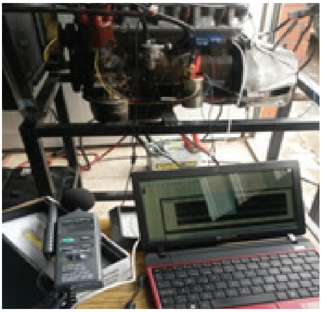

Figure 4. *Spark plug ignition engine and test device*

The single plug spark plug assembled to the engine during the experiment is shown in Figure 4a, the triple plug spark plug in Figure 4b and the iridium spark plug in Figure 4c. The experiments were carried out in a workshop environment at 20-23 ° C. After the engine has been set to operating temperature, the data was saved.

Figure Şekil 4a. *Single-ended spark plug*

Figure 4b. *Three-nail spark plug*

Figure 4c. *İridium spark plug*

3. Findings

Figure 5 illustrates the amount of hydrocarbons produced by the engine which is run at idle (900 rpm) with different spark plug types and nail intervals, and recorded as one millionth (ppm) value.

According to the results of the experiment; Amount of hydrocarbon:

- 0.7 mm spark plug nail spacing; The single-ended spark plug engine HC 1205 ppm measured. Measurements made with three-pronged spark plug increased the amount of HC to 2740 ppm. When the iridium spark plug was measured, the amount of HC was measured as 1854 ppm.

- 0.8 mm spark plug nail spacing; The engine running with a single-ended spark plug HC 1880 ppm measured. In the measurements made with three-pronged spark plug, the amount of HC increased to 2765 ppm. When the iridium spark plug was measured,the amount of HC was reduced to 2154 ppm.

- 0.9 mm spark plug nail spacing; The engine running with a single-ended plug spark plug HC 1270 ppm measured. In the measurements made with three-pronged spark plug, the amount of HC increased 2010 ppm. When the iridium spark plug was measured, the amount of HC was 2805 ppm.

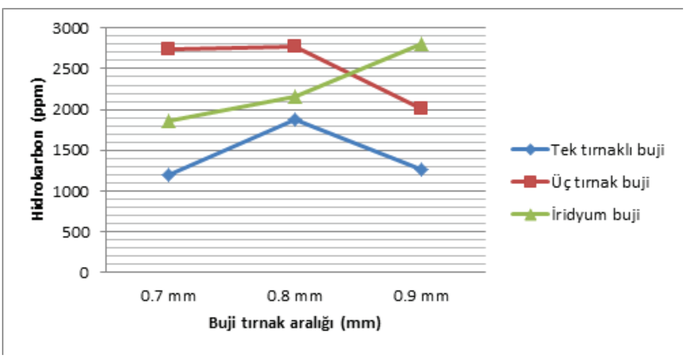

Şekil 5. *Buji tipi, tırnak aralığı ve hidrokarbon bağıntısı*

Figure 6 shows the noise levels produced by the engine which is operated at idle (900 rpm) with different spark plug types and nail intervals. According to the results of the experiment;

- 0.7 mm spark plug in the nail range; 76.8 dBA noise value was detected in the single-nail spark plug-powered engine. The noise value measured by three-nail spark plugs at the same time was 78.3 dBA. The noise value of 76.5 dBA was determined in the iridium spark plug-powered engine.

- 0.8 mm spark plug in the nail range; 79.85 dBA noise value was detected in the single-nail spark plug-powered engine. The noise value measured by three-nail spark plugs at the same time was 77.4 dBA. The noise value of 52.5 dBA was determined in the iridium spark plug-powered engine.

- 0.9 mm spark plug in the nail range; 80.75 dBA noise value was detected in the single-nail spark plug-powered engine. The noise value measured by three-nail spark plugs at the same time was 78.6 dBA. The noise value of 74.7 dBA was determined in the iridium spark plug-powered engine.

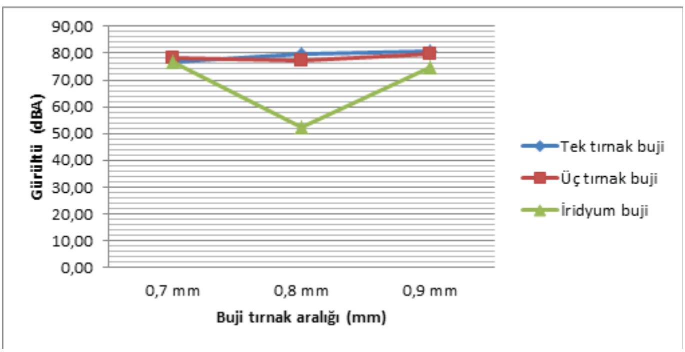

Şekil6. *Buji tipi, tırnak aralığı ve gürültü bağıntısı*

Figure 7 shows the vibration data generated by the engine which is operated at idle (900 rpm) with different spark plug types and nail intervals. When the data is evaluated;

- 0.7 mm spark plug nail spacing; 1.64g vibration value is detected in the engine running with a single fingernail spark plug. 1.61g vibration was measured in the experiment using three-pronged spark plug and 1.85g vibration was determined in the experiment using iridium spark plug.
- 0.8 mm spark plug nail spacing; 1.795 g vibration value is detected in the engine running with a single fingernail spark plug. 1.68g vibration was measured in the experiment using three-pronged spark plug and 1.68g vibration was determined in the experiment using iridium spark plug.
- 0.9 mm spark plug nail spacing; 1.80g vibration value is detected in the engine running with a single fingernail spark plug. 1.66 g vibration was measured in the experiment using three-pronged spark plug and 1.84 g vibration was determined in the experiment using iridium spark plug.

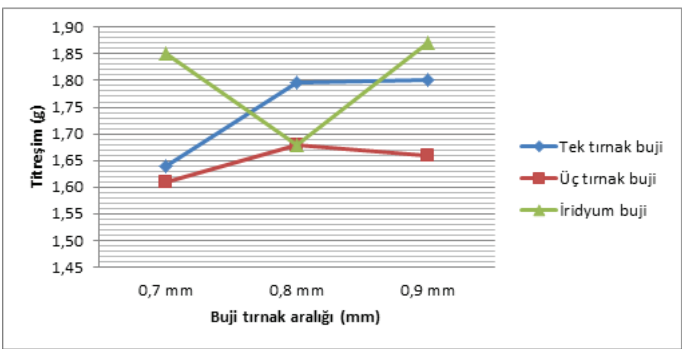

Şekil7. *Buji tipi, tırnak aralığı ve titreşim bağıntısı*

4. Result and Discussion

In this study; The effect of gasoline engine with different types of spark plugs on exhaust emission, noise and vibration was investigated. In addition, the experiments were repeated by changing the spark plug nail intervals to determine the effect of changing the spark gap on these factors. As a result of the experiments; According to the results of the HC measurements, it is found that the use of the recommended single plug spark plug for the engine reduces the emission values. When the noise values were examined, it was found that the noise decreased significantly in the motor experiments using iridium spark plug. When the vibration values were examined, the noise decreased to the minimum level in the experiments performed with three-pronged spark plug. The results obtained from the data are presented in detail below.

a) It has been observed that the effect on emission values, the amount of HC in the single-nail spark plug and the original spark plug nail gap (0.7mm) decreased. It was observed that the increase in spark plug nail spacing (0.8mm) increased the amount of HC, but it decreased slightly when the nail spacing was made 0.9mm. In the experiments using three-pronged spark plug, emission values were found to be high. It has been seen that increasing the iridium spark plug nail spacing gradually increases the emission values. The higher the amount of HC, the worse the burning means. Poor combustion results in more harmful substances released into the atmosphere and increased fuel consumption. Therefore, it is thought that the users who have the maintenance of their vehicles on time will be more advantageous in terms of both economy and comfort.

b) When the noise values were examined, it was found that iridium spark plug and original spark plug nail spacing (0.8mm) produced less noise than other experiments of the engine.

c) When the vibration values were examined, it was found that three nail plugs in the 0.7mm nail spacing produced minimum vibration. However, the amount of vibration produced by the single-ended spark plug is quite low.

The most important point to be considered during vehicle maintenance; is the use of the correct spark plug. Also check the nail spacing of the new spark plug to be installed on the engine. If the spark gap of the spark plugs installed on all cylinders is uneven, the engine will run irregularly, knocking operation, traction drop and fuel consumption will increase. A clear indication of the failure is the fluctuation of idle and engine shake [25,26]

When we evaluate the research in general; The engine used in the experiments is still used in the market and the users think that the use of a three - pronged spark plug or an erythium spark plug has a positive effect on the operation of the engine. For this reason, this type of spark plugs are installed in their engines by paying more. However, in the research, three-pronged and iridium spark plugs are seen to worsen the combustion. As a result, the change in the engine cannot have a positive effect on the engine unless it is supported in other systems. Only the spark plug change in the engine did not affect the performance positively. Because the other parts of the ignition system (coil, spark plug cable, etc.) are insufficient. In the following studies; changes in other parts, improvements in emission noise and vibration are likely to be observed.

REFERENCES

[1] Dale, J.D. ve Oppenheim, A.K., “Enhanced Ignition for I. C. Engines with Premixed Gases”, SAE Technical Paper 810146, 1981.

[2] Çakıroğlu, M., 1996, “Motorlu Taşıt Trafiğinde Egzoz Emisyonları”, I. Ulusal Ulaşım Sempozyumu, İstanbul, Türkiye.

[3] Uyumaz, A., Boz,F., Yılmaz,E., Solmaz, H., Polat, S., (2017), Taşıt Egzoz Emisyonlarını Azaltma Yöntemlerindeki Gelişmeler, Mehmet Akif Ersoy Üniversitesi Fen Bilimleri Enstitüsü Dergisi, 15-24,22

[4] Ergeneman, M., Mutlu, M., Kutlar, O. A. ve Arslan, H., Taşıtlardan Kaynaklanan Egzoz Kirleticileri, Birsen Yayı-nevi, İstanbul, s. 1-14, 1998.

[5] Topgül, T.,Yücesu, S., Okur, M., Buji ile Ateşlemeli Bir Motorda Çalışma Parametrelerinin Egzoz Emisyonlarına Etkilerinin Deneysel Olarak İncelenmesi, Politeknik Dergisi , Cilt: 8 Sayı: 1 s. 43-47, 2005

[6] Ergeneman, M., Mutlu, M., Kutlar, O. A. ve Arslan, H., Taşıtlardan Kaynaklanan Egzoz Kirleticileri, Birsen Yayı-nevi, İstanbul, s. 1-14, 1998.

[7] Soruşbay, C. ve Göktan, A. G., “Motorlu Taşıtlardan Kaynaklanan Çevre Kirliliği ve Kontrolü”, İTÜ 1. Hava Kirlenmesi ve Kontrolü Sempozyumu, İstanbul, s. 157-166, 15-16 Mart 1993.

[8] Soruşbay, C., “Motorlu Taşıtlardan Kaynaklanan Hava Kirliliğinin Kontrolünde Kullanılan Yöntemler”, 2. Motor ve Taşıt Tekniği Sempozyumu, İzmir, 14-15 Ekim 1993.

[9] Yıldırım, A. M. ve Sürmen, A., “Buji Ateşlemeli Motorlarda HC Emisyonlarının Oluşumu ve Alev Geçişi Sonrası Davranımının Matematik Modeli”, 5. Yanma Sempozyumu, Kirazlıyayla, Bursa, s. 176-188, 21-23 Temmuz 1997.

[10] Schafer, F., Basshuysen, R. V., 1995, "Reduced Emissions and Fuel Consumption in Automobile Engines", Springer-Verlag Press, 6, Germany.

[11] Kuş, R., 2000, ''Motorlu Taşıtlarda Emisyon Kontrol Sistemleri'', Ders Notları, Konya, Türkiye.

[12] Kaytakoğlu, S., Var, F., Öcal, S. E., 1995, "Motorlu Taşıtlardan Kaynaklanan Kirlilik ve Giderme Yöntemleri", Yanma ve Hava Kirliliği Kontrolü 3. Ulusal sempozyumu, Ankara, Türkiye.

[13] Soruşbay, C., 2010, "Trafik Kaynaklı Hava Kirliliği ve Otomotiv Sektöründe Alınan Önlemler", 4. Ulusal Hava Kirliliği ve Kontrolü Sempozyumu, 25-27 Ekim 2010, Ankara, Türkiye.

[14] Aktürk, N., Ünal, Y., 1998, "Gürültü, Gürültüyle Mücadele ve Trafik Gürültüsü", Gazi Üniv. Fen Bilimleri Enstitüsü Bülteni, Sayı 3, sf. 21 – 32.

[15] Toprak, R., Aktürk, N., 2001, "Raylı Ulaşım Sistemlerinin Neden Olduğu Çevresel Gürültü" TMMOB Makine Mühendisleri Odası, İstanbul'da Kent İçi Ulaşım Sempozyumu, 28-30 Haziran, İstanbul, Türkiye.

[16] Aktürk, N., Gürpınar, M., 2001, Trafik ve Yol Güvenliği Kongresi, 25-27 Nisan, Gazi Üniversitesi, sf. 346-359, Ankara, Türkiye.

[17] Öge, A., Öğüt, T., 1998, "Bir Otomobil Egzos Sisteminin İç Performans Analizi", IV. Ulusal Akustik Kongresi, 29-31 Ekim , Kaş/Antalya, Türkiye.

[18] Çetin,E., Eroğlu, M.,Aktürk, N., 2002, "Taşıt Motorlarının Neden Olduğu Gürültü", Uluslararası Trafik ve Yol Güvenliği Kongresi ve Fuarı, 8-10 Mayıs 2002, Ankara, Türkiye.

[19] Drugă, C., Barbu, D., Lache, S. 2007,Vibration And The Human Body, Fascicleof Managementand Technological Engineering, 6 (16), 168-173.

[20] Haşimoğlu, C., İçingür, Y., Öğüt, H., 2002, "Dizel Motorlarında Egzoz Gazları Re Sirkülasyonunun (EGR)

Motor Performansı ve Egzoz Emisyonlarına Etkisinin Deneysel Analizi", Tübitak Dergisi, 26 (2002), 127-135.

[21] Hostens, I.,Ramon, H. 2003,Descriptive Analysis of Combine Cabin Vibrationsand Their Effect on the Human Body, Journal of Soundand Vibration, 266: 453-464.

[22] Chu, C. C., 1997,Multiaxial Fatigue Life Prediction Method in the Ground Vehicle İndustry, International Journal of Fatigue, 19: 325-330.

[23] Fonta, M.,Freitas, M., 2009, Marine Main Engine Crankshaft Failure Analysis, Engineering Failure Analysis, 16:1940-1947.

[24] Sert, İ., 2008, Balıkesir İl Merkezinde Motorlu Taşıtlardan Kaynaklanan Emisyon Envanterinin Hesaplanması, Yüksek Lisans Tezi, Balıkesir, Türkiye.

[25] Gültekin, N., 2018, "Buji Ateşlemeli Bir Motorda Üç Tırnaklı Bujinin Tırnak Aralığının Hc (Hidrokarbon) Emisyonuna Etkisinin Araştırılması",III. Uluslararası Multidisipliner Çalışmaları Kongresi, 5-6 Ekim 2018, sf. 116-121, Kiev-Ukrayna.

[26] Gültekin, N., 2018, "Üç Tırnaklı Buji Kullanılan Bir Motorda Tırnak Aralığının Motor Gürültüsüne Etkisi",III. Uluslararası Multidisipliner Çalışmaları Kongresi, 5-6 Ekim 2018, sf. 168-172, Kiev-Ukrayna.

INVESTIGATION OF UNDERFLOOR SPACE HEATING SYSTEMS: FUTURE ASPECTS AND IMPROVABILITY

Ali Özhan AKYÜZ[1], Kazım KUMAŞ[2], Ceylin ŞİRİN[3], Azim Doğuş TUNCER[4], Afşin GÜNGÖR[5]

CHAPTER 18

1 Burdur Mehmet Akif Ersoy University, Bucak Emin Gulmez Vocational School of Technical Sciences, 15300, Burdur, Turkey
2 Burdur Mehmet Akif Ersoy University, Bucak Emin Gulmez Vocational School of Technical Sciences, 15300, Burdur, Turkey
3 Burdur Mehmet Akif Ersoy University, Istiklal Campus, Faculty of Engineering and Architecture, 15030, Burdur, Turkey
4 Burdur Mehmet Akif Ersoy University, Istiklal Campus, Faculty of Engineering and Architecture, 15030, Burdur, Turkey
5 Burdur Mehmet Akif Ersoy University, Bucak Technology Faculty, 15300, Burdur, Turkey. (Akdeniz University, Engineering Faculty, Antalya, Turkey)

INVESTIGATION OF UNDERFLOOR SPACE HEATING SYSTEMS: FUTURE ASPECTS AND IMPROVABILITY

Ali Özhan AKYÜZ[1], Kazım KUMAŞ[2], Ceylin ŞİRİN[3], Azim Doğuş TUNCER[4], Afşin GÜNGÖR[5]

INTRODUCTION

One of the biggest portions in the distribution of energy expenses in the world is spent on heating. Fossil energy sources are running out and efficiency is becoming more important in developing world [1]. Underfloor heating systems are one of the most suitable options for heating large areas with unit energy, heating according to user habits and getting maximum benefit with minimum resources. Underfloor heating basically means that the living spaces are heated from the floor. These systems are designed to feel the ideal temperatures starting from the sole of the foot where we feel the most intense with the principle of rising of the heated air. There are two different applications for underfloor heating. The first one is heating cables that convert electrical energy into heat energy, and the other one is the circulation of heat water inside the pipes laid on the floor.

Underfloor heating systems are more comfortable than radiator system. It does not take up space like a radiator

1 Burdur Mehmet Akif Ersoy University, Bucak Emin Gulmez Vocational School of Technical Sciences, 15300, Burdur, Turkey
2 Burdur Mehmet Akif Ersoy University, Bucak Emin Gulmez Vocational School of Technical Sciences, 15300, Burdur, Turkey
3 Burdur Mehmet Akif Ersoy University, Istiklal Campus, Faculty of Engineering and Architecture, 15030, Burdur, Turkey
4 Burdur Mehmet Akif Ersoy University, Istiklal Campus, Faculty of Engineering and Architecture, 15030, Burdur, Turkey
5 Burdur Mehmet Akif Ersoy University, Bucak Technology Faculty, 15300, Burdur, Turkey. (Akdeniz University, Engineering Faculty, Antalya, Turkey)

and does not interfere with the choice of places to put things in the rooms. Also, this technology prevents the formation of thermal bridges that promote mold growth and damage. The underfloor heating system provides better heat circulation, thus reducing the possibility of cold spots that can cause air currents and promote mold growth [2].

APPLICATION AREAS

Underfloor heating systems are increasingly used in heating applications. In addition to heating in residential buildings; there are various application area of these systems like; roads, ramps, roofs and sports fields where there is possibility of icing [3].

Underfloor heating is used mostly in residential heating today. The most important advantage is that it provides a more comfortable heating and energy saving by providing a homogeneous heat distribution. Warm air always accumulates above because its density is low. Underfloor heating systems are preferred in order to avoid this accumulation in large volume spaces and to use thermal energy efficiently. It can be easily used in large volume spaces, in places with high glass height or in cases where devices such as radiators prevent terrace exits. Because the window fronts are used; since pipes are not laid in the whole room during construction, it is easier to protect the pipes and these operations do not slow down the construction speed of the construction. Also, underfloor heating can be utilized in swimming pools. This heating will evaporate the splashes of water very quickly. When calculating the humidity of the pool, the water evaporated from the pool area must be taken into consideration. This system can also be used on roofs. Winter winds accumulate snow on the roofs. The snow accumulated on the roof starts to melt with the heat flowing from the building to the roof or with the effect of sun rays during hot days. Melting snow is directed towards the eaves and freezes again due to temperature differences between day and night, leading to the formation of ice bars. Melting snow water accumulates behind these barriers. Accumulated water seeps through the roof, damaging the building, and crosses the barrier, causing stalactites to form. Snow, ice and stalactites fall and threaten human health and life. To prevent this; inside the gutters, roof edges, electrical resistances (underfloor heating) can be utilized. In addition, icy roads are always dangerous and therefore many accidents occur each year. To prevent this, underfloor heating is applied to icy roads, especially ramps. The most common system for heating is electric floor heating. In case of water systems installed to prevent icing, the water in the pipes must contain antifreeze against the danger of freezing. With electric floor heating, soil can be heated on the golf and football fields. Grass growth starts in spring; this growth time is accelerated by heating the roots of the grass.

ADVANTAGES OF UNDERFLOOR HEATING SYSTEMS

In radiator and heating systems, as the surface of the heater has high temperature, the indoor air comes into contact with these surfaces and becomes dry, losing moisture. To do this, the air must be humidified, or the room must be ventilated in order to increase the humidity. This results in heat losses and excessive use of energy. Underfloor heating prevents these adverse situations.

Due to the high speed air currents occurring in the heating systems using radiators and heaters, the dust in the surrounding circulated continually in the room, causing contamination in walls. Due to the low air velocities in underfloor heating, the problem of dust and germ circulation in the heated space is minimal. For this reason, underfloor heating is recommended primarily in buildings such as hospitals, sanatoriums, dormitories, dukes dormitories, and nursing homes. There are no visible heating elements, pipes and fittings for underfloor heating. The main control collector is located in the cabinet. Since all kinds of materials such as marble, ceramic, parquet, carpet can be used as floor covering in floor heating, the space can be used for any purpose. Eliminates the problem of the location of the heaters between the architect and the installation engineer [4].

The use of water at a lower temperature increases the energy efficiency. It also makes it possible to use some other resources for heating. Sources such as solar energy, geothermal energy, heat pump are among these sources [5]. The system is almost maintenance-free. As there is less pipe connection, there are no problems such as leakage and corrosion. There is no cathodic corrosion between metals. Even if very long and very short pipe pieces are connected to the same collector, pressure compensation can be done very easily. The system is less likely to heat air and the available air can be taken from the collector or disposed of with an automatic air purge device. The investment in underfloor heating is lower than traditional systems. Heat loss due to thermal insulation is minimal. The use of a smaller boiler provides an advantage in the initial investment. Due to the low water temperature, the use of heating boilers increases the efficiency.

The underfloor heating system is self-regulating. The heat supply of a heated slab decreases or multiplies by itself according to the internal temperature and the wall temperature. Therefore, it controls itself by means of the floor surface temperature according to the outside temperature and thus the heating requirement without the need for expensive control and adjustment devices, even without human intervention. If the heat requirement is reduced, the heat in the system flows to the boiler or to other volumes in need of heat without dissipating it. In underfloor heating, the system has storage feature. This feature is also illustrating the stability of the system. As a result of ventilation and similar factors, heat fluctuations that occur at short intervals are compensated in a short time. The decrease between the surface temperature of the heated area and the room temperature causes a decrease in the heat flux. As a result, the smaller difference between the heated area and the surrounding temperature, the higher the self-adjusting effect.

APPLICATION PROCEDURE

What is valid for both types of laying is that as the modulation range is tightened and the screed thickness increases, the temperature distribution on the floor will be more homogeneous. The most common types of application are shown in the Fig. 1.

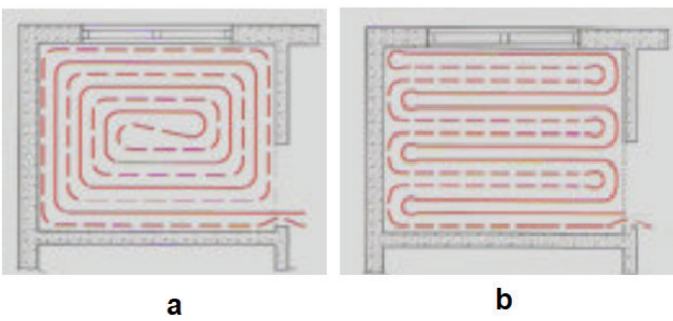

Fig. 1. *Helical piping (a), helical-parallel piping (b)*

Regardless of the type of flooring, the heat requirement of a room must be determined. The exact form of installation depends on the user's demands. The main function of the heating system is not only to meet the heating requirement. The heating system must also provide a relaxing room temperature. Therefore, when deciding on the shape of the floor, it should be remembered that the heat requirement from the outer wall region of a room will be reduced. Many problems can be solved by using different dimensioning techniques in the pipe openings for window fronts and outer wall edges that require more heat. In other words, where high temperature is required, the heating pipes should be installed more frequently. The benefit of helical pipe laying types is that the heat used in the system for the hot water flow is always directly next to the return pipe, thus compensating for the resulting heat and thus evenly distributing the surface temperature. Briefly, when laying underfloor heating pipes, attention should be paid to the common floor spacing in the edge areas, the wide floor spacing in the seating areas, the parallel flooring type in the form of helical bends. This results in the same, noticeable comfort throughout the room, a sufficient base temperature despite the high heat power, and energy savings as less preheating is required.

RECENT DEVELOPMENTS AND DISCUSSION

In a study conducted by Hajabdollahi et al., underfloor heating systems were modeled with empirical data. Designed parameters were also investigated. In analytical method, genetic algoritm and optimization approaches were utilized [6]. Plytaria et al. studied solar assisted heat pump underfloor heating system with and without phase change materials with TRYNSYS software [7]. In another study, Plytaria et al. investigated phase change material integrated solar-assisted heat pump underfloor heating system. As a result, phase change material modification reduced the heating load by 40% [8]. Ploennigs et al. investigated a hybrid HVAC system including underfloor heating system. The system contains gas-fired coiler, heat pump and solar thermal energy assistance. Schematic representation of the investigated system is given in

Fig. 2. They analyzed energy consumption and thermal comfort with the utilization of virtual sensors [5]. Some studies were modeled the thermal comfort and efficiency parameters for various type of underfloor heating systems [9-12]. Underfloor heating is also suggested for aircraft cabins [13].

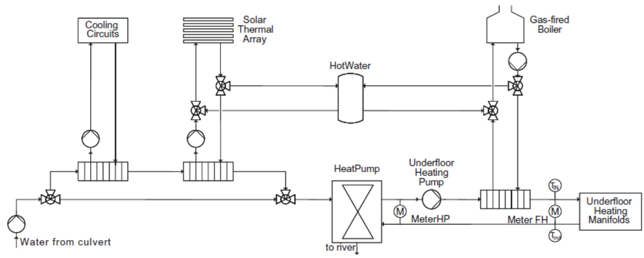

Fig. 2. *Schematic representation of a hybrid HVAC system (incl. underfloor heating) [5]*

When the studies are examined, it is seen that optimization techniques have great importance in terms of analysis. These approaches are critical in the efficient use of energy. In addition, many researchers have integrated renewable energy technologies into this system. There are also systems supported by phase change materials [14,15]. Briefly, the effective use of this technology and its environment-friendly operation depend on optimizing the system during the design and installation phase and supporting it with clean resources.

CONCLUSION

It is of utmost importance that underfloor heating pipes are given worldwide standards and that underfloor heating systems are evaluated within the framework of these standards. In spite of technological advances in our society in recent years, underfloor heating system which is not fully known should be introduced to the society properly. Necessary applications should be made for the development of underfloor heating systems which are economically important due to the decrease in heat load and the availability of the system with renewable energy sources. In addition, adapting the latent heat storage properties of phase change materials to this technology is important for energy saving. Supporting this technology with renewable energy sources will make great progress in the name of sustainability.

REFERENCES

[1] Aktaş, M., Koşan, M., Arslan, E., Tuncer, A. D. (2019). Designing a novel solar-assisted heat pump system with modification of a thermal energy storage unit. Proceedings of the Institution of Mechanical Engineers, Part A: Journal of Power and Energy, 233, 588-603.

[2] Olesen, Bjerna W. (2002). Radiant floor heating in theory and practice: American Society of Heating, Refrigerating and Air-Conditioning Engineers Inc.,

[3] Wietzmann, P., Kragh, J., Roots, P., Svendsen, S. (2005). Modelling floor heating systems using a validated two-dimensional ground-coupled numerical model, Building and Environment, 40, 153–163.

[4] Sattari, S. Farhanieh, B. A. (2006). Parametric study on radiant floor heating system performance, Renewable Energy, 31,1617-1626.

[5] Ploennigs, J., Ahmed, A., Hensel, B., Stack, P., Menzel, K. (2011). Virtual sensors for estimation of energy consumption and thermal comfort in buildings with underfloor heating. Advanced Engineering Informatics, 25, 688-698.

[6] Hajabdollahi, F., Hajabdollahi, Z., Hajabdollahi, H. (2012). Thermo-economic modeling and optimization of underfloor heating using evolutionary algorithms, Energy and Buildings, 47, 91-97.

[7] Plytaria, M.T., Bellos, E., Tzivanidis, C., Antonopoulos, K. A. (2018). Energetic investigation of solar assisted heat pump underfloor heating systems with and without phase change materials, Energy Conversion and Management, 173, 626-639.

[8] Plytaria, M. T., Bellos, E., Tzivanidis, C., Antonopoulos, K. A. (2019). Financial and energetic evaluation of solar-assisted heat pump underfloor heating systems with phase change materials, Applied Thermal Engineering, 149, 548-564.

[9] Zukowski, M. (2006). Modeling and designing heating and ventilation system with underfloor air distribution, Energy and Buildings, 38, 600-609.

[10] Maivel, M., Farrantelli, A., Kurnitski, J. (2018). E xperimental determination of radiator, underfloor and air heating emission losses due to stratification and operative temperature variations, Energy and Buildings, 166, 220-228.

[11] Açıkgöz, Ö., Karakoyun, Y., Yumurtacı, Z., Dukhan, N., Dalkılıç, A.S. (2019). Realistic experimental heat transfer characteristics of radiant floor heating using sidewalls as heat sinks, Energy and Buildings, 183, 515-526.

[12] Kull,T.M., Simson, R., Thalfeldt, M., Kurnitski, J. (2017). Influence of time constants on low energy buildings' heating control, Energy Procedia, 132, 75-80.

[13] Lei, L., Wang, S., Zhang, T. (2016). Inverse design of underfloor heating power rates and air-supply temperature for an aircraft cabin, Applied Thermal Engineering, 95, 70-78.

[14] Devaux, P., Farid, M. M. (2017). Benefits of PCM underfloor heating with PCM wallboards for space heating in winter, Applied Energy, 191, 593-602.

[15] Barzin, R., Chen, J.J.J., Young, B. R., Farid, M. M. (2015). Application of PCM underfloor heating in combination with PCM wallboards for space heating using price based control system, Applied Energy, 148, 39-48.

SOME COMFORT PROPERTIES OF TERRY KNITTED FABRICS MADE FROM COTTON/POLYESTER BLEND

Sena CİMİLLİ DURU[1], Cevza CANDAN

CHAPTER 19

1 Istanbul Technical University, Textile Technology and Design Faculty
cimilli@itu.edu.tr

SOME COMFORT PROPERTIES OF TERRY KNITTED FABRICS MADE FROM COTTON/POLYESTER BLEND

Sena CİMİLLİ DURU[1], Cevza CANDAN

1. INTRODUCTION

Comfort is an important determinant of consumer satisfaction with clothing. It is a subjective response resulting from complex interactions of environmental conditions, fabric properties, garment fit, physiological factors, and the psychological state of the wearer [1]. Slater defined comfort as a state of balance between a person and their environment. Comfort involves both thermophysiological parameters [2]. Fabrics ensure both thermal and sensorial comfort of the people by providing a barrier between the skin and environment. Presence of moisture in the fabric, typically from the wearer sweating, governs not only thermophysiological but also sensorial aspects of clothing comfort. Thermophysiological parameters, like heat transfer, within a clothing system are affected by the moisture present in the system, on the other hand, feelings of dampness and fabric cling are the influential parameters on the sensorial comfort. Effective management of moisture in clothing systems could be facilitated with both moisture vapor and liquid moisture performances as well as drying capabilities of fabrics.

Terry knitted fabrics are widely used in the clothing sector such as towels, socks, baby clothes and sweatshirts etc. These fabrics belong to the group of pile fabrics which have loop piles on one or both sides covering the entire surface. These kinds of fabrics have a higher water absorption property compared to other types of textile

1 Istanbul Technical University, Textile Technology and Design Faculty
cimilli@itu.edu.tr

fabrics. The amount of water absorbed, which includes the ability of material to retain a liquid in its interstice pores, [3] by terry fabrics is very important for its end use. However, this does not give any idea about how quickly a terry fabric absorbs the water or how water absorption changes with respect to time. Previous studies showed that the water absorption capacity of a terry fabric is dependent on yarn material, yarn type and fabric construction [4]. Mallikarjunan, Ramachhandran and Manohari [5] tested lyocell fabrics both pile and twill structure with different combinations for comfort properties and the results showed that lyocell pile, cotton/polyester knitted fleece and cotton/polypropylene plaited knitted fabrics can be used for cold climatic conditions. Also, they found that lyocell pile fabrics have very good water absorbency which immediately absorbs and transfers the moisture to inner layer and gives a dry feel. The study conducted by Petrulyte and Baltakyte [3] presented the investigations into the wetting phenomenon of terry fabrics which were manufactured using linen warp pile yarns. In the study made by Behera and Singh [6], yarns produced from two varieties of cotton (100% J-34 and MCU-5) and their blends with bamboo and poly vinyl alcohol (PVA) with different counts, twist and number of plies were used to prepare terry fabric of varying loop densities, loop lengths and loop shape factors. It was found that loop density is the most important parameter for water absorption rate followed by loop length and yarn twist. For the total amount of water absorbed, loop density is again the most important parameter followed by yarn twist, loop shape factor and number of ply in the pile yarn. Karahan and Eren [7] found that the type of yarns used in the production of terry fabric had the most significant effect on their static water absorption properties and added that two-ply ring-carded yarn showed a higher water absorption value than two-ply open-end yarn and single ply ring-carded yarn. They concluded their study such that an increase in weft and/or warp density reduced the percentage of static water absorption, and an increase in pile length increased the percentage static water absorption of terry fabrics. The effect of pile length on static water absorption was found to be more pronounced compared to warp and weft density. In addition, at another study of Karahan [4], the effects of same parameters on dynamic water absorption were investigated and it was found that the effect of pile length, warp and weft density on the percentage of water absorption remains limited compared to that of yarn type, and no significant effect of these parameters on water absorption is found for the last 100 seconds. Trafder et al [3] made a study about the effects of pile height, pile density, thickness, etc. on the surface water absorption characteristics and wicking phenomenon of different cotton terry fabric. The paper by Petrulyte and Velickiene [8] presented an investigation of the drying ability of terry fabrics with respect to pile height and finishing. The terry fabrics used in the experimental work were made from linen/cotton yarns, and the pile height of the samples was 6 and 12 mm. According to the results, evaporation duration time of finished ones were higher than that of grey ones and the drying of grey fabric with a low unbleached loop pile generally followed more intensively compared with a fabric a with high loop pile, while the reverse tendency was evident in finished fabrics. Krasteva et al [9] showed that higher weft density leads to greater mass of water absorbed by the terry fabrics and by increasing the loops height grows the absorbent surface, which leads to sorption of greater water quantity.

The literature survey showed that the studies conducted on water-related comfort properties of terry fabrics were generally about woven terry fabrics. In addition, in spite of the interest in the drying phenomenon of textiles, no research has been performed into the drying ability of terry knitted textiles. The aim of this study was to conduct experimental research into the drying process as well as transfer wicking terry knitted fabrics with respect to fiber type (cotton and polyester blends) and fabric tightness.

2. MATERIALS AND METHOD

2. 1 MATERIALS

For the study, terry knitted samples were produced at two different tightness factors (slack and tight) on a Sangiacomo Fantasia 1C machine. Ne 30/1 rotor yarns were used whose fiber compositions were 100% cotton, 67%/33% cotton/PET, 50%/50% cotton/PET, and 33%/67% cotton/PET. The properties of the yarns and fabric samples are given in Tables 1 and 2, respectively. First two letter indicates the fabric structure (TR- Terry), the second identification shows the fiber composition percentage; C is for cotton and PET is for Polyester, third group indicates fabric tightness (T-Tight, S- Slack).

All greige fabrics were dyed and finished under the relevant commercial production conditions. Following the dyeing and wet finishing processes the samples were squeezed, dried and then were sanforized.

Table 1: *Yarn properties*

Sample	Hairness				Yarn irregularity				Twist			
	n1	n2	n3	s3	CVm %	Thin places 50%/1000 m	Thick places 50%/1000 m	Neps +200%/1000m	Tour/m	CV %	Load (kgf)	Extension (%)
33% Cotton 67% PET	10688,3	1624,67	417	782,33	14,08	4	46	129	869,6	9,2	0,45731	58,555
50% Cotton 50% PET	15034	3007,33	893,67	1546	15,78	15	145	376	646,6	5,01	0,39959	50,048
67% Cotton 33% PET	20013,3	4460,33	1489,33	2695,67	14,74	7	88	220	871,4	4,13	0,35476	41,893
100 % Cotton	13566	2589,67	819	1424	12,46	0	13	80	893,6	7,56	0,33169	34,278

Table 2: *Fabric properties*

Numune	Stitch density (loop/cm^2)	Thickness (mm)	Porosity (%)	Weight (g/m^2)
TR-33/67 C/P-S	190,65	4,84	97,88	129,90
TR-33/67 C/P-T	218,55	4,85	97,65	144,24
TR-50/50 C/P-S	190,96	5,05	98,11	127,16
TR-50/50 C/P-T	224,75	5,18	97,96	140,22
TR-67/33 C/P-S	197,78	5,06	98,16	129,56
TR-67/33 C/P-T	238,24	4,94	97,93	142,86
TR-100 C-S	179,96	4,86	98,36	121,32
TR-100 C-T	251,72	4,60	97,89	147,52

2.2. METHOD

The dry relaxed fabrics were tested for some comfort-related properties: "Transfer Wicking", based on the method used by Zhuang et al. [10], but with the difference that an external pressure of 15.6 kg/m^2, which was high enough to start transfer wicking, was exerted; and "Drying Rate", based on Coplan's research [11]. Weight and thickness of the fabrics were evaluated according to the standards of TS 251 and TS 391 EN ISO 9237 respectively. The porosity values were calculated according to literature [12].

Decision-making is the art and science of choosing the best course of action or a set of preferred actions from the available alternatives [13]. TOPSIS is a decision making technique and it is a goal based approach for finding the alternative that is closest to the ideal solution. In this method, options are graded based on ideal solution similarity. If an option is more similar to an ideal solution, it has a higher grade. Ideal solution is a solution that is the best from any aspect that does not exist practically and we try to approximate it. Basically, for measuring similarity of a design (or option) to ideal level and non-ideal, it is considered distance of that design from ideal and non-ideal solution [14] The analytic hierarchy process (AHP) is the other most popular multi-criteria decision making method that deals with selection of the best alternative or ranking of alternatives under the presence of a finite number of decision criteria. [13]. The reason of popularity of AHP lies in the fact that it can handle the objective as well as subjective factors and the criteria weights and alternative scores are elicited through the formation of pair-wise comparison matrix, which is the heart of the AHP [15]. This research proposed a combined analytical hierarchy process (AHP) to calculate the weight of each risk criterion and technique for order performance by similarity to ideal solution (TOPSIS) methodology to rank. Main steps of this procedure as below [16-18]:

Step 1: The relevant objective or goal, decision criteria and alternatives of the problem are identified in this step.

Step 2: A decision matrix of criteria and alternatives is formulated on the basis of information avaible regarding the problem. The number of alternatives is M and the number of criteria is N where an element a_{ij} of the decision matrix D_{mxn} represents the actual value of the ith alternative in terms of jth decision matrix.

Step 3: The decision matrix is converted to a normalized decision matrix. The normalized value r_{ij} is calculated as

$$r_{ij} = \frac{a_{ij}}{\sqrt{\sum_{j=1}^{m}(a_{ij})^2}} \qquad j = 1, \dots \dots, m \quad i = 1, \dots \dots, n \qquad (1)$$

Step 4: The relative importance of different criteria with respect to the objective of the problem is determined using AHP. To do so, a pair-wise comparison matrix of criteria is constructed using a scale of relative importance (Table 3).

Table 3: *Nine point scale of relative importance [16-18]*

Intensity of importance on a absolute scale	Definition	Explanation
1	Equal importance	Two activities contribute equally to the objective.
3	Moderate importance of one over another	Experience and judgement slightly favor one activity to another
5	Essential or strong importance	Experience and judgement strongly favor one activity to another
7	Very strongly importance	An activity is strongly favored and its dominance is demonstrated in practice
9	Extreme importance	The evidence favoring one activity over another is of the highest possible order of affirmation.

The normalized weight or importance of the ith criteria (W_i) is determined by calculating the geometric mean of the ith row (GM_i) of the above matrix and then normalizing the geometric means of rows ass:

$$GM_i = \left\{\prod_{j=1}^{N} c_{ij}\right\}^{\frac{1}{N}} \tag{2}$$

$$W_i = \frac{GM_i}{\sum_{i=1}^{N} GM_i} \tag{3}$$

To check the consistency in pair-wise comparison judgment, consistency index (CI) and consistency ratio (CR) are calculated using the following equations

$$CI = \frac{\lambda_{max} - N}{N - 1} \quad \text{and} \quad CR = \frac{CI}{RCI} \tag{4}$$

where RCI is random consistency index and its value can be obtained from Table 3. If the value of CR is 0,1 or less than the judgment is considered to be consistent and therefore acceptable. Otherwise, the decision maker has to be reconsidering the entries of pair wise comparison matrix.

Table 4: *RCI values for different numbers of alternatives (m) [16-18]*

m	1	2	3	4	5	6	7	8	9
RCI	0	0	0,58	0,9	1,12	1,24	1,32	1,41	1,45

Step 5: The weighted normalized value υ_{ij} is calculated as

$$\upsilon_{ij} = W r_{ij} \qquad j = 1, \ldots \ldots, m \qquad i = 1, \ldots \ldots, n \tag{5}$$

where W_i is the weight of the ith attribute of criterion and $\sum_{i=1}^{n} W_i = 1$

Step 6: The positive ideal and negative ideal solution are determined by following formulations:

$$A^{+} = \{v_i^{+}, \ldots\ldots, v_n^{+}\} = \{(max_j v_{ij} | i \in I), (min_j v_{ij} | i \in J)\} \quad (6)$$

$$A^{-} = \{v_i^{-}, \ldots\ldots, v_n^{-}\} = \{(min_j v_{ij} | i \in I), (max_j v_{ij} | i \in J)\} \quad (7)$$

where *I* is associated with benefit criteria and *J* is associated with cost criteria.

Step 7: The separation measure using the n-dimensional Euclidean distance is calculated.

$$d_j^{+} = \left\{\sum_{i=1}^{n} (v_{ij} - v_i^{+})^2\right\}^{1/2} \quad j = 1, \ldots\ldots, m. \quad (8)$$

$$d_j^{-} = \left\{\sum_{i=1}^{n} (v_{ij} - v_i^{-})^2\right\}^{1/2} \quad j = 1, \ldots\ldots, m \quad (9)$$

Step 8: The relative closeness to the ideal solution is determined.

$$R_j = \frac{d_j^{-}}{(d_j^{+} + d_j^{-})} \quad j = 1, \ldots\ldots, m \quad (10)$$

Since $d_j^{-} \geq 0$ and $d_j^{+} \geq 0$ then clearly $R_j \in [0,1]$

Step 9: All the alternatives are arranged in a descending order according to value of R_j. The alternative at the top of the list is the most preferred one.

3. RESULTS &DISCUSSION

3.1. TRANSFER WICKING

The transfer wicking is the transmission of water through the thickness of a fabric that is perpendicular to the plane of the fabric and the mechanism of removal of liquid perspiration from the skin involves its movement through the fabric thickness [19]. In addition to Figure 1 which shows transfer wicking of the fabrics over 30 minutes, our measurements for transfer wicking of the fabrics after 30 minutes are also presented in Table 5.

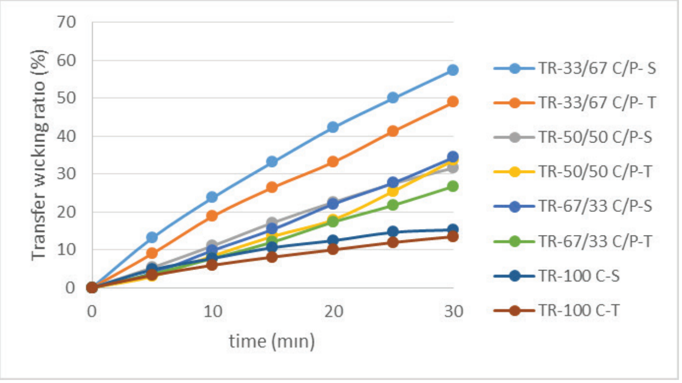

Figure 1: *Transfer wicking of the terry knitted fabrics.*

Table 5: *Transfer wicking ratios of the fabrics after 30 minutes.*

	Slack (%)	TIght (%)
TR-33/67 C/P	57,48	48,91
TR-50/50 C/P	31,63	33,66
TR-67/33 C/P	34,38	26,76
TR-100 C	15,26	13,48

As may be seen from Figure 1 and Table 5, within the first five minutes of the transfer wicking, the greatest wicking was observed for TR-33/67 C/P fabrics, while cotton garments gave the lowest values for the same period. Additionally, as shown in Figure 1, in the first five minutes of the test the transfer wicking ratio had a steep increase for all samples, which then became more gradual. Moreover, the terry fabrics performed such that an increase in polyester fiber percentage had a positive effect on the transfer wicking ratio, which is in agreement with the literature. As is known, liquid transport properties are significantly affected by fiber type. Also the liquid transport within a textile fabric is due to capillary action of fibers and is thus governed by the properties of fiber surface and diameter of yarn which varies with the fiber composition because of the difference in packing factor of each constituent fiber. Bearing these into mind, it may be concluded that the presence of polyester fiber having lower moisture regain and water holding capacity, in the fabrics may increase the transfer wicking ratio of the terry fabrics. The difference between the surface energies of PET and cotton fibers may also contribute this performance. It may also be noted that as the terry fabric became tighter, the transfer wicking ratio tended to decrease, irrespective of the fiber blend ratio. Literature survey showed that thickness and porosity have a sizeable effect on transfer wicking [10, 20-22]. However, as shown in Table 2, both thickness and porosity values of the samples were very close to each other and the differences between these values were not statistically significant. Therefore, this very result may partly be attributed to the differences between inter-yarn pore size as well as pore size distribution of the slack and tight terry fabrics. Also, in the tight fabrics the terry loops may be forced to randomly overlap more, which in turn may not only increase the distance taken by the liquid water, but also break the continuity of capillaries formed by the fibers, which aggravates liquid advancement through the fabric.

3.2. DRYING RATE

The drying properties of the fabrics are given in Table 6 which shows the terry fabrics with polyester fiber tended to dry faster. Due to the non-hygroscopic and highly crystalline character of polyester fibers, water molecules cannot be absorbed within the fibers and wetting occurred only on the surface of the fibers within the yarns. Thus, all the moisture of the polyester fabrics can be assumed to be free moisture, and this leads to shorter drying times. TR-50/50 C/P fabrics, on the other hand, had surprisingly the highest drying time, which is followed by TR-100 C and TR-67/33 C/P. So far as TR-100 C and TR-67/33 C/P terry fabrics are concerned, wet cellulosic fibers have a considerable amount of bound moisture due to the hygroscopic nature, and increase in hygroscopic character increases the drying time which is a good agreement with the literature [23, 24]. When it comes to TR-50/50 C/P fabrics, the relative arrangement of polyester and cotton fibers in the terry loops may create a drowning effect for the polyester fibers in the capillary channels of these loops filled with water thanks to the cotton fibers. This in turn may cause the relevant fabrics behave like cotton-intense and/or 100% cotton terry fabrics [25].

Finally, it was also found that the slack fabrics, independent of fiber blend ratio, tended to have higher drying rates and also larger water diffusion area. This is probably due to the fact that evaporation-drying ability of textiles is closely related to moisture releasing ability as well as fabric thickness, construction and fabric weight [26].

Table 6: *Drying rate and drying time of fabrics*

	Drying time (h)	Drying Rate, (g/h/m^2)
TR-33/67 C/P-S	20,005	88,04
TR-33/67 C/P-T	21,002	87,68
TR-50/50 C/P-S	25,016	115,47
TR-50/50 C/P-T	28,007	90,96
TR-67/33 C/P-S	23,005	104,62
TR-67/33 C/P-T	25,002	90,67
TR-100 C-S	25,001	84,53
TR-100 C-T	26,012	87,62

3.3. PERFORMING HYBRID AHP-TOPSIS APPROACH

With the aim of selection best sock alternative from the investigated fabrics, the relative weights of two decision criteria were determined. Drying rate and transfer wicking of the fabrics are influential and important parameters for the users to feel comfortable. Thus, these two parameters were selected as criteria. The pair-wise comparison matrix of the two decision criteria's with regard to their importance level can be observed in Table 7.

Table 7: *Pair-wise comparison matrix of criteria with regard to objective and codes*

	Transfer wicking	Drying rates	Codes
Transfer wicking	1	3	C1
Drying rates	1/3	1	C2

Then, the normalized weights, weighted normalization matrix, both positive and negative ideal solutions were calculated in turn (see Table 8).

Table 8: *Weighted normalization matrix of the fabric samples*

	C1	**C2**
W=1	0,75	0,25
TR-33/67 C/P- S	88,04	57,48
TR-33/67 C/P- T	87,68	48,91
TR-50/50 C/P-S	115,47	31,63
TR-50/50 C/P-T	90,96	33,66
TR-67/33 C/P-S	104,62	34,38
TR-67/33 C/P-T	90,67	26,76
TR-100 C-S	84,53	15,26
TR-100 C-T	87,62	13,48
Positive ideal solution	0,32	0,14
Negative ideal solution	0,24	0,03

At the next step, the separation of each alternative from the ideal solution was calculated. The relative closeness of the alternatives (R_j) to the ideal solution (A_j) was defined in terms of A^+. Based on the closeness of the coefficient to the ideal solution (R_j value), the ranking of the preference order of all the alternatives in descending order is exhibited in Table 9.

Table 9: *Preference order for the fabric samples*

Fabrics	**Pos Ideal (d+)**	**Neg Ideal (d-)**	**Relative closeness (Rj)**	**Rank**
TR-50/50 C/P-S	0,0642	0,0980	0,60	1
TR-33/67 C/P- S	0,0772	0,1097	0,59	2
TR-67/33 C/P-S	0,0650	0,0767	0,54	3
TR-33/67 C/P- T	0,0810	0,0884	0,52	4
TR-50/50 C/P-T	0,0908	0,0533	0,37	5
TR-67/33 C/P-T	0,1034	0,0372	0,26	6
TR-100 C-S	0,1362	0,0044	0,03	7
TR-100 C-T	0,1344	0,0087	0,06	8

Final ranking of hybrid AHP-TOPSIS method implied that TR-50/50 C/P-S was the best alternative based on water related comfort properties of terry socks. However, different from the subjectively expected, TR-100 C-T performed the worst alternative in the rankings.

4. CONCLUSION

This study aimed to determine the relative effects of fiber type (cotton and polyester blends) and fabric tightness (slack and tight) on drying rate and transfer wicking of terry knitted fabrics. According to the results, it was concluded that the change in cotton/polyester blend ratio from 100/0, 67/33, 50/50 to 33/67 did significantly affect positively the transfer wicking ratios of terry fabrics. Also, slack ones transported the water quickly than those of tight ones. Moreover, the experimental results revealed that the use of polyester fibers can enhance the drying rate that by increasing polyester fiber content in C/P blended fabric, the drying time of the fabric decreased and slacker ones dried faster than those of slacker ones. Due to the fact that analytic hierarchy process (AHP) and the technique for order performance by similarity to ideal solution (TOPSIS) are widely employed methodologies to facilitate this kind of processes, hybrid AHP-TOPSIS multi-criteria decision method was used in this study with the aim of select the best terry fabric. The weights for each criterion were calculated based on Analytic Hierarchy Process (AHP) and then inputted these weights to the TOPSIS method to rank alternatives. Finally, TR-50/50 C/P-S fabric was found to be the best while TR-100 C-T performed the worst one.

REFERENCES

[1] Morris M. A., Prato H. H., White N. L. Relationship of Fiber Content and Fabric Properties to Comfort of Socks. Clothing and Textile Research Journal. 1985; 3(1): 14-19.

[2] Furtak N. T. Socks: Correlation of Wetness Perceptions with Moisture Transport. PhD Thesis. University of Alberta. 2018.

[3] Petrulyte S., Baltakyte R. Investigation into the Wetting Phenomenon of Terry Fabrics. Fibres & Textiles in Eastern Europe. 2008; 16, 4 (69): 62-66.

[4] Karahan, M. Experimental Investigation of the Effect of Fabric Construction on Dynamic Water Absorption in Terry Fabrics. Fibres & Textiles in Eastern Europe. 2007; 15, 3 (62): 74-80

[5] Mallikarjunan, K., Ramachhandran, T., Manohari, B. G. Comfort and Thermo Physiological Characteristics of Multilayered Fabrics for Medical Textiles. Journal of Textile and Apparel Technology and Management. 2011; 7(1): 1-15.

[6] Behera B.K., Singh J.P. Factors Contributing to Absorbency Behavior of Pile Fabrics. Research Journal of Textile and Apparel. 2014; 18(3): 81-93

[7] Karahan, M, Eren, R., Experimental Investigation of the Effect of Fabric Parameters on Static Water Absorption in Terry Fabrics. Fibres& Textiles in Eastern Europe. 2006; 14, No: 2 (56): 59-63.

[8] Petrulyte S., Velickiene A. Investigation of Drying Phenomenon of Terry Woven Fabrics. Fibres & Textiles in Eastern Europe. 2011; 19, 6 (89): 58-63.

[9] Germanova-Krasteva D. S., Kandzhikova G. D., Bochev A. G. Influence of Terry Fabrics Structure on Dynamic Sorption. International Journal of Clothing Science and Technology. 2013; 25(4): 243-256.

[10] Zhuang Q., Harlock S.C., Brook D.B. Transfer Wicking Mechanism of Knitted Fabric Used as Undergarment for Outdoor Activities. Textile Research Journal. 2002; 72: 727–734.

[11] Coplan M.J. Some Moisture Relations of Wool and Several Synthetic Fibers and Blends. Textile Research Journal. 1953; 23: 897–916.

[12] Mukhopadhyay, A., Ishtiaque, S.M.,Uttam, D. Impact of Structural Variations in Hollow Yarn on Heat and Moisture Transport Properties of Fabrics. The Journal of the Textile Institute. 2011; 102 (8): 700–712.

[13] Ghosh A., Mal P., Majumdar A. Advanced Optimization and Decision-Making Techniques in Textile Manufacturing. CRC Press 2019.

[14] Sasi J. C., Digalwar A. K. Application of AHP and TOPSIS Method for Supplier Selection Between India & China in Textile Industry. International Research Journal of Engineering and Technology. 2015; 2(4): 1730-1738.

[15] Banwet D. K., Majumdar A. Comparative Analysis of AHP-TOPSIS and GA-TOPSIS Methods for Selection of Raw Materials in Textile Industries. Proceedings of the 2014 International Conference on Industrial Engineering and Operations Management Bali, Indonesia, January 7 – 9, 2014.

[16] Majumbar, A., Sarkar, B., Majumbar, P.K. Determination of Quality Value of Cotton Fibre Using Hybrid AHP-TOPSIS Method of Multi-Criteria Desicion-Making. Journal of Textile Institute. 2005; 96(5)- 303-309.

[17] Moghassem, A.R., Bahramzadeh, H. Application of Multi-Criteria Analysis for Parameters Selection Problem in Rotor Spinning. Textile Research Journal. 2010; 80(20): 2176-2187.

[18] Shyjith, K., Ilangkumaran, M., Kumanan, S. Multi-Criteria Decision Making Approach to Evaluate Optimum Maintenance Strategy in Textile Industry. JQME. 2008; 14(4): 375-386.

[19] Mallikarjunan, K., Ramachandran T., Manohari, B.G. Comfort and Thermophysiological Characteristics of Multilayered Fabrics for Medical Textiles. Journal of Textile and Apparel Technology and Management. 2011; 7(1).

[20] Ramachandran T., Kesavaraja N. Study on Influencing Factors for Wetting and Wicking Behavior. IE (I) J. 2004; 84: 184–186.

[21] Nyoni A.B., Brook D. Wicking Mechanisms in Yarns—The Key to Fabric Wicking Performance. Journal of Textile Institute. 2006; 97: 119–128.

[22] Cimilli S., Nergis B.U., Candan C. Ozdemir M., Comparative Study of Some Comfort-Related Properties of Socks of Different Fiber Types. Textile Research Journal. 2010; 80: 948–957.

[23] Su, C.I., Fang, J.X., Chen X. H., Wu W.Y. Moisture Absorption and Release of Profiled Polyester and Cotton Composite Knitted Fabrics. Textile Research Journal. 2007; 77: 764-769.

[24] Cay A, Gurlek G., Oglakcioglu N. Analysis and Modeling of Drying Behavior of Knitted Textile Materials. Drying Technology. 2017; 35(4): 509-521.

[25] Yoon, H. N., Buckley A. Improved Comfort Polyester Part I: Transport Properties and Thermal Comfort of Polyester/Cotton Blend Fabrics. Textile Research Journal. 1984; May: 289-298.

[26] Jhanji Y., Gupta D., Kothari V. K. Liquid Transfer Properties and Drying Behavior of Plated Knitted Fabrics with Varying Fibre Types. Indian Journal of Fibre & Textile Research. 2015; 40:162-169.

EXPERIMENTAL INVESTIGATION OF THIN LAYER DRYING KINETICS OF BLACK RADISH

Aytaç MORALAR[1], Halil Nusret BULUŞ[2], Soner ÇELEN[3]

CHAPTER 20

1 Tekirdağ Namık Kemal Üniversitesi, Çorlu Mühendislik Fakültesi, Makine Mühendisliği Bölümü, Tekirdağ, .amoralar@nku.edu.tr, tel: +90 282 250 2370, ORCID ID: http://orcid.org/0000-0002-3964-4909

2 Tekirdağ Namık Kemal Üniversitesi, Çorlu Mühendislik Fakültesi, Bilgisayar Mühendisliği Bölümü, Tekirdağ, nbulus@nku.edu.tr, tel: +90 282 250 2352, ORCID ID: http://orcid.org/0000-0003-1844-6484

3 Tekirdağ Namık Kemal Üniversitesi, Çorlu Mühendislik Fakültesi, Makine Mühendisliği Bölümü, Tekirdağ, scelen@nku.edu.tr, tel: +90 282 250 2366, ORCID ID: http://orcid.org/0000-0001-5254-4411.

EXPERIMENTAL INVESTIGATION OF THIN LAYER DRYING KINETICS OF BLACK RADISH

Aytaç MORALAR[1], Halil Nusret BULUŞ[2], Soner ÇELEN[3]

1. INTRODUCTION

Radish (*Raphanus sativus var. Sativus)*, is a vegetable rich in nutrient content with wide variation, production and range of dispension especially in China, Japan, Korea and South Asia and which holds an important place in meeting the requirements of fresh vegetable of people [1]. Radish production is estimated to be about 7 million tons/year in the world [2]. The black ones of the genotypes of the radish are named as horse radish. Radish is a vegetable rich in vitamin C, sulfur and iodine. Black radish contains folic acid, vitamin C, calcium, iron and potassium minerals. It also contains vitamins B1, B2 and a variety of minerals. The radish grown in Europe is widely consumed fresh. In Asian countries tubers of large radish are consumed as cooked, dried or processed as pickled. It is also denoted that in South America (Mexico) the black radish is used for medical purposes to prevent formation of gallstones and to reduce the fat levels in the blood [3].

Drying process is the oldest and most common food preservation technique in the world, since it reduces the moisture content of the food, diminishes microbiological

1 Tekirdağ Namık Kemal Üniversitesi, Çorlu Mühendislik Fakültesi, Makine Mühendisliği Bölümü, Tekirdağ, .amoralar@nku.edu.tr, tel: +90 282 250 2370, ORCID ID: http://orcid.org/0000-0002-3964-4909

2 Tekirdağ Namık Kemal Üniversitesi, Çorlu Mühendislik Fakültesi, Bilgisayar Mühendisliği Bölümü, Tekirdağ, nbulus@nku.edu.tr, tel: +90 282 250 2352, ORCID ID: http://orcid.org/0000-0003-1844-6484

3 Tekirdağ Namık Kemal Üniversitesi, Çorlu Mühendislik Fakültesi, Makine Mühendisliği Bölümü, Tekirdağ, scelen@nku.edu.tr, tel: +90 282 250 2366, ORCID ID: http://orcid.org/0000-0001-5254-4411.

activity, chemical and physical qualities during storage [4]. There are many different drying methods. One of these methods is microwave drying. Microwave energy is a mode of electromagnetic radiation with frequency of 0.3 GHz to 300 GHz (wave length of 1 m to 1 mm). Microwave frequencies of 915 MHz and 2450 MHz can be utilized for the most applications [5]. Microwave drying, which is an alternative to conventional drying, has improved product quality and has shorter drying time [6, 7].

Microwave energy drying differs remarkably from conventional drying methods. In conventional drying, due to the temperature difference between the hot surface and the colder interior, heat is gradually transferred to the interior of the material. There are two important mechanisms as ionic polarization and dipole rotation that explain the heat generation in the electromagnetic field. Heat is released by the friction of the molecules rotating dipole rotation and the other molecules in the environment. Ionic polarization causes the kinetic energy of the ions moving as a result of collision with each other, turn into thermal energy. During drying, the microwave energy is absorbed by the product and water evaporates due to the heat generated [8]. In microwave applications, microwaves can transport energy to the entire bulk of the material, shortening the processing time and improving the quality of the product [9, 10, 11].

There are many scientific studies on drying of fruits and vegetables using microwave energy. In these investigations, fruits and vegetables such as coriander (Coriandrum sativum L.) leaves [12], potato [13], grape [14], apple [15], mushroom [8], carrot [16], banana [17], pepper [18] and garlic [19] were studied.

Conventional drying systems used today usually have more energy consumption and longer drying times. It is desirable that the product does not lose its nutritional value and color at the end of drying. In this work we used a microwave band dryer in order to increase serial production and reduce energy consumption. In microwave drying, material mass, specific heat, dielectric properties, geometry, heat loss mechanism and power generated in the material must be considered as basic parameters. So radish, which can be found every season in our region, is preferred. And thus in this study, the effect of slice thickness, microwave energy level and conveyor belt speed in dried food production were investigated. The most convenient model was chosen among 10 models to describe the drying behavior during microwave drying of black radish slices. In addition, some drying characteristics (drying rate, drying time, moisture content, effective diffusivity, activation energy) of black radish was determined. The effect of microwave energy was determined by examining color analysis and SEM images of radish.

2. Material and Methods

Black radish with a moisture content of 87 ± 0.5% (w.b.) was obtained from a market in Tekirdag. The programmable and multifunctional microwave conveyor dryer used in the study has the technical specifications of 2.1 kW at 2.45 GHz as seen in Fig. 1. The dryer can be run at 1.05, 1.5 and 2.1 kW. The microwave tunnel sizes were 0.5x0.4x3.5 m. The microwave energy was generated by means of 3 magnetrons of 0.7 kW at 2450 MHz. The conveyor belt speed can be set by the potentiometer of control unit. The weight of the black radish slices was specified with a precision scales (Presica XB620M; made in Switzerland). The energy consumed was measured by a digital device (Enda, Turkey) with 0.1 kWh accuracy. The color analysis of the product was measured by a Spec HP-200 (Jiangsu, China) colorimeter. The inner surface of the dried black radish samples was shown using an FEI brand (QUANTA FEG 250) scanning electron microscope.

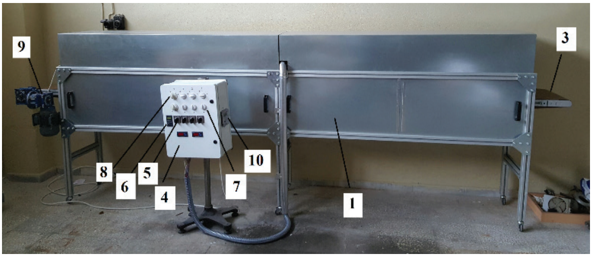

(a)

(b)

1. Experimental setup 2. Magnetrons 3. Teflon belt 4. Control panel 5. Power switch 6. conveyor speed control 7. Power (on/off) 8. Microwave power control 9. Electrical motor 10. Energy consumption meter

Figure 1. (a) The experimental setup, (b) view of dryer inside

2.1 Drying procedure

Before drying, samples were stripped and sliced 4 mm, 6 mm and 8±0.15 mm thickness with a machine. About 14±0.5 g, 16±0.3 g and 23±0.5 g of black radish slices were used for drying, respectively. Samples were chosen from the mature and uniform parts. Initial moisture content was determined as 87±0.5% (at 105 °C during 24 hours). Samples were used in each experiment and were dried to around 12±0.5% (wet basis) moisture value. No pre-treatment was implemented to the black radish prior to the drying. Drying tests were performed at 1.05, 1.5

and 2.1 kW at the frequency of 2450 MHz, conveyor belt speed of 0.175 m/min and 0.245 m/min and for each thickness. Black radish slices were weighed using a scale (Presica XB 620 M; Switzerland with 0.01 g precision and moisture changes were determined. All experiments were performed three times. After each test, the energy consumption of the setup and the color parameters of the radish were measured.

2.2 Mathematical modeling of drying

To design a suitable dryer for the investigated black radish, the analysis of drying kinetics and its mathematical modeling is essential [20]. Different products should be analyzed with different models created using heat, mass and momentum transfer. The moisture ratio (MR) was calculated in Eq.1:

$$MR = \frac{m - m_e}{m_o - m_e} \qquad (1)$$

The values of m_e are very low compared to m or m_o for long drying time. m_e in microwave oven was accepted as zero [21, 22]. The moisture ratio (*MR*) and statistical values can be calculated in Eq. 2-5.

$$MR = m/m_o \qquad (2)$$

In the present study, with the help of non-linear egression analysis method, the modelling of moisture gradient time curves obtained from experiments carried out in different microwave power values, have been made. The black radish drying datas were applied to 10 drying models. The ten drying models of thin layer biological materials used in Table 1 are determined. Some parameters are required to be calculated in order to determine the most convenient model. Corelation coefficient (R^2) is one of the criteria used to determine the curve relevance. MSE is another parameter used to determine the regression relevance [23]. In order to obtain the best fit to the experimental data, the determination coefficient should be close to one and MSE and RMSE should be close to zero. The parameters are defined as in Equation 3-5 [13]:

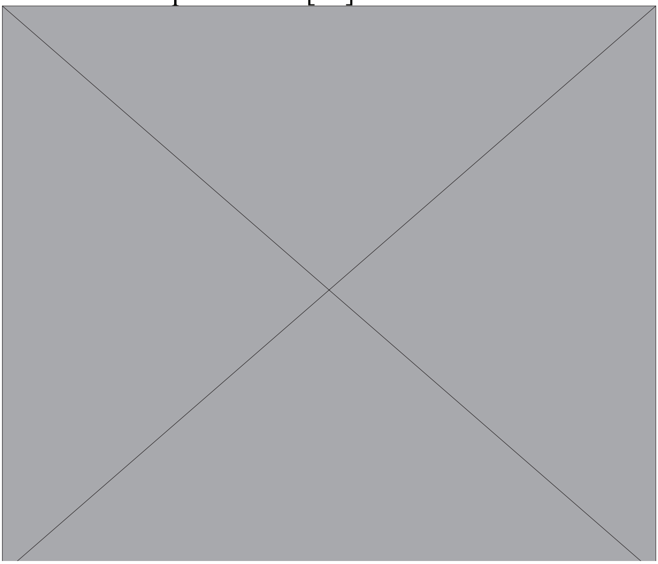

Table1. Mathematical models for drying kinetics [24]

Model Name	Model equation
Newton	$MR = \exp(-kt)$
Page	$MR = \exp(-kt^n)$
Henderson&Pabis	$MR = a\exp(-kt)$
Wang&Singh	$MR = 1 + at + bt^2$
Two term exponential	$MR = a\exp(-kt) + (1-a)\exp(-kat)$
Logarithmic	$MR = a_0 + a\exp(-kt)$
Logistic	$MR = a_0 / (1 + a\exp(kt))$
Midilli *et al.*	$MR = a\exp(-kt^n) + bt$
Two term	$MR = a_1\exp(-k_1 t) + a_2\exp(-k_2 t)$
Verma *et al.*	$MR = a\exp(-kt) + (1-a)\exp(-gt)$

2.3 Effective moisture diffusivity and activation energy

Most of biological materials dry in the falling rate period. The moisture transfer occuring during drying is generally controlled by internal diffusion. D_{eff} and the variables which influence D_{eff} were carried out via an analysis of the falling rate period [25]. A decrease in moisture content may cause a change in the drying characteristics during the drying process that can be controlled by diffusion mechanism [26]. In this study, black radish slices, assumed to be infinite plates which are described by Ficks' second law and the effective moisture diffusivity (D_{eff}) within infinite plates, can be estimated in Eq. (6). In Eq 6, material shrinkage was neglected assuming symmetrical boundary conditions [27].

(6)

Diffusivities were determined by the slope of logarithmic of MR versus drying time (t) in the equation. The plot produces a straight line with the slope given in Eq.7.

$$\text{Slope} = \frac{\pi^2 D_{eff}}{4L^2} \qquad 7)$$

Activation energy, which is the minimum energy, is needed for the movement of molecules of water from one side to another in solids [6]. As it is not possible to determine the temperature accurately in the microwave drying, the Arrhenius equation is revised. Instead of air temperature, effective moisture diffusion is defined according to m/P ratio in Eq. 8 [28, 29, 30]:

$$D_{eff} = D_o . e^{-Ea.m/P} \qquad (8)$$

2.4 Color parameters

For many consumers, color of food is an important feature. Color is an index of the good qualities that are inherent in foods. The parameter a* takes positive and negative values (reddish and greenish), whereas the parameter b * takes positive and negative values (yellowish and bluish). L * gives the approximate value for luminosity. For the calibration of the colorimeter, a standard black and white plate was used. The average color value of dried black radish was measured and recorded in each experiment. Three readings were done randomly and recorded for each sample. Also, average values of color parameters were obtained with standard deviations [12, 31]. These parameters are defined in Eq. 9-12:

$$\Delta L=L_{fresh}-L^* \tag{9}$$

$$\Delta a=a_{fresh}-a^* \tag{10}$$

$$\Delta b=b_{fresh}-b^* \tag{11}$$

$$\Delta E=\sqrt{\Delta L^2+\Delta a^2+\Delta b^2} \tag{12}$$

3. Results And Discussion

3.1 Drying curves

The relationship between drying time and moisture ratio for black radish is shown in Fig. 2-7. The moisture ratio reduces as the drying time increases. Also, mass transfer within the sample was more rapid during higher microwave power heating because more heat was generated within the sample creating a large vapour pressure difference between the center and the surface of the product by reason of characteristic microwave volumetric heating [18]. In all experiments, the drying process was ended when the final moisture level of the radish slices reached approximately 12 ± 0.5% (wet basis).

At the conveyor speed of 0.175 m/min and at the microwave power levels of 1.05, 1.5 and 2.1 kW respectively, drying was carried out at 69, 57 and 42 minutes for 4 mm thickness, 54, 51 and 33 minutes for 6 mm thickness, 84, 69 and 48 minutes for 8 mm thickness. At the conveyor speed of 0.245 m/min and at the microwave power of 1.05, 1.5 and 2.1 kW respectively, drying was carried out at 99, 54 and 51 minutes for 4 mm thickness, 87, 66 and 48 minutes for 6 mm thickness, 102, 66 and 52 minutes for 8 mm thickness.

Therefore, it can be said that the microwave power has a significant effect on the drying process as seen from the drying curves. The increase of the microwave power level decreased the drying time and the moisture ratio rapidly [32]. It is stated by Doymaz [33] and Chinenye [34] that the drying time is diminished by increasing the temperature in a conventional dryer. Lee and Kim [35] investigated that the drying times needed for the radish thickness of 4 mm were 446.50, 326.43, and 275.15 min and for the radish slices of 6 mm were 646.14, 514.22, and 437.91 min at 40, 50, and 60 ^{o}C, respectively. It was seen that the microwave conveyor drying is about five times less than the hot air drying. In terms of drying time, microwave conveyor drying is found to be about five times less than hot air drying.

The moisture content of the material was very high during the initial phase of the drying which resulted in a higher absorption of microwave power and higher drying rates due to the higher moisture diffusion. As the drying progressed, the loss of moisture in the product caused a decrease in the absorption of microwave power and resulted in a fall in the drying rate. The drying rates increased with the increasing microwave power levels. Therefore, microwave power level has an important effect on the drying rates. Our results are consistent with previous studies [36, 37]. However, as can be seen in Figs. 1-3, it cannot be said that the moisture change curves of the product are regular. For this reason, the dryer is an open system, so there can be energy losses. Microwave energy reaches the product in various amounts directly and with reflection. This shows irregularity during the drying period. The water distribution in the product and the product's geometrical structure are non-uniform.

3.2 Drying kinetics modeling

In order to calculate the model curve, the relation between the drying time and the moisture ratio was investigated. Values of the model coefficients, R^2, RMSE and MSE are indicated in Table 2-3. The results show that the most appropriate model in describing the drying curves of black radish is the Midilli model with R^2 in the range of 0.9883-0.9966, and with RMSE in the range of 0.0122–0.0272 and with MSE in the range of 0.0001–0.0007 at 0.175 m/min conveyor speed and with R^2 in the range of 0.9915-0.9985, and with RMSE in the range of 0.0095–0.0261 and with MSE in the range of 0.0001–0.0007 at 0.245 m/min conveyor speed. Among the drying models, the Newton model was determined as the worst. By Lee and Kim, 2009, the logarithmic model was chosen as the most convenient model to represent the drying behavior of radish slices at 40, 50 and 60 ^{o}C for slice thickness of 4 and 6 mm.

Figure 2-7 compares experimental data with those predicted with the Midilli model for black radish slices dried at different microwave powers and different conveyor speeds. As shown in Figure 2-7, dehumidification is rapid at the first stage of the drying process and drying rate slows down as the drying proceeds. It can be seen from Figure 2-7 that the experimental data are closely bounded to the simulated data for Midilli model along the curve.

Table 2. *Regression analysis results for Midilli et al. model at 0.175 m/min conveyor speed*

Slice thickness of radish	Microwave power	Coefficients	R^2	RMSE	MSE
4 mm	1.05 kW	b=0.0020 n=1.9911 k=0.0019 a=0.9308	0.9966	0.0193	0.0004
	1.5 kW	b=0.0021 n=1.7591 k=0.0038 a=0.9557	0.9963	0.0178	0.0003
	2.1 kW	b=0.0015 n=0.5317 k=0.4645 a=1.8893	0.9957	0.0122	0.0001
6 mm	1.05 kW	b=-0.0003 n=2.2045 k=0.0008 a=0.9593	0.9961	0.0229	0.0005
	1.5 kW	b=0.0015 n=1.9543 k=0.0014 a=0.9102	0.9932	0.0259	0.0007
	2.1 kW	b=0.0021 n=1.8199 k=0.0034 a=0.9402	0.9936	0.0240	0.0006
8 mm	1.05 kW	b=0.0005 n=1.2555 k=0.0098 a=0.9866	0.9928	0.0238	0.0006
	1.5 kW	b=0.0013 n=1.3442 k=0.0108 a=0.9061	0.9890	0.0272	0.0007
	2.1 kW	b=0.0017 n=1.5034 k=0.0093 a=0.8666	0.9883	0.0270	0.0007

Table 3. *Regression analysis results for Midilli et al. model at 0.245 m/min conveyor speed*

Slice thickness of radish	Microwave power	Coefficients	R^2	RMSE	MSE
4 mm	1.05 kW	a= 0.9506 k= 0.0034 n= 1.6509 b= 0.0016	0.9971	0.0148	0.0002
	1.5 kW	a= 0.9568 k= 0.0015 n= 1.8974 b= 0.0009	0.9975	0.0165	0.0003
	2.1 kW	a= 0.9636 k= 0.0035 n= 1.8673 b= 0.0025	0.9930	0.0261	0.0007
6 mm	1.05 kW	a= 1.3738 k= 0.2824 n= 0.1970 b= -0.0066	0.9985	0.0095	0.0001
	1.5 kW	a= 1.2141 k= 0.1489 n= 0.3842 b= -0.0069	0.9973	0.0138	0.0002
	2.1 kW	a= 0.9168 k= 0.0003 n= 2.3838 b= 0.0016	0.9974	0.0175	0.0003
8 mm	1.05 kW	a= 1.0888 k= 0.0308 n= 0.8973 b= -0.0003	0.9963	0.0160	0.0003
	1.5 kW	a= 1.8665 k= 0.5073 n= 0.1885 b= -0.0071	0.9971	0.0145	0.0002
	2.1 kW	a= 0.9369 k= 0.0124 n= 1.2227 b= -0.0012	0.9915	0.0260	0.0007

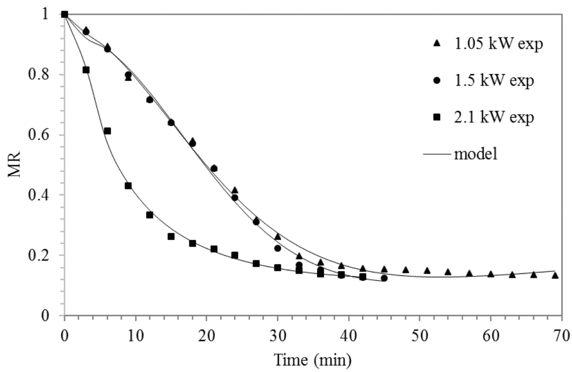

Figure 2. *Suitability of the experimental data to Midilli model for sample with 4 mm layer thickness dried at 0.175 m/min conveyor speed*

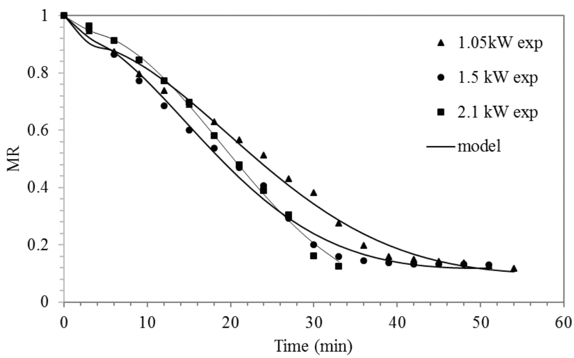

Figure 3. *Suitability of the experimental data to Midilli model for sample with 6 mm layer thickness dried at 0.175 m/min conveyor speed*

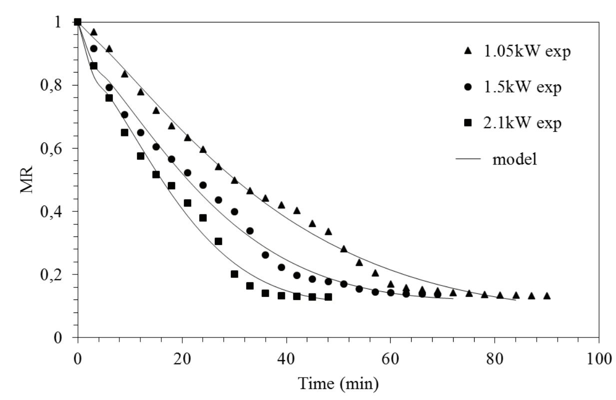

Figure 4. *Suitability of the experimental data to Midilli model for sample with 8 mm layer thickness dried at 0.175 m/min conveyor speed*

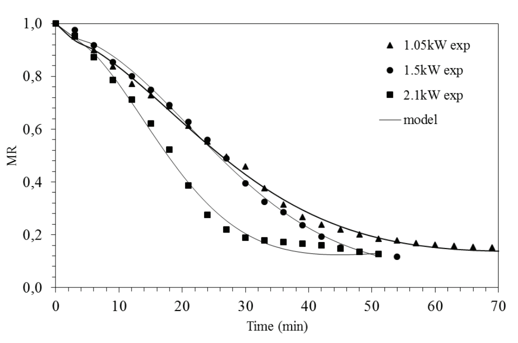

Figure 5. *Suitability of the experimental data to Midilli model for sample with 4 mm layer thickness dried at 0.245 m/min conveyor*

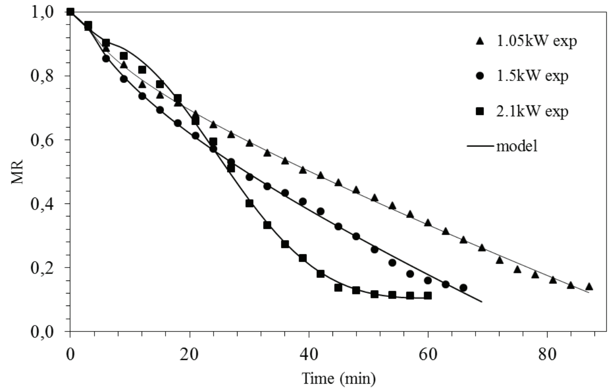

Figure 6. *Suitability of the experimental data to Midilli model for sample with 6 mm layer thickness dried at 0.245 m/min conveyor speed*

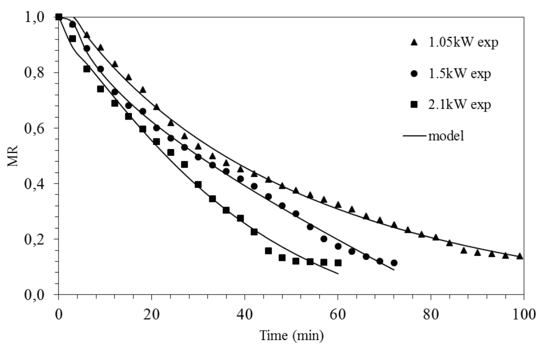

Figure 7. *Suitability of the experimental data to Midilli model for sample with 8 mm layer thickness dried at 0.245 m/min conveyor speed*

3.3 Effective moisture diffusivity and activation energy

The results of the previous researchers have shown that the internal mass transfer resistance controls the drying time due to the presence of a falling rate-drying period. Therefore, the values of effective diffusivity (Deff) at different output powers could be obtained by using Eq. (6).

Effective moisture diffusivity was calculated by using the slope method under different drying conditions. The obtained values of Deff for the black radish slices in this study are comparable with the reported values for microwave power of black radish slices at 1.05 - 2.1 kW, and conveyor speed range of 0.175 - 0.245 m/min.

The effective diffusion coefficients ranged from $1.334.10^{-7}$ to $2.816.10^{-7}$ m^2/s, $5.282.10^{-7}$ to $6.967.10^{-7}$ m^2/s and $5.561.10^{-7}$ to $9.860.10^{-7}$ m^2/s for 4, 6 and 8 mm black radish slices respectively dried at different microwave power of 1.05 kW–2.1 kW and conveyor speed of 0.175 m/min. The effective diffusivities ranged from $1.130.10^{-7}$ to $2.816.10^{-7}$ m^2/s, $2.475.10^{-7}$ to $5.569.10^{-7}$ m^2/s and $1.038.10^{-7}$ to $8.148.10^{-7}$ m^2/s for 4, 6 and 8 mm black radish slices respectively dried at different microwave power of 1.05 - 2.1 kW and conveyor speed of 0.245 m/min.

The effective diffusivity generally is within the range given for food materials (10^{-11} to 10^{-6} m^2/s) [38]. As expected, the diffusivity values increased with the increase of microwave power. This might be explained by the increase in heat energy, which increased the activity of the water molecules leading to higher moisture diffusivity, when samples were dried at higher microwave power due to the rise of temperature and consequently vapor pressure of water [6]. The highest value of $9.860.10^{-7}$ m^2/s was obtained for 8 mm slices while the lowest $1.334.10^{-7}$ m^2/s was obtained for 4 mm slices at 0.175 m/min. The highest effective moisture diffusivity value of $8.148.10^{-7}$ m^2/s was obtained for 8 mm slices while the lowest $1.038.10^{-7}$ m^2/s was obtained for 8 mm slices at 0.245 m/min.

It was reported by Torki-Harchegani et al [39] that microwave drying improved the moisture diffusion considerably in comparison with hot air drying. During microwave drying, it is observed that moisture diffusivity increased greatly with the increase in microwave power levels. High microwave power can be said to increase the moisture gradient and the driving force of the moisture diffusivity and mass transfer.

The activation energy for 4, 6 and 8 mm black radish slices respectively was found to be 44.08 W/g, 15.49 W/g and 24.97 W/g at 0.175 m/min. The activation energy for 4, 6 and 8 mm black radish slices respectively was found to be 104.3 W/g, 35.51 W/g and 24.97 W/g at 0.245 m/min. These values are higher than the value of okra (5.54 W/g) [40], mint leaves (12.284 W/g) [41], sardine fish (14.1383 W/g) [42], pandanus leaves (13.6 W/g) [43].

3.4 Effect of drying on color parameters

Preferred colors are those closest to the original color of fresh sample. Product color is the other quality parameter that needs to be maintained during black radish drying. With the increase of the microwave power, black radish slices got higher L* value and higher b* value. The ΔL, Δa, Δb values of dried black radish slices color with 4, 6 and 8 mm were measured at the examined drying conditions ranging from -4.99 to 2.03, from -3.19 to -2.55 and from -13.25 to -3.53, respectively, for 1.05 kW and 0.175 m/min. The L*, a*, b* values of dried black radish slices color with 4, 6 and 8 mm were measured at the examined drying conditions ranging from -0.12 to 12.14, from -1.28 to -1.65 and from -6.64 to -4.47, respectively, for 1.5 kW and 0.175 m/min. The L*, a*, b* values of dried black radish slices color with 4, and 8 mm were measured at the examined drying conditions ranging from 7.48 to 17.28, from -3.9 to -5.13 and from -13.53 to -5.92, respectively, for 2.1 kW and 0.175 m/min.

The ΔL, Δa, Δb values of dried black radish slices with 4 mm, 6 mm and 8 mm were measured at the examined drying conditions ranging from -2.05 to 16.81, from -15.02 to 4.03 and from -16.12 to -15.02, respectively, for 1.05 kW and 0.245 m/min. The ΔL, Δa, Δb values of dried black radish slices color with 4, 6 and 8 mm were measured at the examined drying conditions ranging from -6.94 to 3.14, from -5.29 to 0.76 and from -15.53 to -12.56, respectively, for 1.5 kW and 0.245 m/min. The ΔL, Δa, Δb values of dried black radish slices color with 4, 6 and 8 mm at the examined drying conditions ranging from -15.06 to 5.61, from -0.21 to -0.86 and from -4.06 to -8.09, respectively, for 2.1 kW and 0.245 m/min. L* values of microwave oven (1.5 kW and 1.05 kW) dried samples were the highest among the other dried samples which were closer to the L* values of fresh sample for 0.175 m/min and 0.245 m/min. Microwave-dried (2.1 kW) sample had the lowest L* value. It is clear that the color values of the dried samples were different than each other. The experimental study also shows that, for the high microwave power levels, a little blackness occurs on the surface of the black radish. This is an important factor determining the quality of the product and, in order to avoid from the blackness, it requires the microwave power of less than 2.1 kW.

Krokida and Maroulis [44] showed that microwave drying prevented color damages during drying. High L* values are desirable in the dried foods [45]. The discoloration during drying may be related to nonenzymatic browning [46]. The change in color values was dependent on the microwave power intensity. Drying microwave power, time and conveyor belt are important parameters for color change during drying. The lower color degradation of microwave dried black radish slices may, therefore, be due to the substantial reduction in drying time. It is quite clear that microwave drying maintained the color quality of the fresh black radish slices compared to the hot air and microwave drying methods alone. Maskan [17] has reported the same results for dried banana. A similar trend was found by Maskan [47] for kiwi fruit microwave drying, increase in a* value and decrease in b* value.

3.5 Determination of energy consumption

The black radish was dried at a thickness of 4 mm at 1.05, 1.5 and 2.1 kW microwave powers (at 0.175 m/min) was measured as 108.38 kWh, 108.18 kWh and 104.99 kWh, as 108.49 kWh, 108.29 kWh and 107.40 kWh, for a 6 mm slice thickness as 109.10 kWh, 108.57 kWh and 107.93 kWh, respectively. The black radish was dried at 1.05, 1.5 and 2.1 kW microwave powers (at 0.245 m/min) was measured as 122.8 kWh, 122.3 kWh, 122.2 kWh for 4 mm slice thickness, as 123.3 kWh, 122.6 kWh, 122.2 kWh 6 mm slice thickness, as 123.6 kWh, 122.7 kWh and 122.3 kWh respectively. The black radish drying of 4 mm slice thickness at 1.05 kW, 1.5 kW and 2.1 kW (at 0.245 m/min) as 122.8 kWh, 122.3 kWh, 122.2 kWh, as 122.6 kWh,122.7 kWh, 122.3 kWh for 8 mm slice thickness, respectively. If the slice thickness increases, the energy consumed increases. If the microwave power increases, the energy consumed decreases. The minimum energy was seen as 104.99 kWh at 2.1 kW and 0.175 m/min for thickness of 4 mm. The maximum energy was found to be 123.6 kWh at 1.05 kW and 0.245 m/min for thickness of 8 mm.

3.6 Microstructure of dried black radish slices

The interface images of dry and wet samples were determined using the Scanning Electron Microscope (SEM). The interface images for 100 μm distance are clearer (Fig. 8-9). The SEM photos in the section of dried black radish slices showed distinct differences in the microstructure of black radish slices subjected to different microwave powers. Fresh samples, there are less open structures and pores as compared to dried samples, which indicates tissue shrinkage during microwave drying.

When the pores in wet and dry products were compared in terms of size, they grew by about 25-50 μm. Growth was observed at high vapor pressures due to the presence of moisture.

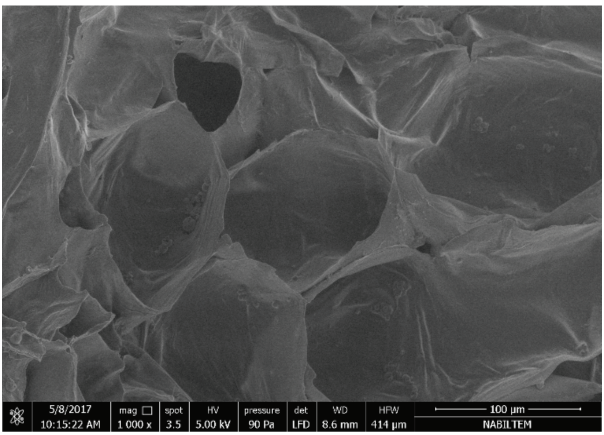

Figure 8. *Cross section observed by SEM (1000x) of fresh black radish*

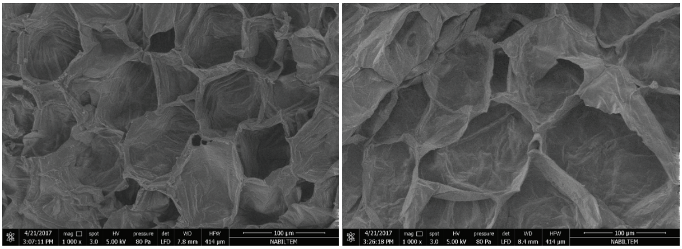

(a) (b)

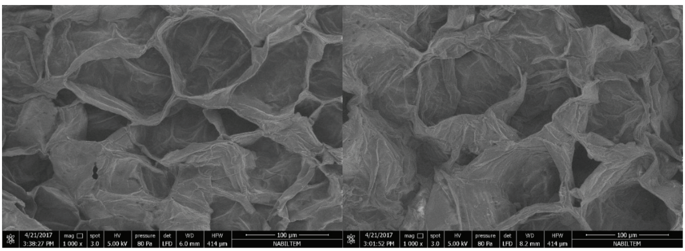

(c) (d)

Figure 9. ***Cross section observed by SEM (1000x) of black radish dried at difference conditions (a) 0.175 m/min / 500 W (b) 0.245 m/ min / 350 W (c) 0.245 m/min / 350 W (d) 0.245 m/min / 500 W***

4. CONCLUSIONS

In this study, the shortest drying time was found to be 36 minutes at 1.05 kW power. In terms of minimum energy consumption, it was determined as 104.99 kWh at microwave power of 2.1 kW, conveyor speed of 0.175 m / min and slice thickness of 4 mm. By increasing the microwave power applied to all slice thickness, drying time and energy consumption values were reduced. A low microwave power may lead to a low drying temperature and a slow drying rate; while a high microwave power may lead to an undesirable high temperature, may enhance the uneven distribution of the microwave energy, and may damage the quality of the final product.

When it's examined in terms of colour criterias, the best results were obtained for 1.05 kW and 0.175 m/min drying operations compared to the other experiments when (ΔL) values are taken into consideration.

On the other hand, it is clear that microwave drying can be performed in very short times compared to the other methods and the dried black radish have somewhat the same colors and odours as the fresh ones, which are very desirable properties by consumers and food industry.

For predicting seperable humidity rate (MR), Midilli model was chosen as the most predictive drying kinetics model with the comparisons made depending on the coefficients of the examined drying models with the highest R^2 value based on microwave power and slice thicknesses in all experiment conditions.

The experimental effective moisture diffusivities were around $1.334.10^{-7}$– $9.860.10^{-7}$ m^2/s for 1.05 kW – 2.1 kW ranges.

The SEM photos in the section of dried black radish slices showed distinct differences in the microstructure of black radish slices subjected to different microwave powers.

As a result, in microwave assisted conveyor drying applications, it can be said that working with the lowest speed belt possible will be more beneficial in terms of product quality. Furthermore, it can be said that this method is more suitable for drying fruits and vegetables where product color and other quality parameters are very important.

Nomenclatures

a, a_o, a_1, a_2, b,	drying constants
k, k_1, k_2, g, n	drying constants
a, b*, L**	color parameters
D_{eff}	effective moisture diffusivity, [m^2/s]
$\mathbf{D}_o$	Constant, [m^2/s]
$\mathbf{E_a}$	activation energy, [W/g]
L	half thickness of the slices, [m]
m	moisture content, [g water/g dry matter]
m_o	initial moisture content, [g water/g dry matter]
m_e	equilibrium moisture content
MSE	reduced chi-square
MR	dimensionless moisture ratio
$MR_{pre,i}$	ith predicted dimensionless moisture ratio
$MR_{exp,i}$	ith experimental dimensionless moisture ratio
n_o	number of observations
n_c	number of constants
P	microwave power, [W]
R	correlation coefficient
$RMSE$	root mean square error
t	drying time, [h]

5. References

[1] Akan, S., Veziroğlu, S., Özgün, Ö., Ellialtioğlu, Ş., 2013. Evaluation of Radish (Raphanus sativus L.) and the Using of this Vegetable as Functional Foods. *Yüzüncü Yıl University Journal of Agricultural Sciences*, **23**, 289-295.

[2] Kopta, T., Pokluda, R., 2013. Yields, quality and nutritional parameters of radish (Raphanus sativus) cultivars when grown organically in Czech Republic. *Horticultural Science (Prague),* **40**, 16-21.

[3] Castro-Torres, I.G., Naranjo-Rodriguez, E.B., Dominguez-Ortiz, M.A., Gallegos-Estudillo, J., Saavedra-Velez, M.V., 2012. Antilithiasic and hypolipidaemic effects of Raphanus sativus L. var. niger on mice fed with a lithogenic diet. *Journal of Biomedicine and Biotechnology,* 1-8.

[4] Loghmanieh, I., Bakhoda, H., 2013. Dehydration Characteristics and Mathematical Modeling of Thyme Leaves using the Microwave Process. *Global Journal of Science Frontier Research Physics and Space Science,* **13,** 14-21.

[5] Puligundla, P., Abdullah, S.A., Choi, W., Jun, S., Oh, S., Ko, S., 2013. Potentials of Microwave Heating Technology for Select Food Processing Applications - a Brief Overview and Update. *Journal of Food Processing & Technology,* **4**, 1-9.

[6] Kumar, V, Sharma, H. K., Singh, K., 2016. Mathematical Modeling of Thin Layer Microwave Drying of Taro Slices. *Journal of The Institution of Engineers (India): Series A*, **97**, 53-61.

[7] Kumar, Y., 2015. Application of Microwave in Food Drying. *International Journal of Engineering Studies and Technical Approach,* **6**, 9-24.

[8] Çelen, S., Kahveci, K., Akyol, U., Haksever, A., 2010. Drying Behavior of Cultured Mushrooms. Journal of Food Processing and Preservetion, 34, 27-42.

[9] Karaaslan, S., Tunçer, İ. K., 2009. Investigating of Drying Characteristics and Determining of a Drying Model for Microwave-Fan Assisted Convection Drying of Red Pepper. *KSU Journal of Natural Sciences*, **12**.

[10] Eren, Ö., Soysal, Y., Öztekin, S., Doğantan, Z. S. 2005. Mikrodalga Sistemi İle Donatılmış Bir Bantlı Kurutucuda Maydanoz Kurutulması", III. Tarımsal Ürünleri Kurutma Tekniği Çalıştayı, Antalya, Türkiye.

[11] Das, S., Mukhopadhyay, A. K., Datta, S., Basu, D., 2008. Prospects Of Microwave Processing: An Overview. *Bulletin of Materials Science*, **31**, 943-956.

[12] Sarimeseli, A., 2011. Microwave drying characteristics of coriander (Coriandrum sativum L.) leaves. *Energy Conversion and Management,* **52**, 1449-1453.

[13] Çelen, İ.H., Çelen, S., Moralar, A., Buluş, H. N., Önler, E., 2015. Mikrodalga bantlı kurutucuda patatesin kurutulabilirliğinin deneysel olarak incelenmesi. *Electronic Journal of Vocational Colleges- Special Issue: The Latest Trends in Engineering*, **5**, 242-287.

[14] Tulasidas, T. N., Ratti, C., Raghavan, G. S. V., 1997. Modelling of microwave drying of grapes. *Canadian Agricultural Engineering*, **39**, 57-67.

[15] Çelen, S., Haksever, A, Moralar, A., 2017. The Effect of Microwave Energy to the Drying of Apple (Gala) Slices. *Karaelmas Science and Engineering Journal*, **7**, 228-236.

[16] Litvin, S., Mannheim, C. H., Miltz, J., 1998. Dehydration Of Carrots By A Combination Of Freeze drying, microwave heating and air or vacuum drying. *Journal of Food Engineering,* **36**, 103-111.

[17] Maskan, M., 2000. Microwave/air and microwave finish drying of banana. *Journal of Food Engineering*, **44,** 71-78.

[18] Darvishi, H., Asl, A. R., Asghari, A., Azadbakht, M. Najafi, G., Khodaei, J., 2014. Study of the drying kinetics of pepper. *Journal of the Saudi Society of Agricultural Sciences,* **13**, 130–138.

[19] Sharma, G. P., Prasad, S., 2001. Drying of garlic (Allium sativum) cloves by microwave-hot air combination. *Journal of Food Engineering,* **50**, 99-105.

[20] Tahmasebi, A., Yu, J., Han, Y., Zhao, H., Bhattacharya, S., 2014. Kinetic study of microwave and fluidized-bed drying of Chinese lignite. *Chemical Engineering Research and Design,* **92**, 54–65.

[21] Simha, P., Mathew, M., Ganesapillai, M., 2016. Empirical modeling of drying kinetics and microwave assisted extraction of bioactive compounds from Adathoda vasica and Cymbopogon citratus. *Alexandria Engineering Journal*, **55**, 141-150.

[22] Dinani, S. T., Hamdami, N., Shahedi, M., Havet, M., 2014. Mathematical modeling of hot air/electrohydrodynamic (EHD) drying kinetics of mushroom slices. *Energy Conversion and Management*, **86,** 70-80.

[23] Kutlu, N., İşci, A., Demirkol, Ö. Ş., 2015.Gıdalarda İnce Tabaka Kurutma Modelleri. *The Journal of FOOD,* **40**, 39-46.

[24] Kahveci, K., Cihan, A., 2008. Drying of Food Materials: Transport Phenomena, Nova Science, New York, USA.

[25] Roberts, J. S., Kidd, D. R., Padilla-Zakour, O., 2008. Drying kinetics of grape seeds. *Journal of Food Engineering,* **89**, 460–465.

[26] BI, J., Yang, A., Liu, X., Wu, X., Chen, Q., Wang, Q., Lv, J., Wang, X., 2015. Effects of pretreatments on explosion puffing drying kinetics of apple chips. *LWT - Food Science and Technology,* **60**, 1136-1142.

[27] Zlatanovic´, I., Komatina, M., Antonijevic´, D., 2013. Low-temperature convective drying of apple cubes. *Applied Thermal Engineering*, **53**, 114–123.

[28] Demirhan, E., Özbek, B., 2008. Microwave-Drying Characteristics of Basıl. *Journal of Food Processing and Preservation,* **34**, 476-494.

[29] Abano, E. E., Haile, M.A, Owusu, J., Engmann, F.N., 2013. Microwave-vacuum drying effect on drying kinetics, lycopene and ascorbic acid content of tomato slices. *Journal of Stored Products and Postharvest Research*, **4**, 11 – 22.

[30] Zarein, M., Samadi, S.H., Ghobadian, B., 2015. Investigation of microwave dryer effect on energy efficiency during drying of apple slices. *Journal of the Saudi Society of Agricultural Sciences*, **14**, 41–47.

[31] Çelen, S., Kahveci, K.,2013. Microwave drying behavior of tomato slices. *Czech Journal of Food Sciences,* **31,** 132-138.

[32] Farhang, A., Hosainpour, A., Darvishi, H., Nargesi, F., 2011. Shrimp Drying Characterizes Undergoing Microwave Treatment. *Journal of Agricultural Science,* **3**, 157-164.

[33] Doymaz, I., 2004. Effect of dipping treatment on air drying of plums. *Journal of Food Engineering,* **64**, 465-470.

[34] Chinenye, N.M., 2009. Effect of Drying Temperature and Drying Air Velocity on the Drying Rate and Drying Constant of Cocoa Bean. Agricultural Engineering International: the CIGR Ejournal. Manuscript, 1091, **11**.

[35] Lee, J. H., Kim, H. J., 2009. Vacuum drying kinetics of Asian white radish (Raphanus sativus L.) slices. *LWT - Food Science and Technology,* **42**, 180–186.

[36] Sharma, G.P., Prasad, S., 2001. Drying of garlic (Allium sativum) cloves by microwave-hot air combination. *Journal of Food Engineering,* **50**, 99–105.

[37] Soysal, Y., 2004. Microwave drying characteristics of parsley. Biosystems Engineering, 89, 167-173.

[38] Maskan, A., Kaya, S., Makan, M., 2002. Hot air and sun drying of grape leather (pestil). *Journal of Food Engineering*, **54**, 81–88.

[39] Torki-Harchegani, M., Ghanbarian, D., Sadeghi, M., 2015. Estimation of whole lemon mass transfer parameters

during hot air drying using different modelling methods. *Heat Mass Transf*er. **51**, 1121–1129.

[40] Dadali, G., Apar, D.K., Ozbek, B., 2007. Microwave Drying Kinetics of Okra. *Drying Technology,* **25**, 917-924.

[41] Ozbek, B., Dadali, G., 2007. Thin-layer drying characteristics and modelling of mint leaves undergoing microwave treatment. *Journal of Food Engineering,* **83**, 541-549.

[42] Darvishi, H., Azadbakht, M., Rezaieasl, A., Farhang, A., 2012. Drying characteristics of sardine fish dried with microwave heating. *Journal of the Saudi Society of Agricultural Sciences*, **12**, 121-127.

[43] Rayaguru, K., Routray, W., 2011. Microwave drying kinetics and quality characteristics of aromatic Pandanus amaryllifolius leaves. *International Food Research Journal*, **18,** 1035-1042.

[44] Krokida, M.K., Maroulis, Z.B., 1999. Effect of microwave drying on some quality properties of dehydrated products. *Drying Technology,* **17**, 449-466.

[45] Doymaz I., Tugrul N., Pala M., 2006. Drying Characteristics of Dill and Parsley Leaves. *Journal of Food Engineering,* **77**, 559 -565.

[46] Feng, H., Tang, J., 1998. Microwave finish drying of diced apples in spouted bed. *Journal of Food Science,* **63**, 679-683.

[47] Maskan, M., 2001. Kinetics of colour change of kiwifruits during hot air and microwave drying. *Journal of Food Engineering,* **48**, 169 – 175.

GECE AKADEMİ

www.gecekitapligi.com

/gecekitapligi /gecekitapligi
/gecekitap